INFN - LNS

Laboratori Nazionali del Sud

ISTITUTO NAZIONALE DI FISICA NUCLEARE

Via Santa Sofia 62 Catania - Italy
+39 095 542111
sis@lns.infn.it
www.facebook.com/infn.lns
twitter: @LNS_INFN
instagram: @lns_infn
www.lns.infn.it
ISSN 1827-1561

ACTIVITY REPORT 2019/2020 INFN - LNS

Laboratori Nazionali del Sud

ACTIVITY REPORT 2020

LNS Director
Santo Gammino
Editorial Staff
Gaetano Agnello
Rosalia Di Mauro
Enzo Greco
Stefano Romano
Aurora Tumino
Cover design and layout
Gresy Torrisi

INFN

LNS

Istituto Nazionale di Fisica Nucleare

Laboratori Nazionali del Sud

•. FOREWORD

It is difficult to summarize the progress of the scientific activities at the LNS during 2020, as it was a weird year for the European and world society and many of the well-established convictions were miserably shredded because of the pandemy and of the resulting limitations. Still in this context, the simple fact that the most of these activities did not stop completely during the lockdown and that immediately after the end of the lockdown many experimental activities restarted, it may be mentioned as a remarkable success for our community. Certainly, some time was unavoidably lost, a number of experiments was postponed and international collaborations were restricted to online meetings, not always so fruitful as vis-à-vis meetings. Nevertheless, LNS research activities obtained a valuable number of achievements and also the technical activities did significant progresses even during the period of limitations of the access to the Laboratories. It is particularly important for the future of LNS that the phases of the upgrading, named POTLNS, kept their pace and did not shift except for one. The cyclotron's cryostat shutdown was a dramatic moment, after more than a quarter of century of activity, and it is great that we can consider it not as an end point but rather a new beginning. Another key activity that increased its pace was the preparation of the detection units for KM3NET: the work done in the previous years led to the preparation of high-quality devices ready to be deployed once that the marine operation could occur, that happened in April 2021.
Let me conclude by saying that INFN-LNS is not only working for the "big projects" but a long list of activities in Astroparticle and Nuclear Physics, in Theoretical and Applied Physics, deserve to be mentioned for their progress in this year. It is not useful to mention the progress of each activity that is better shown in the following pages; I just wish to underline that the quality of the paper is probably higher than in any "normal" year. Therefore I wish to express my gratitude to all people (researcher, technicians, administrative staff, coworkers) as they demonstrated that the LNS community has well interpreted the mission to keep high the level of research in this "weird" year.
We may be satisfied, one can think by reading my words…no, it's not the case as we missed the open access to students coming from all over Sicilian schools and other Italian regions and to the local community, except for a downsized edition of the Researchers' Night and few more occasions. The Visitor Center inaugurated in 2019 could not be adequately used; the limitation of the public engagement activity was disappointing and it must be recovered as soon as possible. To recover and reinforce such a connection will be a key mission for the next years.

Santo Gammino
INFN – LNS Director
gammino@lns.infn.it

REMEMBERING JOHN STUART WINFIELD

John Stuart WINFIELD passed away suddenly at Leicester Royal Infirmary on Tuesday 23rd February 2021, aged 63 years, soon after his retirement as an outstanding physicist. In his long and multifaceted career he had the chance to share with the LNS community almost nine year of his life, giving a big contribution to the laboratory, namely to the construction of the MAGNEX spectrometer.

He reached Catania in 1998, carrying a large experience in experimental nuclear physics maturated in more than a decade spent as physicist at the National Superconducting Cyclotron Laboratory, East Lansing, Michigan and three years at GANIL, at IPN Orsay and LPC Caen. When we met him we were astonished by the fact that, silently he was practically able to complete every single task in a professional way and in time. His competences on magnetic spectrometry, on charge exchange reactions, detector technology, including electronics and data acquisition, together with an excellent capability in programming, made him a key resource to transform MAGNEX from a project to the powerful research tool that everybody can see.

Nonetheless, John was a gentleman, with a rare attitude to politeness and empathy. He was the right person to speak to, even beyond physics, at the coffee break or during a long night shift. He was a very cultured person, getting his master Degree at the Imperial College in London and his Ph.D. at Oxford, which left him the passion for literature, arts, politics, sports and society. He had the rare capability to listen to people, always with his delicate touch, certainly tuned by his weak health conditions, which made him deeply aware of human sufferings.

The heritage that John have left to our community is particularly relevant and we really wish to thank him very much for that!

SPECIAL CONTRIBUTION

The POTLNS project status: internal and external activities

V. P. Bonanno[1], C. Manna[1], A. Miraglia[1], M. S. Musumeci[1], A. D. Russo[1], G. Torrisi[1], G. Vecchio[1]

1) Istituto Nazionale di Fisica Nucleare - Laboratori Nazionali del Sud, via S. Sofia 62, 95123 Catania, Italy

Abstract – The POTLNS project started in June 2019 with the official MUR notification of funding approved. This document reports the POTLNS current status from a project management perspective.

It describes the status of procurement process; the methodology used to lead and monitor the project status and the most relevant internal activities for preparing the facility to the upgrade.

INTRODUCTION

The POTLNS project has been selected and financed by the *National Operative Programme – Research and Innovation 2014 – 2020.* The aim is to upgrade the LNS Research Infrastructure in order to produce high intensity ion beams, mandatory for the next future nuclear reaction studies. To guarantee the achievement of PON requirements and projects' objectives, a Quality Assurance/Quality Control (QA/QC) system has been defined and implemented.

The procurement phase and the reporting activities to MUR are considered strategically relevant for the POTLNS project and its objectives. It is therefore essential that these processes are well-defined and continuously improved in the context of a preventive approach to projects' risks.

The Earned Value Management (EVM) has been chosen to monitor the project deviation respect to the baseline in terms of schedule, cost and budget variances.

LNS are currently involving in a set of logistic activities for preparing and organizing the facility to upgrade such as the disassembling of the Superconducting Cyclotron and the dismantling of some experimental rooms.

This document describes the project organization approach and the tools used to match both the factors external to the project and the ones related to the internal activities of the LNS organization.

QA: PROCUREMENT PROCESS AND REPORT

The procurement phase consists in **a) tender procedure** that includes the call of tender preparation, execution and the award to the best offer; **b) procurement execution and deployment on site** and **c) reporting to MUR**. Each process phase, shown in Figure 1, is characterised by a set of specific activities and documents which must be produced. Much of the documents produced during the tender phase have been standardized in templates (approx. 25) to optimize the efficiency and effectiveness.

Figure 1: procurement process: from call of tender preparation to reporting

The project's documentation is shared on SharePoint platform – in draft version - within the PM office and on Alfresco by using a custom document management system, called "SIstema di GEstione DOcumentale – SIGEDO" which allows to involve suppliers in the procurement phase and to manage the Acceptance Levels, as shown in Figure 2.

Figure 2: a sketch of SIGEDO with the AL1 completed

Every time a SAL is accomplished, for each supply it is mandatory to report in the MUR website the incurred cost together with a required set of documents.

Currently, the status of tendering procedures is shown in Figure 3. The number of calls of tender awarded and launched are twelve, which corresponding at 96% of MURs' budget collocation.

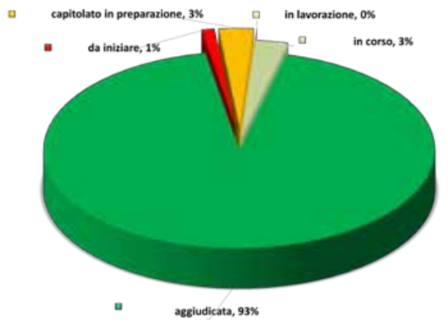

Figure 3: calls of tender status

QC: PROJECT MONITORING AND EVM METHODOLOGY

In order to monitor the status of subproject procurement, every six months a forecast has been tracked to check the deviation respect to the baseline. In March 2021 the forecasting schedule, in Figure 4, shows that there are some deviations with respect to the baseline, related to:

1. call for tendering
2. procurement execution.

Figure 4: half-yearly forecast of supplies - March 2021

In the first case, the deviation is mainly due to a setback on the activities for signing the contracts with the suppliers. In the second one, the deviation is ascribable to raw material shortage due to pandemic emergency and, in turn, procurement of raw material itself.

To monitor the project in terms of schedule, cost and budget, the Earned Value Management analysis has been carried out together with the periodical forecasting schedule. It consists in evaluating the project performance by using the *schedule variance* as effectiveness measure, the *cost variance* as efficiency measure and the *budget variance* to understand how rapidly the budget has been collocated.

In the context of POTLNS project, the **EVM parameters** are defined as follows:

- ***BCWS*** *(budget cost of work scheduled)* is the budget planned and funded by MUR.
- ***ACWP*** *(actual cost of work performed)* is the cost actually incurred at the current date, in other words the cost reported to MUR.
- ***BCWP*** *(budget cost of work performed)* or **earned value**, is the value of deliverables released at measurement data.

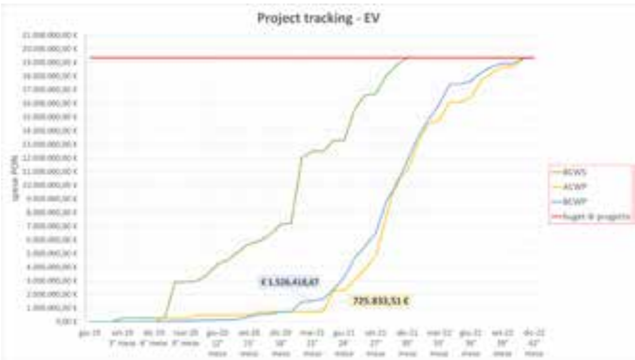

Figure 5: project tracking by using the EV analysis

At measuring date (March 2021) the SV<0 indicates that the completed work was less than the planned one; the CV>0 indicates a lower cost of performance to date; BV>0 demonstrates that the cost reported at MUR (ACWP) is lower than the earned valued (BCWP) (see Figure 5).

LNS PREPARATION FOR THE UPGRADE

Since April 2020 the Laboratori Nazionali del Sud is involved in logistic activities for preparing the facility to the upgrade. The planning had to consider the performing of some external activities related to procurement phase, such as the beam line installation and the concrete shielding realization. In Figure 6 a schematization, on time, of experimental rooms involved in internal/external activities is shown.

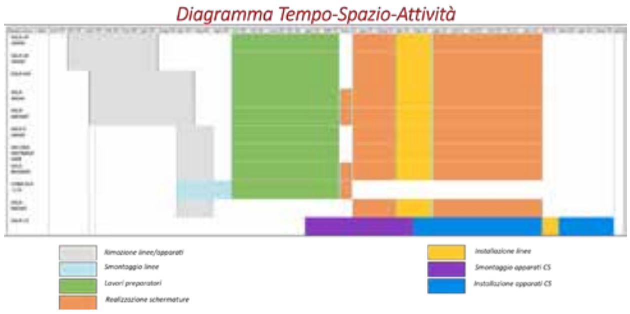

Figure 6: time-space-activities diagram

Before starting with the digging out and the strengthening of embankment, some experimental rooms located in the areas involved in "lavori preparatori" have been dismantled (e.g., ZD room, 20/40-degree rooms, MAGNEX room).

Meanwhile, since October 2020 the LNS personnel has been working on the CS disassembling. I.e., in March 2021 the RF cavities have been removed from the CS as planned in Figure 7.

Figure 7: GANTT chart for disassembling the CS

CONCLUSIONS

The procurement process and the internal activities for preparing LNS to upgrade are in progress although with a acceptable time shift. The project management approach, briefly described in this document, will be used for leading the final phases of the project (installation and commissioning).

REFERENCES

[1] Project Management Institute, *Project Management Body of Knowledge (PMBOK) Guide*, 4th edition, Project Management Institute, (2013).

INDEX

•. EXPERIMENTAL NUCLEAR PHYSICS AND ASTROPHYSICS

ASTROPARTICLE PHYSICS

THEORETICAL NUCLEAR PHYSICS

INSTRUMENTATION AND RELATED TECHNIQUES

ION SOURCES AND ACCELERATORS

•. INTERDISCIPLINARY PHYSICS

EXPERIMENTAL NUCLEAR PHYSICS AND ASTROPHYSICS

Transfer reactions to populate the PDR in ^{96}Mo

T.C. Khumalo[a,b], L. Pellegri[a,b], M. Wiedeking[a,b], F. Cappuzzello[c,d], M. Cavallaro[c], D. Carbone[c], A. Spatafora[c,d], P. Adsley[a,b], C. Agodi[c], G. Brischetto[c,d], S. Calabrese[c,d], I. Ciraldo[c,d], J. Isaak[f], H. Jivan[a,b], S. Jongile[a,e], L. La Fauci[c], E.G. Lanza[c,d], K. L. Malatji[a], A. Netshiya[a,b], R. Neveling[a], E. Sideras-Haddad[a,b], O. Sgouros[c], V. Soukeras[c], D. Torresi[c]

[a] *iThemba LABS, Cape Town, South Africa*

[b] *University of Witwatersrand, Johannesburg, South Africa,*

[c] *INFN Laboratori Nazionali del Sud, Catania, Italy,*

[d] *Universita di Catania, Catania, Italy,*

[e] *Stellenbosch University, Stellenbosch, South Africa,*

[f] *Technische Universität Darmstadt, Darmstadt, Germany.*

Abstract -The study here presented is an attempt to investigate the nature of the pygmy dipole resonance by exploiting the sensitivity of one-particle transfer reactions. The measurements on transfer reactions (p,d) and (d,p) were performed on two different targets to populate the ^{96}Mo resdual nucleus. The ejectiles were detected, identified and momentum-analyzed by the MAGNEX spectrometer installed at the Laboratori Nazionali del Sud (INFN-LNS) in Catania.

INTRODUCTION

The Pygmy Dipole Resonance (PDR), which is a concentration of 1^- states around the neutron separation energy (S_n), has thus far only been observed in neutron-rich nuclei. Bracco *et al.* [1] and Savran *et al.* [2] recently conducted detailed reviews on the PDR, outlining the progress made in the study of dipole excitation. Macroscopically, the PDR was interpreted using the hydrodynamical model as an oscillation of a neutron skin against a proton-neutron core. A substantial amount of work has been done to try to explain the PDR microscopically and, among the different models used, the quasi-particle random phase approximation (QRPA), the relativistic QRPA (RQRPA), and the quasi-particle phonon model (QPM) have been found to best describe the PDR when compared to available experimental results. Significant amount of work has also been done experimentally to study the PDR in order to understand its nature. Previous studies show that the PDR is very probe sensitive and, therefore, two different types of experiments conducted on the same nucleus might give complimentary information on the nature of the PDR. An example where experiments using different probes (isoscalar and isovector) on the same nucleus ^{140}Ce, are compared in ref. [3]. Alpha particles which are considered an isoscalar probe and, thus, will excite only the isoscalar part of the nuclear response are compared to real photons which interact with the whole nucleus, exciting both the isoscalar and the isovector parts of the PDR. The result observed for the ^{140}Ce has also been found in other neutron-rich nuclei raising questions about the isospin mixing of these pygmy states [1]. The interpretation of this excitation mode is not yet clear and lately the collectivity of these states has also been put under scrutiny. At an attempt to interpret this dipole excitation mode some theoretical studies [4, 5] found that although the low-lying states cannot be considered as collective as the Giant Dipole Resonance states, they also cannot be described as a single particle-hole configuration. The response of the PDR to an isovector operator does not show a clear collective nature since the several particle-hole configurations do not contribute coherently to the pygmy state wave function. Contrarily, there are other studies [6,7] where single-particle behaviour of the PDR strength is predicted in relation the observed strong fragmentation, which could be influenced by single-particle shell effects. In attempt to answer this question, direct reactions, specifically transfer reactions owing to their selectivity for exciting single-particle (hole) states, were considered in this work.

THE EXPERIMENT

Two types of transfer reactions, (d,p) and (p,d) on ^{95}Mo and ^{97}Mo respectively, were conducted in order to probe the single-particle/hole configurations of ^{96}Mo. In this report only the data reduction for the (p,d) reaction will be discussed. The thickness of the targets used was 0.6 mg/cm^2 for the (d,p) reaction and 0.4 mg/cm^2 for the (p,d) reaction. During the experiment, the 14-MV Tandem accelerator delivered 10-MeV deuteron and 25-MeV proton beams which impinged on the ^{95}Mo and ^{97}targets, respectively, to excite ^{96}Mo. These energies were chosen because the selectivity of the transfer reactions, especially with light ions, is enhanced at moderate projectile energies [8]. The data were collected for approximately 234 hours at a beam current ranging between 0.9 nA and 5 nA for both reactions. The MAGNEX magnetic spectrometer was used to detect the reaction products [9]. The data were collected at three different angular settings, namely 10^o, 17^o and 24^o in order to allow the measurement of the angular distribution of the scattered particles and deduce the spin/parity of the excited states. The field settings were changed to measure a wide excitation-energy region, up to 8 MeV.

THE DATA REDUCTION PROCESS

The data reduction of the (p,d) reaction measurement is almost completed for the 17^o angular setting. The first part of the analysis consisted of the identification of the scattered deuterons. This information was extracted combining the measurement of the energy loss (ΔE) or the horizontal position (X_f) in the gaseous part of the focal plane detection system with the residual energy (E_{res}) in the silicon detectors. An example of the ΔE-E_{resid} and the X_f-E_{resid} matrices for one silicon detector are shown in Fig. 1 and 2, respectively. Here the scattered particles are clearly identified. Once the deuterons were selected, the vertical position calibration of the focal plane was performed. This procedure allowed extracting the vertical position (Y_f) and the vertical angle (Φ_f) for the events of interest. Since MAGNEX is a large-acceptance spectrometer, a ray-reconstruction software based on a 10^{th}-order transport matrix was applied to the experimental data to extract the excitation energy and initial phase space parameters. The MAGNEX magnetic spectrometer allows particle identification with energy resolution of ($\Delta E/E \sim 1/1000$) [9]. However, the energy resolution is also affected by the energy loss in the target. The preliminary estimation of the energy resolution for the (p,d) reaction is ~40-keV FWHM. Currently underway is the data reduction process for optical angles of 10^o and 24^o.

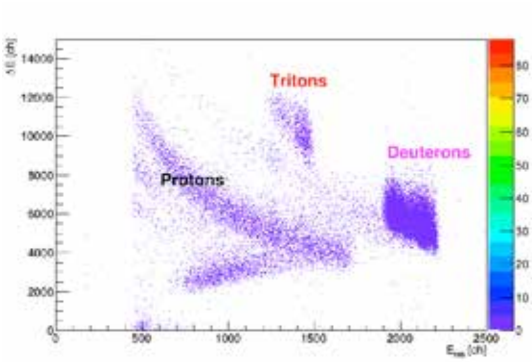

Figure 1: The ΔE-E representation for a silicon detector extracted from the $^{97}Mo(p,d)^{96}Mo$ data collected at an optical angle of 17^o.

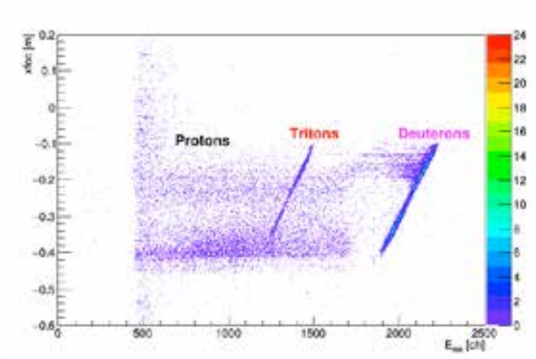

Figure 2: The X_f -E_{resid} representation for one silicon detector extracted from the $^{97}Mo(p,d)^{96}Mo$ data collected at an optical angle of 17^o.

CONCLUSION & FUTURE WORK

The different excited states will be identified and their cross section will be extracted. Comparing experimental data with DWBA calculations enables the extraction of the spectroscopic factor with the Clebsch-Gordon coefficient factor (C^2S). This provides information about the single-particle nature of the populated states. Angular distributions of the scattered particles will be used to determine the spin and parity of the observed states. The results will be compared to theoretical predictions and other experimental data available for ^{96}Mo.

ACKNOWLEDGEMENTS

This work is based on the research supported in part by the National Research Foundation (NRF) of South Africa (grant number 118846).

REFERENCES

1. A. Bracco, E.G. Lanza and A. Tammi, Prog. in Part. Phys. and Nucl. Phys. **106** (2019) 360.

2. D. Savran *et al.*, Prog. in Part. Phys. and Nucl. Phys. **70** (2013) 210.

3. D. Savran *et al.,* Phys. Lett. B **786** (2018) 16.

4. E. Lanza et al. Phys. Rev. C, vol. 79, p. 054615, 2009.

5. X. Roca-Maza et al. Phys. Rev. C, vol. 85, p. 024601, 2012.

6. P.-G. Reinhard and W. Nazarewicz Phys. Rev. C, vol. 81, p. 051303(R), 2010.

7. D. Gambacurta et al. Phys. Rev. C, vol. 84, p. 034301, 2011.

8. H. Feshbach, Theoretical Nuclear Physics: Nuclear Reactions, *Volume 2,* Wiley Classics Library, 1992

9. M. Cavallaro *et al.,* Nucl. Instru. and Meth. B **463**(2020)334

Experimental and theoretical multi-channel study applied to the $^{12}C(^{18}O,^{18}F)^{12}B$ single charge exchange nuclear reaction at 275 MeV

A. Spatafora[1,2], F. Cappuzzello[1,2,3], D. Carbone[1], M. Cavallaro[1], L. Acosta[4], C. Agodi[1], P. Amador-Valenzuela[5], T. Borello-Lewin[6], G. A. Brischetto[1,2], S. Calabrese[1,2], D. Calvo[7], V. Capirossi[7,8], E. R. Chávez-Lomeli[4], I. Ciraldo[1,2], F. Delaunay[7,9], H. Djapo[10], C. Eke[11], P. Finocchiaro[1], S. Firat[11], M. Fisichella[1], A. Foti[13], A. Hacisalihoglu[12], F. Iazzi[7,8], L. La Fauci[1,2], R. Linares[14], N. H. Medina[6], M. Moralles[15], J. R. B. Oliveira[6], A. Pakou[16], L. Pandola[1], H. Petrascu[17], F. Pinna[7,8], G. Russo[2,13], O. Sgouros[1], M. A. G. da Silveira[18], S. O. Solakci[11], G. Souliotis[19], V. Soukeras[1], D. Torresi[1], S. Tudisco[1], A. Yildirin[11], V. A. B. Zagatto[15] for the NUMEN Collaboration

1) *Istituto Nazionale di Fisica Nucleare, Laboratori Nazionali del Sud, Catania, Italy*
2) *Dipartimento di Fisica e Astronomia "Ettore Majorana", Università di Catania, Italy*
3) *Centro Siciliano di Fisica Nucleare e Struttura della Materia, Italy*
4) *Instituto de Física, Universidad Nacional Autónoma de México - México City, México*
5) *Instituto Nacional de Investigaciones Nucleares - Ocoyoacac, México*
6) *Instituto de Fisica, Universidade de Sao Paulo - Sao Paulo, Brazil*
7) *Istituto Nazionale di Fisica Nucleare, Sezione di Torino, Italy*
8) *DISAT, Politecnico di Torino, Italy*
9) *LPC Caen, Normandie Université, ENSICAEN, UNICAEN, CNRS/IN2P3 Caen, France*
10) *Ankara University, Institute of Accelerator Technologies, Turkey*
11) *Department of Physics, Akdeniz University - Antalya, Turkey*
12) *Institute of Natural Sciences, Karadeniz Teknik University - Trabzon, Turkey*
13) *Istituto Nazionale di Fisica Nucleare, Sezione di Catania, Italy*
14) *Instituto de Fisica, Universidade Federal Fluminense - Niteroi, Brazil*
15) *Instituto de Pesquisas Energeticas e Nucleares IPEN/CNEN - São Paulo, Brazil*
16) *Department of Physics and HINP, University of Ioannina - Ioannina, Greece*
17) *IFIN-HH - Magurele, Romania*
18) *Centro Universitario FEI - Sao Bernardo do Campo, Brazil*
19) *Department of Chemistry, National and Kapodistrian University of Athens, Athens, Greece*

Abstract – A broad net of nuclear reactions coming from the ^{18}O + ^{12}C collision was studied to test the capability of state-of-art nuclear structure and reaction theories in describing the direct and transfer components involved in the (^{18}O, ^{18}F) single charge exchange nuclear reactions of interest for the NUMEN collaboration. The experiment, performed by using the MAGNEX magnetic spectrometer and the ^{18}O beam at 275 MeV incident energy produced by the K800 superconductive cyclotron, and the theoretical analysis have been made in Catania, at the Laboratori Nazionali del Sud of the Istituto Nazionale di Fisica Nucleare (LNS-INFN).

INTRODUCTION

A full understanding of the reaction mechanisms involved in double charge exchange (DCE) and single charge exchange (SCE) nuclear reactions is mandatory for the purposes of the NUMEN project. The main goal of the collaboration is indeed to study DCE nuclear reactions to extract information about the Nuclear Matrix Elements (NMEs) of interest in the context of neutrino-less double beta decay ($0\nu\beta\beta$) [1].

Although the theoretical connection between measured cross sections of DCE nuclear reactions and the $0\nu\beta\beta$ NMEs was the most interesting and debated aspect, a crucial point in this context is the capability of the state of art nuclear theories to give the clearest and the most complete description of the DCE reaction mechanism. The direct DCE, called *Majorana* DCE (MDCE) [2] in analogy to the direct $0\nu\beta\beta$ Majorana process, is only part of the complete DCE mechanism.

Although recent studies are excluding a relevant role of the multi-nucleon transfers [3], the role of the double-SCE (DSCE) is to date far from the hypothesis to be considered negligible. In that case the DSCE contribution to the total DCE can be estimated considering a folding of two SCE reaction amplitudes [4]. For that reason, it is particularly important to improve the description of the SCE process with the special purpose of factorizing the corresponding cross section into reaction and structure parts.

The first goal of this work is to produce new experimental data of the angular distributions and energy spectra differential cross-sections measured in the same experiment at the LNS-INFN for a broad network of nuclear reactions induced by the ^{18}O + ^{12}C collisions at 275 MeV. A second goal is to theoretically analyse the experimental data using state-of-art nuclear structure and reaction theories in a unique comprehensive and coherent theoretical calculation. The holistic approach, applied both to the experimental and the theoretical analysis, is the main feature and novelty of the work here presented and justifies the interest of the NUMEN collaboration.

EXPERIMENT AND PRELIMINAR RESULTS

The $^{18}O^{8+}$ beam was accelerated up to 275 MeV by the K800 Superconductive Cyclotron of INFN-LNS. The fully stripped ^{18}O ions impinged on the ^{12}C target located in the object point of the MAGNEX magnetic spectrometer [5], inside its scattering chamber. The 63 ± 3 μg/cm^2 thick ^{12}C isotopically enriched self-supporting target has been built in the INFN-LNS Target Lab and used during the first measurements performed in November 2012. A second measurement was performed in November 2018 using 80 ± 4 μg/cm^2 natural carbon target in similar experimental conditions.

A Faraday cup of 0.8 cm entrance diameter and 3 cm depth, mounted 15 cm downstream of the target, was used to stop the beam and collect the charge. An electron suppressor polarized at -200 V and a low noise charge integrator allowed to keep the charge collection accuracy better than 10% in all the experiment runs.

The ejectiles, produced in the reactions were momentum analysed in different runs in which the optical axis of MAGNEX was oriented, compared to the beam direction, at θ_{opt} = 7.5° and 13.5° in the 2012 and 8° in 2018 measurement. The MAGNEX entrance solid angle was set in the full acceptance configuration (≈50 msr) in the 2012 and it was reduced in the vertical dimension to ≈14 msr during the 2018 measurement by means of slits located at the entrance of the spectrometer. The beam current was optimized at each optical angle configuration in order to reach event rates tolerable by the focal plane detector (FPD) [6]. The overall range of polar angles in the laboratory framework was 3° < θ_{LAB} < 18°.

The magnetic fields of the dipole and quadrupole magnets were set in order to transport the $^{18}F^{9+}$, $^{19}F^{9+}$, $^{17}O^{8+}$ and $^{16}O^{8+}$ ions corresponding to the ejectiles of the nuclear reactions of interest in the region of momentum covered by the FPD. The study of the elastic and inelastic scattering was performed in a different magnetic set because of the magnetic rigidity of the $^{18}O^{8+}$ is too different with respect to the ones of the other ions to be detected in the same magnetic set.

The data reduction strategy includes the position calibration of the FPD, identification of the ejectiles and reconstruction of the momentum vector at the target by inversion of the transport equations following the guidelines presented in previous publications [7]. The accurate set-up and the advanced data reduction have allowed to produce high resolution energy spectra and angular distributions for the many analysed channels.

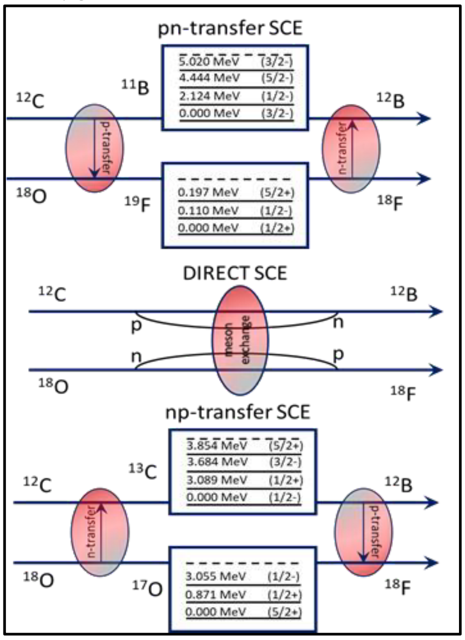

Figure 1 Schematic representation of the three reaction paths involved in the nuclear reaction analysis of the $^{12}C(^{18}O,^{18}F)^{12}B$ SCE at 275 MeV incident energy.

The experimental and theoretical study of the $^{12}C(^{18}O,^{18}O)^{12}C$ elastic and inelastic scattering was performed to access the initial state interaction (ISI) responsible for the distortion of the many-body wave functions of the incoming nuclei. The role of the ISI is crucial to properly describe all the direct nuclear reaction channels.

The $^{12}C(^{18}O,^{16}O)^{14}C$ two-neutron transfer reaction has been already analysed and the results, recently published [8], have confirmed the observation of the giant pairing vibration (GPV). Such observation clarified how the many body nature of the pairing interaction plays a relevant role in the dynamic of the direct reactions in which pairs of nucleons are involved.

In addition to the role of the ISI and the many-body properties of the nuclear wave functions involved in the studied reactions, the most crucial and debated aspect in the study of the SCE nuclear reactions is the competition between the direct process, proceeding via the deeply studied meson-exchange [2] and the sequential neutron-proton or proton-neutron transfer processes. The three main paths and the first excited states of the intermediate partitions involved in the SCE nuclear reaction analysis are shown in Figure 1. The $^{12}C(^{18}O,^{19}F)^{11}B$ one-proton knock-out and the $^{12}C(^{18}O,^{17}O)^{13}C$ one-neutron pick-up reaction channels have been analysed to constraint the single particle components of the many-body nuclear wave functions of the involved nuclei.

ACKNOWLEDGEMENTS

This project has received funding from the European Research Council (ERC) under the European Union's Horizon 2020 research and innovation programme (NURE project, grant agreement No 714625).

REFERENCES

[1] F. Cappuzzello et al., Eur. Phys. J. A (2018) **54**: 72
[2] H. Lenske et al. Prog. in Part. Nucl. Phys. (2019) **109**: 103716
[3] D. Carbone et al. Phys. Rev. C (2020) **102**: 044606
[4] J. I. Bellone et al., Phys. Lett. B (2020) **807**: 135528
[5] F. Cappuzzello et al., Eur. Phys. J. A (2016) **52**: 167
[6] M. Cavallaro et al., Eur. Phys. J. A (2012) **48**: 59; D. Torresi et al, Nucl. Instrum. Methods A (2021) **989:** 164918.
[7] A. Spatafora et al. Phys. Rev. C (2019) **100**: 034620
[8] F. Cappuzzello et al. Eur. Phys. J. A (2021) **57**: 34

The $^{14}N + ^{16}O$ and $^{14}N+^{12}C$ experiments to assess carbon burning at astrophysical energies via the THM

A. Tumino[1,2], N. Soić[3], P.M. Prajapati[2], A. Oliva[2,4], L. Acosta[5], R. Alba[2], F. Barba[6], S. Cherubini[2,4], G. D'Agata[7], D. Dell'Aquila[3], A. Di Pietro[2], J.P. Fernandez[8], P. Figuera[2], D. Galaviz Redondo[6], L. Guardo[2], M. Gulino[1,2], F. Hammache[9], D. Jelavić Malenica[3], A.I. Kiliç[7], M. La Cognata[2], M. La Commara[10,11], L. Lamia[2,4], D. Lattuada[1,2], C. Maiolino[2], G. Manicò[2,4], M. Mazzocco[12,13], M. Milin[3,14], Ma Nanru[15], A. Nurmukhanbetova[16], D. Nurkić[3,14], S. Palmerini[17], T. Parascandolo[8], D. Pierroutsakou[8], R.G. Pizzone[2], R. Popočovski[3], G.G. Rapisarda[2], S. Romano[2,4], D. Santonocito[2], M.L. Sergi[2,4], A. Shotter[18], R. Spartà[2,4], A. Spiridon[19], L. Trache[19], N. Vukman[3] and H. Yamaguchi[15]

1)Facoltà di Ingegneria e Architettura, Università degli Studi di Enna "Kore", Enna, Italy
2)INFN - Laboratori Nazionali del Sud, Catania
3)Rudjer Boskovic Institute, Zagreb, Croatia
4)Dipartimento di Fisica e Astronomia, Università degli Studi di Catania,Catania, Italy
5)Institute of Physics, Universidad Nacional Autónoma de México, Mexico City, Mexico
6)Departamento de Física, Faculdade de Ciências da Universidade de Lisboa, Lisboa, Portugal
7)Nuclear Physics Institute of ASCR, Rez near Prague, Czech Republic
8)University of Seville, Seville, Spain
9)IPN-Orsay, IN2P3-CNRS, Universitè Paris XI, Orsay, France
10)Dipartimento di Fisica "Ettore Pancini", Università degli Studi di Napoli "Federico II", Napoli, Italy
11)INFN-Sezione di Napoli, Napoli, Italy
12)Dipartimento di Fisica, Università degli Studi di Padova, Padova
13)INFN-Laboratori Nazionali di Legnaro, Legnaro, Italy
14)Physics Department, Faculty of Science, University of Zagreb, Zagreb, Croatia
15)Center for Nuclear Study, The University of Tokyo, Tokyo, Japan
16)Nazarbayev University, Astana, Kazakhstan
17)Dipartimento di Fisica, Università degli Studi di Perugia, Italy
18)School of Physics - The University of Edinburgh, Edinburgh, Scotland,United Kingdom
19)Horia Hulubei National Institute for R&D in Physics and Nuclear Engineering, Bucharest-Magurele, Romania

Abstract - The $^{14}N+^{16}O$ and $^{14}N+^{12}C$ reactions have been measured at INFN-Laboratori Nazionali del Sud using a 33.7 MeV ^{14}N beam. The experiments aim to populate the ^{24}Mg and ^{28}Si excited states decaying into p or α channels in the quasi-free reaction off the deuteron in ^{14}N. In particular, the ^{24}Mg excitation region explored in the measurement plays a key role in stellar carbon burning whose cross section is commonly determined by extrapolating high-energy fusion data. The $^{14}N+^{16}O$ reaction will provide data for the $^{12}C+^{16}O$ process in a relative energy region from 7 MeV down to 2 MeV. This will allow to span an energy range from a region where direct data show the existence of prominent resonances, down to the Gamow peak, never reached so far. The $^{14}N+^{12}C$ experiment aims to provide data for $^{12}C+^{12}C$ at relative energies from 5 MeV down to 1.5 MeV in a way to assure a more sound normalization to existing direct data and to overlap with those obtained from a previous indirect measurement of the same reaction, whose cross sections exhibit several resonances responsible for a very large increase of the reaction rate at the relevant temperatures.

INTRODUCTION

Carbon burning represents the ignition of the third nuclear fuel supply after hydrogen and helium burning in the evolution of massive stars, i.e., $M > 8M_\odot$. It determines the properties of massive stars during the most advanced phases of their evolution as well as their contribution to the chemical evolution of the universe [1,2]. In addition, it is the engine of type Ia supernovae and, in turn, it affects their outcomes [3]. Carbon burning proceeds mainly through the $^{12}C + ^{12}C$ and $^{12}C + ^{16}O$ fusion reactions at temperatures of about 6-8 x 10^8 K. A comprehensive investigation of the $^{12}C+^{12}C$ fusion has been recently performed. A much larger reaction rate than predicted at the relevant temperatures was found due to resonances in the cross section [4]. The aim of the new measurement is to assure a larger overlap with existing direct data for a better normalization, while still having superposition with indirect data.

The $^{12}C+^{16}O$ fusion is expected to become important at higher temperatures, above 10^9 K, with respect to $^{12}C + ^{12}C$, due to the higher Coulomb barrier ($V_C \approx 8$ MeV). It

plays a major role in explosive carbon as well as oxygen burning, and possibly during the final stages of hydrostatic carbon and oxygen burning.
The temperature range for $^{12}C+^{16}O$ fusion lies between 10^9 K for hydrostatic carbon burning and 3.6 10^9 K for explosive carbon and oxygen burning. The corresponding center of mass energies are 3 and 7.2 MeV, respectively. As for the $^{12}C+^{12}C$ fusion, the major decay modes are the α and p channels, e.g. ^{24}Mg+α (Q=6.77 MeV) and ^{27}A1+p (Q=5.17 MeV).
Several efforts have been devoted to measure the $^{12}C+^{16}O$ cross sections at astrophysical energies, involving both charged particle and gamma ray spectroscopy ([5] and references therein). Nevertheless, it has only been previously measured down to E_{cm} = 4 MeV. The cross sections for these reactions show a pronounced resonance structure just below the Coulomb barrier, which does not extend below 6 MeV. Instead, a smoother behaviour appears at the lowest energies measured so far. Extrapolations from current data based on different models differ by two orders of magnitude around 3 MeV and in particular, a proposed sub-barrier fusion hindrance effect would drastically reduce the reaction rate at astrophysical energies [6]. It is worth noticing that even variations of the "strength" of the ^{24}Mg+α and/or ^{27}Al+p channels by a small factor would imply large variations in the α/p production for further nucleosynthesis. Thus, further measurements extending down to at least 3 MeV would be extremely important.
In this report, we present experimental details of two experiments: a) the indirect study of the $^{16}O(^{12}C,\alpha)^{24}Mg$ and $^{16}C(^{12}C,p)^{27}Al$ reactions via the Trojan Horse Method (THM) applied to the $^{16}O(^{14}N,\alpha^{24}Mg)^2H$ and $^{16}O(^{14}N,p^{27}Al)^2H$ three-body processes; b) the indirect study of the $^{12}C(^{12}C,\alpha)^{20}Ne$ and $^{12}C(^{12}C,p)^{23}Na$ reactions via the Trojan Horse Method (THM) applied to the $^{12}C(^{14}N,\alpha^{20}Ne)^2H$ and $^{12}C(^{14}N,p^{23}Na)^2H$ three-body processes; both measurements have been performed in the quasi-free (QF) kinematics regime, where ^{2}H from the ^{14}N TH nucleus is spectator to the two-body processes. There is a number of works providing evidence of direct ^{12}C transfer in the $^{12}C(^{14}N,d)^{24}Mg^*$ reaction from 30 MeV of beam energy and above [7] and the successful THM application to the $^{12}C+^{12}C$ reactions using ^{14}N as Trojan Horse nucleus [4].

THE EXPERIMENTS

The $^{16}O(^{14}N,\alpha^{24}Mg)^2H$ plus $^{16}O(^{14}N,p^{27}Al)^2H$ and $^{12}C(^{14}N,\alpha^{20}Ne)^2H$ plus $^{12}C(^{14}N,p^{23}Na)^2H$, reactions were investigated at the INFN-Laboratori Nazionali del Sud by using a ^{14}N beam at 33.7 MeV accelerated by the SMP TANDEM and delivered onto a 458 μg/cm^2 WO_3 and a 212 μg/cm^2 C target. The experimental setups consisted of four triple silicon telescopes (36 μm detector as ΔE-, 1000 μm position sensitive detector (PSD) and 1500 μm PAD detector as E-detectors) placed on both sides with respect to the beam direction in symmetric configuration (two on each side), covering azimuthal angles from 7° to 30° and from 45° to 68°. We have detected the ejectiles of the two-body reactions (either α or p) in coincidence with the spectator d particle. To fulfil the QF condition for the spectator d to preserve beam velocity, it was detected at forward angles. The trigger for the event acquisition was given by the coincidences between one of the two most forward telescopes and any one of the two telescopes on the opposite side with respect to the beam direction. The angular regions covered by the detectors were optimized for measuring the break-up process of interest in QF kinematics, and the investigated range of deuteron momentum values was feasible to check the existence of the QF mechanism.

PRELIMINARY STEPS DATA ANALYSIS

Energy calibration of each detector was performed by means of a standard eight-peak α source. For PSDs also data from elastic scattering of ^{14}N on ^{1,2}H and α particles from $^2H(^{14}N,\alpha)^{12}C$ at beam energies of about 13, 20 and 33 MeV were used, with an overall energy resolution of about 1.5%. Angular calibration was achieved by using grids with equally spaced slits placed in front of each PSD during preliminary runs of the experiment, with an angular resolution of about 0.3°. A typical angle vs. energy PSD calibrated spectrum is shown in Fig.1. The calibration procedure has been finished. Data analysis is in progress.

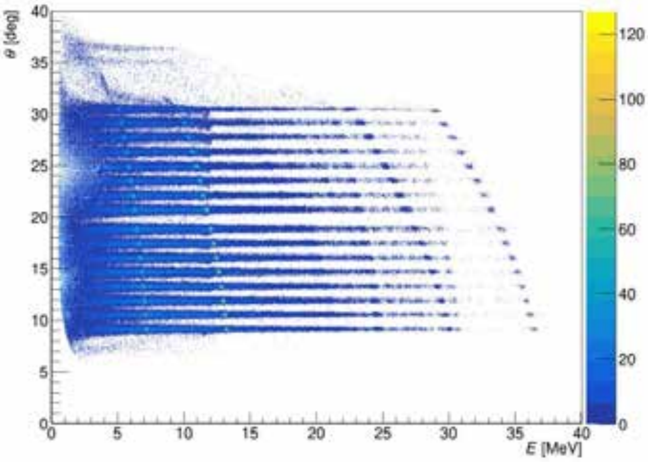

Figure 1: typical angle (θ) vs. energy (E) calibrated spectrum of a PSD.

REFERENCES

[1] C. Iliadis, Nuclear Physics of Stars, (2007), WILEY-VCH Verlag GmbH & Co. KGaA, Weinheim)
[2] D. Page, A. Cumming, Astrophys. J. 635 (2005) L157
[3] L. Piersanti et al., Astrophys. J. 598, 1229 (2003).
[4] A. Tumino et al., Nature, 557, 687 (2018)
[5] X. Fang et al., Phys. Rev. C 96, 045804 (2017)
[6] C.L. Jiang et al, Phys. Rev. C 75, 015803 (2007)
[7] R.W. Zurmùhle et al., Phys. Rev. C 49, 2549 (1994).

Second run of the ^{27}Al(p,α)^{24}Mg reaction at astrophysical energies

M. La Cognata[1], S. Palmerini[2, 3], P. Adsley[4,5], F. Hammache[6], R. Alba[1], S. Cherubini[1,7], A. Di Pietro[1], P. Figuera[1], G.L. Guardo[1,7], M. Gulino[1,8], L. Lamia[1,7,9], D. Lattuada[1,8], C. Maiolino[1], A. Oliva[1,7], R.G. Pizzone[1], P. Prajapati[1], S. Romano[1,7,9], D. Santonocito[1], R. Spartà[1,7], M.L. Sergi[1,7], A. Tumino[1,8]

1) Istituto Nazionale di Fisica Nucleare, Laboratori Nazionali del Sud, 95123 Catania, Italy
2) Dipartimento di Fisica e Geologia, Università degli Studi di Perugia, 06123 Perugia, Italy
3) Istituto Nazionale di Fisica Nucleare, Sezione di Perugia, 06123 Perugia, Italy
4) iThemba Laboratory for Accelerator Based Sciences, Somerset West 7129, South Africa
5) School of Physics, University of the Witwatersrand, Johannesburg 2050, South Africa
6) Institut de Physique Nucléaire d'Orsay, UMR8608, IN2P3-CNRS, Université Paris Sud 11, 91406 Orsay, France
7) Dipartimento di Fisica e Astronomia "Ettore Majorana", Università degli Studi di Catania, 95123 Catania, Italy
8) Facoltà di Ingegneria e Architettura, Università degli Studi "Kore", 94100 Enna, Italy
9) CSFNSM-Centro Siciliano di Fisica Nucleare e Struttura della Materia, 95123 Catania, Italy

Abstract – Right after the Spring 2020 lockdown, we restarted LNS machine-driven research activity with the indirect measurement of the ^{27}Al(p,α)^{24}Mg reaction at astrophysical energies.

In this report we briefly describe the experiment setup and the preliminary results we have obtained. Data analysis is ongoing.

ASTROPHYSICAL MOTIVATIONS

The ^{27}Al(p,α)^{24}Mg reaction is a key process to pin down the predicted abundances of Mg and Al and their ratios, in particular those involving the long-lived ^{26}Al (with 7.17 10^5 y half-life). While its short half-life indicates that its nucleosynthesis is active today in the Galaxy, yet the most likely source of ^{26}Al is still elusive. Some papers (e.g. [1]) support massive objects and supernova progenitors as candidate sources; others indicate low- and intermediate-mass asymptotic giant branch (AGB) stars as likely supplier [2]. The role of the ^{27}Al(p,α)^{24}Mg reaction is especially important when compared with the competing radiative capture process, determining the escape from the Mg-Al cycle. At present, uncertainties are so large to make astrophysical predictions unreliable [3].

THE EXPERIMENT

Following the Trojan Horse Method prescriptions for reactions showing narrow resonances [4], the strengths of the ^{27}Al(p,α)^{24}Mg resonances were intended to be measured via the ^{2}H(^{27}Al,α^{24}Mg)n reaction. A 80 MeV ^{27}Al beam, provided by the LNS Tandem, of intensity about 1 pnA, was delivered onto an isotopically enriched CD_2 target about 100 μg/cm^2 thick, placed at 90° with respect to the beam axis. The beam energy was chosen to span the ^{27}Al+p energy range between zero and 1.5 MeV for direct data normalization and to cover a phase-space region where the contribution of sequential decays

involving ^{25}Mg excited states is negligible. A picture of the experimental setup is shown is fig.1.

Figure 1: picture of the experimental setup. Beam is going from the right to the left.

The experimental setup was made of four 1000-micron double sided silicon strip detectors (DSSSD 16x16 strips, about 3 mm pitch), two at 700 mm from the target, centered at 5.5° and each covering about 4°. The other two DSSSDs were placed at 135 mm from the target at 25°, each covering about 10.5°. The setup was symmetric with respect to the beam axis.

PRELIMINARY RESULTS

Detector calibrations were performed using standard alpha sources as well as using reactions and scattering of ^{27}Al, at energies between 40 and 80 MeV, off Au and CD_2 targets. Angles of detection of the emitted particles were reconstructed by simple geometrical considerations and their accuracy were checked by comparing experimental yields in ^{27}Al+Au runs with simulated ones.

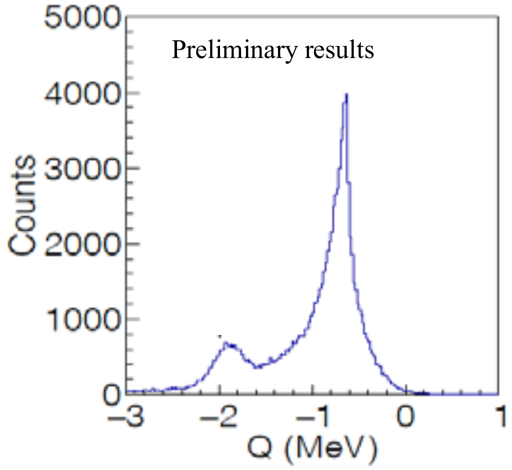

Figure 2: experimental Q-value. Two peaks are found, for ^{24}Mg ground and first excited states

Fig.2 shows the Q-value spectrum. It exhibits two distinctive peaks, one centered at about -624 keV and the other at -1.993 MeV, corresponding to the theoretical values computed from nuclear masses and excitation energies, for ^{24}Mg ground and first excited states. In the data analysis a gate on the Q-value spectrum was set, introducing a ROI spanning $-1.0<Q<-0.2$ MeV, to discard events corresponding to the population of ^{24}Mg first excited state.

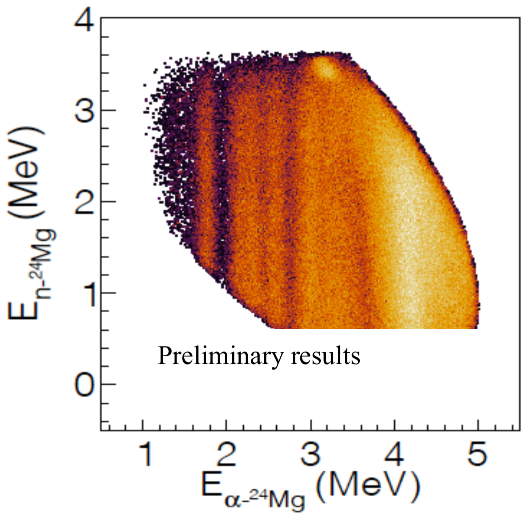

Figure 3: relative energy 2D spectrum

For the selected events, we calculated the $E_{n\text{-}24Mg}$ and $E_{\alpha\text{-}24Mg}$ kinematic variables using energy and momentum conservation laws. In fig.3 they are used to build a 2D spectrum; it shows clear vertical loci corresponding to the population of ^{28}Si states close to the alpha emission threshold, which might be of significant astrophysical interest. Even if no background is present thanks to the selection of the Q-value peak in fig.2, still sequential decay mechanisms possibly leading to the population of ^{5}He or ^{25}Mg excited states might be at work, making it necessary to investigate the reaction mechanism. This will be the subject of future work.

ACKNOWLEDGEMENTS

Authors are grateful to the LNS director and to the technical staff who made it possible to carry out a successful experiment under safe conditions, given the ongoing pandemic.

REFERENCES

[1] C. Iliadis et al., ApJS 134 (2001) 151
[2] S. Palmerini et al., MNRAS 467 (2017) 1193
[3] C. Iliadis et al., ApJS 193 (2011) 16
[4] M. La Cognata et al., ApJ 708 (2010) 796

The cosmic history of the Khatyrka meteorite: A preliminary experiment based on 60MeV proton irradiation of a synthetic sample

R.G. Pizzone[1], G.G. Rapisarda[1,2], S. Romano[1,2,3], L. Bindi[4], R. Catalano[1], G.A.P. Cirrone[1], M. La Cognata[1], L. Lamia[1,2,3], G. Petringa[1], P.M. Prajapati[1], S. Tommasini[4], S. Russo[1] and G. Strazzulla[5]

1) INFN- LNS via S. Sofia 62 Catania, Italy
2) Dipartimento di Fisica e Astronomia "E. Majorana", Università di Catania, Catania, Italy
3) CSFNSM, Catania, italy
4)Università di Firenze, Firenze, Italy
5) INAF – Osservatorio astrofisico di Catania, Catania, Italy

INTRODUCTION

With the discovery of the first natural quasicrystal, named icosahedrite ($Al_{63}Cu_{24}Fe_{13}$), in 2009 [1-3], a new frontier in mineralogy has been opened that could lead to new discoveries in geoscience, astronomy, condensed matter physics, and materials engineering. For the first time, minerals violating the symmetry restrictions of conventional crystallography has been discovered. Quasicrystals, by definition, have an atomic arrangement that is quasiperiodic – two or more types of atomic clusters each repeat at regular intervals whose ratio is irrational. Unlike a periodic crystal, the sequence of atoms never exactly repeats in the sense that no two atoms have exactly the same arrangement of surrounding atoms (if the atomic arrangement is followed sufficiently far out). That nature could accomplish the formation of quasicrystals without human intervention was unexpected, requiring the existence of petrological processes never considered previously. The fact that the quasicrystals were found in a meteorite formed in the earliest phases of the solar system evolution [3-8] means these processes were active 4.5 billion years ago and influenced the mineral composition of the first objects to condense around the Sun. Right after the discovery of the first natural quasicrystal, the question arose: Could other natural periodic or quasiperiodic Al-bearing alloys be discovered? The answer to that question was positive. In fact, in other fragments of the same highly shocked CV3 carbonaceous chondrite (named Khatyrka meteorite by MacPherson et al. [10] two new Al-bearing phases were found, the crystalline steinhardtite, $Al_{38}Ni_{32}Fe_{30}$ [5] and decagonite, $Al_{71}Ni_{24}Fe_5$, which represents the second natural quasicrystal to be found [6-7].

To further characterize the extraterrestrial nature of the samples, recent LA-ICP-MS measurements to obtain the trace elements abundances have been done. However, one of the crucial test would be to carry out isotopic studies directly on the exotic metal constituting the Khatyrka meteorite. For this purpose, the goal of the present project is to use a piece of synthetic $CuAl_2$ (corresponding to the mineral khatyrkite), which is the equivalent of the most common Al-alloys present in the Khatyrka meteorite, and bombard it with protons to investigate the potential formation of ^{26}Al. Such an experiment simulate what can occur in different phases of the evolution of the solid objects in the Solar system that are continually irradiate by cosmic energetic ions. The results of the experiment here presented should serve as good comparison when the natural material will be tested. Indeed, we were looking into the possibility of measuring cosmic-ray spallation produced ^{26}Al in natural khatyrkite (which was calculated to be about 200 dpm/kg at equilibrium, or 10 decays of ^{26}Al in a 100 µg grain per year), which could shed light on the mechanisms of formation of the Al-metal in outer space.

IRRADIATION

In order to induce the ^{26}Al production via the $^{27}Al(p,d)^{26}Al$ or $^{27}Al(p,pn)^{26}Al$ reactions, a piece of synthetic $CuAl_2$ was irradiated with 60 MeV proton beams (a typical energy of the cosmic rays protons) accelerated by the INFN – LNS superconducting cyclotron. The irradiation was performed at the multidisciplinary experimental hall.

Proton beams accelerated by the cyclotron, travel in vacuum for almost eighty meters and reach the multidisciplinary irradiation room where, finally, they exit in air through a 50 um Kapton window. An air-free, plane-parallel ionisation chamber, calibrated in terms of dose in water at the irradiation point and positioned just after the Kapton windows, acts as a real-time dose monitoring. It hence permits the measure of the total fluence received by a given sample at the irradiation position. The chamber also provided a feedback to the beam control system and triggered the immediate irradiation stop once the planned total fluence was reached. An overall error in the released fluence of 3% is envisaged. The beamline was also equipped with a precise positioning system allowing for the accurate placement of the sample. The multidisciplinary irradiation beamline with all its elements is shown in Figure 1.

Figure 1. The multidisciplinary irradiation beamline where the irradiation was performed.

GAMMA-RAY SPECTROSCOPY ANALYSIS

After irradiation the possible production of ^{26}Al has been investigated by gamma-ray spectroscopy. The synthetic $CuAl_2$ sample was brought in the Environmental Physics Laboratory, at LNS where the measurement was carried on using the ORTEC - Detective X detector. The device is equipped with a large, coaxial, P-type high purity germanium (HPGe) detector crystal. The HPGe detector is cooled by a small, highly reliable mechanical cooler to near-liquid-nitrogen temperature. Dimensions of the crystal are nominally 65 mm in diameter by 50 mm long. The detector has a resolution of 2.0 keV and relative efficiency of about 40% for 1.332 MeV gamma energy of ^{60}Co. The output of the detector has been analysed using the GammaVision Software. After irradiation, several spectra have been acquired, covering a time interval of about 3 months.

It is expected that in case of ^{26}Al production the gamma-ray spectrum is characterized by the presence of the 1130 and 1809 keV gamma-ray peaks together with the 511 keV annihilation peak.

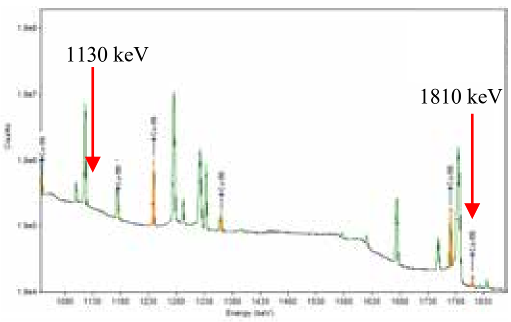

Figure 2: Gamma-ray spectrum from the irradiated synthetic khatyrkite sample. A peak at about 1810 keV shows up, while no evidence of the ^{26}Al 1130 keV line is present in the spectrum.

The acquired spectra are characterized by a gamma-ray line at about 1810 keV, but no evidence of 1130 keV line shows up. A typical spectrum is reported in Figure 2. A zoom of the spectrum around the 1810 keV peak is shown in Figure 3a. The 1810 keV line has been preliminarily attributed to ^{56}Co ($T_{1/2}$ = 77.2 d) a cobalt isotope that can be produced by the ^{64}Cu + p interaction, moreover other characteristic ^{56}Co gamma-ray lines have been observed (see Figure 2). The 1810 keV peak could be also attributed to ^{56}Mn ($T_{1/2}$ = 2.57 h) but the wide difference in half-life rules out this element. Other peaks present in the spectrum (Figure 3a) have been identified as sum-peaks. For example, the 1749 keV peak due to the random coincidence between 1238 keV ^{56}Co and 511 gamma-ray from annihilation, or the 1884 keV peak due to the coincident detection of the 846.7 and 1037.8 keV ^{56}Co gamma-ray lines.

After about one year a new gamma-ray spectrum was acquired showing the strong suppression of the 1810 keV peak (Figure 3b). This confirms that the observed line cannot be due to ^{26}Al ($T_{1/2} = 7.17\times10^5$ y), being consistent with the ^{56}Co origin.

Further analysis will be performed in order to better evaluate the effect of the proton irradiation on the synthetic khatyrkite sample.

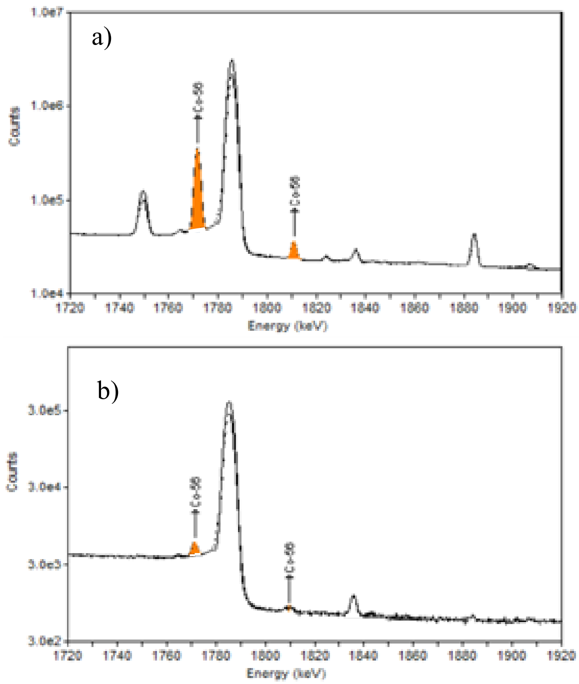

Figure 3: Zoom of the energy region around the 1810 keV peak of interest. (a) Spectrum acquired few days after the irradiation. (b) Spectrum acquired after one year.

REFERENCES

[1] Bindi L., *et al.* (2009) *Science*, 324, 1306.
[2] Bindi L., *et al.* (2011) *Am. Mineral.*, 96, 928.
[3] Bindi L., *et al.* (2012) *Proc. Nat. Acad. Sci. USA*, 109, 1396.
[4] Bindi L., Steinhardt P.J. (2012) *Elements*, 8, 13.
[5] Bindi L., *et al.* (2014) *Am. Mineral.*, 99, 2433.
[6] Bindi L., *et al.* (2015a) *Sci. Rep.*, 5, 9111.
[7] Bindi L., *et al.* (2015b) *Am. Mineral.*, 100, 2340.
[8] Hollister L.S., *et al.* (2014) *Nature Comm.*, DOI: 10.1038/ncomms5040.
[9] Lin C., *et al.* (2017) *Sci. Rep.*, 7, 1637.
[10] MacPherson G.J., *et al.* (2013) *Met. Planet. Scien.* 48, Nr 8, 1499–15

Study of the quasi-free $^3He + ^9Be \rightarrow 3a$ reaction for the Trojan Horse Method

C. Spitaleri[1,2], M. Lattuada[1,2], S. Messina[1] , A. Cvetinovic[3], N. Soic[4], M.Milin[5],S.Cherubini[1,2]P.Colovic[4], G. D'Agata[6], D. Dell'Aquila[4], G.L.Guardo[1], M. Gulino[1,7], M. La Cognata[1], L. Lamia[1,2], D. Lattuada[1,2], Chengbo Li[8] D.Nurkic[5], S.S. Perrotta[1,2], R.G. Pizzone[1], R. Popoconski[4], G.G. Rapisarda[1,2], S,Romano[1,2], N. Skukan[4], R. Spartà[1], M.L. Sergi[1,2], S. Szilner[4], O.Trippella[9], M.Uroic[4], and N. Vukman[4]

1) INFN - Laboratori Nazionali del Sud, Catania, Italy

2) Dipartimento di Fisica e Astronomia "Ettore Majorana", Università degli Studi di Catania, Catania, Italy

3) Jožef Stefan Institute, Ljubljana, Slovenia

4) Rudjer Boskovic Institute, Zagreb, Croatia

5) Department of Physics, Faculty of Science, University of Zagreb, Zagreb, Croatia

6) Czech Acad.Sci.-Nucl. Phys Inst-Rez 25068, Czech Republic

7) Facoltà di Ingegneria e Architettura, Università degli Studi di Enna "Kore", 94100 Enna, Italy

8) Key Laboratory of High Precision Nuclear Spectroscopy, Institute of Modern Physics, Chinese Academy of Sciences, Lanzhou, China

9) INFN-Sezione di Perugia, Italy

Abstract - A new study of the quasi-free contribution to the $^3He+ ^9Be \rightarrow 3a$ reaction (Q-value = 19.004 MeV) at low E3He energy is presented [1]. The reaction was studied in a kinematically complete experiment at beam energy of 4 MeV. The full width at half maximum of the ^4He-^5He inter-cluster momentum distribution inside ^9Be was measured with improved accuracy, by adopting several different approaches that all led to consistent results. These preliminary investigations on the reaction mechanism are fundamental for future studies employing the Trojan Horse Method, with the ^5He unbound nucleus as a virtual projectile [2].

1. INTRODUCTION

The investigation of nuclear reactions induced by unbound nuclei is important for nuclear physics. (see ref. [3]). Several of those reactions may be studied with the Trojan Horse Method (THM) [4-12]. The THM allows one to extract the cross section between two particles B(x, C)D at low energies, relevant for astrophysics, from the selection of the quasi-free (QF) contribution to an appropriate reaction B(A,C D)S (Fig.1) at energies well above the Coulomb barrier. In the case of the $^5He+^3He \rightarrow 2a$ reaction induced by ^5He, to be studied with THM, an appropriate E_{3He} incident energy range is from 3 to 4.5 MeV. Moreover, the separability of the QF contribution, from others that are present in the three-body $^9Be(^3He,\alpha\alpha)^4He$ reaction, must be checked. In this framework, ^9Be represents an interesting candidate to be used as a Trojan Horse nucleus (the cluster system used to transfer the virtual projectile, see the references above for more details) thanks to its pronounced cluster configurations, ^8Be-n and ^5He-^4He. These cluster structures include two of the lightest unbound nuclei (^8Be and ^5He) that are the main responsible for the nuclear gaps (at A=5 and A=8) in the element formation during Big Bang Nucleosynthesis. In an earlier experiment, the THM was applied to the $^2H(^9Be,\alpha^6Li)n$ reaction to investigate the $^8Be(d,\alpha)^6Li$ reaction of astrophysical interest [12].

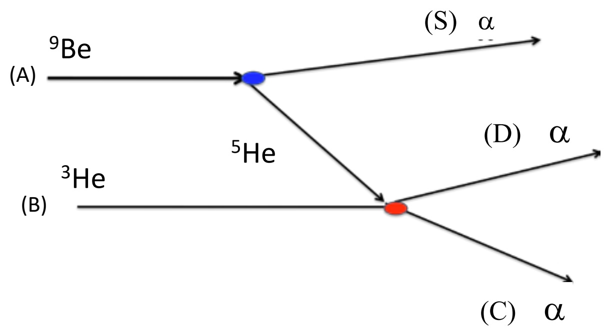

Fig.1 Diagram describing the QF process for $^9Be(^3He,\alpha\alpha)^4He$ reaction (A(B,CD)S reaction),

Similarly, the present study $^9Be(^3He,\alpha\alpha)^4He$ reaction information aims at extracting information on cross section of the $^5He+^3He \rightarrow 2\alpha$ reaction in the next future. Anyway, many steps are needed before we can define the methodology for the investigation of the ^5He induced reactions. This work addresses one of main and fundamental problems to be solved before applying the THM. The present paper reports on a new measurement performed at 4 MeV beam energy. First, new tests to check the existence of the QF mechanisms at low energy were carried out. Then a new and more precise determination of the parameters of the momentum distribution of ^5He-^4He system inside ^9Be was performed. We stress that these steps are essential for the continuation of any further study of the $^5He+^3He \rightarrow 2\alpha$ virtual reaction by means of the THM.

2. EXPERIMENT

The $^9Be(^3He,\alpha\alpha)^4He$ experiment was performed using the EN Tandem Bošković Institute in Zagreb. A 4 and 2 MeV $^3He^+$ Tandem beam with intensity of about 7-10 nA, was delivered onto an isotopically enriched ^9Be target,124 μg/cm^2 thick, evaporated on a carbon backing, 40 μg/cm^2 thick. The beam spot was reduced to1,5 mm in diameter using a collimation system. The beam energies at half target were 3.93 MeV and 1.98 MeV for the 4 and 2 MeV runs, respectively. All further calculations were performed using the beam energies at half target. The experimental setup consisted of single area, two 1000 μm and two 500 μm position sensitive detectors (PSD), 50x10 mm^2 in a coplanar geometry on both sides of the beam direction. The α-α coincidences were measured by any two of the PSD's placed on opposite sides with respect to the beam direction. This set-up allowed us to investigate all kinematical conditions for which the spectator momentum p_S is zero. detectors PSD1 and PSD3 placed at symmetrical angles $\theta_{PSD1}= |\theta_{PSD3}|$ (in coplanar geometry) chosen in such a way that it was possible to accept the condition $p_{\alpha S}=0$ when $p_{\alpha 1}=p_{\alpha 2}$ and $m_{\alpha 1}$ and $m_{\alpha 2}$. Checks were made to determine whether the beam direction coincided whit the axis of scattering chamber by comparing the yield of elastically scattered ^3He ions elastically by the two detectors $\theta_{PSD1} = |\theta_{PSD3}|$ |placed at equal angles on the sides of beam axis. Indeed, the cross section for QF processes is expected to have maxima for these kinematical conditions, since the α-^5He inter-cluster motion in ^9Bee is known to be mainly in an S-state.

3. MOMENTUM DISTRIBUTION

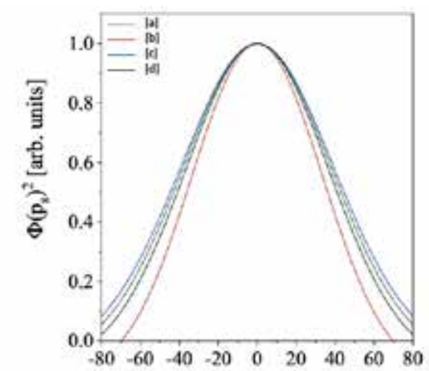

Fig.2 Obtained fits to the experimental momentum distribution extracted by four method listed in Table normalized to their maximum value. The alphabetic letters indicating the method used are the same on those indicate in Table [1].

Following the simpler PWIA, the three-body reaction cross section can be factorized into two terms correspond-ding to the two vertices of Fig.1 and it is given by Ref. [1]:

$$d^3\sigma/(d\Omega_C\, d\Omega_D\, dE)= P\,(KF)\,\phi(p_s)^2\,[d\sigma/d\Omega]^{HOES} \quad (1)$$

where: 1. P is the factor that takes into account clustering probability and/or absorption effects.

2. $[d\sigma/d\Omega]^{HOES}$ is the half-off-energy-shell (HOES) differential cross section for the binary $^5He+^3He \rightarrow 2\alpha$ reaction at the center of mass

Table. Extraction of the momentum distribution from $^9Be(^3He,\alpha\alpha)^4He$ reaction at 4 MeV . adopted Ref:[1]

	Method.	$(FWHM)_{exp.}$ (MeV/c)	$\frac{\Delta FWHM}{FWHM}$ (%)
[a]	Energy sharing	89±9	10
[b]	Angular correlation	86±7	8.1
[c]	Relative energy cut	82±8	9.8
[d]	Momentum bins.	84±8	9.5

energy E_{cm} given in post-collision prescription by: $E_{cm}= E_{\alpha_1\alpha_2} - Q_{2b}$, where Q_{2b} is the Q-value of the binary $^5He+^3He \rightarrow 2\alpha$ reaction and $E_{\alpha_1\alpha_2}$ is the α_1-α_2 relative energy in the exit channel.

3. KF is a kinematical factor containing the final state phase space factor and it is a function of masses, momenta and angles of the detected particles.

4. $\varphi(p_S)^2$ is the square of the Fourier transform of the radial wave function for the ^5He-^4He (Fig.1) inter-cluster motion described in terms of Hankel, function depending on the properties of the x – S system.

4. CONCLUSIONS

The present work shows that the $^5He+^9Be\rightarrow 3\alpha$ reaction at 4 MeV proceeds through the QF reaction mechanism. This is a preliminary study aiming at investigating the possibility to use ^9Bee as a source of ^5He to induce nuclear reaction involving unbound systems. As such, the accurate determination of the ^4He-^5He momentum distribution has a pivotal role, as the momentum distribution is a key factor in the extraction of the cross sections induced by ^5He. In the present work, using different methodologies we were able to extract such momentum distributions, in perfect agreement with each other, and determine an average $(FWHM)_{exp}$ of 85±4 MeV/c. Also, it is important to notice that we proved the occurence of the QF reaction mechanism at beam energies as low as 4 MeV, which is a necessary condition for the application of the method.

References

[1] C. Spitaleri et al. The Eur. Phys. J. A **56**, 18 (2020),
[2] C. Spitaleri et al. The Eur. Phys. J A **57** 20 (2021)
[3] Bjorn Jonson, The Eur.Phys. J.**131**, 2 (2016).
[4] G.Baur, Phys. Lett. **178**, 135 (1986).
[5] S. Cherubini et al. ApJ , 457 855(1996)
[6] C. Spitaleri et al. Nucl. Phys. A **719,** 99 (2003)
[7] S.Typel and G.Baur, Ann. of Phys**. 305**, 228 (2003).
[8] C.Spitaleri,et al. Phys.of Atom. Nuclei **74,** 1763 (2011)
[9] R.E.Tribble et al. Rep. Progr. Phys. **77**, 106901 (2014).
[10] C.Spitaleri et al., The Eur. Phys. J. A **52**, 77 (2016)
[11] C.Spitaleri et al., The Eur. Phys. J. A **55**, 161 (2019)
[12] Q.G.Wen et al. Phys. Rev, C **93**, 035803 (2016)

The $^3He + ^5He \rightarrow 2\alpha$ reaction below Coulomb barrier via the Trojan Horse Method

C. Spitaleri[1,2], S. Typel[3,4], C. A. Bertulani[5], A. M. Mukhamedzhanov[6], T. Kajino[7,8,9], M. Lattuada[1,2], A. Cvetinovic´[10],S. Messina[1], G. L. Guardo[1], N. Soic´[11], M. Milin[12], S. S. Perrotta[1,2,13], Chengbo Li[9], P. Colovic´[1], G. D'Agata[15],D. Dell'Aquila[11], C. G. Fatuzzo[1], M. Gulino[1,16], S. Q. Hou[17], I. Indelicato[1], M. La Cognata[1], L. Lamia[1,2], D. Lattuada[1,16], D.Nurkic´[12], R.G. Pizzone[1,2], R. Popocovski[11], G.G. Rapisarda[1,2], N. Skukan[11], M.L. Sergi[1,2], R, Spartà[1], S. Szilner[11], O. Trippella[18], M.Uroic[3], and N. Vukman[3]

1) INFN, Laboratori Nazionali del Sud, via S. Sofia 62, 95123 Catania, Italy
2) Dipartimento di Fisica e Astronomia "Ettore Majorana", Universitá degli Studi di Catania, Catania, Italy
3) Technische Universität Darmstadt, Fachbereich Physik, Institut für Kernphysik, Darmstadt, Germany
4) GSI Helmholtzzentrum für Schwerionenforschung GmbH, Darmstadt, Germany
5) Department of Physics and Astronomy, Texas A&M University-Commerce, Commerce, TX 75429, USA
6) Cyclotron Institute, Texas A&M University, College Station, TX, USA
7) National Astronomical Observatory of Japan, Mitaka, Tokyo 181-8588, Japan
8) Graduate School of Science, The University of Tokyo, Bunkyo-ku, Tokyo 113-0033, Japan
9) School of Physics, Beihang University, Beijing 100083, People's Republic of China
10) Jožef Stefan Institute, Ljubljana, Slovenia
11) Ruder Boškovic Institute, Zagreb, Croatia
12) Department of Physics, Faculty of Science, University of Zagreb, Zagreb, Croatia
13) Departamento de Física Atómica, Molecular y Nuclear, Universidad de Sevilla, Seville, Spain
14) Beijing Radiation Center, Beijing Academic of Science and Technology, Beijing, China
15) Department of Nuclear Reactions, Nuclear Physics Institute of CAS, Prague, Czech Republic
16) Facoltá di Ingegneria e Architettura, Universitá degli Studi di Enna "Kore", Enna, Italy
17) Key Laboratory of High Precision Nuclear Spectroscopy, Institute of Modern Physics, Chinese Academy of Sciences, Lanzhou, China
18) INFN Sezione di Perugia, Perugia, Italy

Abstract - For the first time in an application to nuclear astrophysics, a process induced by the unstable ^5He = (^4He+n) nucleus, the $^3He+^5He \rightarrow 2\alpha$ reaction, has been studied through the Trojan Horse Method (THM) [2]. For that purpose, the quasi-free (QF) contribution of the $^9Be(^3He,\alpha\alpha)^4He$ reaction was selected at E_{3He}=4 MeV incident energy. The reaction was studied in kinematically complete experiment following two recent publications Ref. [1,2] where for the quasi-+free contribution the momentum distribution between α and ^5He particle cluster in the ^9Be nucleus in the ground state have been extracted. The angular distribution of the QF $^3He+^5He \rightarrow 2\alpha$ reaction was measured at θcm = 78°–115°.
The energy dependence of the differential cross section of the $^3He+^5He \rightarrow 2\alpha$ virtual reaction was extracted in the energy range E_{cm} = 0–650 keV. The total cross section is obtained from the Trojan-horse method.

1. INTRODUCTION

The investigation of nuclear reactions induced by an unbound nucleus x_{unb} is important for nuclear physics in the future. It could also be of interest to nuclear astrophysics if applied to reactions induced on unstable nuclei. At present, the direct investigation of a x_{unb} + B nuclear reaction (with x_{unb} as target or projectile) is not feasible, the most viable method to experimentally study the two-body reaction x_{unb}+B→C+D is to measure the inverse reaction. An alternative way to increase the possibility of measuring the cross sections of this type of nuclear reactions is to apply indirect methods. Those methods have been developed in the last decades mainly

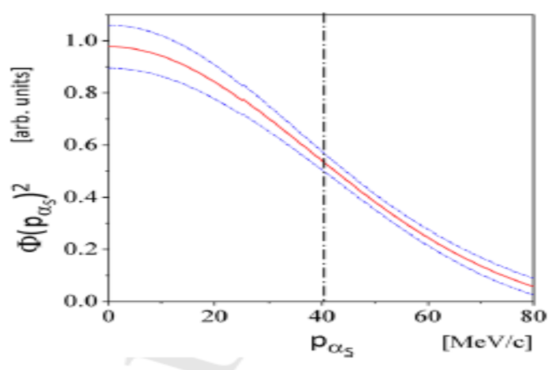

Fig.1 Experimental distribution as obtain in [1]. Tit of extracted average experimental distribution obtained by four different experimental distribution, measured with different methods: energy sharing, angular correlation, relative energy and momentum bins reported in Ref[1].

for astrophysical purpose, aiming to study nuclear reactions at very low energies. Among these the Trojan Horse method (THM) [4-10] can be considered as an attractive way to evaluate the bare nucleus cross sections of rearrangement reactions induced by unstable nuclei

[2,7-10]. In this approach, the reaction A+B→S+C+D with a spectator nucleus S is investigated instead of the reaction x_{unb}+B→C+D. In This report describes the cross section extraction of the cross section of the ^{3}He(^{5}He,α)^{4}He reaction, by means of THM, through the QF contribution of the ^{9}Be(^{3}He,αα)^{4}He reaction. A preliminary study of the reaction mechanisms involved in the ^{9}Be(^{3}He,αα)^{4}He reaction has already been carried out, by testing the presence of the QF contribution at energies suitable for the application of the THM [1] compatible with the particular kinematic conditions. Furthermore, the ^{5}He–^{4}He inter-cluster momentum distribution in the ^{9}Be nucleus was measured with different analysis methods.

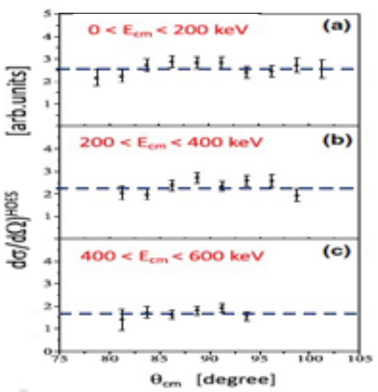

Fig.2 Angular distributions of the THM-differential arbitrary units at different energy range Ref-[2].

These preliminary investigations are the necessary conditions to study of the ^{5}He(^{3}He,α)^{4}He virtual reaction by applying the THM (see Ref. [1]).Moreover, the ^{9}Be(^{3}He,αα)^{4}He reaction at beam energiescomparable to the height of the Coulomb barrier was experimentally investigated by several authors showing a clear evidence of a QF contribution at low incident energies from 2.5 to 12 MeV, see Table in Ref. [1]. In particular, the α–α coincidence cross section for the ^{9}Be(^{3}He,αα)^{4}He reaction at 4 MeV of the beam energy has been measured showing that under some specific kinematic conditions the primary reaction mechanism was a direct interaction between the 3He projectile and the 5He cluster in the target.
To verify whether the contribution of the QF mechanism was present in the low-energy range, the ^{9}Be(^{3}He,αα)^{4}He reaction was studied at different energies (2.5, 2.7 and 2.8 MeV). Moreover, the excitation function of the three-body cross section has been mea7sured both at symmetric and asymmetric detection geometries. The aim of the present work is to determine the excitation function and angular distributions of the ^{3}He(^{5}He,α)^{4}He reaction at low energies in the center of mass system (0≤ Ec.m. ≤ 620 keV).

2. CONCLUSIONS

The results of this work clearly point out that the THM can be used to study nuclear reactions induced by an unbound nucleus x_{unb} when a suitable TH nucleus, characterized by a strong cluster configuration containing x_{unb}, is chosen. Here, for the _first time, the ^{3}He(^{5}He,α)^{4}He nuclear reaction induced by the unbound nucleus ^{5}He, important for nuclear physics, was investigated from 650 keV down to the astrophysical region. For this purpose the THM was applied to the ^{3}He(^{9}Be,α α)^{4}He three-body QF process. The Treiman-Yang Criterion, reported in the literature and previous research, has supported the hypothesis of the three-body cross section factorization (at 4 MeV beam energy) [1]. After the selection of events compatible with the QF mechanism, the virtual two-body cross section has been calculated in arbitrary units at the energy range Ecm = 0-620 keV and angular range θcm =78° - 115°. In addition to this experimental study, the cross section of the ^{3}He(^{5}He,α)^{4}He neutron transfer reaction was calculated employing a _niterange distorted wave approximation with simple many-body wave functions of the clusters.

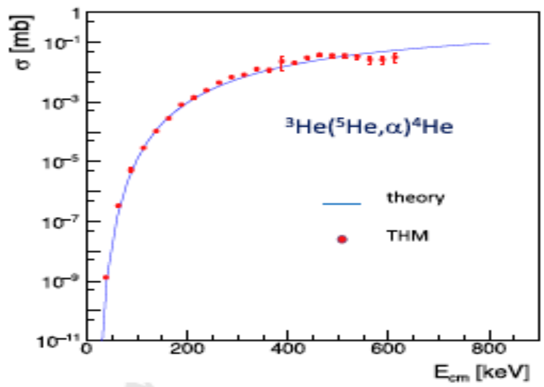

Fig.3 Cross section of the ^{3}He(^{5}He,α)^{4}He reaction from the THM experiment (red circles) and from theory (solid blue line) Ref.[2].

The result was used to normalize the experimental data to absolute values. This will allow to consider this reaction in network calculations of big bang nucleosynthesis and r-process nucleosynthesis in collapsar which is a black-hole forming supernova and has extremely high entropy and neutron-rich conditions where the unstable nuclei like 5He might play an important role Finally, it will be possible to study the effect of electron screening on the cross section at the lowest energies reached, a peculiar feature of the THM. In the present THM experiment only data in a limited center-of-mass angular range were obtained.

References

[1] C. Spitaleri et al. The Eur. Phys. J. A **56**, 18 (2020),
[2] C. Spitaleri et al. The Eur. Phys. J A **57** 20 (2021)
[3] Bjorn Jonson, The Eur.Phys. J.**131**, 2 (2016).
[4] G.Baur, Phys. Lett. **178**, 135 (1986).
[5] C. Spitaleri et al. Nucl. Phys. A **719,** 99 (2003)
[6] S.Typel and G.Baur, Ann. of Phys**. 305**, 228 (2003).
[7] C.Spitaleri,et al. Phys.of Atom. Nuclei **74,** 1763 (2011)
[8] R.E.Tribble et al. Rep. Progr. Phys. **77**, 106901 (2014).
[9] C.Spitaleri et al., The Eur. Phys. J. A **52**, 77 (2016)
[10] C.Spitaleri et al., The Eur. Phys. J. A **55**, 161 (2019

Indirect study of the $^3He(n,p)^3H$ reaction at cosmological energies

C. Spampinato[1,2,3], R.G. Pizzone[1], R. Spartà[1,2], M. Couder[4], Wanpeng Tan[3], L. Boccioli[4,5], V. Burjan[6], K.Y. Chae, G. D'Agata[6], G.L. Guardo[7], M. La Cognata[1], L. Lamia[1,2,3], D. Lattuada[7], J. Mrazek[6], S. Palmerini[5], S. Romano[1,2,3], C. Spitaleri[1,2], A. Tumino[1,8] and M. Wiescher[4].

1) INFN Laboratori Nazionali del Sud Catania Italy
2) Dipartimento di Fisica e Astronomia, Università di Catania, Italy
3) CSFNSM, Catania Italy
4)Physics and Astronomy Department, Notre Dame University, USA
5)INFN and University of Perugia, Italy
6)Cyclotron Institute, Academy of Science of the Czech Rep., Rez, Czech Rep.
7) ELINP, Magurele, Romania
8) Kore University, Enna, Italy

Abstract - Among the reactions present in the Big Bang nucleosynthesis network, the $^3He(n,p)^3H$ has an important role which impacts the final ^7Li abundance. In this work, we apply the Trojan Horse Method to extract the cross section at astrophysical energies for the $^3He(n,p)^3H$ reaction after a thorough study of the $^2H(^3He,pt)H$ three-body process. The data extracted from the present measurement are compared with other published sets.

INTRODUCTION

One of the cornerstones of the Big Bang cosmological model is the Big Bang nucleosynthesis (BBN). A series of reactions [1] converts the initial protons and neutrons into helium isotopes and into a very small, although very important, amount of ^7Li. Primordial abundances are calculated using as input physics not only the cosmological parameters but also the reaction rates which are important in such context. Among them an important role is played by the $^3He(n,p)^3H$ [2] reaction, which needs to be studied at astrophysical energies. Although direct measurements are present (e.g. [3] and reference therein), difficulties arise especially at the low-energy region. For this reason, indirect methods can play an important role within this context, as previously done for other reactions [1]. The THM [4] has been therefore applied to the $^3He(d,pt)H$ reaction to extracting information on the $^3He(n,p)^3H$ reaction cross section at astrophysical energies. The THM is based on the quasi-free process. It implies that deuteron breaks up into a neutron (participant) and a proton (spectator). Then the $^3He(n,p)^3H$ interaction takes place in the nuclear field at relative energies as low as the ones required by astrophysical applications.

EXPERIMENTAL SETUP

In the preparatory phase the best angular and energy region was determined by using a simulation to favour the QF reaction mechanism and to discriminate as much as possible it from other processes occurring in the target. The ^3He beam its 9 MeV energy, reached by the Tandem at the Physics and Astronomy Department of the University of Notre Dame, impinged on a 100μg/cm^2 isotopically enriched (up to 98%) deuterated polyethylene target, which was manufactured at the INFN-LNS target laboratory. Detectors were placed as sketched in figure 1. Three silicon position sensitive detectors (PSD 1-3), 1000 μm thick were used; PSD1

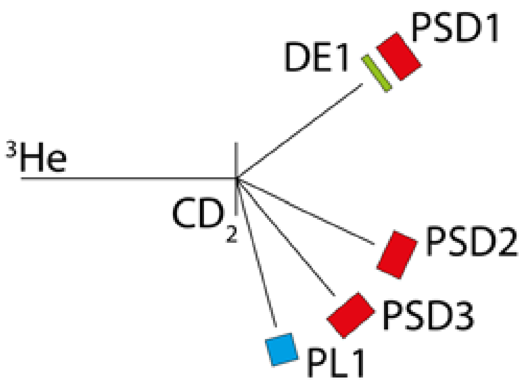

Figure 1: Experimental setup.

was coupled with a 35 μm thin silicon detector for particle identification. Particle identification was not required for the other two detectors, in order to optimizing the energy resolution of the apparatus. Two symmetrical monitor detectors were placed on both sides of the beam to check the beam symmetry. Besides, another point-like silicon detector (PL1) was placed at 45° to on-line monitoring the target thickness and its deuterium content during the experiment. A metal grid, with equally spaced slits, was placed in front of each PSD to perform an accurate angular calibration. In the first step of the experiment, slit positions were measured by optical means with an accuracy of 0.15°, as required by THM. Calibration runs were performed by using a three peaks alpha source and proton and alpha scattering on a gold target at various energies ranging from 3.5 to 9 MeV. The data acquisition system triggered when emitted particles impacted simultaneously two of the PSD detectors. Then data were stored in the DAQ system provided by the University of Notre Dame and converted in ROOT format for online analysis.

DATA ANALYSIS

The first point of the data analysis is the identification of the three-body process of. For this reason, the particle identification is performed for PSD1 via the ΔE/E technique. Once the angle and energy of the two detected particles are measured, it is possible to calculate the energy and the angle of the third, undetected particle, starting from energy and momentum conservation. This allows to extract the Q-value of the three-body reaction as shown in figure 2. A Gaussian is drawn as a red line and gives an average value of -1.55 ± 0.14 MeV, which is compared with an expected value of Q_3 = -1.47 MeV. When the selection of the three-body process is well established, the next step in the data analysis is the identification of the QF mechanism and consequently its separation from other processes [5,2].

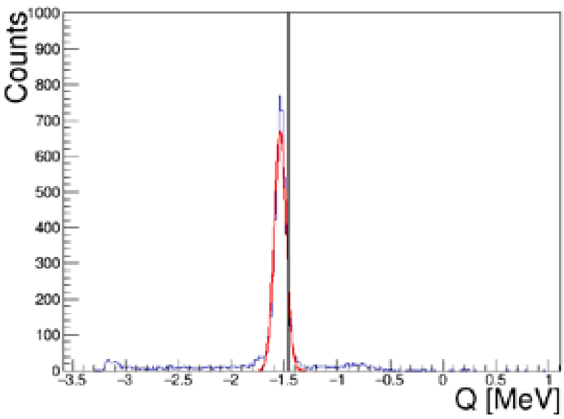

Figure 2: Q-value of the three-body reaction.

After studying the relative energies as it is shown in [6], it is possible to exclude the presence of sequential mechanism leading to 2p and ^{3}H particles in the final state.

CONCLUSION

After the selection of events related to the quasi-free breakup, standard THM prescriptions are followed. Using the post-collision approach for the detection of $E_{cm} = E_{12} - Q_{2b}$, the triple differential cross section, is divided by the product KF $|\varphi(P_S)|^2$ according to the following equation:

$$\frac{d^3\sigma_{TH}}{d\Omega_b d\Omega_B dE_b} \propto K.F.\ |\Phi(p_s)|^2 \left(\frac{d\sigma^{b.n.}_{xA}}{d\Omega}\right)_{HOES}$$

As shown in [7] the distorted momentum distribution, measured experimentally in this present work, was used. The THM data must be multiplied for the penetration factor to be compared and normalized to direct data (see for example references [8]). In the case of a neutral particle at low energies and with l=0, the penetration factor may be approximated by a 1/v factor which should be multiplied by the TH data. After applying this correction, the results are shown in figure 3. The cross section was normalized to the average of the direct data from [4,2] at the energy range E_{cm} 0.2 to 0.35 MeV. A remarkable agreement shows up at the whole energy range. Statistical errors as well as normalization errors were fully considered yielding an average 10% relative errors for the cross section extracted via THM. In conclusion, the cross section of the reaction ^{3}He(n,p)^{3}H, important for Big Bang nucleosynthesis, was measured by means of the THM. The present data set confirms the previous measurements in the energy region E_{cm} 0 to 0.4 MeV. Further analysis are necessary in order to extend the measurement at higher energies, using data from the PSD1-PSD3 coincidence. This will enable to calculate the reaction rate and to evaluate the astrophysical impact of the present measurement.

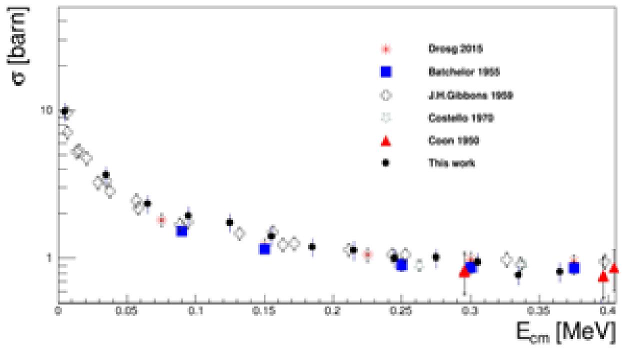

Figure 3: Normalized cross section compared to literature's data.

REFERENCES

[1] R.G. Pizzone, R. Spartà, C. Bertulani, et al., Astrophysical Journal ,786, 112 (2014).

[2] R.G. Pizzone et al., submitted to EPJA 2020.

[3] C. Brune et al., Phys. Rev. C472 (1999) 376.

[4] C. Spitaleri, M. La Cognata, L. Lamia et al. EPJ (2016) A52, 77.

[5] C.Spampinato, et al. EPJ Web of Conferences.Vol.227.EDP Sciences,2020..

[6] L. Lamia et al. 2008, Nuovo Cimento C, 31, 423-431.

[7] M. Gulino et al. 2013, Phys. Rec. C87, 012801.

[8] Guardo, G. L., Spitaleri, C., Lamia, L., et al. 2017, Phys.Rev. C, 95, 025807.

[9] Pizzone, R.G., Spitaleri, C., Cherubini, S., et al. 2005, Phys. Rev. C 71, 058801.

Application of the Trojan Horse Method to a neutron induced reaction: study of the $^{17}O(n,\alpha)^{14}C$ at astrophysical energies.

A. A. Oliva[1,2,3], L. Lamia[1,2], G.L. Guardo[2], S. Cherubini[1,2], A. Cvetinovic[2], G. D'Agata[2,4], N. de Sereville[5], A. Di Pietro[2], P. Figuera[2], M. Gulino[2,6], F. Hammache[5], S. Hayakawa[7], I. Indelicato[2], M. La Cognata[2], M. La Commara[8,9], D. Lattuada[2,], M. Lattuada[1,2], G. Manicò[1,2], M. Mazzocco[10,11], S. Messina[1,2], S. Palmerini[12,13], S.S. Perrotta[1,2], R.G. Pizzone[2], S.M.R. Puglia[2], M.L. Pumo[1,2], G.G. Rapisarda[2], S. Romano[1,2], M.L. Sergi[2], I. Sivacec[4], N. Soic[14], R. Spartà[1,2], C. Spitaleri[1,2], A. Tumino[2,6]

1) Dipartimento di Fisica e Astronomia "E. Majorana", Univ. di Catania, Italy
2) INFN-LNS, Laboratori Nazionali del Sud, Catania, Italy
3) Centro Siciliano Fisica Nucleare e Struttura della Materia - Catania, Italy
4) Nuclear Physics Institute of the Czech Academy of Science, Rez, Czech Republic
5) Institut de Physique Nucléaire, CNRS/IN2P3, Univ. de Paris Sud, Univ. de Paris-Saclay, Orsay, France
6) Facoltà di Ingegneria e Architettura, Univ. "Kore", Enna, Italy
7) Center for Nuclear Study, Univ. of Tokyo, Japan
8) INFN-Sezione di Napoli, Italy
9)Dipartimento di Scienze Fisiche, Univ. di Napoli, Italy
10) Dipartimento di Fisica e Astronomia, Univ. di Padova, Italy
11) INFN-Sezione di Padova, Italy
12)INFN-Sezione di Perugia, Italy
13) Dipartimento di Fisica e Geologia, Univ. di Perugia, Italy
14)Rudjer Boskovic Inst, Zagabria, Croatia

Abstract – The $^{17}O(n,\alpha)^{14}C$ reaction is one of the so-called neutron poisons for the weak component of the s-process, since it removes a neutron from the stellar environment without taking part in the process itself. Neutron induced reactions tends to be challenging to precisely study therefore, even though in literature are already present a series of measurements, both direct and indirect using the THM, there were still further improvements needed. Thus, a new THM experiment, with an improved detection setup, was carried out.

ASTROPHYSICAL SCENARIO

Neutron induced reactions in stars produce nearly all the elements heavier than iron (A>52). In order to precisely evaluate the rate of such reactions the neutron abundance in the stellar environment of interest must be correctly defined. Therefore, both the neutron sources and the so-called neutron poisons, reactions that remove a neutron without taking part in the nucleosynthesis process, must be precisely measured.

The weak component [1] of the s-process occurs mainly in massive stars ($M>8M_\odot$) with the $^{22}Ne(\alpha,n)^{25}Mg$ as its major neutron source, which takes place both during the helium burning ($T_c \sim 1.6\times10^8$ K) and the carbon burning ($T_c \sim 1.1\times10^9$ K). One of the main neutron poisons for the weak component is the $^{16}O(n, \gamma)$ reaction which produces an ^{17}O nuclei. The latter can then take part in various competing branches among which there are the $^{17}O(\alpha,n)^{20}Ne$ reaction, which recycles the neutron previously removed, or the $^{17}O(n,\alpha)^{14}C$, which removes another one. The branching ratios of these two reaction channels must be defined to correctly evaluate the neutron balance.

THE EXPERIMENT

Previous direct measurements of the $^{17}O(n,\alpha)^{14}C$ reaction, evaluated at the energy range of astrophysical interest (from 300 keV down to zero), showed some discrepancies in the cross section for the energy region below ~150 keV. This stimulated two investigations of the reaction by the means of the Trojan Horse Method (THM) [2,3] which revealed the presence of a suppressed resonance, due to its high J^π value, and a subthreshold one, both undetected by the direct measurements. However, the recent results obtained with the THM still had scope for improvements regarding the energy resolution, the statistical error and the angular coverage in the center-of-mass system. Thus, a new indirect measurement has been conducted by applying the THM to the three-body reaction $^{2}H(^{17}O,\alpha^{14}C)^{1}H$.

The experiment was carried out at the Laboratori Nazionali del Sud (LNS-INFN) in Catania, using a ^{17}O beam accelerated by the Van der Graaff Tandem at 43.5 MeV and impinging on a CD_2 target. As it can been seen in

Fig.1 the experimental set-up was symmetrical respect to the beam line and was composed by a Position Sensitive Detector (PSD) for the detection of the α particle and ΔE-E telescope, made up by an Ionization Chamber (ΔE stage) and another PSD (E stage), for the identification and the detection of the ^{14}C nuclei. The detectors were placed at the "Quasi-Free angles" in order to maximize the statistic for the Quasi-Free break-up events.

DATA ANALISYS AND RESULTS

After the events corresponding to the desired reaction channel were singled out from the other possible, by following the standard THM analysis prescriptions as described in detail in [4], the quasi-free contribution was assessed by looking at the momentum distribution of the proton "spectator" $\Phi(P_s)$ [5]. As visible in Fig. 2 the experimental distribution is well fitted by the theoretical one, which confirms the presence of the desired QF break-up. Once only the latter are selected, the normalized coincidence yield for the two-body reaction can be calculated, under the Plane Wave Impulse Approximation (PWIA) as described in [4]. Each resonance is then rescaled by a correction factor to take into account the angular range covered in the center of mass frame ($\theta_{c.m.}$) by the experimental data.

With the TH cross-section now correctly defined, it is then possible to calculate the reduced widths for each of the detected resonance by the means of the modified R-matrix analysis [6]:

$$\frac{d^2\sigma}{dE_{xa}d\Omega_s} = K\sum_i (2J+1)\cdot$$

$$\cdot\left|\sqrt{\frac{k_f\,E_{xa}}{\mu_{cd}}}\,\frac{\sqrt{\{2P_{l_i}(k_{cd}R_{cd}\})}M_i(p_{xa}R_{xa})\gamma^i_{cd}\gamma^i_{xa}}{D_i(E_{xa})}\right|^2$$

where K is a normalization factor, introduced to normalize the data to absolute units, P_{l_i} are the penetration functions in the entrance channel, R are the channel radii, D_i is the standard denominator in the one-level, two-channel R-matrix formula and finally γ are the reduced partial widths we are interested in. It is known [6] that the partial widths obtained in the modified R-matrix are the same for the standard R-matrix, thereby making the results independent from the method.

CONCLUSIONS

This new experiment was successful in obtaining the desired improvements over the past two THM measurements, such as a better separation of the resonances or having higher statistics and larger angular range in $\theta_{c.m}$ covered by the set-up, which made a more precise definition of the angular distributions possible. The obtained resonance widths will be used to perform a new estimation of the $^{17}O(n,\alpha)^{14}C$ reaction rate.

REFERENCES

[1] M. Pignatari et al 2010 ApJ 710 1557
[2] M. Gulino et al. Phys. Rev. C 87, 012801(R)
[3] G.L. Guardo et al. Phys. Rev. C 95, 025807
[4] A. A. Oliva et al. NCC 43 111 (2020)
[5] C. Spitaleri et al. Phys. Atom. Nuclei 74, 1725 (2011)
[6] M. La Cognata et al. ApJL 739 L54 (2011)

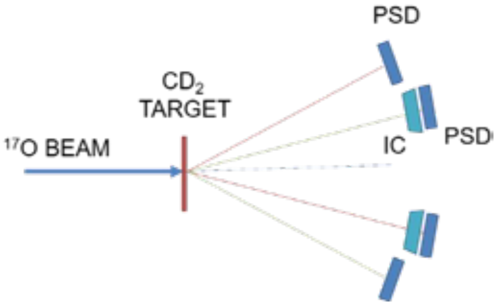

Figure 1: Schematic drawing of the experimental set-up.

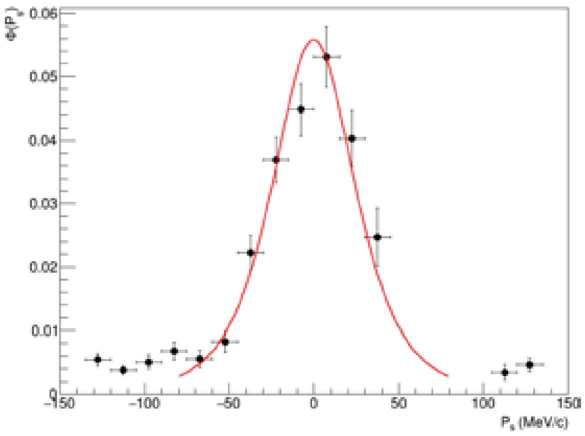

Figure 2: A typical experimental momentum distribution (black dots) for one of the detected resonances, compared with the theoretical curve (red line).

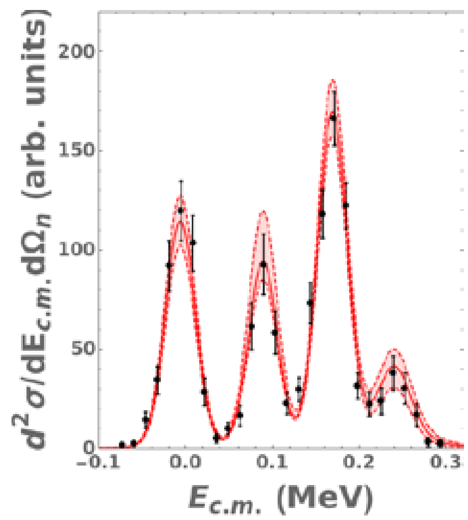

Figure 3: Modified R-matrix fit (red curve) of the double differential cross section for the TH reaction (black dots)

Elastic scattering analysis of the reaction $^{11}Li+^{64}Zn$ at energy around the Coulomb barrier.

J.P. Fernández-García[1,2], A. Di Pietro[3], R. Sparta[3], L. Acosta[4], M. A. G. Alvarez[1], M. La Cognata[3], T. Davinson[5], P. Figuera[2], D. Galaviz[6], J. Gómez-Camacho[1,2], G. L. Guardo[3], I. Martel[7], A. Sánchez-Benítez[8], J. Sánchez-Segovia[7], A. Shotter[5], N. Soic[9], O. Tengblad[10], N. Vukman[9] and D. Walter[11]

1) Departamento de Física Atómica, Molecular y Nuclear, Universidad de Sevilla, Apartado 1065, 41080 Sevilla, Spain.

2) Centro Nacional de Aceleradores, Universidad de Sevilla, Junta de Andalucía-CSIC, 41092 Sevilla, Spain

3) Laboratori Nazionali del Sud LNS-INFN, Catania, Italy

4)Instituto de Física, Universidad Nacional Autónoma de México, Apartado Postal 20-364, Cd. Mx. 01000, Mexico

5)School of Physics and Astronomy, University of Edinburgh - Edinburgh, UK

6)Departamento de Física, Faculdade de Ciências, Universidade de Lisboa, 1749-016 Lisbon, Portugal

7)Departamento de Física Aplicada, Universidad de Huelva, Campus de El Carmen, E-21071 Huelva, Spain

8)Centro de Estudios Avanzados en Física, Matemáticas y Computación (CEAFMC), Department of Integrated Sciences, University of Huelva, 21071 Huelva, Spain

9)Ruder Boskovic Institute, Zagreb, Croatia

10)Instituto de Estructura de la Materia, CSIC, E-28006 Madrid, Spain

11)TRIUMF, V6T2A3 Vancouver, British Columbia, Canada

Abstract – New experimenal data of the reaction $^{11}Li+^{64}Zn$ at the incident energy of 22.5 MeV were meaured and analyzed. Preliminary results of the elastic scatteing will be presented.

INTRODUCTION

The study of collisions induced by halo nuclei can give direct evidence of the effect of the halo, showing suppression of the elastic angular distributions and a strong enhancement of the total reaction cross section due to direct processes, in fact, the authors have devoted many efforts to study the reaction dynamic for reactions induced by the halo nucleus ^{11}Li [1-4]. In Ref.[1], the reaction $^{11}Li+^{208}Pb$ was measured at energies around the Coulomb barrier. It was noticed that the low-energy E1 strength induces a strong dynamic polarization effect on the halo, giving rise to long-range Coulomb couplings. This effect was observed as a strong reduction of the elastic cross-section and a high breakup probability [2]. Moreover, due to the exposition to the strong electric field exerted by the heavy mass target, ^{208}Pb, the weakly bound halo nucleus ^{11}Li, gets distorted and eventually breaks-up. In fact, the optical model analysis of Ref. [4] shows the dominance of Coulomb dipole polarizability on the $^{11}Li+^{208}Pb$ elastic scattering.

In this work, we present new preliminary experimental data of the nuclear reaction induced by ^{11}Li on a medium-mass target, ^{64}Zn, at the incident energy of 22.5 MeV. We compare the experimental elastic scattering angular distribution with an optical model which include the coulomb dipole polarization potential.

EXPERIMENTAL SETUP AND RESULTS

The experiment of the reaction $^{11}Li+^{64}Zn$ at the energy of 22.5 MeV was performed at the TRIUMF laboratory in Vancouver (Canada). The experimental setup was composed by four silicon telescopes. Each telescope consisted in a single sided silicon strip detector (SSSSD) of 20 um thickness, ΔE detector, plus a E detector, a double sided silicon strip detector (DSSSD) of 1000 um thickness. The whole detection system covered a wide angular range, between 9º and 123º. In table 1, the angular range of each telescope is presented. An example of the bidimensional spectrum ΔE versus ΔE+E of the reaction $^{11}Li+^{64}Zn$ at 22.5 MeV MeV is shown in Fig. 1, where a good separation between the elastically scattered ^{11}Li and the ^{9}Li breakup fragments is observed.
In Fig. 3, preliminary experimental data of the elastic cross section angular distribution for the telescopes 1 and 2 is presented. As in the case of $^{11}Li+^{208}Pb$ [1], a dramatic reduction of the elastic cross section with respect to the Rutherford formula, even at forward angles, and non Fresnel-like diffraction pattern are observed.

Table 1: Angular range covered by each telescope

Telescope	Angular range
Telescope 1	9º-37º
Telescope 2	26º-58º
Telescope 3	46º-88º
Telescope 4	75º-123º

Figure 1: Bidimensional spectrum ΔE versus E of the reaction ^{11}Li+^{64}Zn at 22.5 MeV

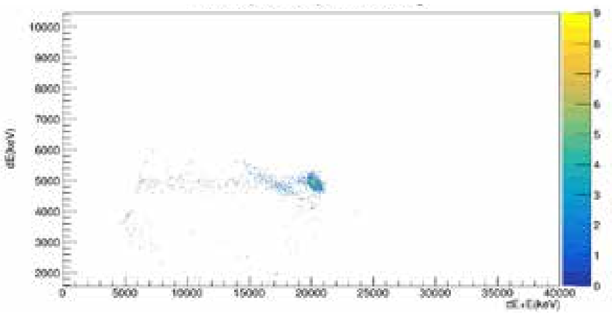

Figure 2. Elastic scattering angular distribution

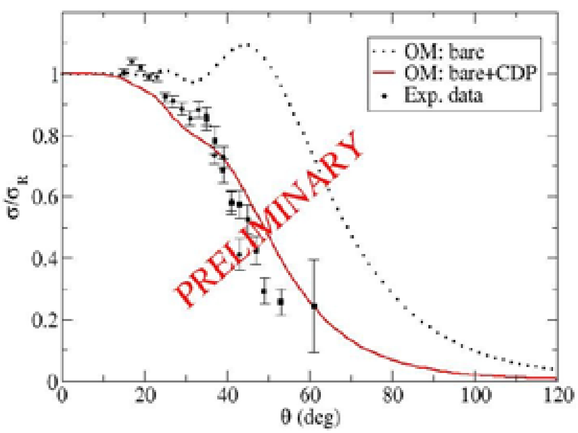

OPTICAL MODEL ANALYSIS

The experimental data of the reaction ^{11}Li+^{64}Zn at 22.5 MeV have been analyzed with the Optical Model (OM) method. The parameter-free optical potential is composed by a bare potential plus a Coulomb dipole polarization potential.

$$U(R)=U_{bare}(R)+U_{CDP}(R).$$

The bare potential is given by

$$U_{bare}(R)=V_{SPP}(R)+i\cdot N_i\cdot V_{SPP}(R).$$

To describe the real and imaginary part of the bare interaction, we adopt the microscopic São Paulo Potential (SPP) given by

$$V_{SPP}(R)=V_{Fold}(R)\cdot e^{-4v^2/c},$$

where c is the speed of light, v is the relative velocity between projectile and target, and V_{Fold} is represented as follows:

$$V_{Fold}=\int\int \rho_1(\vec{r}_1)\,\rho_2(\vec{r}_2)\,V_0\,\delta(\vec{R}-\vec{r}_1+\vec{r}_2)\,d\vec{r}_1\,d\vec{r}_2\,.$$

where ρ_1 and ρ_2 are the projectile and target matter distributions, and $V_0\delta(R-r_1+r_2)$ is the zero-range effective interaction with $V_0 = -456$ MeV [5].

In [6], the average of the imaginary part normalization N_i = 0.78 was obtained from elastic scattering data analyses performed for several systems involving stable nuclei. In the present work, we have assumed such average value.
For the Coulomb dipole polarization (CDP) potential we have used the analytic formula of Refs. [7,8], which depends on directly on the B(E1) distribution and quadratically the atomic number of the target.

The results of the optical model calculations are reprented in Fig. 2. We can notice a strong reduction of the elastic cross section with respect to the bare potential (dotted line). Moreover, a reasonable agreement between the experimental data and the total optical model calculations (solid line), which include the CDP potential, is observed, suggesting the importance of the Coulomb dipole polarization effects in the reactions induced by ^{11}Li on medium-mass target.

CONCLUSIONS

New preliminary experimental data of the reaction ^{11}Li++^{64}Zn at the 22.5 MeV are presented. A clear separation between the elastic scattering and the breakup channel was observed. A parameter-free optical potential reproduce the elasctic scattering experimental data showing the dominance of the Coulomb dipole polarization effects.

REFERENCES

[1] M. Cubero et al. Phys. Rev. Lett 109 (26),262701 (2012)
[2] J. P. Fernández-García et al. Phys. Rev. Lett 110 (26), 142701 (2013).
[3] J. P. Fernández-García et al. Phys. Rev. C 92 (4), 044608 (2015).
[4] J. P. Fernández -García, M. A. G. Alvarez, L. C. Chamon. Phys. Rev. C. 92 (1), 014604 (2015)
[5] L. C. Chamon et al., Phys. Rev. C 66, 014610 (2002).
[6] M. A. G. Alvarez, et al, Nucl. Phys. A 723, 93 (2003).
[7] M. V. Andrés, J. Gómez-Camacho, and M. A. Nagarajan, Nucl. Phys. A 579, 273 (1994).
[8] M. V. Andrés, J. Gómez-Camacho, and M. A. Nagarajan, Nucl. Phys. A 583, 817 (1995).

Status of data analysis and preliminary results of the CHIFAR experiment

P. Russotto[1,*], L. Acosta[2,4], T. Cap[5], G. Cardella[2], E. De Filippo[2], F. Favela[1,6], E. Geraci[2,3], B. Gnoffo[2,3], C. Guazzoni[7], G. Lanzalone[1,8], C. Maiolino[1], N.S. Martorana[1,3], T. Matulewicz[9], A. Pagano[2], E.V. Pagano[1], M. Papa[2], K. Piasecki[9], E. Piasecki[10], S. Pirrone[2], R. Płaneta[11], G. Politi[2,3], F. Risitano[2,12], F. Rizzo[1,3], V. Sicari[7], K. Siwek-Wilczynska[9], I. Skwira-Chalot[9], M. Trimarchi[12]

1) INFN-LNS, Catania Italy
2) INFN-Sezione di Catania, Italy
3) Dipartimento di Fisica e Astronomia E. Majorana, Università di Catania, Italy
4) Instituto de Fisica, Universidad Nacional Autònoma de México
5) National Centre for Nuclear Research, Otwock-Swierk, Poland
6) Instituto de Ciencias Nucleares, Universidad Nacional Autònoma de México
7) Dip. di Elettronica, Informazione e Bioingegneria, Politecnico di Milano, Italy
8) Facoltà di Ingegneria e Architettura, Università Kore, Italy
9) Faculty of Physics, University of Warsaw, Warsaw, Poland
10) Heavy Ion Laboratory, University of Warsaw, Warsaw, Poland
11) M. Smoluchowski Institute of Physics, Jagiellonian University, Krakow, Poland
12) Dipartimento di Scienze MIFT, Univ. di Messina, Messina, Italy

e-mail: russotto@lns.infn.it*

Abstract – An update on the status of the data analysis of the CHIFAR experiment is reported.

INTRODUCTION

The CHIFAR experiment [1] was carried out at LNS in November 2019. Reactions between beams of ^{124}Sn,^{124}Xe and ^{112}Sn, accelerated at 20 AMeV by the CS, and targets of ^{64}Ni, ^{64}Zn and ^{58}Ni were studied by using the CHIMERA multi-detector [2] coupled to 10 telescopes of the FARCOS array [3]. The ten FARCOS telescopes, grouped in 5 couples, were arranged in a ring-like configuration covering about ¾ of the 2π azimuthal range at polar angles, in the laboratory, between 16 and 30 deg.

Main topics of the experiment are the competition between reaction mechanisms and the Intermediate Mass Fragment production phenomenon, aiming to extend towards the low energy regime the studies performed in the REVERSE and InKiIsSy experiments, carried out at beam energy of 35 AMeV [4]. The different combinations of neutron rich and neutron poor beams and targets will allow to investigate the above mentioned topics, also, with respect to the entrance channel Isospin content.

STATUS OF DATA ANALYSYS AND PRELIMINARY RESULTS

In most of the experiment data were collected by requiring at least 2 CHIMERA Silicon detectors fired. Special calibration runs measuring the scattering of p, ^{12}C, ^{16}O beams, delivered by the tandem, on Au target were used for energy calibration of CHIMERA and FARCOS detectors. When needed, data were also collected by using a dedicate trigger for the FARCOS telescopes. We will report here only on the status of the analysis of data collected by using CHIMERA multi-detector. Results of data collected by FARCOS will be reported elsewhere.

The identifications of particles based on ΔE-E and ΔE-ToF techniques, nearly be completed, have been used for the results here presented. Vice versa infos given by the identification of Light Charged Particles by means of Pulse Shape Analysis (PSA) on CsI(Tl) signals and identification of particles stopped in the Silicon detectors by means of the PSA on Silicon signal have not been included here. Differing from most of the previous CHIMERA experiments where ΔE-E is the main identification technique, the lower energy and heavy projectile/target of the CHIFAR experiment make most of the particles, including the heavier ones, being stopped in the Silicon detectors, and identified by using the DE-ToF technique. For this reason, a special attention has been dedicated to this phase of the identification procedures; more details will be given in another contribution of this issue [5].

As preliminary result, the mass number vs component of the velocity parallel to the beam axis, as obtained for the ^{124}Sn+^{64}Ni reaction at 20 AMeV for particles detected between Ring 2 and Ring 15 of the CHIMERA detector, i.e. polar angles between 2.6 and 78 deg, and without any data selection, is shown in Fig. 1.

Figure 1: Mass number vs component of velocity parallel to the beam axis for the $^{124}Sn+^{64}Ni$ reaction at 20 AMeV.

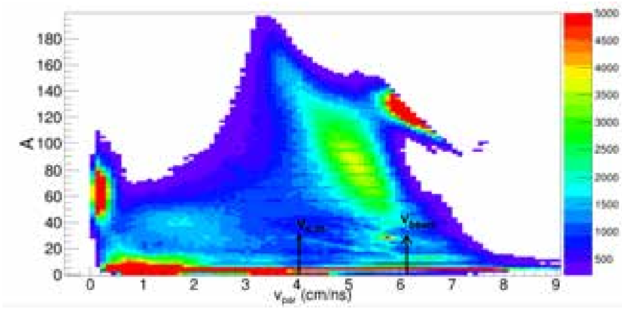

As said before, FARCOS presence causes some reduction of particles seen by the CHIMERA between 16 and 30 deg. We can clearly recognize the region of Projectile-Like-Fragments (PLF), after quasi-elastic collisions, having mass number around the one of the projectile and velocity near to the beam one. The shape observed in the high-populated PLF region indicates the presence of an auto-correlation in the data, i.e. the biggest masses have lowest velocity and vice versa. However, the good reproduction of the masses up to A≈120 region, by means of the ΔE-ToF technique, can be taken as a satisfactory result. Opposite to the PLF, the Target-Like-Fragments (TLF) can also be seen at very low velocity and around A≈ 60. This is a good result too, given the short base-of-flight (40 cm) of CHIMERA detectors in that angular region. In addition to the PLF-TLF quasi-elastic mechanisms, expected to be the main pattern in the peripheral collisions, we see also the presence of heavy fragments with a velocity intermediate between the beam velocity and the C.M. reference system one, in coincidence with the region of A≈40 and $v_{par}\approx$ 2cm/ns. This region corresponds to, both, strongly damped Deep Inelastic Collisions, also followed by PLF/TLF break-up, and fusion/fission mechanism, as typically observed in the low energy-regime [6]. The apparent lack of the "second arm", symmetrical with respect to the faster one here observed, is ascribed to the lack of data in the FARCOS region and to the low probability of fusion reactions with respect to DIC.

The proper sorting of a given mechanism, based on kinematical selections, results here more difficult, with respect to what previously done at 35 AMeV, because the lower PLF-TLF relative velocity tends to superimpose and mix PLF/TLF emitted fragments; in addition, the fusion/fission mechanism tends to populate the same kinematical region. As a first step, in order to try to study features of PLF emission mechanism after quasi-elastic collisions, we have sorted the data requiring, on an event-by-event base, the detection of the TLF fragment, defined by means of a graphical cuts applied to Fig. 1 (not shown here). This represents a strong bias for the data, corresponding to the selection of the sub-class of semi-peripheral collisions where the TLF was properly detected and identified. Nevertheless, this appears, in first approximation, as a reliable method to get rid of those reactions taking place through a "not binary-like" mechanism. After that, we have focused our attention on the PLF splitting, selecting events with two fragments (Z>=3) having v_{par}>2.5 cm/ns. After some additional cuts for better selecting the PLF splitting, the plot of parallel vs perpendicular to the beam axis velocity components for the Heavier of the two fragments (Fig. 2) and for the Lighter one (Fig.3) have been produced for different PLF splitting asymmetries (A_H/A_L). It is nice to see that the expected "Coulomb-rings" are obtained. Search for forward/backward asymmetries in the "Coulomb-rings" by means of angular distributions, as signal of dynamical effects, will be soon pursued.

More complete results, extended also to other projectile/target combinations will be available in the future.

Figure 2: component of velocity perpendicular to the beam axis vs parallel one for the Heavier fragment emitted in PLF splitting, for different splitting asymmetries, in the $^{124}Sn+^{64}Ni$ reaction at 20 AMeV.

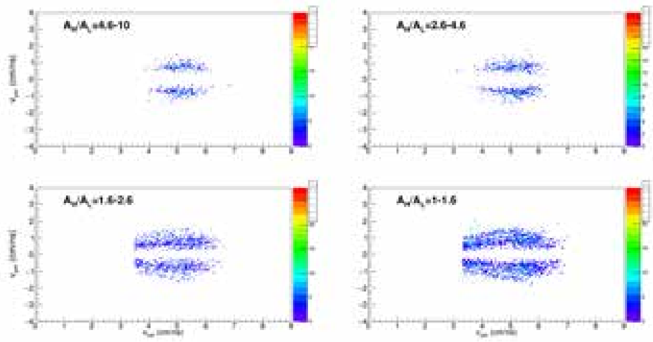

Figure 3: same as Fig. 2 but for the Lighter fragment

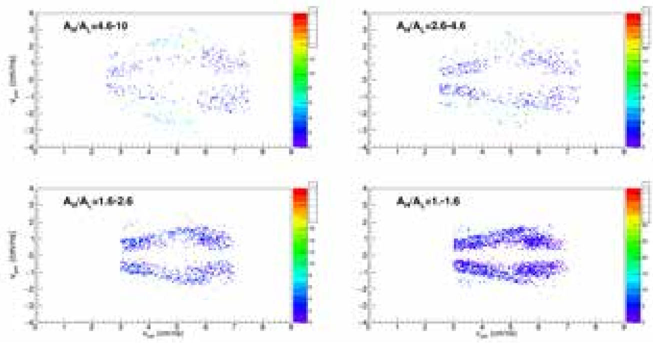

REFERENCES

[1] E.V. Pagano et al., Proposal of CHIFAR experiment, approved by the 2017 LNS-PAC.

[2] E. De Filippo and A. Pagano, Eur. Phys. J A50, 32 (2014) and refs. therein; A. Pagano, Nucl. Phys. News 22, 28 (2012) and refs. therein.

[3] E. De Filippo et al., NIM in preparation; E.V. Pagano et al., EPJ Web Conf. 117, 10008 (2016).

[4] P. Russotto et al., Eur. Phys. J A56, 12 (2020) and refs. therein.

[5] B. Gnoffo et al., see contribution to this issue.

[6] S. Pirrone et al., Eur. Phys. J A55, 22 (2019).

Study of $^{10}Be+^{120}Sn$ reaction dynamics at energies below and above the Coulomb barrier.

F. G. Barba[1] , J.P. Fernández-García[2,3], D. Galaviz[1,4], M. A. G. Alvarez[2], D. Dell'Aquila[5], A. Di Pietro[6], P. Figuera[6], M. Fisichella[6], L. R. Gasques[7], G. L. Guardo[6], M. Gulino[6,8], M. La Cognata[6], L. Lamia[6,9], D. Lattuada[6], R. G. Pizzone[6], S. Romano[6,9], A. Sánchez-Benítez[10], D. Santonocito[6], V. Scarduelli[7], L. Sergi[6], N. Soic[5], R. Sparta[6], A. Tumino[6,8] and P. Prajapati[6]

1)Laboratório de Instrumentação de Física Experimental de Partículas (LIP), Av. Prof. Gama Pinto 2, 1649-003 Lisbon, Portugal.
2) Departamento de Física Atómica, Molecular y Nuclear, Universidad de Sevilla, Apartado 1065, 41080 Sevilla, Spain.
3) Centro Nacional de Aceleradores, Universidad de Sevilla, Junta de Andalucía-CSIC, 41092 Sevilla, Spain.
4)Departamento de Física, Faculdade de Ciências, Universidade de Lisboa, 1749-016 Lisbon, Portugal
5)Ruder Boskovic Institute, Zagreb, Croatia
6) Laboratori Nazionali del Sud LNS-INFN, Catania, Italy
7)Universidade de São Paulo, Instituto de Fisica, Rua do Matao, 1371, 05508-090 São Paulo, São Paulo, Brazil
8) Facoltà di Ingegneria ed Architettura, Università Kore, I-94100 Enna, Italy
9) Dip. di Fisica e Astronomia, Università di Catania, Via S. Sofia, I-95125 Catania, Italy
10)Departamento de Física Aplicada, Universidad de Huelva, Campus de El Carmen, E-21071 Huelva, Spain

Abstract – New experimental data of the $^{10}Be+^{120}Sn$ reaction at energies of 27, 31 and 40 MeV were measured at LNS-INFN laboratory. The preliminary experimental data will be analyzed.

INTRODUCTION

The study of collisions induced by halo nuclei has revealed information about their structure. In fact, an effect in the reaction dynamics has been observed due to their diffuse structure associated with a very low breakup threshold (see e.g. [1]). Moreover, due to its low binding energy, the dissociation of the projectile into two or more fragments is an important mechanism occurring in collisions induced by these radioactive nuclei, and coupling effects to the continuum can deeply affect the other reaction channels around the barrier.

Stable weakly bound nuclei have similar characteristics to halo nuclei, such as a low breakup threshold associated with a cluster structure of their ground state. Therefore, the study of reactions induced by stable weakly bound nuclei can help to provide an understanding of the reaction dynamics with halo nuclei. Moreover, these kinds of reactions can provide a platform to test the validity of new theoretical models.

In the last years, a systematic study of weakly bound nuclei colliding with ^{120}Sn was carried out. In Ref. [2, 3], the reaction $^{10}B+ ^{120}Sn$ has been measured at four different energies around the Coulomb barrier. A simultaneous analysis of the elastic scattering, inelastic excitation of projectile and target and one-neutron pickup transfer have been performed within the coupled reaction channels (CRC) formalism, where a new value of the quadrupole transition in ^{10}B was deduced. Recently, in Ref. [4], theoretical calculations within the CRC formalism have provided an overall good agreement with inelastic, one-neutron stripping, one-proton pickup, one-deuteron pickup, and ^{3}He stripping transfer data. However, to improve the description of the experimental elastic scattering data, the inclusion of additional channels in the coupling scheme might be necessary.

In Ref. [5], the reaction $^{9}Be+ ^{120}Sn$ at energies around and below the Coulomb barrier has been studied, four-body CDCC calculations have reproduced the experimental data, showing that the inclusion of the ^{9}Be continuum is relevant. This result suggests that breakup is important even at low energies.

The ^{10}Be nucleus is a beta decay nucleus with a long half-life of $1.5\cdot10^{6}$ years, it has an excited state 2^{+} at 3.368 MeV and the neutron binding energy is 6.812 MeV [6]. Moreover, a cluster structure $^{6}He+^{4}He$ has been observed in [7] and [8]. The reaction dynamics of ^{10}Be are not yet fully understood since only three sets of non conclusive experimental data of reactions induced by ^{10}Be are found in the literature [9-12].

In this work, we present new preliminary experimental data of the nuclear reaction induced by ^{10}Be on a ^{120}Sn target at incident energies around and above the Coulomb barrier, 21, 31 and 40 MeV.

EXPERIMENTAL SETUP AND RESULTS

The experiment was carried out at the Laboratori Nazionali del Sud. The newly developed ^{10}Be radioactive beam with an average intensity of 700 pA was produced by the SMP Tandem Van de Graaff accelerator and transported into the CT2000 scattering chamber, at the incident energies of 27, 31 and 40 MeV. Taking into account the statistics and the energy resolution a target of ^{120}Sn 211 μg/cm² thickness was used.

The experimental setup included four silicon telescope detectors and two silicon single channel monitors. The telescopes were used to characterize the products of the reaction from 34º to 156º (see Table 1) and consisted of a front SSSD (ΔE) with thickness of ~20 μm and a back DSSD (E) with thickness of ~1000 μm. The monitors were placed at 25º to monitorize beam position and for normalization purposes. In figure 1, a sketch of the experimental setup is presented.

This configuration allowed us to separate the different fragments coming from the reaction ^{10}Be+^{120}Sn. In figure 2, a preliminary bidimensional diagram of the reaction ^{10}Be+^{120}Sn at 40 MeV at the laboratory scattering angle of 70º is shown. Figure 2 presents a clear particle separation in mass and charge, in fact, ^{6}He and ^{4}He particles can be observed, revealing a possible cluster structure ^{6}He+^{4}He of ^{10}Be.

Telescope	Angular range
Telescope A	34º - 76º
Telescope B	90º - 133º
Telescope C	59º - 101º
Telescope D	114º - 157º

Table 1: Angular range covered by each telescope

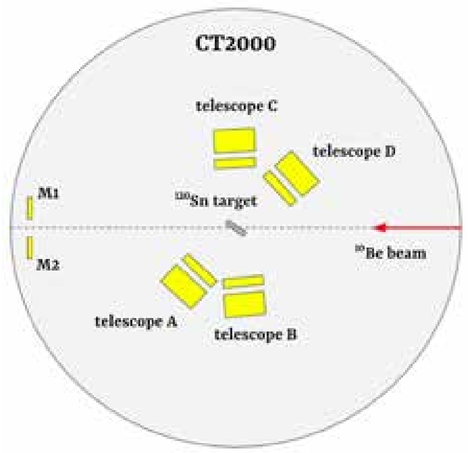

Figure 1. Sketch of the experimental setup

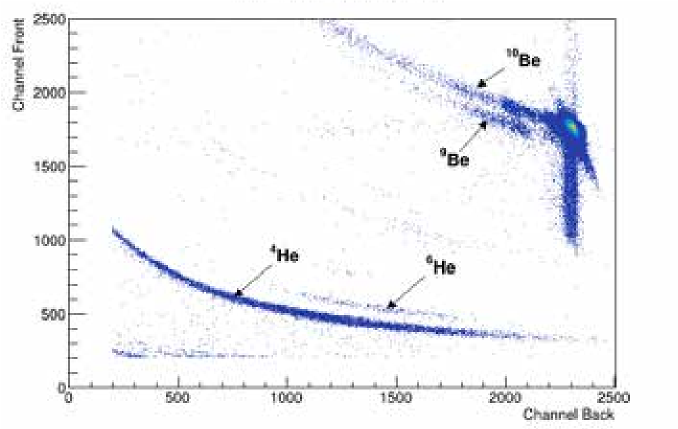

Figure 2: Bidimensional spectrum ΔE versus E of the reaction ^{10}Be+^{120}Sn at 40 MeV

CONCLUSIONS

We have measured the reaction ^{10}Be+ ^{120}Sn at three different incident energies around and above the Coulomb barrier (27, 31 and 40 MeV.). Preliminary experimental data show particles of ^{6}He and ^{4}He coming from the cluster structure of ^{10}Be and also ^{9}Be coming from the n+^{9}Be breakup channel. A detailed analysis of this experiment will help us to understand not only the elastic scattering of ^{10}Be+^{120}Sn but also different breakup channels and structure of the radioactive nucleus ^{10}Be

REFERENCES

[1] L. Canto et al, Physics Reports 596, 1 (2015).
[2] M. A. G. Alvarez et. al, Phys. Rev. C 98, 024621 (2018)
[3] L. R. Gasques et. al, Phys. Rev. C 97, 034629 (2018)
[4] L. R. Gasques et. al, Phys. Rev. C 103, 034616 (2021)
[5] A. Arazi et. al, Phys. Rev. C 97, 044609 (2018)
[6] R. C. Greenwood, Phys. Lett. 23, 482 (1966)
[7] D. Dell'Aquila et. al, Phys. Rev. C 93, 024611 (2016)
[8] N. Soic et. al, Europhys. Lett. 34, 7-12 (1996)
[9] J. J. Kolata et. al, Phys. Rev. C 69, 047601 (2004)
[10] J. C. Zamora et. al, Phys. Rev. C 84, 034611 (2011)
[11] C. Signorini et. al, Eur. Phys. J. A 13, 129 (2002)
[12] A. Di Pietro et. al, Phys. Rev. Lett. 105, 022701 (2010)

Characterizing Si-He thin films with heavy ions for nuclear reaction experiments in inverse kinematics.

F. G. Barba[1], D. Galaviz[1,2], P. Figuera[3], F. J. Ferrer[4,5], M. La Cognata[3], A. Fernández[6], B. Fernández[4,5], J. P. Fernández-García[4,5], E. Galiana[1], V. Godinho[6], J. Gómez-Camacho[4,5], G. L. Guardo[3], L. Lamia[3], A. di Pietro[3], P. Prajapati[3], A. M. Sánchez-Benítez[7], R. Sparta[3], P. Teubig[1], A. Tumino[3] and M. Xarepe[1]

1) Laboratório de Instrumentação de Física Experimental de Partículas (LIP), Av. Prof. Gama Pinto 2, 1649-003 Lisbon, Portugal.
2) Departamento de Física, Faculdade de Ciências, Universidade de Lisboa, 1749-016 Lisbon, Portugal
3) Laboratori Nazionali del Sud LNS-INFN, Catania, Italy
4) Departamento de Física Atómica, Molecular y Nuclear, Universidad de Sevilla, Apartado 1065, 41080 Sevilla, Spain.
5) Centro Nacional de Aceleradores, Universidad de Sevilla, Junta de Andalucía-CSIC, 41092 Sevilla, Spain.
6) Instituto de Ciencia de Materiales de Sevilla (CSIC, U. Sevilla), 41092 Sevilla, Spain.
7) Centro de Estudios Avanzados en Física, Matemáticas y Computación (CEAFMC), Department of Integrated Sciences, University of Huelva, 21071 Huelva, Spain

Abstract – In the view of the preparation works for the approved experiment INVERSE-ALPHA [1], a test to evaluate the thin Si-He [2] films by exposing them to high energy nickel beams, as considered for the experiment, was performed. Preliminary results indicate the potential of using this type of target in inverse kinematic experiments with stable and radioactive ion beams.

INTRODUCTION

The majority of the natural stable nuclei heavier than iron are produced in stellar nucleosynthesis processes dominated by neutron capture reactions. The *s*-process [3] and *r*-process [4], together with other neutron capture processes like the *i*-process [5], are responsible for the production of almost all heavy isotopes in the universe. There are however about 35 nuclei, which cannot be produced through the previously mentioned neutron capture processes. The synthesis of the so-called p-nuclei still remains an open question in nuclear astrophysics [6].
Furthermore, uncertainties in the nuclear knowledge are still present in the description of the γ-process [6,7], being the most dominant those associated with the knowledge of the α-nuclear potential. Sensitivity studies [8] have identified this nuclear quantity as one of the main sources of uncertainty in the description of the nucleosynthesis process.
The search for alternative experimental approaches to reduce the uncertainty in the determination of nuclear alpha potentials motivated the experimental proposal "INVERSE-ALPHA" [1], which proposed the use for the first time of newly developed thin silicon films with a high helium content [2]. The approved experiment intended to measure the elastic scattering reaction process in inverse kinematics using ^{58}Ni and ^{62}Ni beams at energies around the Coulomb barrier of the α-Ni system.
In the framework of that approved experiment, a test beam-time was scheduled and executed at LNS in February 2020. In this work, the experimental approach adopted for the test is described, and a preliminary analysis of the measured data is presented. Despite the fact that the execution of the INVERSE-ALPHA experiment was severely affected by the pandemic situation in 2020, the test beam-time was extremely useful in verifying the use of these thin Si-He films in experiments considering heavy beams in inverse kinematics.

EXPERIMENTAL SETUP AND RESULTS

The test beam time was executed at the Laboratori Nazionali del Sud using the CT2000 scattering chamber, the same location where the INVERSE-ALPHA run was planned. The Tandem accelerator produced a ^{58}Ni beam (charge state 12^+, terminal voltage 11.522 MV) that was accelerated to an energy of 150 MeV. During the test run a target developed following the description given in [2] was used. A first characterization of this type of targets was carried out [9], indicating a He to Si ratio of 1/2.
The experimental setup for the test consisted of three different detection systems: a photodiode, a surface barrier

silicon detector (E1), and a telescope system based on silicon detectors (ΔE2-E2). The detectors were placed on two rotating arms, allowing for the coverage of the angular distribution of interest for the test. Measurements of the emitted particles were done at angles 80º ≤ Θ_{lab} ≤ 40º.

As the expected energies of the various recoil nuclei had large differences, the signals from each of the detection systems were injected into two electronic chains with different amplification gains. The thickness properties and the dynamic range for each detection system are listed in table 1.

Table 1: Angular range, thickness and dynamic ranges covered by the detectors considered during the test run.

Detector	**Thickness (µm)**	**Dynamic Ranges (MeV)**	
		Low-gain	High-gain
E1	1000	50	6
ΔE2	14	90	10
E2	1000	100	10
Photodiode	300	50	8

During the test beam time the elastic scattering process of the incident ^{58}Ni beam of the various elements present in the target was observed. They are well separated in both the single-channel detectors, as well as in the telescope. This is shown respectively in figures 1 and 2, where the spectrum registered by the Photodiode, and the telescope detectors are presented.

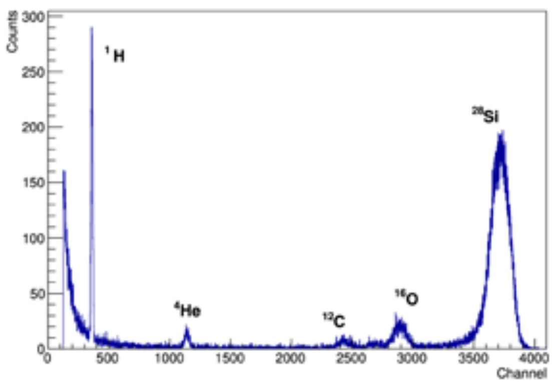

Figure 1: Spectrum measured with the Photodiode detector at Θ_{lab} = 50º. The labels indicate the position of the various isotopes present in the target scattered off the ^{58}Ni beam.

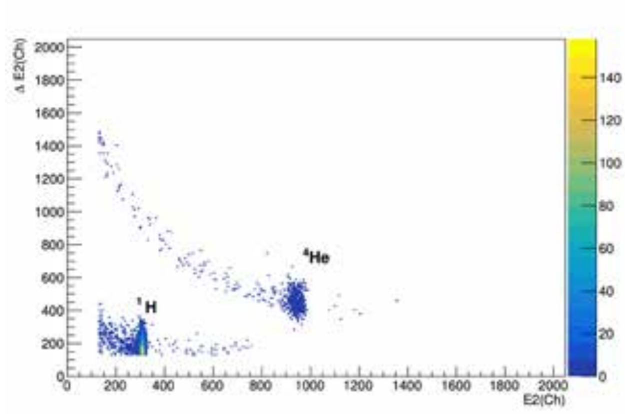

Figure 2: Spectrum measured with the telescope detector at Θ_{lab} = 50º. The labels indicate the position of the light elements scattered off the ^{58}Ni beam.

We also observed a minor degradation of the target during the irradiation. Correlations to the total charge deposited on the target are presently under study.

CONCLUSIONS

In the scope of the approved experiment INVERSE-ALPHA, a test experiment was performed by exposing high energy ^{58}Ni isotopes to the newly developed Si-He films. The results from the test indicate that these targets are very suitable to study reactions on the helium nuclei in inverse kinematics, opening the door to future studies with radioactive isotopes. A complete analysis of the measured data is on-going.

REFERENCES

[1] D. Galaviz *et al.,* LNS Proposal T-136 (2018)
[2] V. Godinho *et al.,* ACS Omega 2016, 1 (6), 1229 (2016)
[3] F. Käppeler *et al.*, Rev. Mod. Phys. 83, 157 (2011)
[4] F.-K. Thielemann, *et al.*, Lecture Notes in Physics, vol 812, 153 (2011)
[5] F. Herwig *et al.*, Astrophys. J. 727, 89 (2011)
[6] M. Arnould and S. Goriely, Phys. Rep. 384, 1 (2003)
[7] M. Pignatari *et al.*, Int. J. Mod. Phys. E 25, 163003 (2016)
[8] A. Simon *et al.*, J. Phys. G: Nucl. Part. Phys. 44, 064006 (2017)
[9] J. Ferrer *et al.*, Eur. Phys. J. Plus 135, 465 (2020)

Status of the FRAISE facility at the Laboratori Nazionali del Sud-INFN

N.S. Martorana [1,2], C. Altana[2], A. Amato [2], L. Calabretta [2,3], G. Cardella [4], A. Caruso [2], L. Cosentino [2], M. Costa [2], E. De Filippo [4], G. De Luca [2], E. Geraci [1,4], B. Gnoffo [1,4], C. Guazzoni [5], L. Lo Monaco [1], C. Maiolino [2], E.V. Pagano [2], S. Pirrone [4], G. Politi [1,4], S. Pulvirenti [2], F. Risitano [6,4], F. Rizzo [1,2], A.D. Russo [2], P. Russotto [2], D. Santonocito [2], A. Trifirò [6,4], M. Trimarchi [6,4], S. Tudisco[2], G. Vecchio [2]

1) Dipartimento di Fisica e Astronomia"Ettore Majorana", Università degli Studi di Catania, Italy
2) INFN-LNS, Catania, Italy
3) INFN-LNL, Legnaro, Italy
4) INFN-Sezione di Catania, Italy
5) DEIB Politecnico Milano and INFN Sez. Milano, Italy
6) Dipartimento MIFT, Università di Messina, Italy

Abstract - At the Laboratori Nazionali del Sud of INFN, the upgrade of the Superconductive Cyclotron (CS) and the building of a fragment separator, FRAISE (**Fra**gment **I**n-flight **Se**parator), are currently ongoing. FRAISE will permit to produce **R**adioactive **I**on **B**eams (RIBs) with intensity in the range of 10^3-10^7 pps, using the In-Flight Fragmentation method. An intense R&D program has been started to develop the FRAISE facility, as well as a new diagnostics system and the fragmentation target. In this contribution, the status of the FRAISE facility and the R&D program are reported.

INTRODUCTION

At INFN-LNS RIBs have been produced, since 2001, employing the In Flight Fragmentation method by means of the FRIBs facility. The main limitation of the FRIBs facility was the maximum power delivered by the CS (100 W). Because of this, investigations have been focused on nuclei not too far away from the stability, being the yields for very exotic nuclei not enough to carry out experiments with high statistics.

The project of the Superconductive Cyclotron upgrade aims to provide stable ion beams with a power up to 10 kW [1-3]. This will allow to obtain beams, at intermediate energies and for ions from carbon to argon, with intensities up to 10^{13} pps [1-3]. Currently, the building of a new fragment separator, named FRAISE, is ongoing to exploit the capabilities of the CS upgrade for providing high intensity and high quality exotic beams. The new facility will be installed in a new hall, located in the region of the previous LS-20 and LS-40 experimental halls, as displayed in Fig. 1 [1-3]. The details about the FRAISE facility are discussed in Ref. [4].

Figure 1: Schematic view of the INFN-LNS beam lines and halls. The positions of the FRIBs and FRAISE facilities are indicated with circles [2].

FRAISE AND R&D PROGRAM

In the FRAISE facility, due to radioprotection issues, the power of the primary beams will be limited to ≈ 2 kW. This value will permit to increase the yield by a factor 20 with respect to the FRIBs facility. The region that will host FRAISE will be managed to allow a safe air treatment and an appropriate shielding of walls, floor and roof. The latter ones will be made with materials suitable for slowing down and absorbing radiations, mainly neutrons and γ-rays, and to avoid a contamination in adjacent halls. Furthermore, a dedicated radio-protection system for the first magnetic dipole will be required. This dipole represents a crucial point, because the residual primary beam, stopped in the dipole, will deposit a high dose. Also a new production target, CLIM, will be used in the FRAISE facility. Such target will be composed of a rotating system of circular beryllium or carbon targets, in order to increase the active surface and to avoid depositing the total intensity of the beam on a single spot. The target will be significantly activated, after and during experiments, and it will be impossible to remove it manually. For this reason, a remote control system will be used in order to automatically proceed with the replacement of the target and its storage in an appropriate area, located close to the first magnetic dipole. In such a facility, there will be two collimation devices: the first one will be placed in the dispersive plane, and the second one will be placed at the exit of the separator, in order to stop the undesired isotopes of the cocktail beam. Furthermore, the slit placed at the center of separator on the dispersive plane, where the value of energetic dispersion is high, will allow to vary the acceptance of $\Delta p/p$ of the fragment separator from typical values of $\Delta p/p \approx 1.2$ % to lower values. After the central slit, it will be possible to insert an aluminum wedge/degrader, in order to perform a separation of ions with the same A/Z. Using FRAISE, it will be possible to deliver exotic beams towards the CHIMERA [5] and MAGNEX [6] halls. Moreover, the GiRa chamber will be also installed at the exit of the fragment separator, as discussed in the report of A.D. Russo [4]. The high beam intensity achieved with FRAISE requires the use of diagnostics and tagging systems able to operate in a strong radioactive environment and in a wide intensity range, from 10^3 pps, as typical for very exotic isotopes, to 10^7 pps, as typical for exotic isotopes close to the stability valley. Moreover, the diagnostics and tagging systems should be able to sustain several experiments per year. The RIBs composition will be investigated by measuring the ΔE energy loss of ions and TOF between two detectors, or with respect to a time signal synchronous with the primary beam, arrival on production target, as the Cyclotron Radiofrequency signal. For the aforementioned reasons, we are investigating the possibility to use SiC detectors for the FRAISE diagnostics system [7]. In detail, we are studying to build an array of detectors based on the SiC technology, where the single detection unity pad will be 5x5 mm^2 and 100 μm thick. By assembling an array of several pads will be possible to cover ≈ 8x4 cm^2, enough for RIBs distribution in the high dispersion point. Using such a segmentation, each pad will need to sustain a maximum flux of 10^6 pps, even in the region where the beam profile is peaked.

A feasibility study is already started, performing simulations and preliminary tests on the use of SiC detectors. Preliminary investigations, performed both with tests and simulations, allowed to obtain a first reference study fixing the features of such diagnostics system. Simulations about several physics cases are reported in Ref. [8]. First tests using SiC detectors have been performed at INFN-LNS and Dipartimento di Fisica e Astronomia, "Ettore Majorana". The tests have been performed using an α source of 3 MeV and a mixed α source. During these tests, SiC detectors with a surface of 24 mm^2 and thickness of 10 μm, as shown in Fig. 2, have been used. These preliminary tests allowed to obtain a first reference study fixing features of diagnostics system.

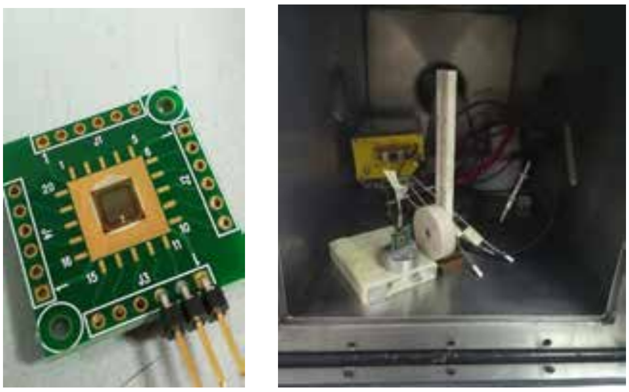

Figure 2: (left) Photo of a SiC detector (24 mm^2, 10 μm). (right) Photo of the experimental setup used during a test with an α source.

Further steps will concern the production of SiC arrays and the validation of the system, using both radioactive sources, low energy stable beams and unstable beams. Moreover, in order to decrease the beam commissioning time and to allow for powerful control of the beam quality, also a fast integrated electronics, coupled to innovative software tools, based also on machine learning, is under development.

CONCLUSION

In this contribution, the status of the FRAISE facility as well as the R&D program have been reported. The R&D program allowed to develop the layout of the FRAISE facility, the design of the beam lines and control systems, the design of the GiRa chamber and of the new diagnostics system. The next steps will concern the assembly and tests of the whole facility, using primary and exotic beams.

REFERENCES

[1] N.S. Martorana, Nuovo Cimento, 44 C, (2021) 1.
[2] A.D. Russo A. et al., Nucl. Instrum. Methods B, 463 (2020) 418.
[3] P. Russotto et al., J. Physics: Conf. Ser., 1014 (2018) 012016.
[4] A.D. Russo et al., Activity Report LNS (2020).
[5] A. Pagano et al., Nucl. Phys. A, 734 (2004) 504.
[6] F. Cappuzzello et al., EPJ A, 52 (2016) 167.
[7] S. Tudisco et al., Sensors, 18 (2018) 2289.
[8] F. Risitano et al., Activity Report LNS (2020).

The Recoil Directionality (ReD) Experiment at LNS

S. Sanfilippo[1, 2] , S. Albergo[3,4], G. Cappello[3,4], M. Gulino[5,6], L. Pandola[6] and A. Tricomi[3,4]

1) Dipartimento di Matematica e Fisica, Università degli Studi Roma Tre, 00146 Roma, Italy;
2) INFN – Sezione di Roma Tre, 00146 Roma, Italy;
3) Dipartimento di Fisica e Astronomia, Università degli Studi di Catania, 95123 Catania, Italy;
4) INFN – Sezione di Catania, Italy, 95123 Catania, Italy;
5) Facoltà di Ingegneria e Architettura, Università di Enna Kore, 94100 Enna, Italy;
6) INFN – Laboratori Nazionali del Sud, 95123 Catania, Italy

Abstract - Directional sensitivity to nuclear recoils could provide a smoking gun for a possible discovery of dark matter in the form of WIMPs. Given the potential importance of such a capability in the framework of dark matter searches, a new dedicated experiment, ReD (Recoil Directionality), was designed as part of the programme of the DarkSide Collaboration, in order to scrutinize this hint. Since its deployment in the 80° beam line of LNS during 2019, ReD was completely integrated and commissioned. This contribution describes the ReD physics run which was performed with the TANDEM beam in February 2020, just before the stop of the activities due to the COVID-19 pandemic.

INTRODUCTION

The main goal of the ReD experiment is to demonstrate the directional sensitivity to nuclear recoils in liquid argon by using a small scale, dual-phase Liquid Argon Time Projection Chamber (LAr TPC). The recoil of an Ar nucleus in the liquid gives both a prompt scintillation signal and ionization charges. Electrons are drifted by an electric field towards the Ar gas and produce a delayed scintillation by electroluminescence. The optical signals are collected by means of newly developed silicon photomultipliers (SiPMs), working at cryogenic temperature [1, 2]. Directional information is potentially available in a LAr TPC by exploiting the recombination effect. Indeed, columnar recombination models [3] suggest that the magnitude of the electron-ion recombination effect should vary with the angle between the electric field and the recoil track direction. Consequently, a difference in the TPC response is expected when the ionizing track is either parallel or perpendicular to the electric field. In order to investigate this possibility, recoils at different angles can be produced by neutrons having a well-defined direction and energy.

The ReD experiment is part of the DarkSide program, so it may provide a fully scalable technology to bring the future dark matter experiments based on LAr to the multi-ton scale, i.e. DarkSide-20k [4].

NEUTRON BEAM PRODUCTION AND ^{7}BE SELECTION

Neutrons are produced by the p(^{7}Li,^{7}Be)n reaction. A ^{7}Li ion beam is accelerated up to 28 MeV by the 15 MV TANDEM available at the LNS-INFN. It is driven towards the 80° experimental room, where it impinges on a CH_2 target hosted inside a vacuum scattering chamber. CH_2 targets of 300 μg/cm^2 up to 550 μg/cm^2 were used during all the data taking period. The targets are mounted on a holding support that allows for a fast replacement without opening the scattering chamber. A beam current in the range of 10 nA up to 15 nA was achieved. The target ageing was monitored by a Si detector placed in the scattering chamber, measuring the H/C ratio in the target. Due to ageing, the targets had to be replaced every ~ 12 hours.

Neutrons with energy of about 7 MeV and at a specific angle with respect to the beam line, traveling in the direction of the LAr TPC were selected by detecting the associated ^{7}Be reaction product. Therefore, the vacuum scattering chamber was equipped with a ΔE-E telescope (ΔE ~ 20 μm and E ~ 1000 μm thick, respectively) of Si detectors, allowing for a Z identification of the detected particle. The telescope was placed at an angle of 5° (θ_{Be}) with respect to the beam direction at a distance of 46.5 cm from the target. The tagging of ^{7}Be at a fixed angle made it possible to calculate the exit angle and energy of the neutron. Moreover, the p(^{7}Li,^{7}Be)n reaction plane is selected so that the direction of the neutrons impinging into the TPC forms an angle of about 71° with the (vertical) direction of the electric field. This allows the production of recoils parallel and orthogonal to the direction of the field. An example of ^{7}Be identification by means of the ΔE – E technique is displayed in fig. 1.

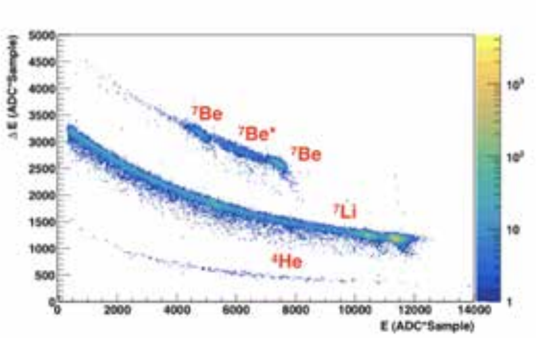

Figure 1: ΔE - E spectrum for the p(^{7}Li,^{7}Be)n reaction for the particle identification. Clear loci due to the presence of the ^{7}Be reaction byproduct are visible together with the ^{7}Li primary beam and some α events.

The upper part of the spectrum is populated by the ^{7}Be particles, while the ^{7}Li from the elastic scattering of the primary beam is clearly visible in the central part.

The silicon telescope detector was mounted on a stepper-motor that allows for a fine tuning of its position without stopping the beam and opening the scattering chamber.

Figure 2: Picture of the stepper-motor that housed the silicon detectors for the particle identification inside the scattering chamber.

Figure 2 shows a picture of the motor system with the silicon detectors as they are mounted inside the scattering chamber. Neutron-Ar interactions producing 20-100 keV nuclear Ar recoils were then recorded in the TPC, while the scattered neutrons were intercepted by a set of nine 3-inch neutron detectors (LSci), allowing to estimate the argon recoil direction. All LSci are placed such to tag recoils having the same energy, i.e. the same scattering angle with respect to the incident neutron, but different angle with respect to the drift field of the LAr TPC.
The 80° experimental hall is displayed in Fig.3 together with the ReD cryogenic system that housed the TPC, the neutron spectrometer array behind it, and the scattering chamber at its own left side.

BEAM DATA ANALYSIS

A total of 124 runs (241.7 hours, 10.07 days) taken with different trigger and drift field conditions were selected for the final analysis.

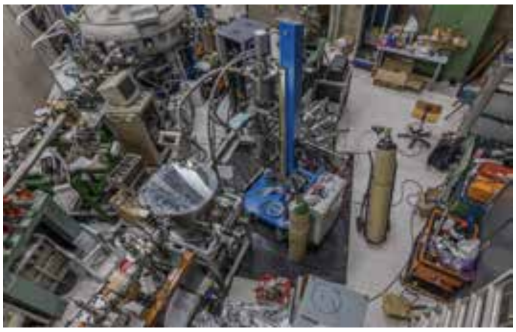

Figure 3: 80° experimental hall where the ReD experiment is located at LNS.

The ultimate goal is to scan the events looking for a ^{7}Be signal in the silicon detector, a signal compatible with a neutron elastic scattering in the TPC, that in turn interacts in the neutron spectrometer, i.e. a triple coincidence. A total of ~ 7000 such events were found with the proper timing and energy (about 70 keV$_{nr}$), which are undergoing fine analysis. Figure 4 shows a scatter plot of neutrons and gamma identified events with an energy deposition in one Lsci with a proper time tag in both the silicon and TPC detectors.

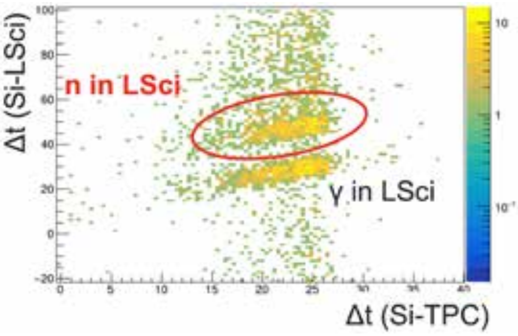

Figure 4: Scatter plot of neutrons (red locus) and gammas in one liquid scintillator detector in time coincidence with TPC and silicon detector.

The directionality pattern has to be searched by a statistical approach looking for scintillation-ionization (S1-S2) anti-correlation, and, if the hint by the SCENE experiment confirmed [5], it should be possible to measure a discrepancy of about 8% between parallel and perpendicular recoil tracks with respect to the electric field.

REFERENCES

[1] C. E. Aalseth et al., (The DarkSide Collaboration), J. Instr. **12**, P09030 (2017);
[2] F. Acerbi et al., IEEE Trans. Electr. Dev. **64**, 521-526 (2017);
[3] G. Jaffè, Ann. Phys. **42**, 303 (1913) ; G. Jaffè, Phys. Rev. **58**, 968 (1940);
[4] C. E. Aalseth et al. (The DarkSide Collaboration), Eur. Phys. J. Plus **133**, 131 (2018);
[5] H. Cao et al. (The SCENE Collaboration), Phys. Rev. D **91** (2015) 092007.

•. ASTROPARTICAL PHYSICS

The integration of the KM3NeT Detection Units at LNS

G. Battiato, G. Cacopardo, C. Calì, C. D'Amato, M. Anastasi, L. D'Antoni, A. Grmerk, P. Litrico, G. Larosa, G. Passaro, G. Pastore, S. Pulvirenti, G. Riccobene, P. Sapienza, D. Santonocito, S. Vinciguerra on behalf of the KM3NeT Colaboration

Laboratori Nazionale del Sud -INFN

Abstract – The main objectives of KM3NeT are the search of high energy neutrinos from cosmos with ARCA and the study of neutrino properties with ORCA. The two neutrino telescopes are located in two deep sites in the Mediterrean Sea: ARCA 80 km off-shore Capo Passero (Sicily, Italy) at 3500 m depth and ORCA 20 km off-shore Toulon (France) at 2500 m depth respectively. Several institutes of the KM3NeT collaboration take part to the construction of both ARCA and ORCA. LNS plays a key role in the construction of the ARCA Detection Units.

Introduction

The KM3NeT telescope is made of Detection Units (DU). The modularity allows a phased implementation of the telescoped with increasing scientific potential. The DUs are made of several parts, some of them are produced within the KM3NeT collaboration, while others are provided by external suppliers. Each DU hosts 18 Digital Optical Modules (DOMs) that collect the Cherenkov light emitted by the charged particles produced in neutrino interactions. The DOMs have been designed and built to withstand pressure up to 350 times the atmospheric pressure. Each DOM is made of 31 photomultiplier tubes arranged to look in all directions for capturing light emitted by particles passing by from all directions. The time of arrival of the light is registered by the DOM, and is used to reconstruct the neutrino direction thus allowing to localize the neutrino sources.

The DOMs are attached via a titanium collar to two parallel Dyneema® ropes. Additional spacers are added in between the DOMs to maintain the rope parallels. Attached to the ropes there is the vertical electro-optical cable, a pressure balanced, oil-filled, plastic tube that contains two copper wires for the power transmission and 18 optical fibres for the data transmission. At each storey two power conductors and a single fibre are branched out via the breakout box. The power conductors and optical fibres enter the glass sphere via a penetrator. A buoy at the top of the DU allows to reduce the horizontal displacement of the top relative to the base due to sea currents. The DU is coiled around a large spherical frame, the so-called launcher for optical modules (LOM). The LOM is mounted on the anchor and deployed as a whole in the seabed. The Detection Unit is then connected to the seafloor network through an electrooptical cable branched to a connector mounted on the anchor. The connection is performed by a ROV operated from the vessel. After the connection with the seabed infrastructure, the LOM is released from the anchor allowing the DU to unfurl and reach its nominal configuration. The LOM is recovered when it reaches the sea surface and reused for further DU deployments.

The Detection Unit integration is very challenging and requires expertise in electronics, optics and mechanics. It has been split into six processes that are summarized in Figure 1. For each process detailed procedures, including test reports to be filled during all integration steps, have been established and are constantly updated. The workflow starts with the integration of the DOMs to the VEOC and ends with the final functional tests on the DU uploaded on the LOM and assembled with the anchor. The calibration of the DU, process 3, is carried on by a different team that takes in charge the DU after the integration of the Base and hand back it ready for the uploading on the LOM.

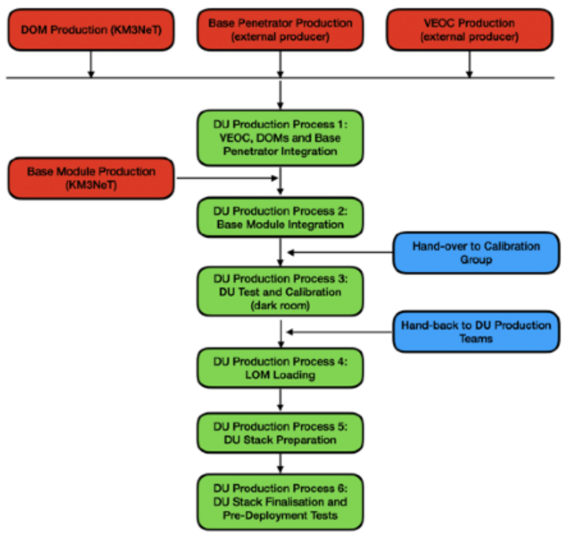

Figure 1: DU integration work flow

In process 1 the fibres that comes from the VEOC, provided by an external producer, are spliced at the exit of break out box (BOB) with the fibre coming from the DOM and the electrical wires are connected. At the end of the VEOC the fibres are spliced with the fibre coming to

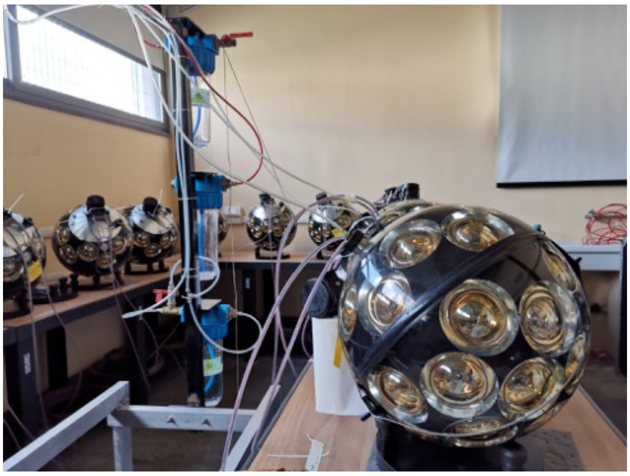

Figure 2: ARCA DU during DOM-VEOC integration

the Base penetrator. At the end of this phase the VEOC is power up and the optical budget of each DOM is recorded. If the DOMs pass the acceptance test the BOB caps are welded with a dedicated tool and the BOBs are filled with oil.

In process 2 the fibres from the penetrator are spliced with the corresponding fibres from the Base Module, the connectors, the penetrator and the CLB board are mounted. Before closing the Base module, the VEOC is power up again and the optical budget of each DOM is recorded. If the values are inside the nominal range the Base is closed and the DU is moved to the Dark Box where the calibration is performed.

After the calibration the DU is loaded on the LOM (process 4). The winding procedure of the ropes and the VEOC, that have a length of about 700 m ,has to be done with an accuracy of less than 1 cm in order to guarantee the correct tension of the ropes and the unfurling. In process 5 at the end of the winding, the buoy is installed in the LOM and connected to the ropes. The LOM fully assembled is moved on the anchor. Then the DU uploaded on the LOM and the Base are mounted on the anchor , the Base connected to the electro-optical jumper cable which ends with a wet-mateable connector fixed on the anchor frame. During this process the release system is also mounted on the anchor.

Eventually, the finalization of the stack, the last checks and functional tests are performed before the deployment.

.

Figure 3: ARCA DU fully integrated before deployment

REFERENCES

[1] Letter of intent for KM3NeT 2.0 J. Phys. G: Nucl. Part. Phys. 43 (2016) 084001 (130pp)

[2] ARCA DU Production & Test Report Process 1 *KM3NeT google drive internal document*

[3] ARCA DU Production & Test Report Process 2 *KM3NeT google drive internal document*

[4] ARCA DU Production & Test Report Process 4 *KM3NeT google drive internal document*

[4] ARCA DU Production & Test Report Process 5 *KM3NeT google drive internal document*

KM3NeT ARCA-PHASE I SHORE STATION

E.Giorgio[1], S.Pulvirenti[1] on behalf of the KM3NeT Collaboration

1) Laboratori Nazionali del Sud, Istituto Nazionale di Fisica Nucleare

Abstract – KM3Net is a collaboration that is constructing two neutrino detectors in the Mediterranean Sea. The detectors will be hosted in two different sites: the detector ARCA (Astroparticle Research with Cosmics in the Abyss) in a site near the Sicilian coasts and the ORCA (Oscillation Research with Cosmics in the Abyss) detector in a site in France off shore the Toulon coasts. In particular, ARCA site is situated 80 km off the coast of Portopalo di Capo Passero in Sicily. The detectors will be composed of hundreds of detection unit (DU) each composed of 18 Digital Optical Modules (DOM). In the following paragraphs will be described the ARCA shore station architecture from the data trasmission to the data acquisition (DAQ) network point of view.

INTRODUCTION

The KM3NeT detector is connected to the shore station through a 100 km electro-optical cable called MEOC (Main Electro-Optical Cable). For each Detection Unit, the main stream of data comes from the 31 Photomultiplier Tubes (PMT) installed in each DOM which required up to 300 Mb/s of bandwidth. Due to the long distance and the big amount of data is necessary to use the fibre optics as physical layer for data transmission. The MEOC hosts 20 optical fibres which are divided in five connectors inside the CTF (Cable Termination Frame) at 3500 m depth. KM3NeT phase I will be composed of 31 DUs connected to three Junction Boxes (JB) that provide electrical power from shore to the DUs and manage the optical signals by mean of several multiplexer and optical amplifiers. For each DU is defined a type, which refers to the DOM wavelength assignment. In fact, 4 DU types are defined: A,B,C,D. Each JB can manage up to 12 DUs, divided in two or three groups of DU types. The networking infrastructure of the KM3NeT detector is implemented with both White Rabbit Switch (WRS) and standard high performances switches[1]. This network features an asymmetric design and the data rate adopted for each channel is 1.25 Gb/s Ethernet [2]. All the timing synchronization information is addressed through the SC (slow control) downstream from the shore station in broadcast to the DOMs and DUs BM (Base Module). On the same fibre the DC (detector control) channel is routed from the BM back to the shore station.

General Layout

The general architecture idea onshore is to have a single hybrid rack (Figure 1) for each JB where are installed all the hardware components that manage the optical path signals until the first DOM front end switches (DFES). The DFES have each an uplink to a core switch (SCSF), that interface servers implementing a star center layout. Same path is repeated for the White Rabbit infrastructure that provides to DUs the high-accuracy time signal. In the JB rack are mounted: the WR broadcast and level 1 switch, the JB MCU (Monitoring and Control Unit), optical EDFA (Erbium Doped Fibre Amplifier) and Raman amplifiers, DOM and BM channel multiplexer, Optical Box (where are installed custom optical component to manage the SC, DC and JB channels) and the DFES receive and manage the data coming from DOMs. There is a 1-1 mapping between DU and DFES.

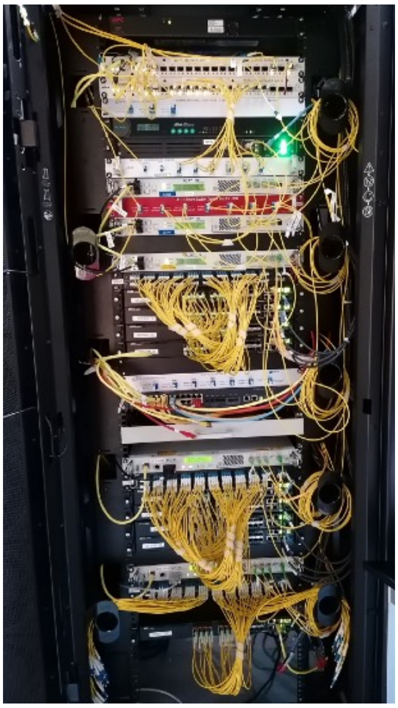

Figure 1: JB Hybrid Rack

OPTIC INFRASTRUCTURE

In order to minimize the number of fibre optic involved, the DWDM (Dense Wavelength Division Multiplexers) technique is used. Each wavelength is allocated in a frequency grid of 50 GHz spacing between near channels that can share the same optical fibre. The optical system is composed by 3 parts: the DOM data, the SC - DC (Detector control) and the JB control and command segments. Each JB has 4 optical fibres:

- The first fibre is the bidirectional one where the SC, DC, MCU and ICE (instrumentation control electronics) channels share the same path.
- The second to the fourth fibre manage the DOM data handling 4 DU (A,B,C,D type) in each fibre.

Each DOM is connected to shore with an upstream direction through a point-to-point optical link, assigning a precise wavelength grid to the DOMs. A vertical electro-optical cable (VEOC) routes the single fibre of the DOM to the DU BM which communicate with 2 fibres to the JB.

The shore station transmits the GPS clock through the transceiver plugged in the WRS broadcast by mean of the SC channel to DOMs and BMs. The SC by mean of an add&drop (AD) filters travels on the same fibre with the two JB controls and command channels (one is redundant) and the ICE channel plugged in the Bridge WRS. These 4 channels are then boosted by an EDFA T, which output is routed to a circulator. The circulator bidirectional port is then connected to the MEOC. In the same bidirectional fibre a cascade of AD filters drops the JB control and command and ICE from the DC to the MCU and WR Bridge receivers and the DC channels to a demultiplexer a before arrive to the Avalanche PhotoDiode (APD) receivers plugged in the WRS Level 1. The JB, ICE and DC channels are first preamplified by the EDFA U. The DOM channels coming from a group of 4 DU are routed to an EDFA S or Raman two pumps amplifier and after routed to a 80 channel demultiplexer where finally will be received by the APD receivers hosted in the DFES.

DAQ AND NETWORK INFRASTRUCTURE

In the shore station three separate LAN are physically deployed: Raw data. Control/Management, and LNS LAN. The raw data LAN is the high-performance network where data gathered from detector travels. It features a star centre architecture, where the access nodes, DFES and the DAQ servers, are connected by the SCSF with 10 Gb/s connections (exploiting only a small part of SCSF capability, that can achieve up to 100 Gb/s). RAW network spans only on the rack that handle data, so JB and DAQ racks. This LAN has two types of switches, both somehow special. The WRS, that are essential in order to achieve the needed time accuracy, while DFES and SCSF feature an SDN (software defined networking) implementation required by the network asymmetry. The SDN implementation disables the mac-address learning feature of the switch and provide static routes for the network flows, overcoming the potential collisions inducted by the broadcast communication described above.

The control/management LAN (CTRL) spans all over the racks of the data centre. The idea is to provide an internal bus able to reach every node in the data centre, without exposing it outside. Exploiting VLANs, this network features more than a LAN: the most used is the one connecting DAQ KM3NeT nodes. This VLAN is characterized by the IP addressing, that univocally identifies each unit within the data center: the IP follows the schema 172.30.X.Y, where X is the rack id (rack 1.1 = 11, rack 2.1=21, and so on) while Y is the position within the rack, generally from 1 to 42. The number 30 recalls the VLAN ID. There are also smaller VLANs created for special needs, for instance the one featuring a private connection between Junction Box frontend MCU with the Junction Box SC server. There is no need of high performance here, so this LAN is implemented with standard Gigabit switches, most of which have a 10 Gb/s uplink.

Finally, there is the LNS LAN, mostly used when to reach directly some node from outside. It is used mostly for monitoring purposes, when the monitoring tools do not support proxying. The VLAN implementation allows also to share, when needed, network switches between LNS and CTRL LANs. Since broadcast domains are separated and there is no possibility of collisions. This concept has been expanded, for providing a sound cable routing across racks, and avoid unneeded inter-rack cable passing. For each of the two rows forming the data center, two 10 Gb/s switches, with uplink to 40 Gb/s, have been put as concentrators, interfaced by patch-panels. Then, for each rack in the row, 4 ethernet cables have been passed (two for LNS, two for CTRL), to land on one or more rack-switch. Finally, the row patch panels have been interlinked, completing rack interconnection. Figure 2 shows DAQ servers with the different colour cable that maps different LANs, making easier manutention and operation on servers.

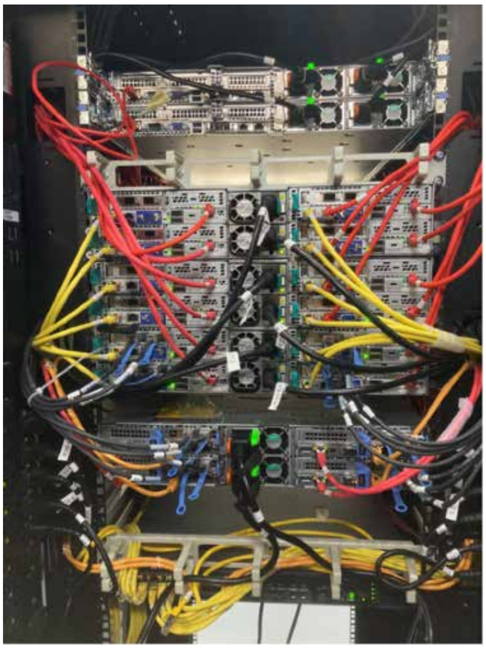

Figure 2: LAN cable colours. Black for raw data, red for LNS LAN and yellow for the control/management.

REFERENCES

[1] Tommaso Chiarusi and Emidio Giorgio on behalf of the KM3NeT Collaboration, EPJ Web of Conferences 207, 06009 (2019) - https://doi.org/10.1051/epjconf/201920706009r

[2] S. Pulvirenti, F. Ameli, A. D'Amico, G. Kieft, and J.-W. Schmelling for KM3NeT Collaboration, EPJ Web of Conferences 116, 2016 https://doi.org/10.1051/epjconf/201611605006

The autonomous acoustic beacon of KM3NeT

M. Bonfanti[3], M. Calì[1, 3], C. D'Amato[1], A. Grimaldi[2], A. Grmek[1], K. Leismueller[1], E. Leonora[2], F. Librizzi[2], P. Litrico[1], F. Longhitano[1,2], A. Orlando[1], N. Randazzo[2], G. Riccobene[1], S. Viola[1], on behalf of the KM3NeT Collaboration

1 Laboratori Nazionali del Sud -INFN

2 Sezione INFN Catania

3 DIE I- Univeristy of Catania

Abstract – In the framework of the KM3NeT project, the two neutrino telescopes are under construction in two deep sites in the Mediterranean Sea: ARCA 80 km off-shore Capo Passero (Sicily, Italy) at 3500 m depth and ORCA 20 km off-shore Toulon (France) at 2500 m depth respectively. For both detectors an acoustic positioning system has been designed and implemented to recover in real time the position of the detector's active sensors. A set of key elements of the acoustic positioning system are autonomous acoustic beacons that provide a seafloor-anchored long-baseline used to triangulate the position of the detector elements. The autonomous acoustic beacon is described in this report.

Introduction

The KM3NeT Collaboration [1] is building in two marine sites of the Mediterranean Sea a new generation cubic kilometre sized neutrino telescope. The detector consists of a grid of photosensors sensitive to the Cherenkov radiation emitted in water by particles produced by a neutrino interaction. Each photosensor is called Digital Optical Module (DOM). The arrival time of the Cherenkov light on the DOMs and the knowledge of their spatial positions are used to reconstruct the trajectory of the particles. The optical sensors are suspended in water in vertical structures, called Detection Units (DUs). In the deep sea, the DU move under the effect of currents, thus their positions must be continuously determined and monitored. A crucial component of the KM3NeT detector is therefore the Acoustic Positioning System [2]. It provides the position of DOMs and DUs in the deep sea with an accuracy of about 10 cm. The system is based on the acoustic triangulation of sound transit time differences between fixed seabed emitters and receiving hydrophones. The acoustic emitter consists of a beacon autonomously powered by a battery pack that provides the power to the inner electronics. The beacon and the battery packs are placed on an iron tripod. A fiberglass pole holds the beacon at a total height of about 4 m from the seabed. The object is designed to stay subsea for 3 years and then, to be quickly recovered, change the battery and redeploy it for a total lifetime of more than 20 years.

The battery pack

The aim of the battery pack is to supply the voltage (12 VDC) to the beacon in the deep-sea environment and to allow continuous operation of the beacon for 3 years subsea. All the components of the battery pack are included inside a watertight pressure resistant vessel. The vessel is a 17-inch diameter Nautilus Vitrovex® Deep Sea Floatation Glass Sphere. The core of the whole battery pack is a cluster of batteries positioned inside the glass housing. They are high-energy batteries Lithium-Thionyl Chloride (Li-SOCl2). Electrically, each battery provides a nominal capacity of 17.0 Ah, with a nominal voltage (at 0.7 mA 20°C) of 3.6 V.
The cluster of batteries consists of a set of 4 boards used to stack 96 batteries. Each board hosts 24 batteries, electrically connected in order to produce 14.4 Volt, with a total capacity of 410 Ah. In order to obtain the 12 Volt DC for the beacon, 2 diodes are connected in series to the output positive cable to drop the voltage to the required voltage. In order to increase the operating time of the beacon in water, a duty cycle operating mode for the battery pack has been implemented. An electronic switch, controlled by a microcontroller, connects the beacon to the battery pack only for a defined interval time. The duty cycle is 10%, with a period time of 10 minutes. That means that every 10 minutes the beacon is connected to the battery pack for 1 min. During the other 9 minutes the beacon is disconnected. With the 410 Ah battery pack capacity and the expected current consumption of the beacons, almost 4 years of operating time is planned in deep-sea water.

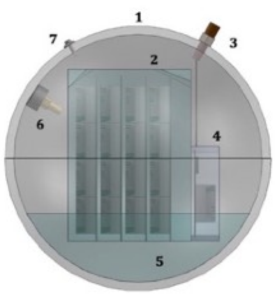

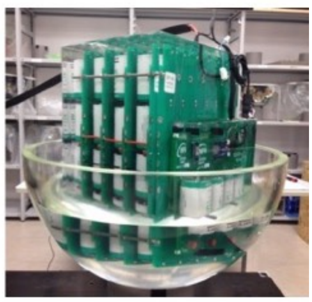

Figure 1: Left. A drawing in scale of the main elements of the battery pack: 1. glass housing; 2. Battery cluster; 3. external connector; 4. Wake-up board; 5. Silicon glue; 6. Internal pressure gauge. Right: a picture of the open battery pack with the battery cluster and the wake-up board.

The tripod

The mechanics of the autonomous beacon is formed by an iron (Fe-510) tripod, that ensures: a) stability on the sea-bottom; b) support for the battery pack and for the beacon. The tripod is equipped with a metallic base, to hold the battery pack, a main rod to support a fiberglass pole to keep the beacon vertical and at a distance of about 4 m from the sea-bottom, 3 eye-pads to be used as safety holder in case of emergency recovery. A rotating lever arms is installed to deploy the structure vertically from ship and then free the field of view of the beacon. A 5m-long sling is folded to the structure and attached to a pad eye to facilitate recovery from ROV. The weight of the structure is 950 kg.

All parts are realised with certified materials and manufacturing is performed agreement with relevant UNI standards and welding is tested with penetrating liquids. The structure design has been analysed both analytically and numerically and its use even in rough sea conditions (approximately Sea State 4) has been demonstrated. In particular, the analytical and numerical analysis made it possible to evaluate the value of the safety coefficient of the structure even in severe accidental conditions, such as the installation and recovery of the device. This safety coefficient, even in these extreme cases, shows a considerable magnitude, ensuring conditions of maximum safety. The carbon steel parts are painted with marine paint (Carboguard 1209) and a proper over paint (yellow RAL 1004 or white). The Norosok standard System 7B for painting is used. Protective zinc-anodes are used to extend lifetime of the structure over 20 years.

Figure 2: A set of 3 autonomous beacon tripods onboard the ship ready to be deployed at the KM3NeT/ARCA site.

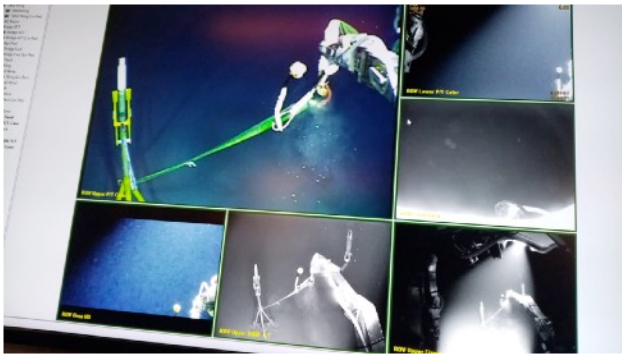

Figure 3: Recovery of a tripod. The ROV grabs the recovery sling and connects it to the ship winch. The beacon is then recovered on the ship for maintenance.

Cabling

The cable must transmit power over pins 1 (GND) and 6 (12VDC). The cable is terminated with two connectors Subconn MCIL-6-M (mating MCBH-6-F battery pack side) and Seacon MCIL-6-F (mating MCBH-6-M on beacon side). Connectors must be connected using marine grade silicon grease before mating. Length of the cable is 5 m and conductor area is 1.5 mm^2

The beacon

The beacon is an acoustic transducer manufactured by MSM (Spain), capable to emit acoustic signals, preferably in the range of frequencies between 20 kHz and 40 kHz with maximum power of about 180 dB@1m [2]. For the autonomous emitters, the external vessel is in hard anodised aluminium and it uses a Seacon MCBH-6-M connector. The signal type, repetition rate and power are pre-set before installation. The used typical signal is a 5 ms long sweeps of 2 to 4 kHz band in the frequency range between 20 and 40 kHz.

REFERENCES

[1] Letter of intent for KM3NeT 2.0 J. Phys. G: Nucl. Part. Phys. 43 (2016) 084001 (130pp)

[2] The positioning system for km3net. EPJ Web of Conferences 207, 07005 (2019)

The FOCUS-ERC project: real-time fiber-optic monitoring of active faults offshore Catania connected to the INFN-LNS marine infrastructures

S. Aurnia[1,2], M.A Gutscher[1], C. D'Amato[2], A. Grmek[2], S. Murphy[3], L. Quetel[4], E. Giorgio[2], S. Pulvirenti[2], G. Riccobene[2], S. Viola[2]

1)LGO, CNRS, University of Brest, Plouzane, France
2) INFN-LNS, Catania, Italy
3) IFREMER, Plouzane, France
4) IDIL, Lannion, France

Abstract – In the framework of the ERC funded FOCUS project we installed a real-time system to perform measurement of strain along a 28+6 km long submarine cable, located offshore Catania, through Brillouin optical time-domain reflectometry (BOTDR). The main objective is to test the capability of the BOTDR technology to contribute to the seismic monitoring and exploration of faults of the investigated area. This is the very first time that BOTDR measurements are performed on the subsea flank of Mt. Etna and crossing active submarine faults.

INTRODUCTION

The aim of the FOCUS project [1] -funded from the European Research Council (ERC Advanced Grant) under the European Union's Horizon 2020 research and innovation program [2][3]- is to develop a new seismic monitoring system of the seafloor through the use of fiber optic cables and laser reflectometry using optical BOTDR (Brillouin Optical Time Domain Reflectometry) to improve hazard assessment and increase early warning capacity to detect signs of seismic activity. BOTDR Laser reflectometry is commonly used for structural health monitoring of large-scale engineering structures (e.g., bridges, dams, pipelines, etc.) to measure tiny strains (< 1 mm) at vast distances (10 - 200 km). It has never been used to monitor deformation caused by active faults on the seafloor. FOCUS aims at demonstrating that this technique can measure small (<2 cm) displacements of seabed. A dedicated 6 km long cable deployed by FOCUS was connected to the INFN-LNS main electro optical cable deployed offshore Catania. The FOCUS optical subsea cable crosses the recently mapped North Alfeo Fault at four positions (Figure 1).

.MOTIVATION AND THEORETICAL FRAMEWORK

BOTDR (Brillouin Optical Time Domain Reflectometry) is performed by firing a laser pulse from one end into an optical fiber where a small amount of the incident light is backscattered. This method requires access to only one end of a fiber, as with conventional optical time-domain reflectometry (OTDR). As laser light diffracts off microscopic imperfections in the fiber it produces several characteristic peaks Rayleigh, Brillouin and Raman. The Rayleigh peak is sensitive to short period strain vibrations, the Raman peak varies with temperature, and the Brillouin peak varies with both strain and temperature.

If the fiber has been subjected to strain, the Brillouin spectrum will vary between successive measurements at a distance along with the fiber corresponding to the position where this change occurred. By measuring the variation of the Brillouin frequency, it is possible to determine the stress to which the fiber is subjected, so it is possible to detect any movements carrying out measurements in relative mode, making a comparison with an existing trace used as reference.

The strain experienced by the fiber is commonly defined as a relative elongation of the thread, and the admitted unit is the με micro-strain (1 ε) = 1μm elongation / 1m of fiber).

INFRASTRUCTURE

A custom-designed 6-km long and 9 mm diameter fiber-optic cable (manufactured by Nexans Norway) was deployed across an active fault on the seafloor (the North Alfeo Fault) to monitor possible tectonic movement using BOTDR laser reflectometry. The cable comprises five fibers: three tightly bound in the core (6 km each) and two loosely wrapped in a tube. In October 2020, the FOCUS cable was connected to the TSS (Test Site South) seafloor infrastructure of INFN served by a 28 km-long existing cable. The FOCUS cable connection to the main INFN Cable was performed via a dedicated Y-junction frame (designed by INFN-LNS to operate at the same time the FOCUS-BOTDR and the INFN SMO-OnDE acoustic array) and via a cable-end module.

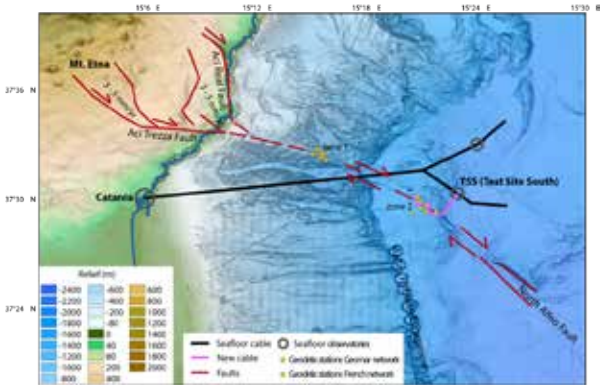

Figure 1: The INFN and the FOCUS cable deployed offshore Catania and crossing the North Alfeo fault

On shore, two BOTDR interrogators (Viavi MTS8000 and Febus G1-R-19001) are connected to the main cable end to interrogate the fibers. Measurements are performed every 2 m with high averaging acquisition to reduce noise in continuous mode. Strain rate data is integrated in time to provide local strain measurement. Dedicated software developed on the LabView platform allows data analysis in real-time acquired by the Viavi MTS8000 through scpi commands and a python program for subsequent data analysis (Figure 2).

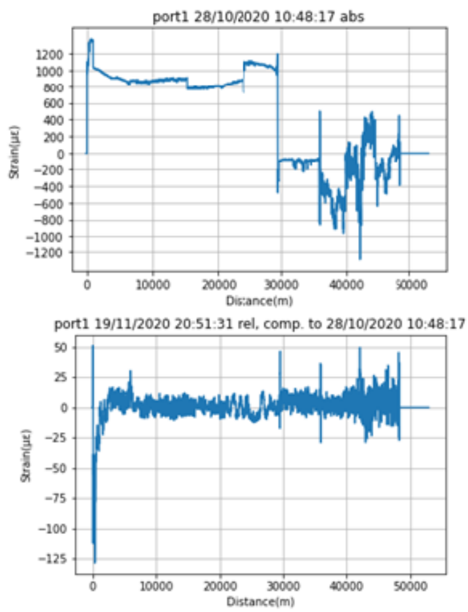

Figure 2: An example of absolute and relative measurement of the BOTDR

Data are stored in a dynamic memory REDIS database that enables on-line display on the project's web portal and in long-term storage.
The DAQ and instrument control systems have been fully automated for remote operation: a Zabbix server monitors the entire control system, instruments, and elements to verify their correct functioning and resources.
In addition a network of 8 seafloor geodetic stations was deployed on both sides of the fault to provide an independent measure of relative seafloor movements. A micro-bathymetric mapping and a video camera survey using the ROV Victor6000 were performed to select the best path for the cable track and deployment sites for geodetic stations. The simultaneous use of laser reflectometry, seafloor geodetic stations as well as seismological land and sea stations will provide an integrated system for monitoring a wide range of slipping event types along the North Alfeo Fault (e.g., creep, slow-slip, rupture).

RESULTS AND PERSPECTIVES

Our preliminary results show that the BOTDR interrogator connected to the subsea cable deployed offshore Catania can detect fault movements. For the first time, BOTDR measurements detected seafloor displacements consistent with ≥1 cm dextral strike-slip on the North Alfeo fault. The laser observations indicate significant elongation (20 to 40 microstrain) at two fault crossings, with most of the movement, occurring between 19 and 21 November 2020.
Further data analysis will help us to better understand the North Alfeo Fault movements and demonstrate that underwater cables can monitor activity in the Etna area. Comparison with observations from other equipment (e.g., OTDR-based iDAS [4] and subsea hydrophones [5]) could provide additional information on the validity of the BOTDR for seismology activities and volcanic events.
This novel use of subsea cables represents a potential breakthrough in seismology, tectonics, and natural hazard early warning capability, turning Earth's future undersea communication infrastructure into a seismological monitoring network.

AKNOWLEDGMENTS

This project has received funding from the European Research Council (ERC Advanced Grant) under the European Union's Horizon 2020 research and innovation program (Grant No 786304 - ERC - 2017 - ADG).

REFERENCES

[1] Gutscher et al., 2019. Fiber optic monitoring of active faults at the seafloor: the FOCUS project, Photoniques, EDP Sciences, pp.32-3. https://doi.org/10.1051/photon/2019S432[
[2] European Research Council site https://erc.easme-web.eu/?p=786304
[3] Gutscher et al., 2021 First deployment of a 6-km long fiber-optic strain cable and a seafloor geodetic network, across an active submarine fault (offshore Catania, Sicily): The FOCUS experiment, EGU General Assembly 2021, https://doi.org/10.5194/egusphere-egu21-2498.
[4] Currenti et al., 2020. Fibre optic Distributed Acoustic Sensing of volcanic events at Mt Etna. Display 1625, EGU2020 GA-SGO.
[5] Viola and Riccobene, 2019. 15 years of acoustic detection studies at LNS. EPJ Web of Conferences 216, 01002 (2019) https://doi.org/10.1051/epjconf/20192160100

THEORETICAL NUCLEAR PHYSICS

Impact of off-shell dynamics on the transport properties and the dynamical evolution of Charm Quarks at RHIC and LHC temperatures

M.L. Sambataro[1,2], S. Plumari[1,2], V. Greco[1,2]

1) University of Catania, Department of Physics and Astronomy, Via Santa Sofia 64 ZIP-95125 Catania, Italy.
2) National Institute of Nuclear Physics, Laboratori Nazionali del Sud, Via Santa Sofia 62ZIP-95125 Catania, Italy.

Abstract - We describe the propagation of charm quark in hot and dense nuclear matter by means of a Boltzmann transport approach. In order to evaluate the impact of the off-shell dynamics on the transport properties of charm quark, we evaluate both transport coefficients and the time evolution of the phase-space distribution function of charm quark comparing a quasi-particle approximation with on-shell constituents of the QGP medium and a dynamical quasi-particles model with off-shell bulk medium at finite temperature T.

INTRODUCTION

Heavy quarks (HQs), namely charm and bottom, are considered as a solid probe to characterize the matter created in the QGP phase [1]. They are produced in the early stage of the collisions by pQCD process and being M_{HQ}>>$T_{RHIC,LHC}$ also the thermal pair production and annihilation processes are negligible. The large mass also leads to collisions with small momentum transfer, therefore the HQ propagation through the QGP medium can be described as a diffusion process assimilated to a Brownian motion that it has been quite often treated within the Fokker-Planck approach, valid in soft scattering approximation and solved by a set of stochastic equations named Langevin equations [2]. However, the evidence of non-perturbative interaction and the large initial temperatures at Large Hadron Collider (LHC), M_C (1.3 GeV)~3T~<p_{bulk}>, hint at a scattering dynamics more appropriately described by a Boltzmann collision integral that implies significant deviations from a gaussian fluctuation around the average momentum of the charm quark that is typical of the momentum evolution within the Langeving calculation [3] . Being the QGP strongly interacting, a full quantum description of the charm quark interaction should include in principle also the off-shell dynamics: we present a first study of the time evolution of the charm momentum in a bulk medium at fixed temperature T comparing directly the Langevin evolution, the Boltzmann on-shell evolution and an extension of the Boltzmann collision integral to include off-shell dynamics.

MODEL DESCRIPTION

The starting point in the study of propagation of heavy quark in QGP medium is the relativistic Boltzmann transport equation. In the present study, we assume that the plasma is uniform so that each variation of the distribution function of charm quark is due to collisions with light partons of the bulk and the Boltzmann equation is simplified to a integro-differential equation only respect to time:

$$p^0 \partial_0 f_{HQ} = C\left[f_g, f_q, f_{HQ}\right] \qquad (1)$$

where f_{HQ} is the single HQ distribution function in the phase-space and $C[f_{HQ}]$ is known as collision integral which contains all the interaction mechanisms between HQ and bulk partons. A successful way to treat non-perturbative effects in HQ scattering is given by Quasi-Particle approach (QPM), in which the interaction is encoded in the quasi-particle masses and the coupling constant g(T) is fitted to lQCD thermodynamics in order to have a non-perturbative behaviour of the coupling especially for T→T_c [4]. In this work the extension to the off-shell dynamics has been taken into account through the dynamical quasi-particle model (DQPM) which describes QGP in terms of strongly interacting massive effective quasi-particles dressed by non-perturbative spectral functions [5-6]:

$$A_i^{BW} = \frac{2}{\pi} \frac{m_i^2 \gamma_i}{(m_i^2 - M_i^2)^2 + (m_i \gamma_i)^2} \qquad (2)$$

where M_i is the pole mass of quark or gluon defined by the same formulas both in QPM and DQPM approach and γ_i is the width associated to each particle mass [4-6]. In this work, both the transport coefficients and the numerical solution of Boltzmann equation are obtained by a code that implement a Monte-Carlo integration method for the full collision kernel both in on-shell and off-shell approach[7].

RESULTS

We have considered a plasma in equilibrium in a box with constant temperature T. Our results show that the drag coefficient, describing the variation of mean momentum of HQ due to collisions with bulk partons [1], in the off-shell mode decreases of about 30% with respect to the on-shell one in the temperature regime of $T \sim 1{-}2\ T_C$ and similar conclusion we get also for the diffusion coefficient B_T [7]. We have checked if the decrease in the drag in the off-shell mode can be a mere effect of the decrease of the equilibrium energy density ε, therefore we have calculated the A(p)/ε ratio at fixed T = 0.2 GeV as shown in Fig. 1. Comparing the black solid line with the red one, we observe a scaling between on-shell and off-shell calculation for $p \geq 2 - 3$ GeV and breaking a lower momentum.

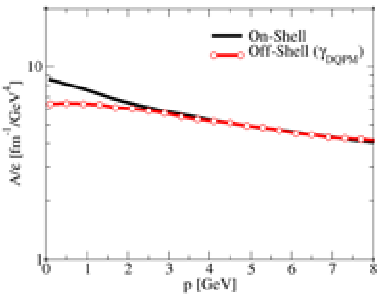

Figure 1. A(p)/ε ratio as function of charm momentum at T = 0.2 GeV both in on-shell and off-shell approach.

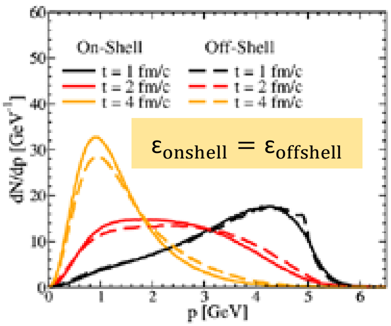

Figure 2. On-shell and off-shell evolution of the distribution function of charm quark renormalized to the energy density in a thermal bulk at T = 0.2 GeV.

In this scheme, we make a comparison between the time evolution of charm distribution function in on-shell and off-shell mode renormalizing the energy density of both approaches, the result is shown in Fig. 2. Since the off-shell drag coefficient remains smaller than on-shell one especially at low momenta, the off-shell dynamics is slightly slower with respect to the on-shell case, but the effect remains quite small. We have performed another calculation where we upscale the on-shell scattering matrix $|M_{HQ}|^2$ in order to reproduce the same drag coefficient obtained with the off-shell collision integral. This corresponds to multiply the on-shell scattering matrix $|M_{HQ}|^2$ by a function k(p). In this way we can compare Boltzmann approach, its extension to the off-shell dynamics and Langevin calculations. As shown in Fig.3, the off-shell extension does not make significant difference with respect to the on-shell one. Both approaches still remain different with respect to the Langevin gaussian shape momentum evolution.

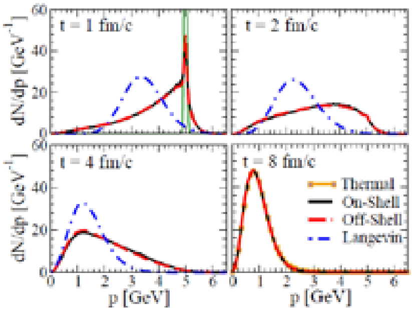

Figure 3. Charm quark momentum distribution at different time steps within on-shell, off-shell and Langevin approaches.

ACKNOWLEDGEMENTS

S.P. , M.L.S., and V.G. acknowledge the support of INFN-SIM national project and linea di intervento 2, DFA-Unict.

CONCLUSIONS

We have studied the impact of off-shell dynamics both on transport coefficients and energy loss of charm quark, comparing different approaches. We have found that if one just include the off-shell dynamics we have a moderate decrease of drag and diffusion charm coefficients due to smaller off-shell energy density but renormalizing it between the two modes the pure off-shell dynamics does not show relevant differences and this suggests that on-shell Boltzmann equation is still a quite good approximation to study the evolution of the charm momentum distribution. We can also assert that if quantum off-shell effects are taken into account Boltzmann approach seems to be a better approximation than Langevin one, at least for charm quark.

REFERENCES

[1] B. Svetitsky, Phys. Rev. D37 (1988), 2484.
[2] H. van Hees, V. Greco, R. Rapp, Phys. Rev. C73 (2006), 034913.
[3] S.K. Das, F. Scardina, S. Plumari, V. Greco, Phys. Rev. C90 (2014), 044901.
[4] S. Plumari, W.M. Alberico, V. Greco, C. Ratti, Phys.Rev.D84(2011), 094004.
[5] H. Berrehrah et al., Phys. Rev. C 89 (2014), 054901.
[6] H. Berrehrah et al., Phys. Rev. C 90 (2014), 064906.
[7] M.L. Sambataro et al.,Eur.Phys.J.C 80 (2020)12, 1140.

Hadron production within a full transport approach with statistical hadronization mechanism at RHIC and LHC energies

G. Galesi[12], S. Plumari[12], V. Greco[12]

1) Department of Physics and Astronomy, University of Catania, I-95125 Catania, Italy
2) Laboratori Nazionali del Sud, INFN-LNS, I-95123 Catania, Italy

Abstract – We present, for the first time, results on final hadron production in ultrarelativistic heavy ion collisions at RHIC and LHC center of mass energies obtained combining a full 3+1D RTB (Relativistic Transport Boltzmann) approach with the SHM (Statistical Hadronization Model). The resulting framework naturally includes both shear and bulk viscosity effects. The non-perturbative interaction between quarks and gluons is described by means of a quasi-particle approach that permits to have an EoS (Equation of State) close to lattice QCD one. The full transport evolution is converted to hadrons by means of a realistic freeze-out hypersurface considering all known hadron resonances and by performing resonance decays.

INTRODUCTION

Relativistic viscous hydrodynamics has shown to be able to describe very well the final hadron spectra and flow harmonic coefficients observed in ultra-relativistic heavy ion collisions in the low p_T region [1,2]. In the statistical hadronization mechanism the information contained in the energy-momentum tensor is converted to hadrons applying the CF (Cooper-Frye) formula on a freeze-out hypersurface. This framework is thus able to furnish constraints on QGP (Quark-Gluon Plasma) properties like shear viscosity over entropy density ratio η/s which is fixed a priori for the dynamical evolution. Nevertheless, in order to transfer the viscous correction information $\delta T^{\mu\nu}$ to the final hadron particle distribution function an ansatz is needed for the deviation δf. Further, it does not allow for arbitrary far from-equilibrium initial conditions. A kinetic approach should be able to treat self-consistently both these situations because the one-particle distribution function is always known during the dynamical evolution. For this reason we developed a transport approach at fixed η/s. On the one hand this allows for a direct comparison with viscous hydrodynamics and on the other it makes it suitable for the investigation of specific dissipation properties of QGP. In order to test the validity of our approach we extract a hydro-like freeze-out hypersurface at fixed temperature to perform statistical hadronization and to make a direct comparison with experimental data.

THE MODEL

In our approach we describe QGP matter with an on-shell one-particle distribution function f whose evolution is governed by the following RTB equation:

$$\left(p^\mu \partial_\mu + \frac{1}{2}\partial_i m^2 \partial^i_{(p)}\right) f = C[f], \tag{1}$$

where $C[f]$ is the collision integral for $2 \to 2$ collision processes. In order to reproduce the right EoS taken from lattice QCD in the equilibrium limit, we furnish a suitable thermal mass to our quasi-particles, which in turns determines the appearing of a field term in the equation so that particles are accelerated according to the local mass gradient. This equation is solved through the test particle method in which the collision integral is gauged to the desired η/s through the Chapmann-Enskog approximation and is computed by means of a stochastic algorithm [3,4,5,6].

During the dynamical evolution of f we evaluate the energy-momentum tensor on a (x, y, Y_s)-grid, being Y_s the longitudinal space rapidity, according to the formula

$$T_c^{\mu\nu} = \frac{1}{N_{test} V_c} \sum_{i \in c} \frac{p_i^\mu p_i^\nu}{p_i^0}, \tag{2}$$

where N_{test} is the number of test particles per real particle, V_c the cell volume, p_i^μ the test particle 4-momentum and being the sum over all test particles in the c-cell. From that we self-consistently extract the local temperature T and the thermal mass, and local flow u^μ. Once we have the temperature field we interpolate a freeze-out hypersurface Σ which is the input for the hadronization process. We perform it by using the THERMINATOR 2 code [7], which is a Monte-Carlo event generator that produces final hadrons according to the SHM and by using the following CF formula:

$$p_h^0 \frac{d^3 N_h}{d^3 p} = (2 s_h + 1) \int_\Sigma d\Sigma_\mu p_h^\mu f_h, \tag{3}$$

being $\frac{d^3 N_h}{d^3 p}$ the spectrum for the h-resonance, s_h the relative spin quantum number and f_h the following equilibrium distribution:

$$f_h = \frac{1}{(2\pi)^3}\left(\exp\left(\frac{p_{h,\mu} u^\mu}{T}\right) \pm 1\right)^{-1}, \tag{4}$$

where the sign is chosen according to the statistics of the resonance. Customizations of this formula which use modified versions of the distribution function to take into account local deviation from equilibrium are of course possible but for a first test of our approach we consider Fermi-Dirac and Bose-Einstein distributions only. All known hadronic resonances are considered and, once primordial particles are generated on Σ, resonance decays are performed on unstable resonances.

In this way we can extract potentially all final hadron observables and compare them with the available data from

RHIC and LHC experimental collaborations in order to fix the free parameters, which are the initial central temperature T_0 for the most central collision, the freeze-out temperature T_{FO} and η/s. In particular we concentrate on AuAu collisions at RHIC with a center of mass energy $\sqrt{s} = 200\,A$ GeV and PbPb collision at LHC with $\sqrt{s} = 2.76\,A$ TeV.

RESULTS

For the simulations we initialize test particles in the transverse plane according to an OGM (Optical Glauber Model) for the scaling of particle number or energy density with mixed contributions from number of wounded nucleons N_{part} and binary collisions N_{coll} and with a tilted function of rapidity, while the longitudinal profile has a plateau in the mid rapidity region with gaussian tails whose parameters are set to reproduce final pseudorapidity hadron yields. In momentum space we distribute according to a 3D isotropic thermal distribution with Bjorken flow. Initializations is performed at fixed proper time $\tau_0 = 0.25$ fm/c for both the systems under study.

In Figure 1 we plot the pion, kaon and proton mid-rapidity spectra (filled curves) obtained in a semi-peripheral LHC collision at $b = 7.7$ fm/c with $T_0 = 670$ MeV, $T_{FO} = 145$ MeV and $\eta/s = 1/4\pi$, and compared to ALICE data for the centrality class 20-30 %. The pion and kaon spectra are quite well reproduced over all the p_T region shown while protons seem to be underestimated above 1.5 GeV. We attribute this fact to the missing hadronic afterburner which can have an important effect for heavier particles, and which could be taken into account in future works by using other more sophisticated numerical code like SMASH [8].

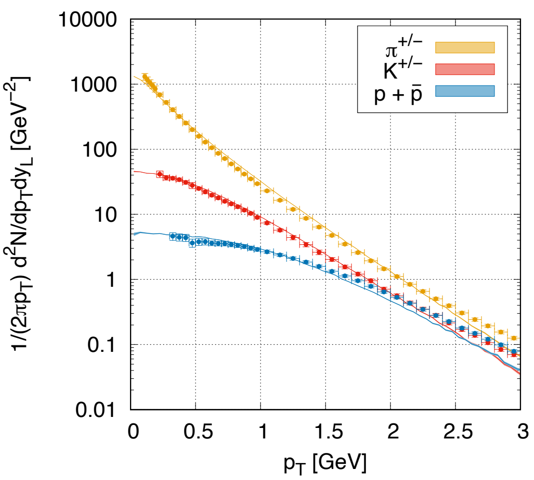

Figure 1: Hadron spectra for collisions at LHC

We also show in Figure 2 the corresponding differential elliptic flow generated by the conversion of the initial space anisotropy into a momentum one. This final hadron anisotropy is due only to the shape of the freeze-out hypersurface and local flow information interpolated on it because we don't consider any non-equilibrium effect in the hadron distribution function. Nevertheless, we have a good comparison with experimental data. We also observe a strong dependence of this quantity from the initial mixing factor of the OGM and it seems that at LHC energies should be considered a greater contribution from N_{coll}.

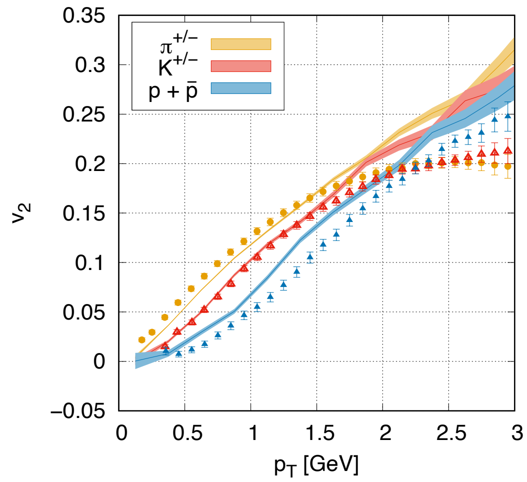

Figure 2: Hadron elliptic flow for collisions at LHC

CONCLUSIONS

Summarizing, we have shown that within our framework we are able to reproduce quite well final hadron observables and we believe that it is still possible a further fine tuning on the free parameters to have a better agreement with experimental data. This validation test opens to many possible applications of this code. For example, it will allow us to investigate the isotropization and hydrodynamization processes starting with non-equilibrium initial conditions and the possibility to make a direct comparison between a microscopic hadronization model like coalescence plus fragmentation [9] with a macroscopic one like the SHM presented here using an underlying common framework.

REFERENCES

[1] U. Heinz and R. Snellings, Ann. Rev. Nucl. Part. Sci. 63, 123 (2013).

[2] M. Alqahtani, M. Nopoush, M. Strickland, Progr. in Part. and Nucl. Phys., Vol. 101, 204-248 (2018).

[3] S. Plumari, W. M. Alberico, V. Greco, and C. Ratti, Phys. Rev. D 84, (2011), 094004.

[4] S. Plumari, A. Puglisi, F. Scardina, and V. Greco Phys. Rev. C 86 (2012), 054902.

[5] A. Gabbana, S. Plumari, G. Galesi, V. Greco, D. Simeoni, S. Succi, and R. Tripiccione Phys. Rev. C 101 (2020), 064904

[6] Z. Xu and C. Greiner, Phys. Rev. C 79 (2009) 014904.

[7] M. Chojnacki, A. Kisiel, W. Florkowski, W. Broniowski, Comput. Phys. Commun. 183 (2012) 746–773. arXiv:1102.0273.

[8] J. Weil et Al., Phys. Rev. C 94 (2016) 5, 054905.

[9] V. Minissale, F. Scardina, V. Greco, Phys. Rev. C 92 (2015) 5, 054904.

One- and two-particle transfer calculation of the $^{6}Li + p \rightarrow {}^{3}He + \alpha$ reaction at sub-Coulomb energies

S. S. Perrotta[1,2,3], M. Colonna[3], J. A. Lay[2,4]

1) Dipartimento di Fisica e Astronomia, Università degli Studi di Catania, Catania (Italy)
2) Departamento de Física Atómica, Molecular y Nuclear, Universidad de Sevilla, Seville (Spain)
3) Laboratori Nazionali del Sud, Istituto Nazionale di Fisica Nucleare, Catania (Italy)
4) Instituto Interuniversitario Carlos I de Física Teórica y Computacional (iC1), Seville (Spain)

Abstract - The $^{6}Li + p \rightarrow {}^{3}He + \alpha$ reaction below the Coulomb barrier was studied theoretically as a direct transfer process in first- and second-order Distorted-Wave Born Approximation (DWBA). We examine how the energy dependence of the reaction cross-section is affected by the structure describing the reactants.

INTRODUCTION

In this work, we attempt to describe theoretically the sub-Coulomb behaviour of the $^{6}Li + p \rightarrow {}^{3}He + \alpha$ reaction cross-section, without adjusting any ingredient of the calculation on experimental data regarding the transfer channel. We focus on the impact of the reactants structure, by comparing different one- and two-particle transfer calculations based on a fixed set of potentials. Here, only the description of each reactant ground state is discussed. In particular, no "dynamical" effect, i.e. coupling to excited states or other channels, is included.

In prospect, the study aims at exploring possible implications to the electron-screening problem, the anomalous cross-section enhancement experimentally observed in several reactions at astrophysical energies in fixed-target experiments. Recently, it was suggested that the anomalies might be related to nuclear clustering effects [1]. Reactions destroying ^{6}Li are also interesting for studying pre-main-sequence stars and with respect to the lithium depletion problem (see [2] and references therein).

MODEL DESCRIPTION AND RESULTS

Figure 1 shows a sample of astrophysical *S*-factors calculated as detailed below, as a function of the centre-of-mass collision energy *E*. Given the angle-integrated cross-section, $\sigma(E)$, for a pair of reactants with charge numbers Z_1 and Z_2 and reduced mass *m* in the initial state, the corresponding astrophysical factor *S* is defined as $S(E) = E\, e^{2\pi\eta(E)}\, \sigma(E)$, where $\eta(E) = \alpha_e Z_1 Z_2 \sqrt{m\, c^2/(2E)}$, being α_e the fine-structure constant and c the speed of light.

Direct transfer of a deuteron

The blue solid line in figure 1 corresponds to the direct transfer of a deuteron, d, in first-order DWBA. ^{6}Li and ^{3}He are described in a two-cluster model, as α + d and p + d *s*-wave bound states respectively, with each cluster being inert and structure-less. Below 1 MeV, this calculation

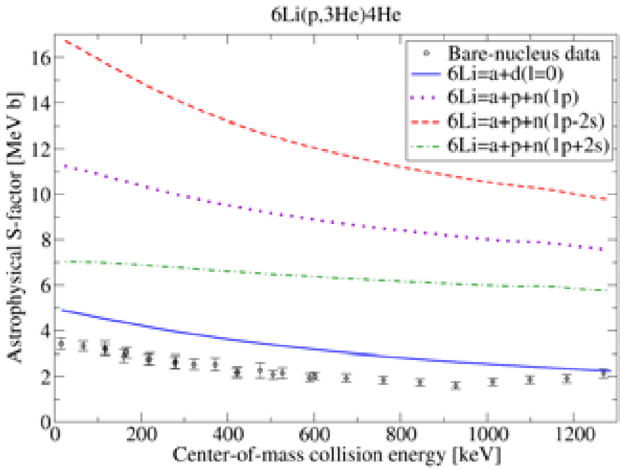

Figure 1: Preliminary astrophysical *S*-factor for $^{6}Li + p \rightarrow {}^{3}He + \alpha$ reaction, as a function of the centre-of-mass collision energy. Black points are experimental bare-nucleus data in [2, 3]. The blue solid line is the first-order DWBA deuteron transfer. The purple dotted line is the second-order DWBA p + n transfer performed placing the transferred nucleons only in the 1*p* shells of ^{6}Li. The red dashed and green dash-dotted lines are p + n transfers with transferred nucleons in both 1*p* and 2*s* shells of ^{6}Li, combining the contribution from each shell with different relative phase. See text for details.

reproduces very well the experimental energy dependence, even though the absolute values are overestimated by a factor of about 1.4. Around 1 MeV the trend deviates: this is expected, as the adopted potentials are not meant to reproduce the ^{7}Be resonance at 1.6 MeV above the ^{6}Li + p threshold.

Two-nucleon transfer

All other lines in figure 1 are obtained treating the reaction as a two-nucleon transfer of a proton and a neutron, in second-order DWBA, so that ^{6}Li and ^{3}He are now described as bound states of three particles, α + p + n and p + n + p respectively. The three-particle wave functions are constructed in a way that fully takes into account the relative kinetic energy between the two transferred nucleons.

^{3}He is described placing all nucleons in the first *s*1/2 shell. Figure 2 shows a contour plot for the reduced radial probability density function. All shapes in which each particle is equally distant from the other two lie on the black solid line in the plot. Qualitatively, ^{3}He most important configurations are expected to resemble an equilateral triangle, apart from deformations due to the different electric charge and spin projection of the nucleons. The result found here agrees with this expectation.

^{6}Li is described placing the transferred nucleons either in the first $p3/2$ and $p1/2$ shells, in the configuration suggested by shell model, or in the second $s1/2$ shell. The weight for each configuration is taken from a Faddeev three-body calculation in [4]. There are two possible choices for the relative phase of the contributions: the associated reduced radial probability density functions are shown in figure 3. The corresponding astrophysical factors are the red dashed line and the green dash-dotted line in figure 1. The purple dotted line is instead the case where the ^{6}Li $2s$ shell contribution is removed.

In all cases, the ^{6}Li wave-function exhibits two peaks: one can be linked to "clustered" configurations, where the two transferred nucleons are more strongly correlated in space, while the other can on the contrary be connected to "cigar-like" configurations. However, the tail behaviour of both peaks is different for each choice. The phase choice giving rise to a longer "clustered" tail (lower panel in figure 3, red line in figure 1) yields higher absolute cross-sections and enhances more the reaction at lower energies, compared to all other ^{6}Li structures considered in figure 1. Similarly, the opposite choice (green line in figure 1), which favours "cigar-like" configurations, also hinders the transfer reaction, especially at lower energies. However, the calculations, at present, do not reliably reproduce the experimental cross-section. This is attributed to the fact that several potentials could not be adjusted satisfactorily to elastic scattering data, especially those regarding ^{5}Li states, which are in fact unbound.

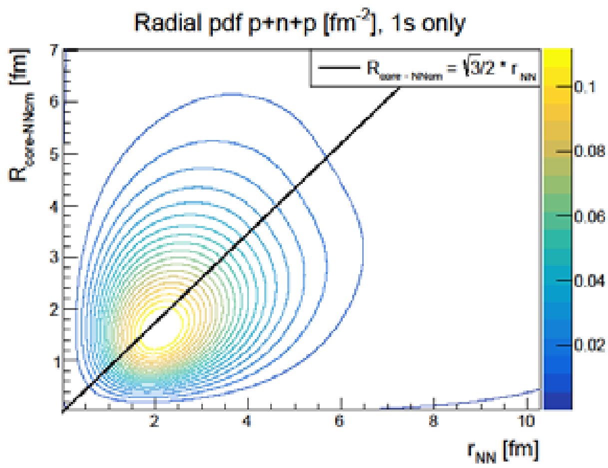

Figure 2: Contour plot for the reduced radial probability density function (pdf), in fm^{-2}, for the core + p + n state of ^{3}He. The x-axis is the distance between the transferred p and n, while the y-axis is the distance between the core and the p-n centre-of-mass. The black solid line obeys the equation in the legend (see text for details).

CONCLUSIONS AND FUTURE WORK

The choice of the reactants structure, and in particular the ^{6}Li configuration and the clustering strength for the transferred nuclei, is found to have a relevant impact on the cross-section absolute value and energy trend. This suggests that it is worthy to explore more complex and realistic models for the reaction, as it may be possible not only to reproduce better the experimental findings, but also to pinpoint which characteristic is responsible for a given behaviour.

Several approaches to improve the calculations are thus under study. Some double-folding optical potentials are in preparation. Regarding the deuteron transfer calculation, a continuum-discretised coupled channels scheme is currently being tested. Concerning instead the two-nucleon transfer calculation, a study to construct the ^{6}Li wave-function through a full three-body calculation is going to be carried out.

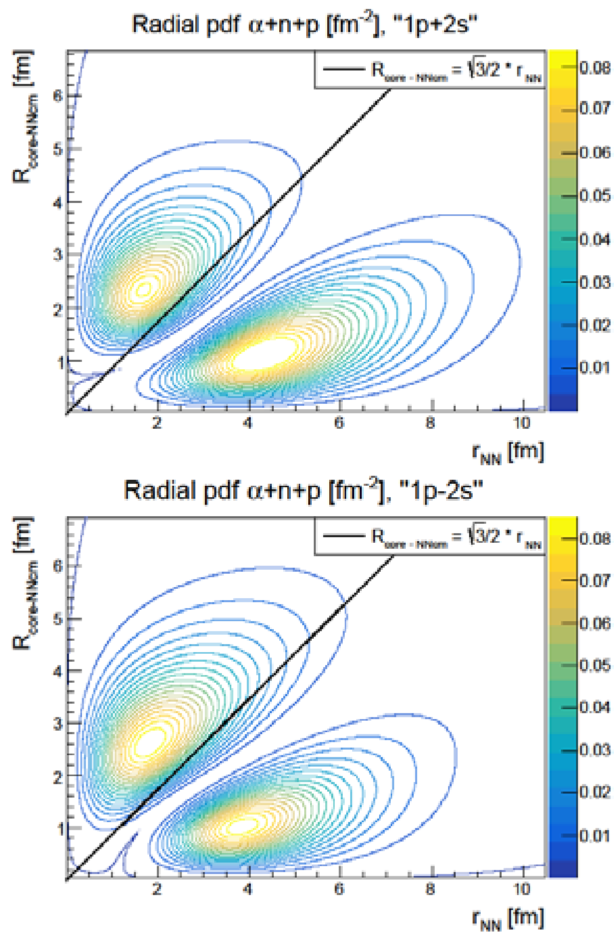

Figure 3: Same as figure 2 but for ^{6}Li. The two panels correspond to the possible choices for the relative phase of the contributions due to the $1p$ and $2s$ shells (see text).

REFERENCES

[1] C. Spitaleri et al., Physics Letters B755 (2016) 275.
[2] L. Lamia et al., Astrophys. J. 768 (2013) 65.
[3] A. J. Elwyn et al., Phys. Rev. C20 (1979) 1984.
[4] J. Bang et al., Nuclear Physics A313 (1979) 119.

Isoscalar monopole and quadrupole modes in Mo isotopes

G. Colò[1,2] , D. Gambacurta[3] , W. Kleinig[4] , J. Kvasil[5], V. O. Nesterenko[6,7,8], A. Pastore[9]

1) Dipartimento di Fisica "Aldo Pontremoli", Università degli Studi di Milano, via Celoria 16, I-20133 Milano, Italy

2) INFN, Sezione di Milano, Via Celoria 16, I-20133 Milano, Italy

3) LNS-INFN,Laboratori Nazionali del Sud, 95123 Catania, Italy

4) Laboratory of Theoretical Physics, Joint Institute for Nuclear Research, Dubna, Moscow region, 141980, Russia

5) Institute of Particle and Nuclear Physics, Charles University, CZ-18000, Praha 8, Czech Republic

6) State University "Dubna", Dubna, Moscow Region, 141980, Russia

7) Moscow Institute of Physics and Technology, Dolgoprudny, Moscow region, 141701, Russia

8) Department of Physics, University of York, Heslington, York, YO10 5DD, UK

Abstract - The Isoscalar Giant Monopole Resonance (ISGMR) and Isoscalar Giant Quadrupole Resonance (ISGQR) in the Molybdenum chain are analysed within a fully self-consistent Quasiparticle Random Phase Approximation (QRPA) approach with the Skyrme interaction, in which pairing correlations and possible axial deformations are taken into account. Theoretical results are compared with the experimental data recently obtained at RCNP. The need of describing simultaneously the ISGMR and ISGQR data is stressed, as well as the need of possible extensions of the QRPA to deal with soft systems is also envisaged.

INTRODUCTION AND MOTIVATION

The Equation of State (EoS) of nuclear matter (NM) plays a key role in nuclear physics and astrophysics. There is still a high theoretical and experimental effort in the determination of its parameters. Among these parameters, the nuclear incompressibility K and the isoscalar effective mass m^*/m are of paramount importance in several studies, such as , giant resonances, heavy-ion collisions and astrophysical processes, just to mention a few.

The incompressibility of symmetric NM (SNM) is related to the second derivative of the EoS around this minimum, measuring the stiffness of SNM with respect to the compression. It can be linked to compressional modes of finite nuclei, in particular to the isoscalar giant monopole resonance (ISGMR).

When a nucleus displays an axial deformation in its intrinsic frame, a deformation-induced splitting of the ISGMR is expected. The total angular momentum J is no longer a good quantum number and the nuclear states are characterised by the projection K of the angular momentum on the intrinsic symmetry axis. In general such states are superpositions of contributions from different J of the same parity. In particular, K = 0 monopole states are coupled to K = 0 quadrupole states, which can lead to an appreciable mixing of the ISGMR and K = 0 ISGQR. Then, the monopole strength is redistributed and, in addition to the main ISGMR, there appears a minor low-energy monopole branch at the same energy as the K = 0 ISGQR branch. Therefore, models able to describe microscopically the nuclear deformation and to reproduce equally well the monopole and quadrupole strengths are needed. In this study, we make use of fully self- consistent Skyrme QRPA model, to study the ISGMR and ISGQR in ^{92,94,96,98,100}Mo. More details can be found in Ref [1].

RESULTS

In Figure 1, we plot the potential energy curves (PECs) obtained by minimization of the total ground-state energy under the constraint of a fixed quadrupole deformation β. Pairing makes the spherical minima more favoured but, overall, Mo isotopes look soft against quadrupole deformation. The softness increases with the neutron number. Even in ^{92}Mo the potential is not steep although the spherical minimum is well defined. In the heavier isotopes, the potential is increasingly shallow and the spherical minimum is not well defined at all.

In the following, we will compare two sets of QRPA calculations. The first method, called here as QRPA-I, is introduced in Refs. [2]. In this method, the nuclear mean field and pairing field are computed with the code SKYAX [3] using a two-dimensional mesh in cylindrical coordinates. The second method, called as QRPA-II, follows closely Ref. [4]. The Hartree-Fock-Bogoliubov (HFB) equations are solved in an axially deformed harmonic oscillator (HO) basis by using the code HFTHO [5]. QRPA eigenvalues and eigenvectors are found by using diagonalization techniques for sparse matrices.

In Figure 2, we plot, as a test case, the QRPA monopole (panel a) and quadrupole (panel b) response provided by the two calculation schemes for ^{98}Mo, whose experimental deformation is 0.168, as a function of the excitation energy.

In panel a), the monopole strengths obtained by QRPA-I and QRPA-II at close deformations β = 0.168 and 0.172 are compared. Though the implementations are slightly different, the QRPA-I and QRPA-II curves are pretty consistent with each other. The somewhat higher ISGMR peak energy in QRPA-II can be partly explained by the larger deformation.

By comparing in panel (a) two QRPA-II results with different ground state deformations (β = 0 and 0.172), we clearly see that even a modest deformation can significantly shift upward the ISGMR peak energy, by ≈ 0.8 MeV in this case. Moreover, the ISGMR has a single peak in the spherical case (β = 0), and it acquires a noticeable low-energy shoulder at deformation β = 0.172.

In panel (b), the deformation splitting of the ISGQR into branches with K = 0, 1, 2 is shown. It is easy to see that the ISGMR shoulder of QRPA-I in panel (a) and the K = 0 branch of the ISGQR in panel (b) lie in the same energy interval. This confirms that the shoulder arises due to the deformation-induced coupling of the monopole and quadrupole modes.

We should also note that, from Fig. 2, SkM* significantly overestimates both ISGMR and ISGQR experimental peak energies. This indicates that the values SkM* K = 217 MeV and m_*/m = 0.79 are not optimal. For a better reproduction of the experimental data, smaller (larger) values of K (m_*/m) are desirable.

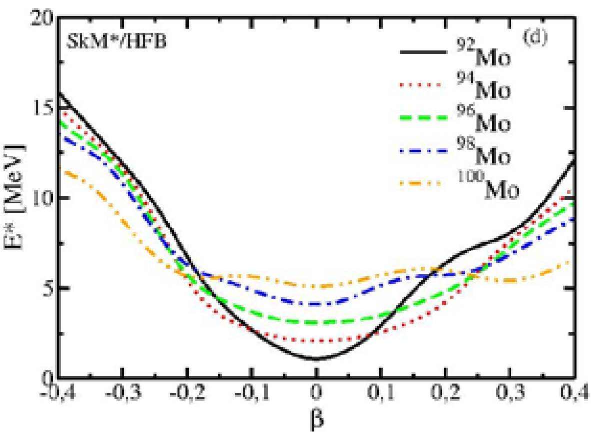

Figure 1: Potential energy curves obtained by constrained calculations with the HFB approach.

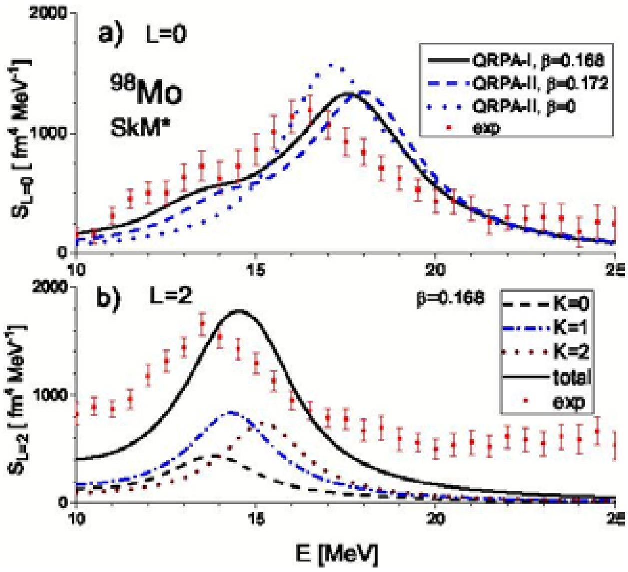

Figure 2: Theoretical monopole e quadrupole strength distributions compared with experimental data.

CONCLUSIONS AND OUTLOOK

We have studied the monopole and quadrupole response in neutron-rich Mo isotopes, by employing the deformed HFB plus QRPA approach. We have shown that the inclusion of pairing and the breaking of spherical symmetry play important roles. The monopole strength displays the main peak and a lower-energy shoulder, produced by the deformation-induced coupling of ISGMR and ISGQR. However, it is worth to be noticed that, for soft nuclei, theories that account properly for shape coexistence like multi-reference, should be explored. Unfortunately, so far, they have been applied to low-lying spectroscopy but not to giant resonances. Because of all these related aspects, Mo isotopes themselves and extraction of EoS parameters there- from, deserve in future a more careful analysis.

REFERENCES

[1] G. Colò, D. Gambacurta et al., Physics Letters B 811 (2020), 135940

[2] A. Repko, et al., The European, Physical Journal A 53 (2017) 221.

[3] P. G. Reinhard, Skyax code, unpublished

[4] C. Losa et al., Phys. Rev. C 81 (2010) 064307.

[5] M. Stoitsov et al., Computer Physics Communications 167 (2005) 43.

[6] K. Howard et al., Phys. Lett. B 807 (2020) 135608.

Gamow-Teller strength in medium mass nuclei with the charge-exchange subtracted second random-phase approximation

D. Gambacurta[1], M. Grasso[2] and J. Engel[3]

1) INFN-LNS, Laboratori Nazionali del Sud, 95123 Catania, Italy

2) Université Paris-Saclay, CNRS/IN2P3, IJCLab, 91405 Orsay, France

3)Department of Physics and Astronomy, CB 3255, Chapel Hill, North Carolina 27599-3255, USA

Abstract - We apply for the first time the self consistent subtracted second random-phase approximation for the study of charge exchange excitation modes in atomic nuclei. The Skyrme interaction is employed. We study, in particular, the Gamow-Teller excitations in the doubly-magic nucleus ^{48}Ca and in ^{78}Ni, the single-beta-decay rate of which is known. The explicit inclusion of two-particle – two-hole configurations strongly improve the agreement with the experimental data, avoiding the use of "ad hoc" quenching factor usually needed in other types of theoretical models.

INTRODUCTION

Charge-exchange (CE) excitations play important roles in nuclear physics [1,2] and astrophysics [3,4]. They are relevant also to the neutrino-less double-β (0νββ) decay [5-7], in which two neutrons change into two protons. The experimental observation of the 0νββ decay would imply new physics beyond the Standard Model that could be related to the matter-antimatter asymmetry in the universe. For this reason, a strong effort is currently devoted by the theoretical and experimental community ti to its investigation.

The rate of 0νββ decay depends on nuclear matrix elements that may only be determined theoretically. At present, predictions for these matrix elements differ from one model to the next by factors of two or three, an amount that is too large to allow the efficient planning and interpretation of experiments.

Among the different CE excitations, the Gamow-Teller (GT) plays a fundamental role. However, current theoretical models do not correctly describe the available data for GT excitations and β-decay half-lives and must resort to ad hoc “quenching factors” to obtain reasonable results for GT strength. Among the most employed models, the random phase approximation (RPA) approach is widely applied, yet presenting the just mentioned quenching problem. The Second RPA, which includes 2p2h configurations for a richer description of the excited states, incorporates beyond-mean-field correlations which can be very important.

The CE second RPA presented here is fully self consistent and includes the subtraction procedure correcting the response to make it consistent with ground-state density- functional theory at zero frequency. More details can be found in Ref. [8].

RESULTS

In panel (a) of Figure 1 we show the subtracted second RPA (SSRPA) strength distribution for ^{48}Ca, compared with the RPA one and experimental data. To compare more directly the theoretical and experimental strengths, we have folded our response functions with a Lorentzian distribution of width 1 MeV. In panel (b) of the same figure, we show the cumulative sum with respect the excitation energy.

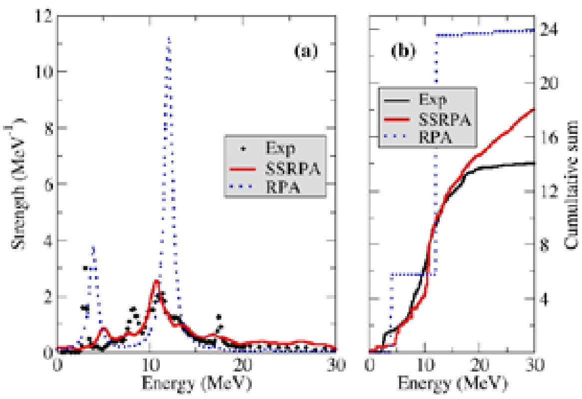

Figure 1: (a) GT strength distributions in RPA and SSRPA for ^{48}Ca. The experimental points are extracted from Ref. [9]. Cumulative strengths up to 30 MeV.

The SSRPA cumulative strength is strongly reduced from the RPA one and is in much better agreement with the experimental value. Moreover, the SSRPA curve is smooth and follows much better the experimental profile. The ratio between the experimental and the theoretical integrated strength below 20 MeV is 0.58 for the RPA and 0.93 for the SSRPA, showing that quenching factors are not needed in SSRPA. The key ingredient of the SSRPA scheme is the explicit inclusion of 2p2h configurations. Their density strongly increases with the excitation energy, leading to a high-energy tail in the spectrum.

A similar behaviour is found for the nucleus ^{78}Ni, shown in Figure 2, for which the GT spectrum has not been measured yet, but its β-decay life- time is known [10]. The figure also displays two other theoretical values for the integrated strength at 20 MeV, from the beyond-mean- field calculations of Refs. [11] and [12]. Our value is significantly lower than those of both the RPA and the other two beyond-mean-field calculations.

Finally, we use our computed GT strength to obtain the β-decay half-life of ^{78}Ni. Because beyond mean field correlations are explicitly included, we do not introduce any ad-hoc quenching in our approach, we use the bare value (1.28) for the weak axial-vector coupling constant. Our result appears in panel (b) of Figure 2. The SSRPA half-life is 0.19 seconds, very close to the experimental half-life. The RPA half-life, by contrast, is 9.51 seconds. The predictions of Refs. [11] (in the most complete scheme that includes polarization effects related to CE phonons) and [12] (with the interaction SGII) are 0.04 and 0.69 seconds respectively. Both these results are farther from the experimental half-life than ours.

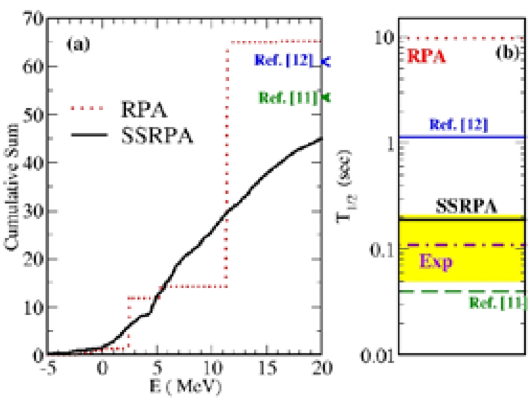

Figure 2: (a) Cumulative sum for different models (see the text for more details) for the nucleus ^{78}Ni; (b) β-decay

CONCLUSIONS AND OUTLOOK

We have presented a crucial improvement in the description of the GT strength for the lightest double-β emitter, the nucleus ^{48}Ca, and the heavier nucleus ^{78}Ni. This achievement was made possible by the beyond-mean-field CE-SSRPA, developed for the first time. We have used this approach to compute GT strengths, and shown that it reproduces the complex fragmented spectrum in ^{48}Ca much better than does the RPA. We showed that the same effects reduce the GT strength in the nucleus ^{78}Ni, so that the predicted β-decay half-life agrees better with experiment than do other beyond mean field models. The ability to describe CE strength may have a strong impact in astrophysical scenarios where GT resonances play an important role. It also promises to improve current predictions of the nuclear matrix elements governing 0νββ decay, a process at the intersection of several scientific domains.

REFERENCES

[1] F. Osterfeld, Rev. Mod. Phys. 64, 491 (1992).
[2] M. Ichimura, H. Sakai, and T. Wakasa, Prog. Part. Nucl. Phys. 56, 446 (2006).
[3] K. Langanke and G. Martínez-Pinedo, Rev. Mod. Phys. 75, 819 (2003).
[4] H.-T. Janka, K. Langanke, A. Marek, G. Martínez-inedo, and B. Müller, Physics Reports 442, 38 (2007).
[5] F. T. Avignone, S. R. Elliott, and J. Engel, Rev. Mod. Phys. 80, 481 (2008).
[6] J. Engel and J. Menéndez, Reports on Progress in Physics 80, 046301 (2017).
[7] J. Menéndez, Journal of Physics G: Nuclear and Particle Physics 45, 014003 (2017).
[8] D. Gambacurta, M. Grasso, and J. Engel Phys. Rev. Lett. 125, (2020) 212501
[9] K. Yako et al., Phys. Rev. Lett. 103, 012503 (2009).
[10] P. T. Hosmer et al. Phys. Rev. Lett. 94, 112501 (2005).
[11] C. Robin and E. Litvinova, Phys. Rev. C 98, 051301 (2018).
[12] Y. F. Niu et al., Phys. Rev. Lett. 114, 142501 (2015).

INSTRUMENTATION AND RELATED TECHNIQUES

Commissioning of FARCOS telescopes with a proton beam

G. Cardella[1*], L. Acosta[1,8], M. Anastasi[3], A. Castoldi[5,6], M. D'Andrea[1], E. De Filippo[1], F. Favela[1], F. Fichera[1], E. Geraci[1,2], B. Gnoffo[1,2], C. Guazzoni[5,6], G. Lanzalone[3,7], P. Litrico[3], C. Maiolino[3], N.S. Martorana[2,3], F. Noto[3], A. Pagano[1], E. V. Pagano[2,3], M. Papa[1], T. Parsani[5,6], S. Pirrone[1], M. Piscopo[3], G. Politi[1,2], F. Risitano[1,4], F. Rizzo[2,3], P. Russotto[3], G. Saccà[1], V. Sicari[5,6], A. Trifirò[1,4], M. Trimarchi[1,4].

1) INFN Sezione di Catania, Italy

2) Dipartimento di Fisica e Astronomia, Università di Catania, Italy

3) INFN Laboratori Nazionali del Sud, Catania - Italy

4) Dip. di Scienze MIFT Universita' di Messina - Messina, Italy

5) INFN Sezione di Milano - Italy

6) Politecnico di Milano, Dip. Elettronica, Informazione e Bioingegneria, Italy

7) Facoltà di Ingegneria e Architettura, Università Kore, Enna, Italy

8) Instituto de Física, Universidad Nacional Autónoma de México, Mexico City, Mexico

** cardella@ct.infn.it*

Abstract - The final test-beam of 8 FARCOS telescopes was performed in June 2020. The complete electronics setup developed for FARCOS was tested showing the expected good performances. Some examples of the obtained results are given.

INTRODUCTION

Due to the COVID-19 restrictions it was not possible to perform experiments on the measurement of the pygmy resonance [1] and on the study of clustering [2] with CHIMERA [3] and FARCOS [4]. We had only the possibility to test 8 FARCOS telescopes with a proton beam just before the stop of accelerators for the POTLNS upgrading. Some of the results obtained during the test are reported.

THE EXPERIMENT

A proton beam delivered by the tandem accelerator was used on various targets in order to test the last 8 FARCOS telescopes that were mounted at forward angles by using a simple support installed in the center of rings 9-7. Fig.1 shows a picture of the detectors during the alignment phase.

Description of the electronics

A complete test of the electronic setup was performed starting from the CAEN power supply with outputs connected to the so called "power air distributor" where HV and LV signals are collected from the power supply and shared to the 8 HV-LV cables used to supply the bias to each telescope. These cables were sent to the new FARCOS flanges, each one collecting signals and HV-LV cables for two telescopes. Signals generated by the telescopes are distributed from the detector mother boards to the digital electronics by using 32 lines differentials Samtec cables, one for each mother board, while another 8 lines differential cable is used for the CsI and pulser signals of each telescope. The front signal of both 300 μm

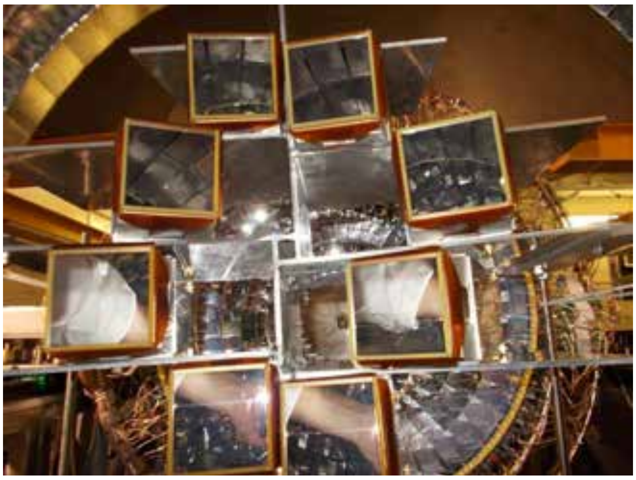

Figure 1: The 8 FARCOS telescopes during the alignment phase.

and 1500 μm stages are sent to new 64 channels HSDR (High Speed Differential Receiver) developed by INFN Sezione di Catania coupled to the entrance stage of the Double Variable Gain (DVG) modules previously developed for CHIMERA CsI. The HSDR are able also to generate "or" signals of the input stages. Such signals are used for trigger purposes. Two DVG modules are coupled to one ASAD card for the readout and conversion with the GET electronics [3]. The back signal of each telescope was sent to a Single Gain 256 (SG256) channel module developed by Politecnico di Milano directly coupled to the ASAD card, while CSI signals were sent to a Double Fixed Gain (DFG) module also developed by Politecnico Milano and again directly coupled to the ASAD card. The trigger signals generated by HSDR were combined to the multiplicity trigger of CHIMERA detector to start the ACQ system.

All used modules used are remotely accessible via usb ports connected to a pc and this is fundamental for the Slow Control System (SCS) of the apparatus. A first prototype of the SCS interface was tested on beam. It was developed using python language on Linux. It allows the very important monitor of the temperatures of some crucial part of the electronics as mother boards and DVG. Moreover, the SCS allows the setting of parameters as the gains of mother board and DVG modules or the offset of DVG; moreover it can be used to enable or disable the filter stages of SG256 and DFG.

Results of the performed tests.

Fig.2 shows an on-line plot of the ΔE-E scatter plots for

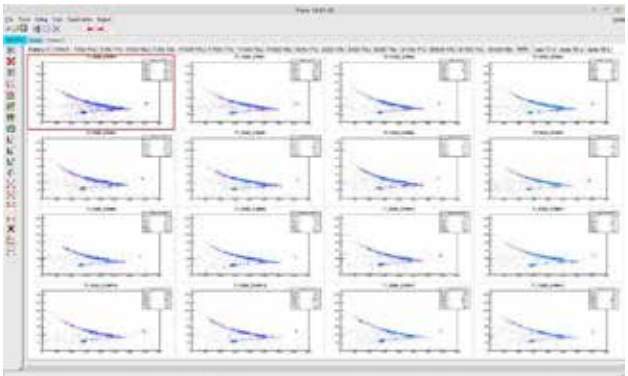

Figure 2: ΔE-E scatter plots for 16 strips of one telescope.

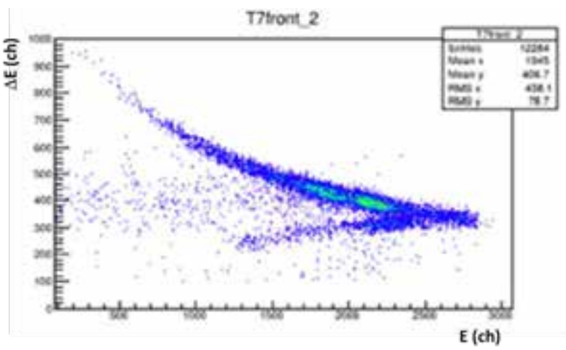

Figure 3: Rough ΔE-E identification plot.

16 strips of one telescope. This plot was obtained during the irradiation of a deuteron target. The line of protons can be observed. The different slope of the branch of particles punching through the second stage is well visible with the proton elastic peak. Such particles are stopped in the CsI(Tl) stage. A small peak can be noted at high ΔE and E channels produced by the backscattered deuterons detected in the telescopes.

Some analysis of the data collected to test how to solve problems like the inter-strip signals that could deteriorate the resolution of the identification plots was performed. Fig.3 displays a ΔE-E identification plot collected with large statistics. We note in the region of ΔE channels from 300 to 500 a strange noisy region. Cutting events in which in both ΔE and E stages the adjacent strips of the detectors do not see any signal, this noise region disappears as can be seen in fig.4. Such region is therefore due to inter-strip signals; work is in progress to reconstruct the energy of such particles.

In conclusion notwithstanding the COVID-19 pandemic a complete test of 8 FARCOS telescopes was performed before the stop of LNS accelerators for the POTLNS upgrading. Results were satisfactory, validating the whole electronic chain and allowing to positively conclude the FARCOS construction phase.

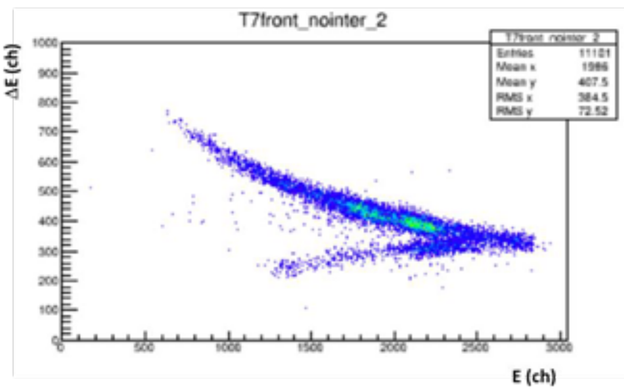

Figure 4: ΔE-E identification plot without inter-strip signals.

REFERENCES

[1] N.S.Martorana et al Phys. Lett. B 782 (2018) 112.
[2] D.Dell'Aquila et al Phys. Rew. C **93**, 024611 (2016).
[3] A. Pagano et al., Nucl. Phys. A 681, 331 (2001).
[4] E. V. Pagano et al., EPJ Web of Conf. 117, 10008 (2016), and refs. therein.
[5] E.Pollacco et al NIMA 887 (2018).

FARCOS response test in stability and temperature

F. Risitano[1,2,*], L. Acosta[1,3], G. Cardella[1], A. Castoldi[4,5], M. D'Andrea[1], E. De Filippo[1], F. Favela[1,3], F. Fichera[1], E. Geraci[1,6], B. Gnoffo[1,6], C. Guazzoni[4,5], C. Maiolino[7], N.S. Martorana[6,7], E.V. Pagano[7], T. Parsani[4,5], S. Pirrone[1], G. Politi[1,6], F. Rizzo[6,7], P. Russotto[7], G. Saccà[1], V. Sicari[4,5], A. Trifirò[1,2], M. Trimarchi[1,2]

1) INFN-Sezione di Catania, Italy
2) Dipartimento MIFT, Università di Messina, Italy
3) Instituto de Física, Universidad Nacional Autónoma de México, Mexico
4) Dipartimento di Elettronica, Informazione e Bioingegneria, Politecnico di Milano, Italy
5) INFN-Sezione di Milano, Italy
6) Dipartimento di Fisica e Astronomia "Ettore Majorana", Università degli Studi di Catania, Italy
7) INFN-LNS, Catania, Italy
8) Università Kore, Enna, Italy

*e-mail: *farisitano@unime.it*

Abstract - The FARCOS array is a compact detection system, featuring high angular and energetic resolution, consisting of 2 DSSSD layers followed by 4 CsI scintillators. FARCOS, in stand-alone mode or coupled with the CHIMERA 4π detector, is generally used for the study of heavy ion reactions at intermediate energy, including especially those inducted by Radioactive Ion Beams (RIBs).

In this work, the DSSSDs features have been studied by varying different filter algorithms and temperature of the boards.

INTRODUCTION

FARCOS (Femtoscope ARray for COrrelation and Spectroscopy) is a modular array made up, in its final configuration, by 20 telescopes, each constituted by two Double Sided Silicon Strip Detectors (DSSSDs) stages, 300 μm and 1500 μm thick, followed by four CsI(Tl) scintillator crystals, readout by a photodiode [1]. The DSSSDs consist of a grid of 32 front strips and 32 backs, with a pitch of about 2 mm, covering a total active area of 6.4 cm × 6.4 cm. Main features of FARCOS DSSSDs have been studied, through the analysis of α particle spectra collected with digital acquisition [2], as a function of the filter shape and duration and of the temperature of the FARCOS frontend, in order to best filter parameters suitable to obtain energy resolutions of ~10 keV for each strip.

ANALYSIS

A test on FARCOS DSSSDs has been performed, aimed at studying the main characteristics and performance of the first 300 μm thick silicon layer, by means of a 3-α peak Pu-Am-Cm radioactive source. The test was carried out under vacuum inside the CHIMERA chamber, in which the telescope was placed lying on its side horizontally on a support including a cooling system for the frontend plates. The radioactive source was positioned far enough to consider the α particles perpendicular to the detector and distribute them over its entire surface. The spectra obtained for each detector strip have been fitted at least square with the sum of six Gaussian functions. Each spectrum was then calibrated in energy, also taking into account the energy loss of α particles through the 300 nm thick aluminium covering the detector (see Fig. 1).

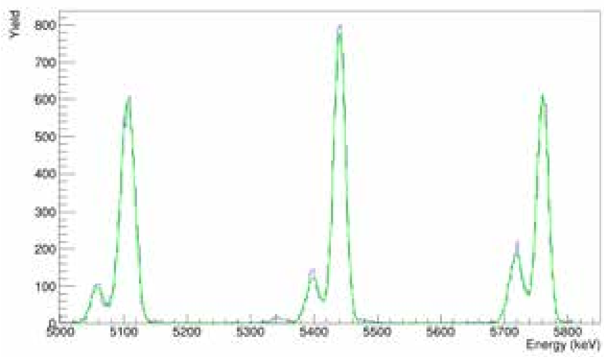

Fig. 1: Spectrum of the 3-α radioactive source measured on front-side strip 8 of a FARCOS 300 μm thick DSSSD. The green line shows the least square fit.

The output waveforms were digitally sampled at 50 MS/s and the impact of different triangular filters lasting from 11 to 351 taps on the achievable resolution has been studied [3]. The rms value σ of the ^{241}Am gaussian peak has been plotted as a function of the filter duration (see Fig. 2): as expected, the resolution improves increasing the filter duration, reaching the lowest values after 251 taps, at about 11 °C.

The σ value was then used to estimate the energy resolution of each strip of the DSSSD. For a fixed value of the triangular filter (251 taps in this case), a plot of the σ for each strip was obtained (Fig. 3). From this plot an estimation of the resolution of the silicon strip of the detector can be obtained, with an average value of about 9.7 keV.

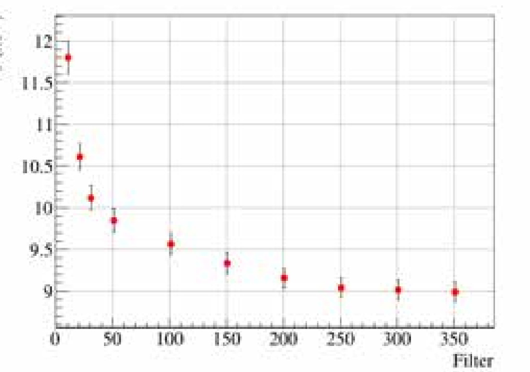

Fig. 2: Energy resolution rms of the central peak vs. the filter value used, data acquired for strip 8 of the DSSSD.

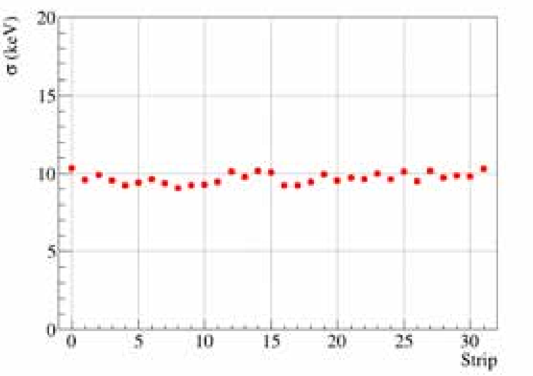

Fig. 3: Energy resolution (keV rms) for each strip of the DSSSD.

Furthermore, the effect of the temperature on the FARCOS detector energy resolution and on the performance of the electronics has been studied. Temperature can affect the characteristics of various components of the FARCOS motherboards and indirectly of the detector. This in turn affects the noise of the signal collected, which results in a variation of the energy resolution. Moreover, changes of energy calibration can also occur due to changes of electronic parameters, due to the temperature variation.

The measurement was done by shutting down the cooling system of the motherboards, and continuously gathering data from a starting temperature value of 11°C to a saturated temperature value of about 34°C.

A plot of the σ value of the peaks as a function of the temperature has been obtained (Fig. 4). It shows that higher values of the motherboard and detector temperatures, correspond to higher values of the σ of the peaks. The errors shown are greatly affected by the rapidity of the increase in temperature of the system, up to a stable temperature once the cooling system is turned off.

Fig. 5 shows a plot of the gain calibration parameter as a function of the temperature, showing the variation of the gain parameter as the temperature of the FARCOS motherboards increases. The variation is of the order of $4 \cdot 10^{-4}$ (kev/Ch)/°C, appreciable only thanks to the excellent resolution of the detector.

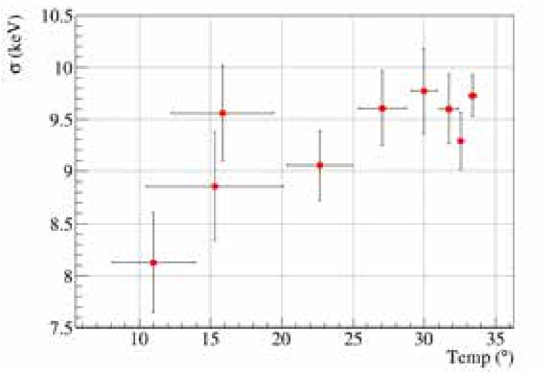

Fig. 4: σ value of the rightmost peak of strip 19 of the DSSSD vs. different temperature values.

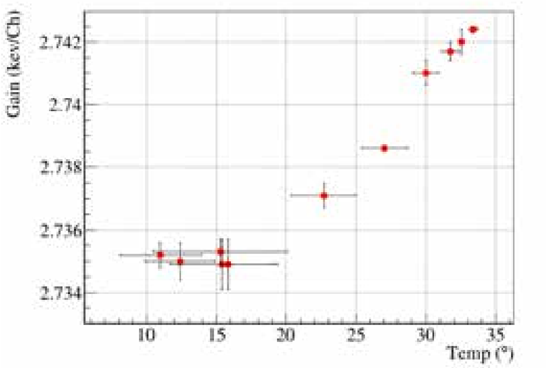

Fig. 5: σ value of the rightmost peak of strip 19 of the DSSSD vs. different temperature values.

CONCLUSIONS

A test on FARCOS 300 µm thick DSSSDs has been performed, studying the main features of the detector by varying the width of a triangular filter applied to the sampled digital signal, showing that a resolution of about 9.7 keV rms can be reached for an optimal value of the filter width of about 251 taps. Furthermore, a test of stability of the resolution by varying the temperature of the FARCOS motherboard was performed, showing that not only the resolution of the signal is affected by temperature, but also a change on the gain parameter as temperature increases can be registered.

REFERENCES

[1] E.V. Pagano et al., EPJ Web Conf. 117, 10008 (2016), and refs. therein.

[2] L. Acosta et al., J. Phys. Conf. Ser. 730, 012001 (2016).

[3] S. Smith, “The scientist and engineer's guide to Digital Signal Processing”.

[4] L. Acosta et al., IEEE Nuclear Science Symposium and Medical Imaging Conference (NSS/MIC), Atlanta, GA, (2017) 1-4.

Chimera and FARCOS DAQ at LNS: data synchronization improvements

E. De Filippo[1,*], G. Cardella[1], S. Cannizzaro[2], M. D'Andrea[1], E. Geraci[3,1], B. Gnoffo[1,2], C. Guazzoni[5,6], P. Litrico[2], C. Maiolino[2], N.S. Martorana[2,3], A. Pagano[1], E.V. Pagano[2], S. Pirrone[1], G. Politi[3,1], F. Risitano[4,1], F. Rizzo[3,2], P. Russotto[2], V. Sicari[5,6], M. Trimarchi[1,4]

1) INFN Sezione di Catania, Italy

2) INFN Laboratori Nazionali del Sud, Catania - Italy

3) Dipartimento di Fisica e Astronomia, Università di Catania, Italy

4) Dip. di Scienze MIFT Universita' di Messina - Messina, Italy

5) INFN Sezione di Milano - Italy

6) Politecnico di Milano, Dip. Elettronica, Informazione e Bioingegneria, Italy

**e-mail: defilippo@ct.infn.it*

Abstract - The CHIMERA and FARCOS data acquisition uses partly the GET front-end electronics, based on a digital pulse shape acquisition, and partly (mainly for CHIMERA silicon detectors) a front-end electronics based on analogue codifiers housed on the VME bus. The data coherence for the same event trigger in both sub-systems is now assured by a 100 MHz clock timestamping distributed by the GET data readout system towards the VME bus.

INTRODUCTION

Recently, before the stop of LNS accelerators in 2020 for the POTLNS upgrade, various complete experiments and tests coupling the CHIMERA 4π detector and several modules of the FARCOS array [1] have been performed at LNS. In all those experiments a generic and scalable electronic system, based on GET (General Electronics for TPCs) [2], covering signal readout and digitalization and triggering, has been adopted for FARCOS readout and for the readout of the CsI(Tl) detectors of CHIMERA. Each FARCOS telescope is composed by three detection stages: the first ΔE is a 300 μm thick DSSSD silicon strip detector with 32x32 strips; the second is a DSSSD, 1500 μm thick with 32x32 strips; the final stage is constituted by 4 CsI(Tl) scintillators, each one of 6 cm in length. The FARCOS array is made of a maximum of 20 independent telescopes. The total number of GET channels for CHIMERA and FARCOS array (20 telescopes) is around 6000.

A hybrid data acquisition [3] couples the GET digital acquisition with the Silicon detector readout of CHIMERA telescopes handled by analogue codifiers housed on the VME bus. The GET data acquisition is described in detail in Ref. [2]. It is based on CoBo (concentration Board) readout modules and the MuTanT (Multiplicity Trigger and Time), both housed in a μTCA bus.

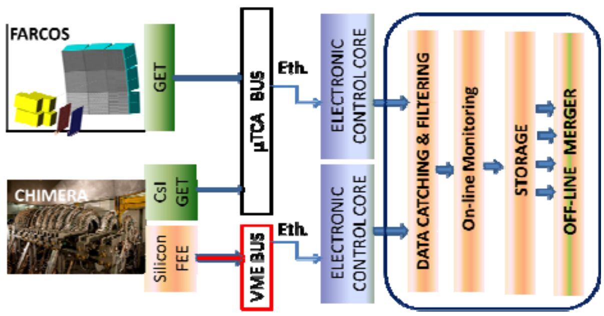

Figure 1: Schematic view of the FARCOS-CHIMERA DAQ showing the two sub-systems operating respectively in the VME bus and MicroTCA bus.

The VME collects data through the CAEN A3818 controller and V2718 VME-PCI-x bridge communicating via optical fiber link. The data merging between different acquisitions can be based on Timestamps and/or event number counter that have to assure the event correlation for each event generated by the same trigger in different DAQ sub-systems. In the following we shall report the solutions adopted for data synchronization, new developments achieved in 2020 and outlooks for the usage of the FRAISE radioactive beams in the future.

RESULTS

As a first solution the event correlation between GET and VME is assured by the event counter that acts as a trigger number counter for VME and GET sub-systems. This method is only valid if a common trigger is used and the dead time (busy signals) is shared between the two acquisition systems. This is a necessary but not sufficient condition for data correlation. In order to check event-by-event the validity of data coherence we use the multiplicity signal of the CHIMERA detector that is splitted and sent to both acquisitions for each valid trigger.

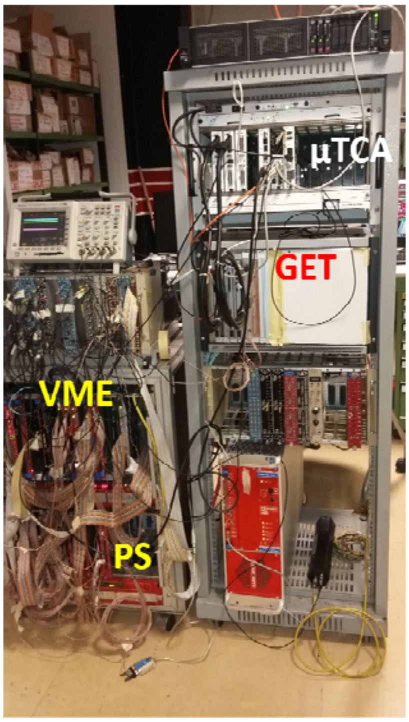

Figure 2: The compact VME-GET DAQ test station installed in the CHIMERA acquisition room. It can be easily separated in two standalone DAQs handling respectively VME or GET or can run with both sub-systems.

A better solution is the use of a timestamp clock reference. Timestamping is independent from the type of acquisition (digital or analogue) and supports different types of triggering or even triggerless data acquisitions. In 2020-21 a very compact test point DAQ was installed in CHIMERA acquisition room at LNS, with a GET and a VME sub-systems handled by a single Linux server workstation. The MuTanT trigger handles a Global Master Clock (GMC) at 100 MHz and a 48 bit timestamp with a precision of 10 ns synchronizing all CoBos in the µTCA crate. An intermediate card, BEAST (Back-End Adaptor for Synchronization of Timestamps) developped at GANIL, can interface the GET system with external data acquisition systems: in our configuration (named MuTanT "sync mode") it transmits both the timestamp and the event number (received by the µTCA backplane) to a mezzanine card developed by CENBG-Bordeaux, mounted on a V1495 programmable logic system developed by CAEN. The VME acquisition program [4] handles the readout and cleaning operations of the 48 bit timestamp buffer from the V1495 after receiving the data-ready logic signal at each accepted trigger. The system was tested by means of the DT4800 CAEN detector emulator by sending an appropriate sequence of pulses to both VME and GET acquisitions with a random poissonian acquisition input rate.

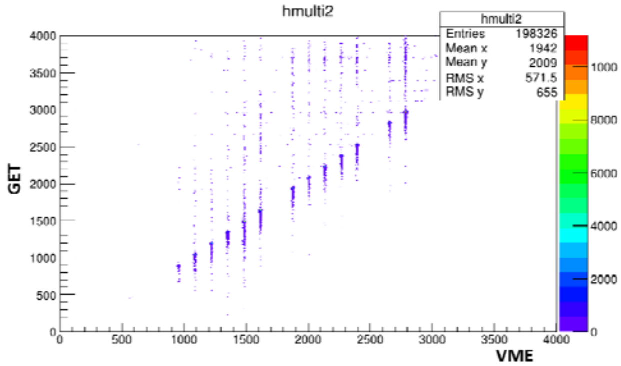

Figure 3: 2D correlation plot, generated after the merging of data having the same timestamp, of the signals (emulating a pulser generator with variable amplitude) sent for each trigger to the VME and GET sub-systems.

The coherent pattern observed is shown in Fig. 3 as a result of the off-line merging analysis. The diagonal line indicates correlated events having the same timestamp. The vertical lines beyond the diagonal are due to high rate pile-up in the signals sent to the GET sub-system for digital acquisition (pile-up is suppressed by the VME front-end analogue electronics).

In the future a further development is needed. With the FRAISE radioactive beams data acquisitions need to be correlated with external and distributed DAQ collecting data from sensor detectors distributed along the beam-line and/or tagging systems. Data synchronization and correlation can be only achieved by using a more general "timestamping" technique, in order to distribute clock and time information along the DAQ nodes with the data events. This is the only technique suitable for on-line and off-line correlations of events generated by self-triggering or triggerless sparse node systems. We have to study and to adapt the choice of a given standard (the White Rabbit timestamp [5] in use at FAIR-GSI and CERN could be an example), with the specific DAQs operating at LNS in order to distribute the timestamp information to final users and distributed nodes.

REFERENCES

[1] E.V. Pagano et al., EPJ Web of Conf. 117, 10008 (2016), and refs. therein.
[2] E.C. Pollacco et al., NIM A887, 81 (2018).
[3] E. De Filippo et al., Journal of Physics Conference Series 1014, 012003 (2018).
[4] E. De Filippo, The KaliMera data acquisition library: User's Manual.
[5] https://ohwr.org/project/white-rabbit/wikis/home

Calibration procedures for FARCOS in CHIFAR experiment

E.V. Pagano[1] , L. Acosta[2,4], T. Cap[5] , G. Cardella[2] , E. De Filippo[2] , F. Favela[1,6], E. Geraci[2,3], B. Gnoffo[2,3], C. Guazzoni[7] , G. Lanzalone[1,8], C. Maiolino[1] , N.S. Martorana[1,3], T. Matulewicz[9] , A. Pagano[2] , M. Papa[2] , K. Piasecki[9] , E. Piasecki[10], S. Pirrone[2] , R. Płaneta[11], G. Politi[2,3] , F. Risitano[2,12], F. Rizzo[1,3], P. Russotto[1], V. Sicari[7] , K. Siwek-Wilczynska[9] , I. Skwira-Chalot[9] , M. Trimarchi[12]*

1)INFN- LNS, Catania, Italy
2) INFN-Sezione di Catania, Italy
3) Dipartimento di Fisica e Astronomia E. Majorana, Università di Catania, Italy
4) Instituto de Fisica, Universidad Nacional Autònoma de México
5) National centre for Nuclear Research,Otwock-Swierk, Poland
6) Instituto de Ciensas Nucleares, Universidad Nacional Autònoma de México
7) Dip. Di Elettronica, Informazione ebioingegneria, Politecnico di Milano, Italy
8) Facoltà di Ingengeria e Archidettura, Università Kore, Enna
9) Faculty of Physics, University of Warsaw, Warsaw, Poland
10)Heavy Ion Laboratory, University of Warsaw, Warsaw, Poland
11)M. Smoluchowky Institute of Physics, Jagiellonian University, Krakow, Poland
12)Dipartimento di Scienze MIFT, Univ. di Messina, Italy

*e-mail:epagano@lns.infn.it

Abstract – In this report we briefly discuss the calibration procedures for the Double Sided Silicon Strip Detectors of the correlator FARCOS in the CHIFAR experiment.

INTRODUCTION OF THE EXPERIMENT

The CHIFAR experiment [1] was carried out at LNS in November 2019. Reactions between beams of ^{124}Sn,^{124}Xe and ^{112}Sn, accelerated at 20 AMeV by the CS, and targets of ^{64}Ni, ^{64}Zn and ^{58}Ni were studied by using the CHIMERA multi-detector [2] coupled to 10 telescopes of the FARCOS array [3]. The ten FARCOS telescopes, grouped in 5 couples, were arranged in a ring-like configuration covering about ¾ of the 2π azimuthal range at polar angles, in the laboratory, between 16 and 30 deg. Main topics of the experiment are the competition among different reaction mechanisms in the Intermediate Mass Fragment (IMF) production phenomenon. It aims at extending towards the low energy regime the studies already performed in the REVERSE and InKiIsSy experiments, carried out at the beam energy of 35 AMeV [4]. The different combinations of neutron rich and neutron poor beams and targets will allow us to investigate the above mentioned topics, also, with respect to the entrance channel Isospin content.

FARCOS DESCRIPTION

FARCOS (Femtoscope ARray For COrrelations and Spectroscopy) is a modular three-telescope array arranged in a single cluster, each one has three stages. The first two stages consist of Double Sided Silicon Strip Detectors (DSSSDs) made by a 300 μm (first stage) and the 1500 μm (second stage) of thickness having an active area of 64 x 64 cm^2. Each (DSSSDs) has 32 strips in the front side and 32 in the back one. The third stage consists of four CsI(Tl) crystals (3.2 x 3.2 cm^2) of 6 cm of thickness read by photodiodes (18 x 18 mm^2).

CALIBRATION DESCRIPTION

In order to perform the energy calibration of the DSSSDs we decided to use the punch through method. It consists in the construction of the 2-Dimensional DE-E identification matrix in which the Y axis contains the particle's energy loss (in electronic channel) deposited in the first stage, and in the X axis the particle's energy loss (in electronic channel) deposited in the second stage. Then it is important to record the channel number for which the particle is stopped in 1800 μm of silicon (sum of the first and the second stage). Once, for every strips, this channel is recorded it is possible to associate the corresponding energy loss. The final step is to perform a linear function fit (since the Silicon detector response of the energy loss is supposed to be linear) in order to obtain the calibration parameters of the straight line (y=ax+b) and to complete the calibration procedure. In our case, the punch through values of the ^{7}Li, ^{7}Be and ^{9}Be were used. The procedure is time consuming because it is necessary to take in account the corresponding electronic channel for all the strips of the two DSSSDs, for every telescope (ten in the case of CHIFAR experiment). After this procedure the identification of the particles is very fast because it is possible to construct a 2-Dimensional ΔE-E identification matrix in MeV by mixing together all the strips for each telescope. The punch through energies used (by LISE++ [5]) are 13,57 MeV, 18,52 MeV and 20,82 MeV for the three particles in transmission in the first DSSSD and 125,38 MeV, 172,68 MeV and 192,68 MeV for the three particles stopped in the second DSSSD.

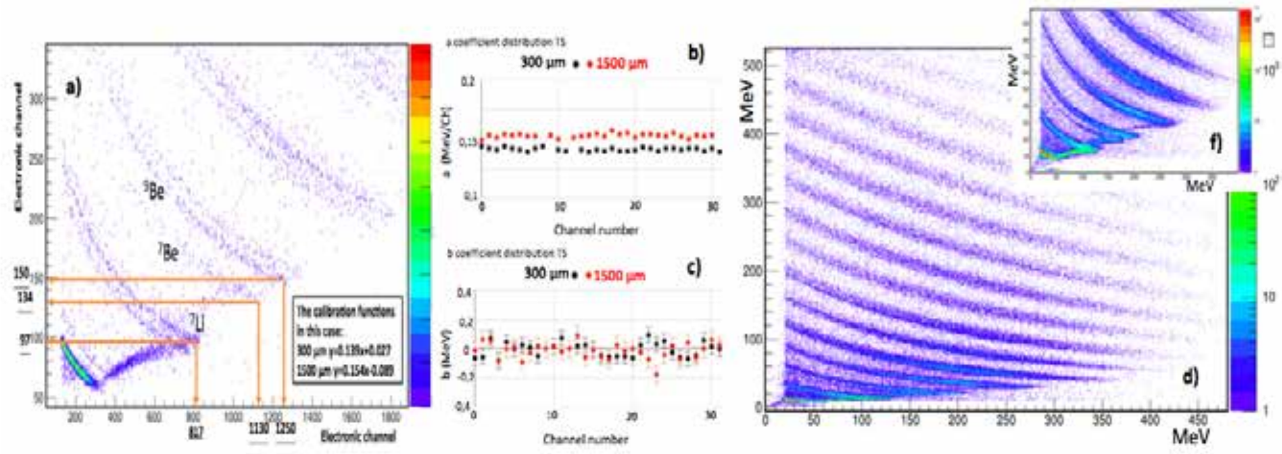

Figure 1: example of a full-width figure showing the latest LNS Activity Report cover

The panel a) of Figure 1 shows an example of the punching through selection in the case of the strip number six for the first (y-axis) and second (x-axis) DSSSDs in coincidence in the telescope number five. In the picture the orange arrows guide the eyes in the considered electronic channel. The right-down box in panel a) shows the resulting calibration parameters of the linear function for these two strips, assuming the nominal thickness of 300 µm and 1500 µm. In the panels b) and c) the results of the fits for the two DSSSDs of the telescope 5 are summarized. In particular, in the panel b) and c), the ***a*** linear coefficient in MeV/ch and the coefficient ***b*** in MeV for all the channels are reported . It is possible to observe a good stability around a mean value of 0.1413(0,0002) for the 300 µm with a σ=0.002 for the single channel (black dots) and of 0.1527(0,0003) for the 1500 µm with a σ=0.002 for the single channel (red dots). The distribution has a mean value of -0.005(0.009) for the 300 µm with a σ=0.05 for the single channel (black dots) and of -0.46(0,01) for the 1500 µm with a σ=0.06 for the single channel (red dots). For the latter case it is possible to observe that although the relative error is large for the single value (about 100%), almost all of them show vanishing values within the error bars. However, the statistical values of the errors in energy (50 - 60 keV) are negligible with respect to the silicon detector resolution (about 1%). The panel d) shows the 2-Dimensional identification matrix calibrated in energy (MeV) in which full statistics of all the strips of the two strip detectors for the telescope 5 is collected. As it is possible to observe, the performed calibration is very good showing a good separation among the atomic number of the detected particles, ranging from Z=2 to Z=16. For the atomic number between two (alpha particles) and eight (oxigen nuclei) also the isotopic separation is very good, as it is possible to observe in the zoom present in the panel e) of the Figure 1.

CONCLUSIONS AND PERSPECTIVES

The calibration procedure of the FARCOS detector array is almost ultimate in the CHIFAR experiment. The procedure, although time consuming in this present form, shows very good results in terms of stability of linearity and accuracy. The energy calibration allows to collect all statistics in only one identification matrix for each telescope, that is very fast for the identification procedure. The next steps will be the CsI(Tl) Calibration in order to detects high energy protons and isotopes. The so called "pixelations" problem, i.e. the association to every detected particle its own position in the laboratory frame by identifying the pixel corresponding to the hit front and back strips of the first stage of the detection, will be also solved. Besides, a semi-automatic procedure for the calibration is envisaged.

REFERENCES

[1] E.V. Pagano et al., Proposal of CHIFAR experiment, approved by the 2017 LNS-PAC.
[2] E. De Filippo and A. Pagano, Eur. Phys. J A50, 32 (2014) and refs. therein; A. Pagano, Nucl. Phys. News 22, 28 (2012) and refs. therein.
[3] E. De Filippo et al., NIM in preparation; E.V. Pagano et al., EPJ Web Conf. 117, 10008 (2016).
[4] P. Russotto et al., Eur. Phys. J A56, 12 (2020) and refs. therein.
[5] M.P. Kuchera et al., NIM B 376 (2016) 168 and referece therein.

A laser-based system for high-resolution positioning of FARCOS array

A. Trifirò[1,2], L. Acosta[1,3], G. Cardella[1], A. Castoldi[4,5], M. D'Andrea[1], E. De Filippo[1], F. Fichera[1], E. Geraci[1,6], B. Gnoffo[1,6], C. Guazzoni[4,5], P. Litrico[7], C. Maiolino[7], N.S. Martorana[6,7], A. Pagano[1], E.V. Pagano[6], G. Passaro[7], S. Pirrone[1], G. Politi[1,6], L. Quattrocchi[2], F. Risitano[1,2], F. Rizzo[6,7], P. Russotto[6], G. Saccà[1], V. Sicari[4,5], M. Trimarchi[1,2]

1) INFN, Sezione di Catania
2) Dipartimento di Scienze MIFT, Università di Messina
3) Instituto de Física, Universidad Nacional Autónoma de México
4) INFN, Sezione di Milano
5) Dipartimento di Elettronica, Informazione e Bioingegneria, Politecnico di Milano
6) Dipartimento di Fisica e Astronomia, Università di Catania
7) INFN, Laboratori Nazionali del Sud, Catania

Abstract – During last years in the framework of CHIMERA [1,2] collaboration it has been developed FARCOS (Femtoscope ARray for COrrelation and Spectroscopy) [3], a new generation apparatus conceived for high precision measurements of two- and multi-particle correlations.

In order to ensure the highest angular resolution, the position of every telescope of the array should be precisely known; for this purpose, it has been developed a laser-based system that can provide angular measurements with a resolution of the order of 0.01°.

INTRODUCTION

FARCOS is variable-geometry modular array of telescopes that can be coupled to other detection system in order to improve energy and angular resolution in particularly key regions of the solid angle. Every telescope is composed of two double-sided silicon strip detectors followed by CsI(Tl) crystals; the intersection of vertical and horizontal strips identify pixels of 2×2mm^2, then the angular resolution required for the specific case study can be obtained by choosing a suitable target-telescope distance. Therefore, the variable-geometry structure is an essential feature of FARCOS array but compelled the development of a system able of locating reference points with resolution capability better than millimeter.

SYSTEM DESCRIPTION

This system is based on a laser source placed along the beamline, 5m after the target position. The out-coming laser beam is very stable and is characterized by a divergence of 1.0 mrad and a diameter of 0.8mm; in order

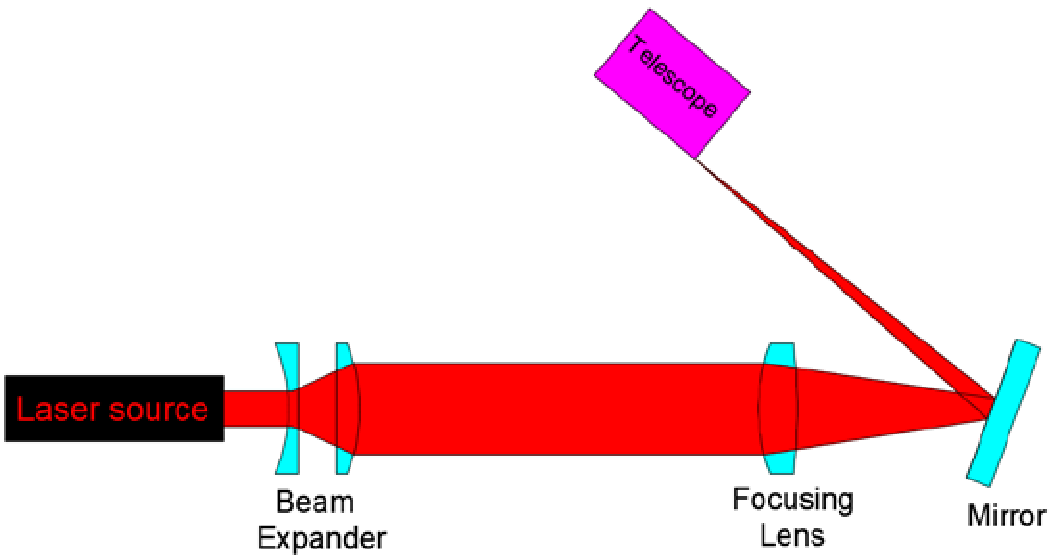

Figure 1: Outline of the laser beamline designed for the exact positioning of every Farcos telescope.

to improve the optical localization, this diameter has been further reduced by coupling the source with a beam expander followed by a focusing lens (see fig. 1), so the final beam can be focused on a spot as small as 0.3mm in diameter.

The optical beam is directed on a mirror placed in the target position and reflected towards the reference points chosen on every telescope, as shown in fig. 1. The mirror is mounted on the axis of a scanning Galvo system (fig. 2) that can rotate it around a horizontal axis with angular resolution of 0.0008°.

Figure 2: Galvo system and rotation stage used for the rotation of the mirror around two orthogonal axes.

For the rotation around the vertical axis, the Galvo system, in turn, is mounted on a high precision rotation stage with 0.01° resolution, which entails a theoretical resolution of 0.02° for the direction of reflected beam.

DISCUSSION AND RESULTS

After a suitable calibration, this positioning system can ensure the placing of telescopes with a precision adequate to the expected physics cases.

Angular measurements obtained could be affected by systematic and random errors. The main systematic error is related to a displacement of the mirror and can be easily restricted assuring that the vertical rotation axis intersects the horizontal one in the target centre; for instance, a displacement of the mirror of 1mm along the beamline could induce an error on the polar angle increasing from 0° (in the region around 0°) to 0.12° (in the region around 90°), while for a displacement in a transverse direction at the same azimuthal angle of the reference point this error could range from 0° (in the region around 60°) to 0.06° (in the regions around 0° and 90°), as shown in fig. 3.

Besides these systematic errors, further indeterminacy on angular position can be introduced by the described system because of non-reproducibility of measurements mainly due to thermal instability of mechanical and electronic components (random errors). Reproducibility tests revealed variations of the order of 0.001° for measurements carried out at time intervals of 1 minute, and maximum variations of 0.003° for measurements carried out after 24 and 48 hours at a fixed temperature of 23 °C. Similar measurements were also carried out changing the temperature of experimental hall from 20 °C to 30 °C; also during these tests, variation of measurements were very little (below 0.005°).

Figure 3: Difference between the true polar angle θ of a reference point, and the measure obtained with the system represented in fig. 1 if the mirror is displaced 1mm along the beamline (red symbols) or in a direction normal to the beamline, at the same azimuthal angle of the reference point (green symbols).

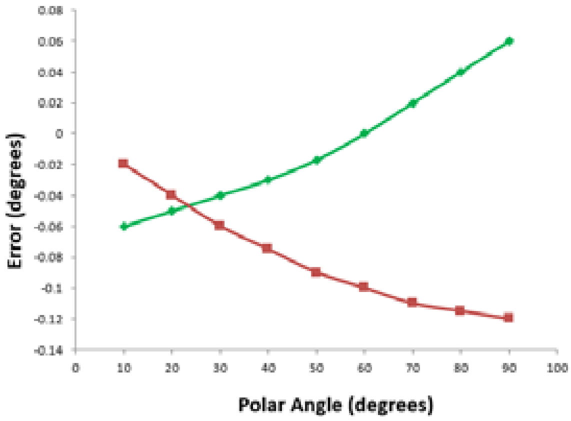

CONCLUSIONS

The present paper reports on a positioning system that has been developed for the Farcos array but can be employed for high-precision angular characterization of similar detectors or general apparatus. After suitable installation and calibration, the system can provide absolute angular positions with an indeterminacy lower than 0.02° for target-detector distance greater than 1m. The described system so can guarantee the required degree of accuracy, and in the next future could be upgraded introducing a laser source that can be pulsed in short bunches, in order to produce a detectable signal on the fired strips of the first silicon detector of Farcos telescopes.

REFERENCES

[1] E. De Filippo and A. Pagano, Eur. Phys. J A50 (2014) 32 and refs. Therein.

[2] A. Pagano, Nucl. Phys. News 22 (2012) 28 and refs. therein.

[3] E. De Filippo et al., NIM in preparation.

Beam test of new scintillation materials and read out systems for simultaneous detection of neutrons and charged particles

E.V. Pagano[1], G. Politi[2,3,*], A. Simancas[2], G. Cardella[3], E. De Filippo[3], E. Geraci[2,3], B. Gnoffo[2,3], C. Guazzoni[4], C. Maiolino[1], N.S. Martorana[1,2], A. Pagano[3], S. Pirrone[3], F. Rizzo[2,1], P. Russotto[1], M. Trimarchi[5,3].

1) INFN, Laboratori Nazionali del Sud, Catania, Italy
2) Dipartimento di Fisica ed Astronomia" Ettore Majorana", Università di Catania, Catania, Italy
3) INFN, Sezione di Catania, Catania, Italy
4) Politecnico di Milano e Sezione INFN di Milano, Milano, Italy
5) Dipartimento di Scienze MIFT, Università di Messina, Messina, Italy
**email: giuseppe.politi@ct.infn.it*

Abstract - The aim of this activity is to investigate the possibility of using some innovative scintillating materials, coupled with compact photo-sensors as read-out devices, to be the basic elements of a segmented and modular versatile multi-detector prototype, detecting at the same time neutrons and light charged particles, both with high angular and energy resolution.

EJ276 scintillator coupled to a SiPM read-out system has been studied, using reactions with heavy ions performed at LNS. The neutron detection efficiency for a given geometrical configuration has also been studied with some Monte Carlo simulations.

INTRODUCTION

The basic idea of this project is to realize a new modular detector sensitive both to neutrons and charged particles within the same detection cell, featuring both good energy and angular resolution and reasonable neutron efficiency. The device will be an array of single elementary detection cells of plastic scintillator, providing a fast signal for time-of-flight measurement, needed for neutron energy measurement, and with pulse shape discrimination to separate gamma from neutron. The final geometry will be defined by dedicated simulation, in order to optimize the global efficiency, the position and angular resolution, the time-of-flight measurement and the multiple-hit reconstruction capability, necessary to select well detected neutron.

To start this project, the discrimination properties of a basic element realized with a first candidate for the plastic scintillator (EJ-276) coupled to PMT, were tested with radioactive sources emitting gammas, neutrons and alpha particles [1], as well as with an ion beam of ^{24}Mg at 71.5 MeV and 81 MeV impinging on a $^{92}ZrO_2$ target [2], showing a good pulse shape discrimination in both cases.

Another result of a previous work [3] is the estimation of the neutron detection efficiency, based on the GEANT4 software simulations, for one detection cell and for one simple cluster of four consecutive elementary cells.

This report presents the results of the next step, namely the tests of the scintillator with a more compact light sensor, replacing the PMT with a silicon-based photon-electron transducer, a silicon photomultiplier (SiPM), to determine the performances in terms of pulse shape identification capabilities. Moreover, a more complex cluster has been studied with GEANT4 software.

MATERIALS AND METHODS

The 3x3x3 cm^3 plastic scintillators is EJ-276 type, delivered by Eljen Technology, whose main characteristic can be found in [4]. Plastic has been wrapped in white Teflon and aluminium tape on the lateral side and in aluminized Mylar on the entrance side of particle; coupling with read-out has been realized with an optical grease on the opposite side. SiPM reading has been performed with the commercial integrated device i-Spector from CAEN, equipped with an integrated SiPM, a preamplifier stage, an integrated power supply for SiPM biasing with temperature feedback loop and a monitor for temperature, current and voltage. The SiPM is the Hamamatsu S14160-60520HS with 16 (4x4) channels and 3531 pixels per channel, each one with a pitch of 50 μm. The preamplifier integrated has a bandwidth greater than 1 GHz, a gain of x5 and a shaping time of 180 ns.

EXPERIMENTAL RESULTS

The detector combination i-Spector + EJ-276 has been tested during the CHIFAR experiment performed at LNS. The setup was placed inside CHIMERA's scattering chamber at an angle of 11° in the laboratory frame. The i-Spector was biased with 40 V and the signal was digitized by using the GET electronics [5], working at 50 MHz signal sampling frequency, 12 bit dynamic and a maximum input voltage of 2 V (from -1 to 1 V), acquiring in this way the whole shape of each signal with a dedicated data acquisition system. Sampled signals can be manipulated by on purpose realized algorithm, to obtain signal characteristics (rise and decay time) and its integration on different time windows. The detector was tested under the reactions $^{124}Sn+^{64}Ni$ and $^{124}Sn+^{64}Zn$ at 20 MeV/A.

Pulse shape discrimination has been studied with the method of the charge integration in different time gates, by looking in this case to fast (Q_{fast}) and slow (Q_{slow}) components of the signal, and by means of the study of its decay time, also depending on particle type, with heavier particles showing a globally slower signal.

The results of the two gates method are shown in figure 1 for $^{124}Sn+^{64}Ni$ system, similar pictures have been observed for the other reaction. The inset shows the Q_{slow} histogram of the selected data (orange region) with the gaussian fits, obtained to calculate the FoM [2].

Figure 1: PSD based on pulse slow and fast components for the i-Spector + EJ-276 detector, for $^{124}Sn+^{64}Ni$

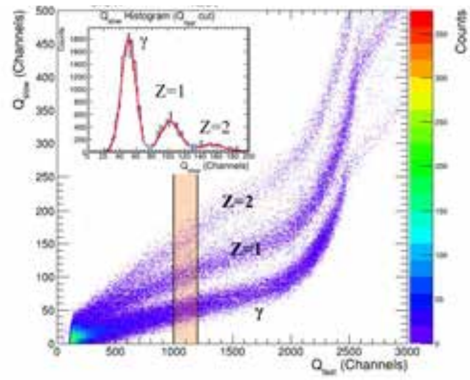

Results for the two different targets are summarised in table 1. At high value of Q_{fast} a saturation effect for this variable is clearly visible, due to not fully adapted gain of i-Spector preamplifier.

Table 1: FoM of the PSD based on pulse slow and fast components between gamma rays and Z=1 particles, and between Z=1 and Z=2 particles, for ^{64}Ni and ^{64}Zn targets.

Target	FoM (γ, Z=1)	FoM (Z=1, Z=2)
^{64}Ni	1.04	0.73
^{64}Zn	1.11	0.82

The decay time analysis provides results presented in figure 2 for $^{124}Sn+^{64}Zn$ system, with in the upper part the plot of pulse decay time versus total component Q_{tot} and in the lower part the decay time histogram for selected data regions: yellow for gamma rays and mixed light charged particles (LCP), orange for gamma rays, Z=1 and Z=2. Comparable data have been observed for the other system.

Figure 2: PSD based on the Decay Time of the pulses for the i-Spector + EJ-276 detector, for $^{124}Sn+^{64}Zn$

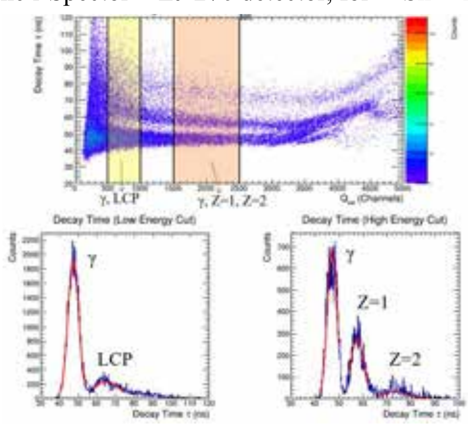

Again, the global FoM obtained with Gaussian fits are summarised in table 2 for the two studied systems.

Table 2: FoM of the PSD by pulse decay time between γ-rays and LCP, γ-rays and Z=1, Z=1 and Z=2, for the two systems

Target	FoM (γ, LCP)	FoM (γ, Z=1)	FoM (Z=1, Z=2)
^{64}Ni	0.69	0.97	0.85
^{64}Zn	0.73	0.93	0.90

MONTE CARLO SIMULATIONS

The Monte Carlo based simulation software GEANT4 has been used to calculate the neutron intrinsic detection efficiency as a function of energy for a cluster of 36 single cells of EJ-276 with size equal to tested detectors, arranged in 3x3x4 geometry with an empty region of 0.5 cm between cells. This quantity depends also on the capability of plastic scintillator to detect the recoiling proton, having energy ranging from a given maximum to zero. For this reasons energy threshold in proton detection is a very important parameter for this calculation. Results on intrinsic efficiency calculated with GEANT4 are illustrated in fig 9, as a function of neutron energy and for different values of detection threshold.

Figure 3: Simulated neutron detection efficiency for a 36-cell array of EJ-276 scintillator.

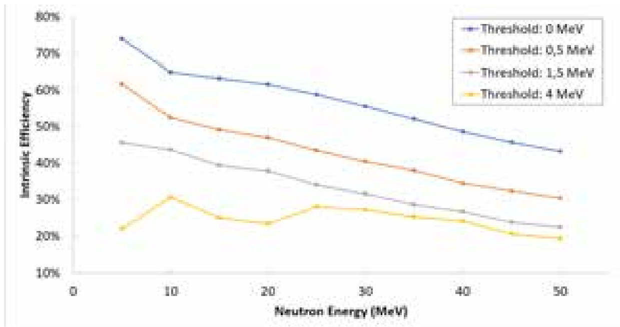

CONCLUSIONS

The response of EJ276 plastic scintillator coupled to a SiPM has been studied with in beam tests, in terms of PSD capabilities. Two PSD techniques have been used, namely the signal integration comparison and the exponential decay time of pulses, this latter providing slightly better results. An estimation of the neutron efficiency of a 36-cell array has been obtained with GEANT4 calculation, reporting a mean efficiency of around 30% with 1.5 MeV recoiling proton detection threshold.

REFERENCES

[1] E.V. Pagano et al., NIM A889 (2018) 83
[2] E.V. Pagano et al., NIM A905 (2018) 47
[3] E.V. Pagano et al., Nuovo Cimento 43 (2020) 1
[4] https://eljentechnology.com/products/plastic-scintillators/ej-276
[5] E. C. Pollacco et al., NIM A887 (2018) 81

Source test of new scintillation materials and read out systems for simultaneous detection of neutrons and charged particles

E.V. Pagano[1], G. Politi[2,3,*], A. Simancas[2], G. Cardella[3], E. De Filippo[3], E. Geraci[2,3], B. Gnoffo[2,3], C. Guazzoni[4], C. Maiolino[1], N.S. Martorana[1,2], A. Pagano[3], S. Pirrone[3], F. Rizzo[2,1], P. Russotto[1], M. Trimarchi[5,3].

1) INFN, Laboratori Nazionali del Sud, Catania, Italy

2) Dipartimento di Fisica ed Astronomia" Ettore Majorana", Università di Catania, Catania, Italy

3) INFN, Sezione di Catania, Catania, Italy

4) Politecnico di Milano e Sezione INFN di Milano, Milano, Italy

5) Dipartimento di Scienze MIFT, Università di Messina, Messina, Italy

** email: giuseppe.politi@ct.infn.it*

Abstract - The aim of this activity is to investigate the possibility of using some innovative scintillating materials, coupled with compact photo-sensors as read-out devices, to be the basic elements of a segmented and modular versatile multi-detector prototype, detecting at the same time neutrons and light charged particles, both with high angular and energy resolution.

Two suitable scintillator materials with the requested characteristics have been studied, coupled to different read-out systems, using alpha particle and gamma sources.

INTRODUCTION

The basic idea of this project is to realize a new modular detector sensitive both to neutrons and charged particles within the same detection cell, featuring both good energy and angular resolution and reasonable neutron efficiency. The device will be an array of single elementary detection cells of plastic scintillator, providing a fast signal for time-of-flight measurement, needed for neutron energy measurement, and with pulse shape discrimination to separate gamma from neutron.

To start this project, the discrimination properties of a basic element realized with a first candidate for the plastic scintillator (EJ-276) coupled to PMT, were tested with radioactive sources emitting gammas, neutrons and alpha particles [1], as well as with an ion beam of ^{24}Mg at 71.5 MeV and 81 MeV impinging on a $^{92}ZrO_2$ target [2], with the detector placed at 30° in the laboratory setting. A good pulse shape discrimination was obtained in the low-energy regime and some other important quantities were determined, such as the detection threshold and the intrinsic resolution of the scintillator. Furthermore, the presence of a high background with beam tests, did not affect the good PSD capabilities shown by the plastic.

Another result of a previous work [3] is the estimation of the neutron detection efficiency, based on the GEANT4 software simulations, for one detection cell and for one simple cluster of four consecutive elementary cells.

This report presents the results of the next step, namely the tests of the scintillator with a more compact light sensor, replacing the PMT with a silicon-based photon-electron transducer, a silicon photomultiplier (SiPM). At the same time the use of a green shifted version of the scintillator (EJ-276G) obtained by adding a wavelength shifter, has been explored, in order to better match the spectral response of photosensor. Obtained results concern thus testing with alpha and gamma sources of the compact light sensor (SiPM) coupled to the two plastic scintillators to determine their performances in terms of light yield and pulse shape identification capabilities.

MATERIALS AND METHODS

Two 3x3x3 cm^3 plastic scintillators have been used, one EJ-276 one in the its green version EJ-276G, delivered by Eljen Technology; their main characteristics can be found in [4].

Plastics have been wrapped in white Teflon and aluminium tape on the lateral side and in aluminized Mylar on the entrance side of particle; coupling with read-out has been realized with an optical grease on the opposite side.

A PMT model 9544Q manufactured by EMI, already used in [1,2], has been also used for comparison with that previous results. SiPM reading has been performed with the commercial integrated device i-Spector from CAEN, equipped with an integrated SiPM, a preamplifier stage, an integrated power supply for SiPM biasing with temperature feedback loop and a monitor for temperature, current and voltage. The SiPM is the Hamamatsu S14160-60520HS with 16 (4x4) channels and 3531 pixels per channel, each one with a pitch of 50 μm. The preamplifier integrated has a bandwidth greater than 1 GHz, a gain of x5 and a shaping time of 180 ns.

Gamma (^{133}Ba, ^{137}Cs, ^{60}Co) and alpha (^{241}Am) sources were employed for light yield study, energy calibration and to determine the PSD capabilities of the detectors.

The i-Spector system has been coupled to both plastic scintillators, while PMT has been used only with EJ276G, as the combination PMT + EJ276 was already tested in previous works [1-3] and under similar conditions.

SiPM preamplifier output and PMT direct output have been both processed by a desktop digitizer (DT5720 from CAEN) with 250 MHz sampling frequency, 12 bits dynamic and 2 V maximum input voltage. The digitizer was controlled through the DPP-PSD Control Software in the PC, where numerous parameters of the acquisition and signal processing can be configured; the more relevant for this work are the time windows for the charge integration of the different components of the pulses (short gate, long gate) and the dynamic for integrated charge conversion. Data acquisition and storing was performed by the same Control Software.

EXPERIMENTAL RESULTS

To perform the light yield calibration of the detectors we acquired for all the gamma sources the spectrum of total component of signal Q_{tot}, obtained by integrating it in a sufficient long gate (700 ns). Due to the low density of the plastic scintillators, we can observe only the structure of the spectrum produced by the Compton effect; gamma Compton edges at 50% have then been used for energy calibration.

Pulse shape discrimination has been performed acquiring the amount of charge integrated in two different time gates, the already mentioned Q_{tot} and Q_{fast}, the former proportional to total pulse and the latter to its fast component. These quantities are actually affected in different ways by particle specific energy loss, quite different for gamma/electrons and alpha particles; in particular, heavier particles will have a higher contribution from the slow component than from the fast one. Identification performances have been analysed by looking to a Particle Identification Parameter PIP = $1-(Q_{fast}/Q_{tot})$ versus the total light yield, calibrated in energy for gamma rays (keVee). Different values of length for fast gate have been used to optimize the discrimination between ^{241}Am alpha particles and ^{137}Cs gamma rays, simultaneously detected in the plastics. Figures 1 and 2 reports as example the best performances obtained for two of the three studied detector combinations. The inset in each figure shows the PIP histogram of the selected data (pink region) with two gaussian fits, and the corresponding Figure of Merit (FoM), calculated as the difference between the two peak average values divided by the sum of their Full Width at Half Maximum (FWHM); values of FoM greater than one are associated to a good discrimination capability.

Figure 1: PIP vs Energy spectrum with ^{241}Am and ^{137}Cs sources for the i-Spector + EJ-276 detector

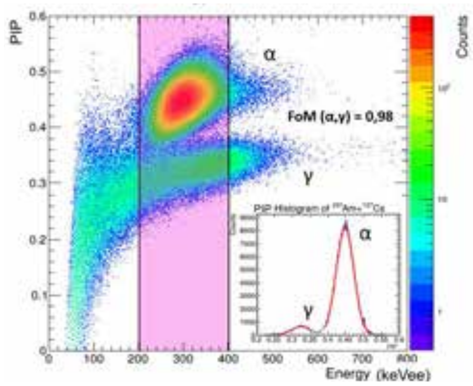

Figure 2: PIP vs Energy spectrum with ^{241}Am and ^{137}Cs sources for the i-Spector + EJ-276G detector.

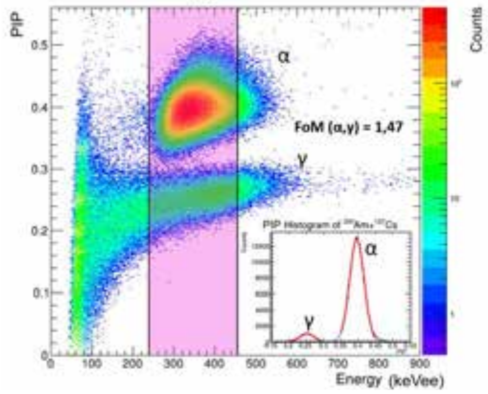

The obtained FoM for all the configurations and the relative acquisition parameters are summarised in Table 2.

Table 2: Acquisition parameters for each detector combination with the best Figure of Merit for the alpha-gamma discrimination with ^{241}Am and ^{137}Cs.

Detector combination	Fast Gate (ns)	Total gate (ns)	FoM
SiPM + EJ-276	108	700	0.98
SiPM + EJ-276G	120	700	1.47
PMT + EJ-276G	48	700	1.03

We can properly conclude that the PSD capabilities studied in [1] under low background conditions are conserved after the change of the photosensor from PMT to SiPM; moreover, the change of scintillator to the version with wavelength shifter seems to not affect the time shape of light output and the discrimination capabilities.

CONCLUSIONS

The response of various combinations of photosensor + plastic scintillator has been studied in terms of light output yield and their PSD capabilities. Energy calibration has been obtained by using the Compton edges of monoenergetic and quasi-monoenergetic showing a quite linear behaviour in the domain 200 - 1000 keVee.

Two gate PSD techniques have been used, providing a good discrimination for gamma-rays and alpha particles, with the maximum FoM for the i-Spector+EJ-276G configuration.

REFERENCES

[1] E.V. Pagano et al., NIM A889 (2018) 83
[2] E.V. Pagano et al., NIM A905 (2018) 47
[3] E.V. Pagano et al., Nuovo Cimento 43 (2020) 1
[4] https://eljentechnology.com/products/plastic-scintillators/ej-276
[5] E. C. Pollacco et al., NIM A887 (2018) 81

Energy Calibration of CHIMERA CsI for α particles based on the Time of Flight

B. Gnoffo[1,2*], S. Pirrone[2], G. Politi[1,2], L. Acosta[2,3], G. Cardella[2], E. De Filippo[2], E. Geraci[1,2], C. Guazzoni[4], G. Lanzalone[5,6], C. Maiolino[5], N.S. Martorana[1,5], A. Pagano[2], E.V. Pagano[5], M. Papa[2], F. Risitano[2,7], F. Rizzo[1,5], P. Russotto[5], V. Sicari[4] and M. Trimarchi[2,7]

1) Dipartimento di Fisica e Astronomia E. Majorana, Università di Catania, Italy
2) INFN-Sezione di Catania, Italy
3) Instituto de Fisica, Universidad Nacional Autònoma de México
4) Dip. di Elettronica, Informazione e Bioingegneria, Politecnico di Milano, Italy
5) INFN-LNS, Catania Italy
6) Facoltà di Ingegneria e Architettura, Università Kore, Italy
7) Dipartimento di Scienze MIFT, Univ. di Messina, Messina, Italy

e-mail: brunilde.gnoffo@ct.infn.it*

Abstract – Some interesting physical quantities (temperature, density levels parameter, and so on) characterizing the compound systems produced in ^{78}Kr+^{40}Ca and ^{86}Kr+^{48}Ca collisions, realized at 10 AMeV, could be investigated by looking to the features of the emitted light particles.

Very important information are provided by the energy spectra, so a good energy calibration of the detectors is necessary.

In particular, α particles, which are the light reaction products we are interested in, mainly release most of their energy in CsI(Tl) scintillators, and for this reason we have developed a special method for the calibration of these detectors, here described.

INTRODUCTION

The energy spectra of light particles can be correlated to some of the characteristics of their emission source, such as temperature, level density parameter and so on and provides information on the nature (dynamical or statistical) of the reaction mechanisms by which they are produced.

For the calculation of the temperature, it is possible to apply the method of the slope thermometer [1], if the shape of the energy spectra of α particles is maxwellian, as expected in the case of an emission by an equilibrated source.

In order to be able to gain information about the temperatures and other quantities relative to the compound nuclei, formed in the reaction ^{78}Kr+^{40}Ca and ^{86}Kr+^{48}Ca, realized at 10 AMeV [2], and studied by using the CHIMERA device [3], a method for the calibration of its CsI(Tl) detectors, has been developed.

In fact, the most of the light decay products are emitted with sufficient energy to punch through the first stage of CHIMERA telescopes, a silicon detector of about 300 μm of thickness and are stopped in CsI (Tl) scintillators.

By the knowledge of the thickness of the silicon layer and by the measurement of the particle's energy loss ΔE in this detector it is possible to calculate, with the help of the energy loss tables, the initial total energy and by subtraction, the residual energy deposited in the scintillator.

However, the procedure, based on the energy loss in silicon detector, is not optimal for the more energetic α particles, because they present almost the same energy loss by increasing their energy; a different method, described in the next section, has thus been developed.

α particles energy calibration of CsI detectors

The special method, developed to perform the energy calibration of CsI(Tl) scintillators, is based on the Time of Flight.

First of all, in our procedure, we have selected α particles, punching through the silicon detector, by using ΔE-E identification technique [4]. The total energy of these particles, is obtained from the velocity, directly measured thanks to the Time of Flight technique. As detailed in an another contribution of this issue in the calculation of the Time of Flight a fundamental step is the determination of the t_0 [5], the constant which takes into account all the effects affecting the time response of the reaction products. In the case of particles, punching

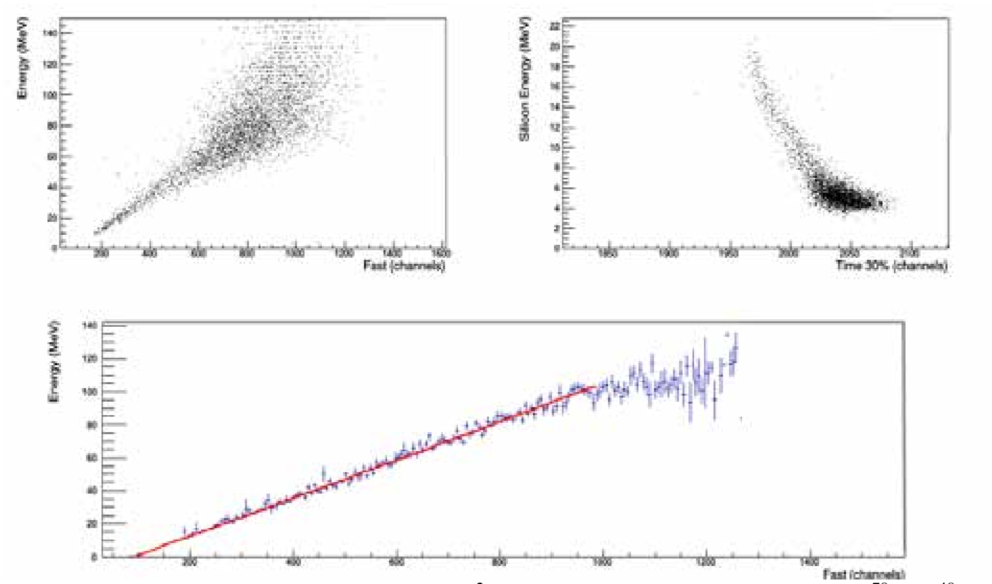

Figure 1: a) Residual energy in MeV, calculated as ½ Mv^2, vs fast for the products of reactions ^{78}Kr+ ^{48}Ca at 10 AMeV detected at 13.5°; b) ΔE-ToF plot; for α particles, punching through the silicon detector; c) profile plot of matrix in panel a), with red line representing the second-degree polynomial used for the fit.

through the silicon detectors, t_0 exhibits an ideal behaviour, as it is independent from particle energy and mass and for this reason it is called saturated t_0. The saturated t_0 is determined, detector per detector, for particles with well-known mass and charge and punching through energy, the one necessary to traverse a silicon detector of a given thickness. Once the saturated t_0 has been fixed, the velocity is determined and consequently the total energy E as ½ Mv^2. The residual energy, deposited in the CsI scintillator after punching through the silicon detector, is obtained as the difference between the total energy E and the energy loss ΔE. In panel a) of figure 1, the residual energy, in MeV, calculated as said before, is plotted as function of the fast component of the light output response of the CsI(Tl) scintillator, photodiode readout, for the particles lying in the ΔE-ToF plot, panel b) of Figure 1. In order to complete the calibration procedure a second degree polynomial, the red line in panel c), is used as the fitting function of the experimental points in the profile diagram corresponding to the residual energy versus fast plot. The calibration of the fast is fundamental because, for some detectors, the measurement of the time of the most energetic α particles is not good, because a saturation of this variable, at high energy, is observed. For these detectors, a selection cut is used around the particles with good time measurement in ΔE-ToF plot and the procedure, as described before, is performed; obviously, in these cases, the calibration is extrapolated at large values of the energy, following the trend of the second degree polynomial, which results from the best fit.

Examples of energy spectra, calibrated in MeV by using the described procedure, for alpha particles for different CHIMERA telescopes located at 15°, are shown in Figure 2.

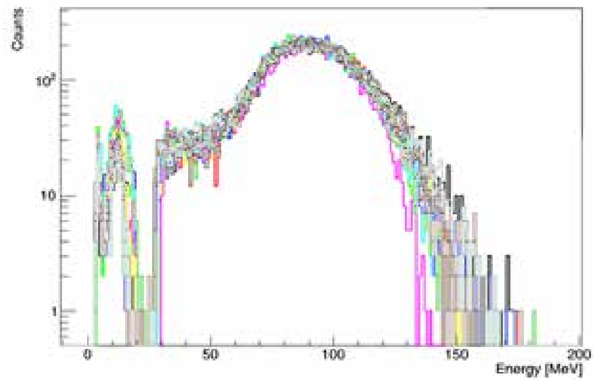

Figure 2: Examples of calibrated α energy spectra, each colour corresponds to each CHIMERA telescope at 15°.

CONCLUSIONS

A special method, based on the time of flight, has been developed, in order to calibrate the CsI(Tl) detectors. The procedure is performed detector per detector, by using as fitting function, a second degree polynomial. The good results, obtained for α particles, will allow the study of the energy spectra and consequently the investigation of important characteristic of their emission source.

REFERENCE

[1] V.F. Weisskopf, Phys. Rev. 52 (1937) 29
[2] S. Pirrone et al., EPJ A55, (2019) 12695
[3] A.Pagano et al., Nucl. Phys. A681 (2001) 331
[4] G.Politi et al, IEEE Nuclear Science Symposium Conference Record, N 28- 5 (2005) 1140
[5] B. Gnoffo et al., see contribution to this issue

Particles identification based on the Time of Flight technique in CHIMERA silicon detectors

B. Gnoffo[1,2*], P. Russotto[3], E. De Filippo[2], L. Acosta[2,4], G. Cardella[2], E. Geraci[1,2], C. Guazzoni[5], G. Lanzalone[3,6], C. Maiolino[3], N.S. Martorana[1,3], A. Pagano[2], E.V. Pagano[3], M. Papa[2], S. Pirrone[2], G. Politi[1,2], F. Risitano[2,7], F. Rizzo[1,3] and M. Trimarchi[2,7]

1) Dipartimento di Fisica e Astronomia E. Majorana, Università di Catania, Italy
2) INFN-Sezione di Catania, Italy
3) INFN-LNS, Catania Italy
4) Instituto de Fisica, Universidad Nacional Autònoma de México
5) Dip. di Elettronica, Informazione e Bioingegneria, Politecnico di Milano, Italy
6) Facoltà di Ingegneria e Architettura, Università Kore, Italy
7) Dipartimento di Scienze MIFT, Univ. di Messina, Messina, Italy

*e-mail: brunilde.gnoffo@ct.infn.it

Abstract – The description of the procedure developed for the application of the Time of Flight identification technique, in the silicon detectors of CHIMERA device is presented.

This procedure gives a method for full mass identification, for particles stopped in silicon detectors.

INTRODUCTION

The study of the physics of heavy ions implies the knowledge of key variables such as velocity, energy, charge, mass and detection angle of the produced fragments. This need requires the use of high performing devices. The CHIMERA multidetector [1] is a unique tool in the field of heavy ions collisions mainly thanks to the direct measurement of the velocity through the Time of Flight (ToF) identification technique [2].

In fact, ToF technique provides the velocities of reaction products and gives information about the mass of the particles stopped in silicon detectors. The velocity is given by:

$$v=\frac{d}{ToF} \quad (1)$$

where ToF is the time required to cover the base of flight d.

By combining the measured energy E and ToF, the mass (M) assignation, neglecting the relativistic corrections, to the fragments stopped in silicon detectors, is achieved by:

$$M = \frac{2ToF^2E}{d^2} \quad (2)$$

The measurement of ToF, in CHIMERA, is obtained as the difference between the delayed signal of the radio frequency of the cyclotron and the logic signal from the Constant Fraction Discriminator (CFD), acting on the pulse signal from each Silicon detector, with a fraction set at 30% of the pulse height [3]. This time difference is converted into channels t_{ch} by a TDC. In the calibration of the TDC, the ToF will be given by:

$$ToF = a(t_0 - t_{ch}) \quad (3).$$

where a is the linear coefficient of the calibration and t_0 a time constant, in channel units, depending on the specific detector and its electronics and taking into account delays due to cables, to the phase of the cyclotron and to the effect of signal formation in the silicon detector.

For particles which stop in silicon detectors t_0 is not really a constant but it shows a dependence on particles species and mass and on their energies. In fact, the plasma delay effect, affecting signal formation time, is not negligible for fragments of Z>2, for which the specific energy loss is high; moreover, for low energy signals near the CFD thresholds, the walk effect affects the time response of CFD, and this is more relevant for light particles.

The procedure, specially developed for the determination of t_0, for these fragments will be described in the next section.

DESCRIPTION OF THE METHOD

The method consists of a fitting procedure performed detector per detector. The starting point is the determination of 5 free parameters par[…] of the following function, which tries to take into account all the effects affecting the time response of detector and front-end and that has proven to be able to reproduce the trend of the data:

$$t_0=par[0]+par[4]\sqrt{\frac{A}{\Delta E\text{-}par[1]}}-par[2](S\text{-}R)\left(1\text{-}e^{\left(-\frac{A}{par[3]}\right)}\right) \quad (4)$$

where A is the mass number, S is the thickness of the detector, in µm, R is the range of the particles in silicon (µm) and ΔE is the energy deposited in the detector.

In the top panel (a)) of Figure 1, an example of the bidimensional plot ΔE-t is shown; the particles which stop in silicon detectors, occupy the part of the picture, tagged as A, where it is easy to recognize the lines corresponding to different masses. The black lines in

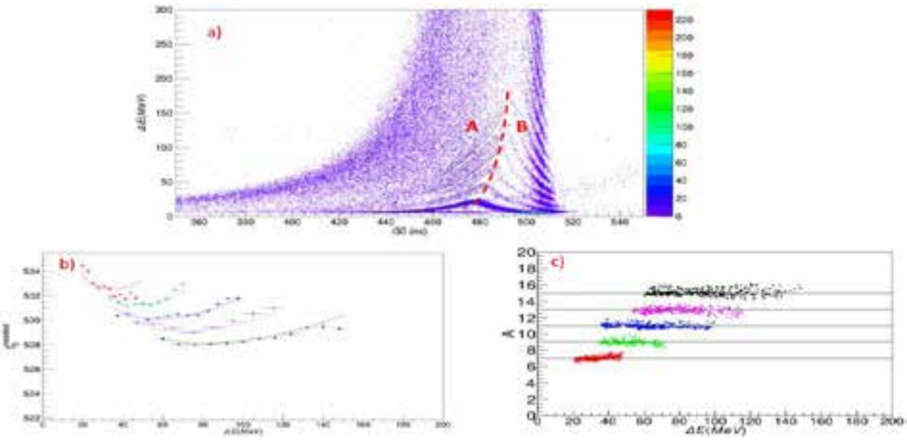

Figure 1: a) ΔE-T plot for all particles produced in the reaction ^{124}Xe+ ^{64}Ni at 20 AMeV and detected at 13.5°; b) For particles, inside the black lines in panel a): t0 vs ΔE (points), fitted by using the formula (4) (lines); c) reconstructed masses vs energy for selected ions.

this plot, represent the graphical cut, used for the selection of particles with well-separated mass lines and thus, with recognizable atomic mass numbers (7-9-11-13-15). For these selected particles, it is possible to determine the ToF and consequently, t_0 by inserting the mass in the equation (2). The t_0, thus obtained, are plotted as function of the energy, they are represented by the points in the picture of panel b) for different masses. In the same plot, the lines are the result of the fitting procedure, by using the semi-empirical formula (4).
In order to check the parameters, fixed as previous described, t_0 is determined through formula (4) and then inserted in formula (2), for the calculation of the masses of the selected particles. The correlation between the obtained atomic mass numbers and energy is plotted in panel c) of Figure 1. It is possible to observe that the masses are well reproduced and a linearization is reached for each mass.
Since the heavier fragments don't show well-separated mass lines and to avoid time consuming gates drawing for lighter ones the t_0s are obtained through an automatic and iterative procedure. Once the five free parameters are fixed, par [0] is used as start t_0, and it is introduced in equation (2) in order to determine a "starting" mass to put in formula (4). The obtained value of t_0 is then reintroduced into the formula (2) and the procedure is repeated until the convergence (the difference between the values of the masses obtained in two successive iterations) $M_{i+1} - M_i < 0.5$, is reached. In any case, at most, 20 iterations are performed.
When the convergence is not reached, e.g. the obtained masses start to oscillate between two values, a "smoothed" iteration procedure is used, where $M_{i+1}=(M_{i+1}+M_i)/2$; this helps convergence and gives acceptable masses assignments; if also this method fails, M is assigned as average of last 18 iterations, $M = \frac{\sum_{i=2}^{20} M_i}{18}$.
Otherwise, if out-of realistic range mass values are obtained, a bad code is assigned to the particle and it is not used in the analysis.
In figure 2 it is possible to appreciate the good quality of the procedure used, the mass lines obtained with this method, shown in different colours, well represent masses from A= 4 up to A=16, (bottom) as well as masses around A=124 (top) which is approximately the mass of the projectile.

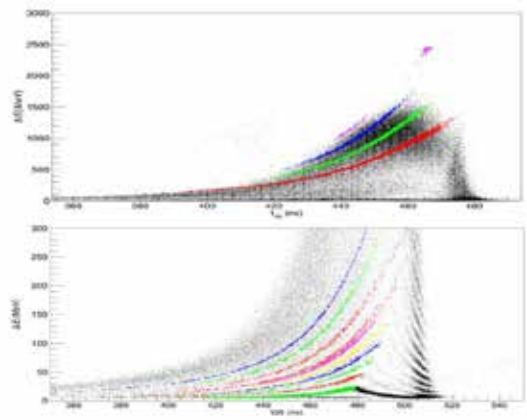

Figure 2: ΔE-ToF plot for a telescope at 13.5°, with the lines in different colours, in the top for masses 60, 80, 100, 120, and in the bottom for masses 4, 7, 9, 11, 13, 15, 16, 20, 25, 30

All the pictures are relative to the collision ^{124}Xe+ ^{64}Ni [4], at 20 AMeV, but similar results are obtained for reactions performed at other energies and with systems of different sizes.

REFERENCES

[1] A. Pagano et al., Nucl. Phys. A681(2001) 331
[2] G. Lanzalone et al., LNS Activity Report, (2004) 125
[3] M.Alderighi et al., NIM A 489 (2002) 257
[4] P. Russotto et al., Eur.Phys.J.A 56 (2020) 12

Simulation study of radioactive ion beams production with FRAISE

F. Risitano[1,2,*], L. Calabretta[3,4], G. Cardella[1], L. Cosentino[3], E. De Filippo[1], E. Geraci[1,5], B. Gnoffo[1,5], C. Maiolino[3], N.S. Martorana[3,5], E.V. Pagano[3], S. Pirrone[1], G. Politi[1,5], F. Rizzo[3,5], A.D. Russo[3], P. Russotto[3], D. Santonocito[3], M. Trimarchi[1,2]

1) *INFN-Sezione di Catania, Italy*
2) *Dipartimento MIFT, Università di Messina, Italy*
3) *INFN-LNS, Catania, Italy*
4) *INFN-LNL, Legnaro, Italy*
5) *Dipartimento di Fisica e Astronomia "Ettore Majorana", Università degli Studi di Catania, Italy*

*e-mail: *farisitano@unime.it*

Abstract - The new fragment separator FRAISE (FRAgment In-Flight SEparator) is currently under construction at Laboratori Nazionali del Sud of INFN (INFN-LNS). With respect to the previous fragment separator FRIBs, the new setup will allow to produce radioactive beams with better energy resolution, purity, and higher intensities. Through the simulation software LISE++, the production and optimization of several radioactive ion beams (RIBs) has been studied, also considering the many new features of the separator, such as the possibility of a new tagging and diagnostics systems based on SiC detectors, and the use of slits and aluminium degraders.

INTRODUCTION

From June 2020, the new fragment separator FRAISE is being constructed at Laboratori Nazionali del Sud [1]. Thanks to an upgrade of the Superconducting Cyclotron, it will be possible to produce stable beams with energies between 30 and 70 MeV/u, for ions from carbon to argon, with much higher intensity up to 10^{13} pps, corresponding to an intensity of 10 kW, about 10^2 times more than before. This improvement in the production of stable beams and the construction of the new fragment separator FRAISE will open new research possibilities, as it will be possible to produce radioactive beams with higher intensity and purity and even more exotic beams, farther from the stability line, never produced before with the FRIBs apparatus.

Many simulations have been carried out using the LISE++ software for several RIBs, showing the new capabilities of the future fragment separator. Different features of the separator, such as the thickness of the ^{9}Be fragmentation target and the rigidity of the magnetic dipoles, have been adjusted to optimize the production of a desired beam. Furthermore, a detailed study has been performed on the optimization of the aperture of the slits of the fragment separator: the first one, located at its centre, is responsible for the acceptance of the separator; the second one, located at its exit, is necessary for the rejection of impurities in the cocktail beam. These results will be made available to the LNS users and are to be considered of importance for tracing the future scientific research developments at LNS in this field.

SIMULATION WORK

The goal of this simulation study was to find the proper settings, case by case, of the fragment separator to optimize the production of several isotopes interesting for many research topics.

The first aim of the simulations was primarily to understand the effect of a new tagging system on the characteristics of the produced beams. A new tagging and diagnostics systems based on SiC detectors is in fact being developed at LNS [2,3]. For this reason, in the simulation of the standard structure of the fragment separator, two silicon carbide (SiC) 100 μm thick detectors were added, placed respectively at the symmetry plane and at the exit of the separator [4].

The presence of a detector on FRAISE's symmetry plane serves primarily as a tagging detector, providing the start signal of the TOF measurement between the symmetry plane and the exit of the separator, and secondarily as an *active* degrader, to partially clean the cocktail beam and to maximize the relative yield of a desired isotope.

A simulation of the production of a ^{15}C radioactive beam, using a ^{18}O primary beam (55 MeV/u, 2 kW) fragmented on a 1250 μm ^{9}Be target is described.

Fig. 1 (above) shows the profile of the cocktail beam at the exit of the separator, obtained for a full aperture of the symmetry plane slit, with a $\Delta p/p$ acceptance of 1.32%. This profile has been obtained in absence of the SiC detector and the purity of the ^{15}C component relative to the whole cocktail beam (consisting of more than 10 different isotopes) is about 65%.

By adding the SiC degrader on the symmetry plane and optimizing the rigidity of the dipoles of the second part of the FRAISE line, the purity of the ^{15}C component is increased up to 90%, while maintaining the same yield production (Fig. 1 below). By adding a further 200 μm aluminium homogeneous degrader at the symmetry plane, by optimizing the rigidity of the dipoles and the aperture of the exit slit, an almost pure ^{15}C beam isotope can be obtained, with purity of the order of 99.8% (Fig. 2).

Table 1: Preliminary simulations of production of various RIBs produced with FRAISE, adding two 100 µm SiC detectors, one on the symmetry plane and the other at the exit of the separator.

Primary beam / Energy (MeV/u) / Intensity (kW)	Primary Product	^{9}Be Target Thickness (µm)	Al Wedge Thickness (µm)	Expected yield (kHz)	Purity (%)	Exit Energy (MeV/u)	ΔE (%)	Δp/p (%)
^{18}O / 55 / 2	^{15}C	1250	200	21600	100	44	2.27	1.32
^{18}O / 55 / 2	^{16}C	1250	0	6800	99	46	2.1	1.32
^{18}O / 55 / 2	^{14}Be	1250	200	1.59	100	47	2.13	1.32
^{12}C / 62 / 2	^{8}B	2250	0	2400	58	47	2.1	1.32
^{13}C / 55 / 2	^{11}Be	1500	0	5830	97	47	2.06	1.32
^{36}Ar / 50 / 2	^{34}Ar	500	0	7360	61	33	2.8	1.32
^{48}Ca / 45 / 2	^{46}Ar	500	0	1650	93	30	2.2	1
^{24}Mg / 50 / 2	^{20}O	750	0	191	97	40	2.3	1.32
^{40}Ar / 40 / 2	^{38}S	250	0	4320	93	29	2.5	1.2
^{70}Zn / 50 / 1	^{68}Ni	250	0	753	78	36	2.1	1
^{16}O / 40 / 2	^{13}N	750	0	22500	95	28	2.5	1.32
^{16}O / 40 / 2	^{14}O	750	0	4460	72	27	2.7	1.32

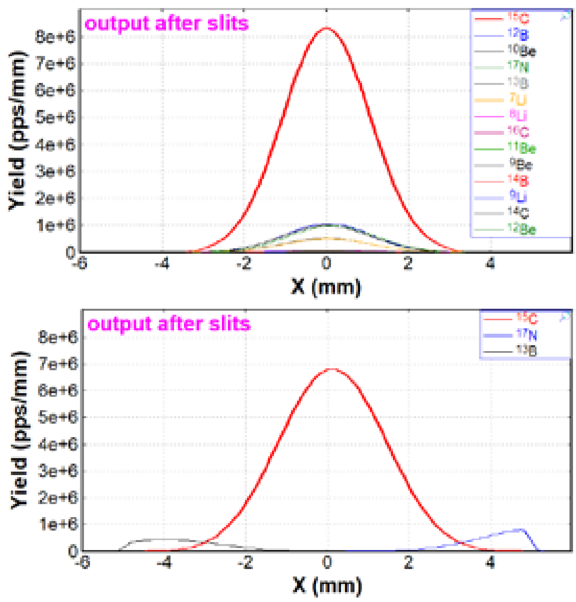

Figure 1: Horizontal distribution of the cocktail beam components at the exit of the fragment separator, with both exit and centre slits fully opened. It is possible to see the effect of the SiC detector on the symmetry plane (below), with respect to the configuration in which it is absent (above).

Table. 1 summarizes the results obtained for the optimization of several beams [4]. These beams will allow to explore a wider variety of research topics, such as nuclear exotic structures (^{16}C, ^{14}Be, ^{11}Be, ^{8}B), isospin effects in heavy ion reaction mechanisms (^{34}Ar, ^{46}Ar), collective resonances such as the Pygmy dipole one (^{38}S, ^{68}Ni), or reactions of astrophysical interest (^{13}N, ^{14}O).

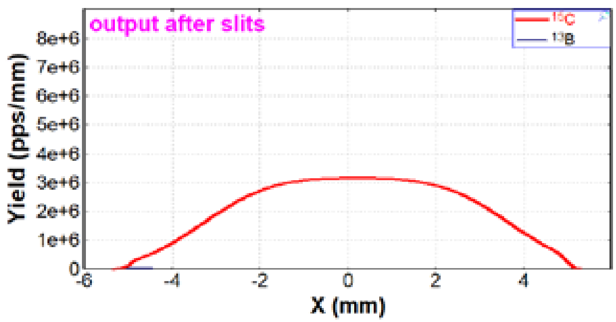

Figure 2: Output of the cocktail beam after the exit slit, with the SiC detector and aluminium degrader on the symmetry plane and with exit slit closed on 10 mm width, allowing only the extraction of the ^{15}C desired isotope.

CONCLUSIONS

The future fragment separator FRAISE will open new research possibilities in heavy ion physics at LNS, allowing the production of more intense and exotic RIBs. In this context, many simulations of production of beams have been carried out. These simulations, for which a more accurate description is available in Ref. [4], constitute an important starting point for the design of future experiments to be performed with FRAISE.

REFERENCES

[1] P. Russotto et al., Jour. of Phys.: Conf. Series, 1014, (2018) 012016 and ref. therein.
[2] S. Tudisco et al., Sensors (2018), 18.
[3] N.S. Martorana et al., Nuovo Cimento C 44 2021 1.
[4] F. Risitano, Master's Thesis, Università Di Messina, Jul 2020.

THGEM characterization for the NUMEN gas tracker prototype

I. Ciraldo[1,2], G. A. Brischetto[1,2], C. Agodi[1], F. Cappuzzello[1,2], M. Cavallaro[1], F. Delaunay[1], M. Fisichella[1], V. Soukeras[1], D. Torresi[1]

For the NUMEN collaboration

1) *Istituto Nazionale di Fisica Nucleare, Laboratori Nazionali del Sud - Catania, Italy*
2) *Dipartimento di Fisica e Astronomia "Ettore Majorana", Università di Catania - Catania, Italy*

Abstract - The characterization of the electron multiplication stage of the gas tracker prototype for the new focal plane detector of the MAGNEX spectrometer has been performed. Two different types of THGEM have been tested with radioactive source and beam at LNS.

INTRODUCTION

The present Focal Plane Detector (FPD) gas tracker [1,2] is based on six drift chambers and on the use of long multiplication wires. It can cope a maximum rate of few kHz and this makes it unsuitable for the LNS upgraded facility, which will deliver ion beams of the order of 2-10 kW to the MAGNEX spectrometer [4]. Such upgrade is required by the tiny values of involved cross sections and the resolution requirements for NUMEN [3] purposes.

A new tracker system for the MAGNEX focal plane detector is under development and one of the main upgrades consists in using Multiple-Thick GEM (M-THGEM) able to bear the expected high rate.

For the multiplication stage of the gas tracker prototype a Micro Pattern Gas Detector (MPGD) has been chosen [6]. Among the MPGD, the most suitable are the Thick-GEM (THGEM) foils [7,8], that can guarantee a high intrinsic rate capability.

Multiple-THGEM (M-THGEM) [9] are composed by two or three layers of THGEM stacked together. They ensure suitable characteristics for NUMEN purposes as they are able to reach high gain at low voltage and low pressure thanks to the avalanche confinement.

EXPERIMENTAL SET-UP

The experimental apparatus used in the tests of the M-THGEM is composed by the gas tracker prototype, an alpha source and a shutter, placed inside a gas chamber, as shown in Figure 1.

The gas chamber is filled with isobutane (iC_4H_{10}) and the tests are performed at four different pressure: 10, 20, 30, and 40 mbar.

The gas tracker prototype is a module of 100 x 185 x 108 mm^3 with the same structure and working principles of the final FPD but it is smaller in the dispersive direction.

Figure 1: Picture of the top view of experimental set-up used in the tests.

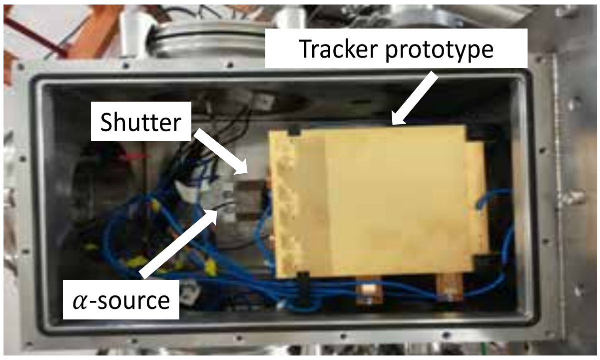

The structure of the tracker is made up with three main regions:

- A drift region, the active volume of the detector crossed by the charged particles where the ionization occurs
- An electron multiplication stage, based on Multiple-Thick GEM
- A read-out electrode made of a segmented anodic plate

The alpha source is ^{241}Am and emits 5.5x10^4 alphas per second. The shutter is used to allow (open) or stop (close) alpha particles arriving to the tracker and the rate is reduced to 140 alphas per second after it.

A multi-channel power supply based on CAEN SY5527 mainframe and A1515 high-voltage board [5] is used to bias the anode, each THGEM layer and the cathode.

The acquisition system is an ammeter that measures the currents flowing in all the electrical segments of the prototype.

CHARACTERIZATION OF THGEM

Two M-THGEM have been used in the tests and their main characteristics are shown in Table 1. Both of them are made of three layers and have an area of 107 x 107 mm^2, but they show different hole patterns (Figure 2). In the first one, FULL THGEM, the holes are uniformly distributed over the active surface. In the second one, ROW THGEM, the holes are arranged in five rows, orthogonal to the strips on the anode.

Using the FULL THGEM the electrons coming from the drift region arrive near the holes and are accelerated in a strong electric field, then, they are directed to the segmented anode.

The ROW THGEM has a not conventional geometry. Just the electrons produced in correspondence of the rows are multiplied by the THGEM and can generate a signal in the read-out electrode.

Table 1: The main characteristics of the tested THGEM.

	FULL	ROW
Substrate material	Ceramic SD103K	PCB
Finish board thickness [mm]	1.4 ± 0.1	1.28
Dimension [mm^2]	107x107	107x107
Rim size [mm]	0.1	0.2
Rows	143x143	5
Holes	20449	143
Hole diameter [mm]	0.30 ± 0.05	0.28
Hole spacing	0.75	0.75

Performing the characterization of the THGEM is possible to study the main features of the prototype as the applied voltages, the gas pressure and the multiplication factor.

The method of measurement consists of varying properly the pressure of Isobutane, the voltage of THGEM, the voltage of induction region and the voltage of drift region. Each current-voltage characteristic is measured changing only the relevant parameter and keeping fixed the others. For example, keeping fixed the gas pressure, the voltage of drift region and the voltage of induction region, the voltage of THGEM is changed by a small step.

The measurements allow to estimate the maximum working voltage, the ion back flow and the gain of the THGEM. A complete study of these parameters is under development and a comparison between FULL and ROW THGEM performances will be performed.

Figure 2: THGEM hole patterns: a) FULL THGEM, b) ROW THGEM.

a)

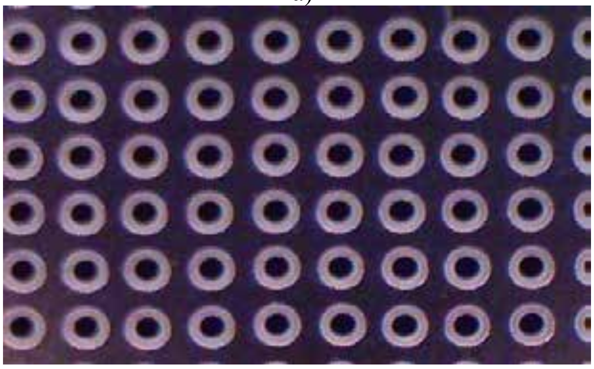

b)

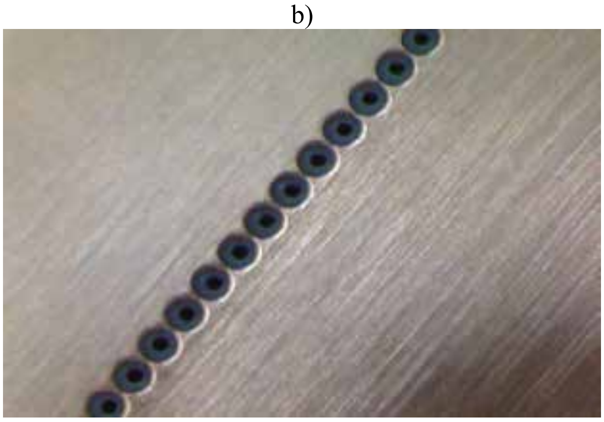

ACKNOWLEDGEMENTS

This project has received funding from the European Research Council (ERC) under the European Union's Horizon 2020 research and innovation programme (NURE project, grant agreement No 714625).

REFERENCES

[1] M. Cavallaro et al., M. Cavallaro et al., Eur. Phys. J. A (2012) **48**: 59.

[2] D. Torresi et al. NIM A 989 (2021): 164918.

[3] F. Cappuzzello et al., Eur. Phys. J. A 54: 72 (2018).

[4] F. Cappuzzello, C. Agodi, D. Carbone, and M. Cavallaro, Eur. Phys. J. A52, 167 (2016).

[5] https://www.caen.it/

[6] F. Sauli, Nucl. Instr. Meth. A 805 (2016) 2–24. doi:https://doi.org/10.1016/j.nima.2015.07.060.

[7] R. Chechik, A. Breskin, C. Shalem, D. M¨ormann, Nucl. Instr. Meth. A 535(2004) 303–308. doi:https://doi.org/10.1016/j.nima.2004.07.138.

[8] A. Breskin, R. Alon, M. Cortesi, R. Chechik, J. Miyamoto, V. Dangendorf, J.Maia, and J. D. Santos, Nucl. Instr. Meth. A 598 (2009) 107–111. doi:https://doi.org/10.1016/j.nima.2008.08.062.

[9] Cortesi M., et al., Review of Scientific Instruments 88.1 (2017): 013303.

ION SOURCE AND ACCELERATORS

The LNS Accelerator Division

Luigi Cosentino on behalf the LNS Accelerators Division

INFN - Laboratori Nazionali del Sud

Abstract – 2020 is the year of the last experiments for the Superconducting Cyclotron, being concluded the life cycle of its current cryostat, which will be replaced by a new one in the framework of the POTLNS activities, finalized to enhance the beam intensity up to a factor 100. Six months of experiments were originally planned with an intense beam time calendar, including also the first beams produced with the recently upgraded superconducting ions source SERSE. Unfortunately the forced closures due to covid19 disease did not allow to complete the experimental program, also due to the mandatory deadlines of the POTLNS project. As a consequence 12 experiments for about 2400 hours of beam time were lost for both the accelerators, being able to recover just a few experiments that were possible to make from mid-May until mid-June 2020. In October the cryostat of the Cyclotron has been warmed-up up to room temperature, after which the disassembly procedures of the cryostat have been started. Included in the potlns project is also the new fragment separator FRAISE that leads to the rearrangement of a large part of beam lines and most of the experimental sites. Also the Tandem is involved in renewing operations in order to guarantee a further life time of at least ten years and the availability of the new ion source of noble gases.

INTRODUCTION

A total of 1150 hours for the Cyclotron and 1650 hours for the Tandem have been allocated for the experiments during the year, including two CATANA proton therapy sessions [1]. In comparison to the original beam time calendar, almost 2400 hours have been lost and 12 experiments were cancelled for Covid19, also because no enough time to recover was available due to the start of activities related to POTLNS [2]. Unfortunately because of these time constraints no experiment with beams produced with SERSE was performed. However after the closure of the experimental activity, we were able to make some measurements finalized to collect data useful for the upgraded Cyclotron, in particular to find the working conditions for beams that will be extracted by ion stripping and to compare some experimental data with the calculated ones. In next years the Cyclotron will allow to accelerate the beams with significantly enhanced intensity, which in some cases is up to a factor 100, with consequent new and wider experimental opportunities available at LNS. Concerning the technical crew of the Accelerator Division, due to the high number of retirements in these years, four new technicians were recently recruited as permanent staff.

THE ACCELERATORS

When the warm-up of the Superconducting Cyclotron is started, we were well aware to stop 25 year of honourably activity of the accelerator, which perfectly worked until the last accelerated ion. In the few weeks available in 2020, nine experimental activities were performed including two CATANA sessions, as shown in fig.1. Unfortunately the commissioning of SERSE was abruptly interrupted during the lockdown and the related experiments were cancelled. In any case exploiting the availability of the helium liquefier, a first part of the commissioning of SERSE has been completed after the stop of the experimental activities, even if some cryogenic troubles still persist and a new design of the extraction system is required, in order to significantly increase the beam intensity. Up to now 300uA of $^{16}O^{6+}$ beam was produced with the extraction voltage fixed at 30kV, the value needed to extract the beam by ion stripping.

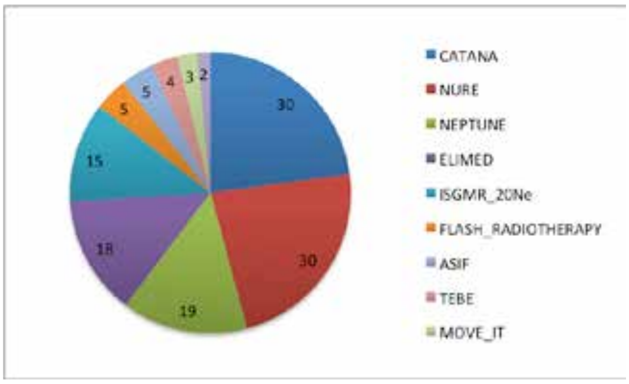

Figure 1: Experiments with Cyclotron beams performed in a few months of 2020. In total 1150 hours of beam in the target have been assigned.

With the Tandem eight experiments were completed and seven have been cancelled, fig. 2. Even the Tandem perfectly worked until the last days of the experimental activity and even if not directly involved in the POTLNS, it is going to be revamped to guarantee at least ten years of high performances activity. In particular the high voltage stabilization system is going to be replaced with a new one, the vacuum and SF_6 controls as well as the whole control system will be renewed and developed with the same approach of the Cyclotron. The aim is to restart with the Tandem beams for the second half of 2022.

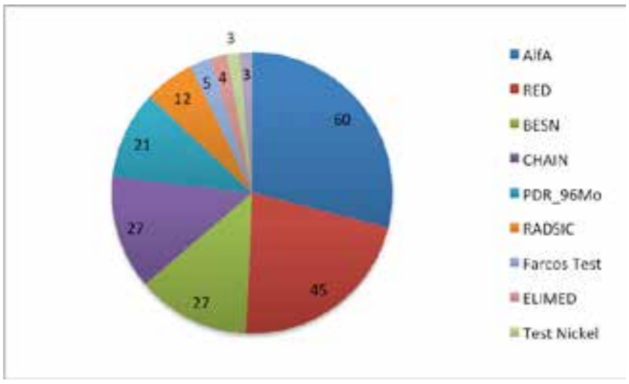

Figure 2: Experiments with Tandem beams. In total 1650 hours of beam in the target have been assigned during 2020.

An important step forward has been done with the installation of the Nestor ion source in the platform of the Tandem injector, fig. 3 [3]. The control system and the Lithium charge exchange cell will be in operation in the late 2021, so that the first beam of noble gases will be available within the end of the year.

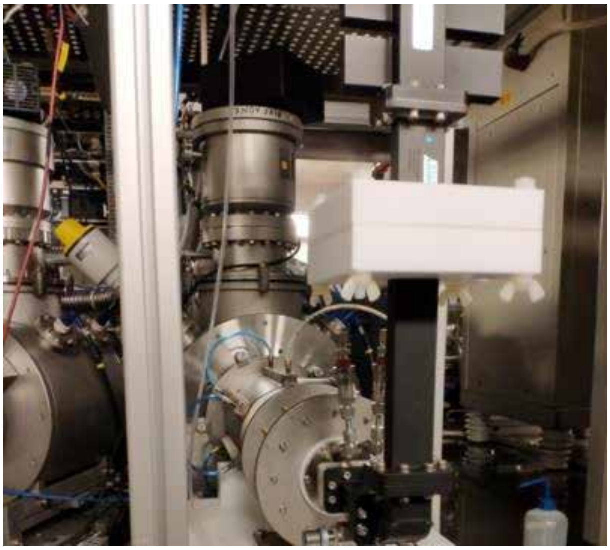
Figure 3: NESTOR ion source installed onto the high voltage platform of the tandem injector.

Test and measurements with the Cyclotron

Before the warm up of the cyclotron, some weeks have been dedicated to perform a few tests finalized to collect useful data for the future Superconducting Cyclotron. In fact some beams that will be extracted by ion stripping have been produced, in particular $^{18}O^{6+}$ and $^{40}Ar^{13+}$ accelerated from 20MeV/A to 60MeV/A, whose the operating point will be used for the commissioning of the new accelerator. Moreover we measured the charge distribution after strippers of different thickness, confirming the conformity of the calculated data to respect the experimental ones. Last but not least, we performed the first attempts of a systematic study to evaluate the dependence of the accelerated beam by its transversal emittance, fig. 4. For this aim the new beam diagnostics installed in the axial beam line was decisive, in particular the Allison emittance meter. In future this approach should be adopted systematically and in combination with a deep rearrangement of the axial beam line, in order to optimize the matching between the ion source and the Cyclotron. This represents a focal point to inject the required beam intensity needed to extract the kW beams in the forthcoming accelerator.

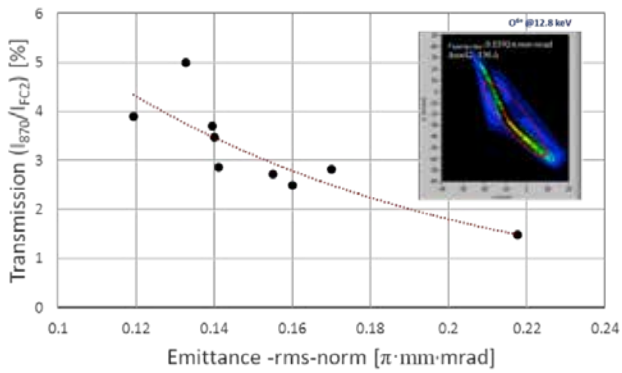

Figure 4: Beam transmission as a function of the beam emittance of $^{18}O^{6+}$ at 45AMeV. The accelerated beam is measured in the probe inside the Cyclotron.

CONCLUSIONS

The experimental activity with the accelerators has been concluded by mid-2020, after which the several activities related to the POTLNS project have been started. Unfortunately the Covid19 strongly affected the experimental program although we made all the best to recover what was possible. In parallel to POTLNS and profiting of the long shutdown, a careful maintenance of the Tandem is going to be performed, together with the development of new noble gas ions beams.

REFERENCES

[1] https://acceleratori.lns.infn.it/beamcalendar.html
[2] https://potlns.lns.infn.it/it/
[3] M. Mazzaglia et al., report LNS 2019.

Experimental characterization of the AISHa ion source

L. Celona[1], G. Calabrese[1], G. Castro[1], F. Chines[1], O. Leonardi[1], G. Manno[1], D. Mascali[1], A. Massara[1], A. Miraglia[1], D. Siliato[1], G. Torrisi, and S. Gammino

1) INFN-LNS, Via S. Sofia 62, 95123 Catania, Italy

Abstract - The Advanced Ion Source for Hadrontherapy (AISHa) has been designed to generate high brightness multiply charged ion beams for hadron therapy applications. In 2018/19 a few criticalities have been fixed during the first commissioning phase and different improvements have been carry out. Here we briefly describe the results of the subsequent operations with a single 18 GHz Klystron amplifier.

INTRODUCTION

The AISHa source is an Electron Cyclotron Resonance Ion Source (ECRIS) [1] designed with the typical requirements of hospital facilities where the minimization of the mean time between failures and the fast maintenance operations are key issues together with the low ripple, high stability, and high reproducibility of beams produced.

During the first commissioning phase a few criticalities have been observed and fixed in 2018/19. In detail, the cooling of the entire injection assembly has been improved, while in the extraction area has been slightly varying the electrode position and changing the location of the negative electrode feedthrough and its shielding. The improvements introduced allowed to increase the performance of the source, electing it as a substitute for the CAESAR source as new injector of the LNS Superconducting Cyclotron (CS) to satisfy the stringent requirements of the Numen project [2,3].

Figure 1 shows a view of the ion source in the experimental area.

The AISHa hybrid magnetic system consists of a permanent hexapole magnet and a set independently energized superconducting coils enclosed in a compact cryostat equipped with two double-stage cryocoolers that allow us to reach the operating conditions in around 40 h [4] in He-free operation.

The microwave injection system has been designed for maximizing the beam quality through a high-power klystron amplifier operating in the 17.3–18.4 GHz band that allows us to fine tune the frequency by a Digital Fast Tuner System (DFTS). It is coming a 21 GHz-1.5 kW power amplifier to upgrade the microwave injection system to operate in both single and double frequency modes to exploit, at the same time, the Frequency Tuning Effect (FTE) [5] and the Two Frequency Heating (TFH).

The plasma chamber, designed to operate around 18 GHz and to hold a maximum power rate of 2 kW [6] is placed at a high voltage (up to 40 kV) and insulated to the ground by a waveguide DC break, designed to permit reliable operation up to 50 kV [7].

Figure 1: The AISHa source INFN-LNS in Catania

The beamline consists of a focusing solenoid placed downstream of the source, a 90° bending dipole for ion selection, and two diagnostic boxes. Each diagnostic box consists of a Faraday Cup (FC), two beam wire scanners, and four slits allowing a complete characterization of the beam.

EXPERIMENTAL RESULTS

Figure 4 shows the characterization of the C^{4+} beam intensity as a function of operative frequency at 400 W to avoid operations with high reflected power.

Figure 5 shows the oxygen charge state distribution for $^{16}O^{6+}$ optimization measured with 1400 W microwave power and 20 kV extraction voltage. Helium has been used as a mixing gas. In such conditions, AISHa was able to generate up to 1200 eμA $^{16}O^{6+}$ and 200 eμA $^{16}O^{7+}$.

Figure 6 shows the carbon charge state distribution for the ion source tuned for the $^{12}C^{4+}$ charge state. In this case, more than 400 eμA $^{12}C^{4+}$ has been produced in the best experimental configuration by using 1300 W of microwave power and 24 kV extraction voltage.

Figure 7 shows the argon charge state distribution for the ion source tuned for the $^{40}Ar^{11+}$. Oxygen has been used as a mixing gas. In this case, the microwave power limitation at 1.5 kW plays a key role in the achievement of higher currents.

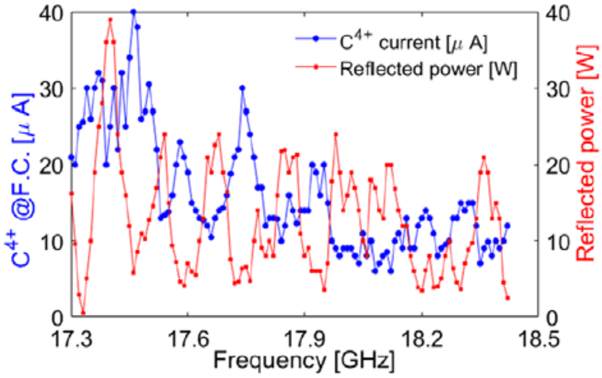

Figure 4: C^{4+} current at the FC as a function of the frequency within the klystron operative range.

The values obtained during the recommissioning are comparable with those obtained in other 18 GHz ECRISs [9-10] and with the requirements of the CS upgrade project except for the $^{12}C^{5+}$ and $^{40}Ar^{14+}$ ion beams.

The requirement regarding $^{12}C^{5+}$ is expected to be fulfilled by means of an upgrade of the heating system by the upgrade to a 21 + 18 GHz heating configuration.

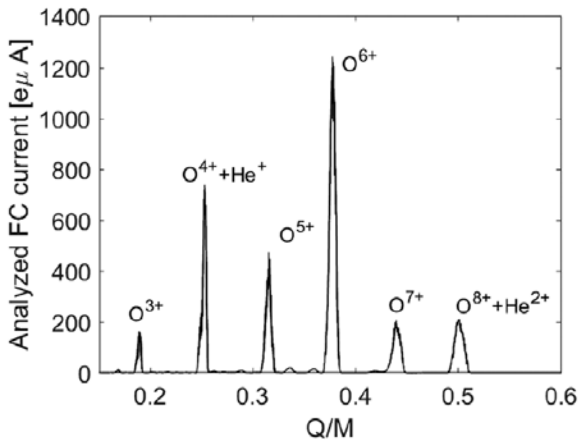

Figure 5: Oxygen charge state distribution for the ion source tune optimized for the O^{6+} charge state.

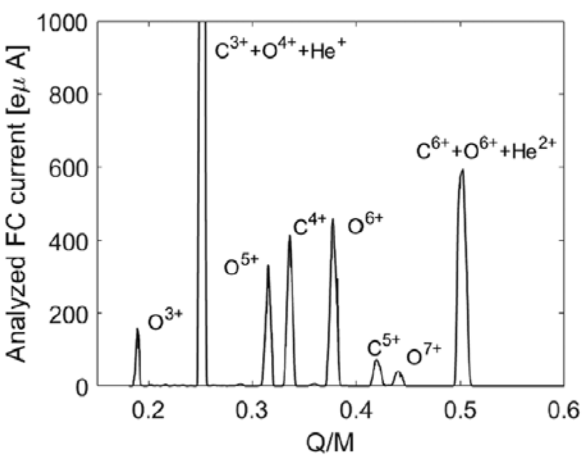

Figure 6: Carbon charge state distribution for the ion source tune optimized for the C^{4+} charge state.

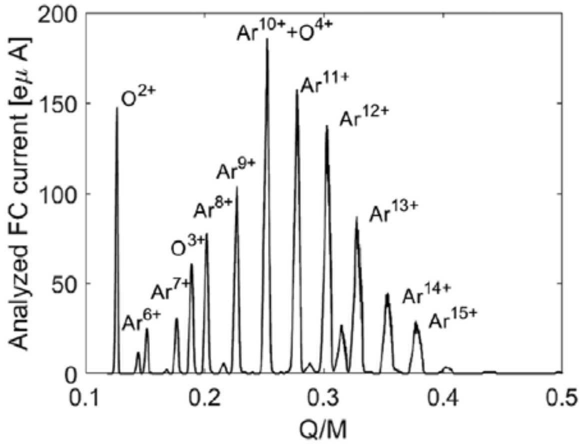

Figure 7: Argon charge state distribution for the ion source tune optimized for the Ar^{11+} charge state.

CONCLUSIONS AND NEXT STEPS

During last summer the tests performed on carbon and oxygen beams verified that the AISHa source is able to satisfy a large part of the requirements of the CS upgrade project. A requirement concerning $^{12}C^{5+}$ is expected to be fulfilled by means of an upgrade of the heating system.

In the next few months, AISHa will be equipped with a second high power klystron amplifier in the range of 21–22 GHz in order to probe the two frequency heating mechanism and consequently improve its performance. Systematic studies of the extracted beam and transverse emittance, measured by means of an Allison emittance scanner, already present on the beamline, are planned for next fall with the aim to optimize the brightness of the beam as a function of the different ion source parameters.

REFERENCES

[1] R. Geller, Electron Cyclotron Resonance Ion Source and ECR Plasmas, Inst. of Physics, Philadelphia, 1996.

[2] L. Calabretta et al., Mod. Phys. Lett. A **32**, 1740009 (2017).

[3] F. Cappuzzello et al., Eur. Phys. J. A **54**, 72 (2018).

[4] L. Celona et al., Proc. of ECRIS16, August 2016, Busan, South Korea, paper WEPP15.

[5] F. Maimone et al., Rev. Sci. Instrum. **82**, 123301 (2011).

[6] F. Noto et al., in ICCM2015, Auckland, NZ, 14–17 July 2015.

[7] O. Leonardi et al., Microwave. Opt. Technol. Lett. **60** (12), 3026–3029 (2018).

[8] T. Nakagawa et al., Rev. Sci. Instrum. **75**, 513 (2004).

[9] D. Leitner et al., in Proc. of IPAC Portland (USA) (IEEE, 2003), p. 86.

•. INTERDISCIPLINARY PHYSICS

Clinical activities at CATANA eye-proton facility of INFN-LNS

G. Cuttone[1], G.A.P. Cirrone[1], G. Privitera[3], V. Salamone[1,2], C. Spatola[1,2], L. Raffaele[1,2], A. Amato[1], R. Catalano[1], L. Liardo[2], R. Milazzotto[2], G. Messina[1], G. Petringa[1], A. Russo[1,2], E. Zappalà[1]

1)Laboratori Nazionali del Sud of Istituto azionale di Fisica Nucleare (INFN-LNS), Via S. Sofia 62, Catania, Italy
2)Azienda Ospedaliero Universitaria "Policlinico — Vittorio Emanuele", Presidio Gaspare Rodolico, Via Santa Sofia 78, Catania, Italy

Abstract - The CATANA protontherapy center was the first Italian clinical facility making use of energetic (62 MeV) proton beams for the radiative treatment of solid tumours. Since the date of the first patient treatment in 2002, 294 patients have been successful treated whose majority was affected by choroidal and iris melanomas. In this paper, we report on the current clinical and physical status of the CATANA facility describing the last dosimetric studies and reporting on the last patient follow- up results

CATANA, THE ITALIAN EYE PROTON THERAPY FACILITY

The CATANA (Centro di AdroTerapia Applicazioni Nucleari Avanzate) facility, built thanks to the collaboration between INFN-LNS and Public Health Policlinic named AOU-Vittorio Emanuele of Catania (I), is operational since 2002 and successfully treated more then
300 patients. The facility is dedicated to the radiation treatment of ocular melanomas with the 62 MeV proton beams accelerated by the INFN-LNS superconducting cyclotron. The most frequent neoplasia treated with proton beams is the uveal melanoma, followed by other eye diseases like choroidal metastases, conjunctival and eyelid tumours [1,2]

The CATANA facility is based on a passive transport system of a 62 MeV proton beam. The proton maximal range, at the irradiation point, is about 30 mm, ideal for the treatment of eye tumours. The necessary maximum range and energy modulation are achieved by means of a set of Perspex absorbers, variable in thickness, and modulator wheels.

The main characteristics of the beam line

The CATANA beamline has been developed at INFN-LNS of Catania (Figure 1).

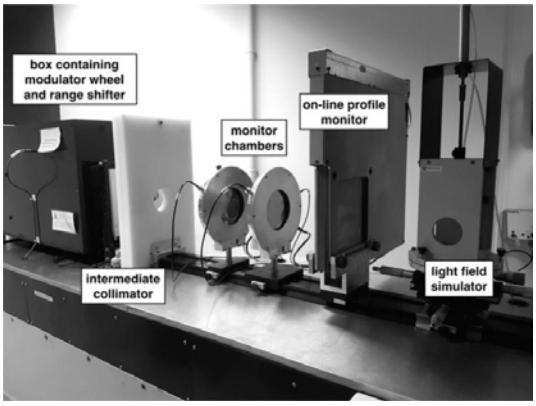

Figure 1: Central section of the CATANA protontherapy beamline with some transport (collimators, modulators, range shifters) and diagnostic (monitor chambers, on-line profile monitoring, field simulator).

Accelerated protons exit in air through 50 um Kapton window. Upstream the exit window, a first thin (15∝m) tantalum scattering foil, is placed in a vacuum: it performs a first broadening of the beam. After the Kapton window, in the air, a second thicker (25∝m) tantalum foil, equipped with a brass stopper of 4 mm in diameter, is used to perform the second beam scattering. This double foil scattering system is designed to obtain an optimal homogeneity of the final proton beam, in terms of lateral dose distribution contemporary minimising the energy losses.

A typical experimental transversal dose distribution for the 62 MeV clinical proton beam, is shown in Figure 2.

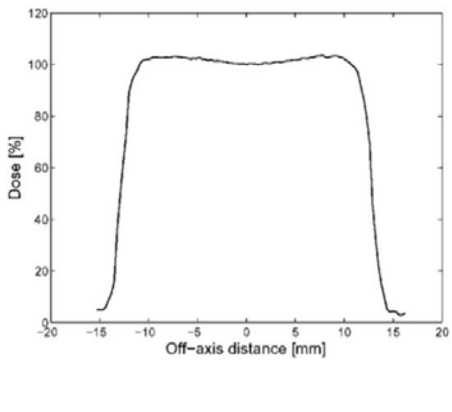

Figure 2: Experimental lateral dose distribution acquired with a silicon diode. This picture reproduced with the permission of the authors

Reported data are acquired in water with a Hi-pSi diode (0.6 mm detector diameter) at 12 mm water-equivalent in depth, corresponding to the middle of a Spread-Out Bragg Peak (SOBP).

Range shifter and range modulator are positioned downstream of the scattering system. The radiation field is simulated using a diffused light field. Two transmission monitor ionization chambers, providing the on-line control of the dose delivered to the patient represent the key elements of the patient dosimetry system [3,4,5]

CLINICAL ACTIVITY: TREATMENT PROCEDURES AND RESULTS

Treatment procedure and patient positioning

The knowledge of the tumour exact position is essential for eye protontherapy.

In order to achieve this, radio-opaque Tantalum clips, implanted around the lesion on the outer sclera, are used as reference points during the planning and irradiation phase. The surgeon also defined the tumour position and measurements as transverse and longitudinal base diameters, elevation or height, distance to the optic disk and to the macula.

The final result of this procedure is a precise virtual reconstruction of the tumour and healthy tissue around it. Eye and tumour are reconstructed by the EYEPLAN treatment planning system that provides correct proton dose distributions and eye position during the treatment.

Before the treatment starts the patient is immobilised. First of all, a fixation device is made by means of a customized thermoplastic mask and bite block, with the patient in a seated position. It is required for the patient to gaze at a light point and two orthogonal X-ray images (axial and lateral) are acquired.

The radiographic system, based on two flat panels HAMAMATSU model C7921CA-02, is able to identify the eye position at the isocenter point through a comparison between the radiographic images and simulated reconstructions obtained by using of EYEPLAN. The patient positioning chair is then moved in order to remove all misalignments.

A measurement of the eyelid thickness and slope is also carried out to complete the planning procedures. The EYEPLAN software schematically displays a model of the patient eye, (including the other anatomical parts like lens, optic nerve and fovea) and it provides a finally drawn of the tumour by means of the specified measurements and positions.

The planned isodose levels for 90%, 50%, and 20$\%$ of the prescribed dose and the DVH of the tumour and the organ at risk are reported by the treatment planning system. Before the treatment is also verified the patient position because if eyelids cannot be retracted completely outside the irradiation field, they have to be included in the treatment plan, as well.

A CCD camera, is used to continuously verify the eye position during the irradiation. The treatment time is between 30-60 sec.

Last clinical results

During the first 14 years of clinical activity, more than 300 patients have been treated at CATANA facility. Uveal melanoma has been the most frequently treated tumour, accounting for 252 treatments. Some other neoplasia has been treated by means of proton beams: conjunctival melanoma 5 patients, orbital rhabdomyosarcoma 3 patients, orbital non-Hodgkin lymphoma 4 patients, conjunctival papilloma 1 patient, eyelid and periorbital tissue carcinoma 18 patients, choroidal metastases and other orbital tumours 11 patients

Patients	
Sex	Male: 176
	Female: 118
Age	Range between: 12-88
	Median: 59
Diagnosis	Uveal melanoma: 252 pts
	Conjunctival melanoma: 5 pts
	Orbital rhabdomyosarcoma: 3 pts
	Orbital non-Hodgkin lymphoma: 4 pts
	Conjunctival papilloma: 1 pt
	Eyelid/periorbital carcinoma: 18 pts
	Other orbital tumors: 11 pt

(Figure 3).

Figure 3: Characteristics of the first 297 treated patients.

Proton beam dose applied was the same for all melanoma patients: 60 Gy[RBE] are delivered in a hypofractionation regimen, with 4 fractions on 4 consecutive days. An RBE of 1.1 is applied for the whole physical dose distribution (SOBP). For other tumours, a lower total dose was given, ranged between 30 to 48 Gy[RBE], with the same hypofractionated regimen.

Proton beam radiation therapy (PBRT) is considered a gold standard in the eye-conservative treatment of uveal melanoma, the most frequent ocular tumour in the adult, having demonstrated a tumour control rate and an overall survival rate compared to those of enucleation trials [6,7,8]. There are no available data from randomized trials for the application of proton beams to the treatment of other histologies, but only anecdotal data from case studies or single institution experiences. Then, inspired by the results of the proton beams in the treatment of uveal melanoma, so also for the other tumours of the orbital and peri-orbital region a conservative approach with protontherapy has been applied for 42 patients, for which there were no other therapeutic options.

Follow-up is available for all patients treated. It ranges from few months to 14 years, so the data can be considered mature for statistical considerations. Taking in account patients affected by uveal melanoma, according to the TNM-AJCC staging system (VII edition, 2010), they were classified as follow: T1 for 13 patients, T2 for 67 patients, T3 for 172 patients (252 patients in total) (Figure 4).

Uveal melanoma patients	
TNM stage	T1: 13 pts T2: 67 pts T3: 172 pts
Location	Posterior to equator (choroid only): 69% Choroid + Ciliary body: 24% Iris: 6%

Figure 3: Stage and location distribution (uveal melanoma).

The majority of uveal melanomas were located posteriorly to the eye equator (75%), in close vicinity to the vision OARs, optic disc and macula. A tumour local control is the primary endpoint of ocular protontherapy: it is defined as a dimensional reduction or stabilization of the elevation of uveal tumor from the retinal surface. A surrogate of dimensional evaluation is the increasing tumor ultrasound reflectivity, especially in the case of thickness stabilisation. According to these definitions, our patients have obtained a tumor control in 96% of cases (Figure 5).

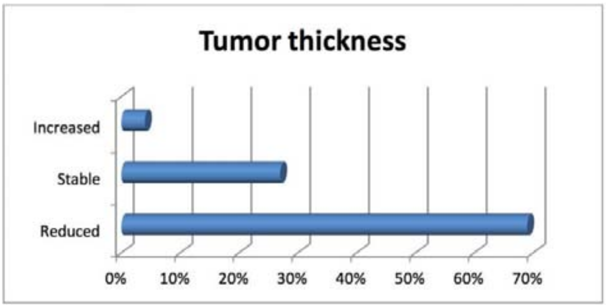

Figure 2: Local control response by tumour tissue

A secondary endpoint of ocular tumor protontherapy, as a conservative approach alternative to eye enucleation, is the maintenance of the eye [7]. Independently from the tumor control and from the residual visual function, 229 patients (90%) have maintained their eye. The major cause of secondary radiation-induced eye enucleation was neovascular glaucoma, in many cases occurring for big tumor volumes, conditioning an irradiation of large retinal surface. The time of enucleation ranged between 1,5 and 4 years from the completion of PBRT. In the group of patients with other histologies, a secondary enucleation was required.

Another goal of ocular protontherapy is the maintenance of a functional eye, with an acceptable visual acuity. This is, of course, only possible in patients with a tumour located, at diagnosis, away from optic disc or macula, and with a visual function not yet compromised by other eye diseases. Taking into account these premises, in our series a functional eye was maintained in about 40% of patients [9,10]

Ocular protontherapy is the treatment of choice in most ocular and orbital tumours, due to the high conformal treatment isodoses and the ability to spare the healthy surrounding tissues better than photon-beam treatment techniques. Despite this, due to the local extension and location of disease onset, the development of radiation-induced damages is often unavoidable. In our experience, radiation retinopathy of various degree was seen in 22% of patients, radiation-induced cataract was detected in 35% of patients, neovascular glaucoma developed in 18% of patients.

Cause-specific survival was 92%, since 18 patients affected by uveal melanoma and 3 affected by other tumours died from metastatic disease. Ocular melanoma, both uveal or conjunctival, has a strong tendency to metastasize, especially in the liver, after many years from diagnosis, regardless of the local control of the primary tumour.

CONCLUSION

CATANA is the first Italian proton therapy facility were 62 MeV protons have been used for the radiotherapy treatment of ocular melanomas.

Since 2002, about 294 patients have been treated and follow-up results are consistent with the statistics so far produced (see PTCOG web site: \textit{http://www.ptcog.ch/}).

Many research studies have been triggered by proton therapy activities. Among these, the development of new detectors, radiobiology studies and quality assurance methodologies are of particular interest.

In 2021 an X-Ray machine (maximum energy 300 KVp) will be installed and will be used for reference radiobiology experiments.

REFERENCES

[1] D.W., M. et al. Med. Phys. XXI, 1995
[2] M. Fuss, L. Loredo, et al. Int. J. Radiat. Oncol. Biol. Phys. (2001) 49, 1053
[3] Cuttone, G., Cirrone, G., et al. Part. J. Proton Therapy Co-Operative Group 28, (2002)
[4] Cuttone, G., Cirrone, G., Di Franco, G., et al. Catana protontherapy facility: The state of art of clinical and dosimetric experience. Eur. Phys. J. Plus (2011)126
[5] Cirrone, G., Cuttone, G., et al. IEEE Trans. Nucl. Sci. (2004) 51, 860
[6] Damato, B., Kackperek, A., Chopra, M., et al. (2005). Int. J. Radiat. Oncol. Biol. Phys. 63, 109
[7] Levin, D., Kooy H., J., Loeffler, et al. (2005). British J. Cancer 93, 849
[8] Egger, E., Schalenbourg, A., Zografos, L., Beati, D., et al. (2003). Int. J. Radiat. Oncol. Biol. Phys. 55, 867
[9] Spatola, C., Privitera, G., Raffaele, L., Cirrone, G., et al. (2008). Riv. Med. 14, 98
[10] Spatola, C., Privitera, G., Raffaele, L., et al. (2003)

MA-XRF analysis of two large-dimension paintings by Caravaggio

C. Caliri[1,2], A. Busacca[1,2], C.G. Fatuzzo[1,2], L. Pappalardo[1,2], D.P. Pavone[1,2], G.M. Privitera[1,2],

F. Rizzo[1] and F.P. Romano[1,2]

1) INFN, Laboratori Nazionali del Sud, Via Santa Sofia 62, 95123, Catania, Italy.
2) CNR, Istituto di Scienze del Patrimonio Culturale, Via Biblioteca 4, 95124 Catania, Italy.

Abstract - In the framework of a scientific collaboration between the LANDIS laboratory of LNS-INFN and ISPC-CNR (Catania), the University of Campania *Luigi Vanvitelli* (Naples) and the National Museum of Capodimonte (Naples), the research activity focused on the investigation of two large dimension masterpieces by Caravaggio is here presented. The study was aimed to investigate the original materials used by Caravaggio, his pictorial technique, and the creative process through the application of the non-destructive MAcroscopic -X-Ray Fluorescence imaging technique (MA-XRF).

INTRODUCTION

Many artworks such as large-dimension paintings are practically unmovable and consequently difficult to analyse. Furthermore, often their large dimensions can inhibit the analysis of the entire work for reasons due to the time restrictions available for measurements, thus the analyses are often limited to selected parts of the artwork. The advanced portable analytical techniques and innovative methodologies developed by the LANDIS laboratory of INFN-LNS and CNR-ISPC allow us to overcome these limitations and to approach numerous challenges in the study of heritage objects. Here we briefly report the study of two large dimension paintings by Caravaggio entitled "Seven Works of Mercy" (oil on canvas, 1606-1607) and “The Flagellation of Christ” (oil on canvas, 1607-1608), both are located in Naples (Italy) and they can be admired at the *Pio Monte della Misericordia Museum* and at the *National Museum of Capodimonte* respectively.

EXPERIMENTAL

The study of the paintings has been carried out by applying in situ the non-invasive MAcro X-Ray Fluorescence (MA-XRF) imaging technique. The technique consists in scanning the painted surface by using a micrometric X-ray beam and the analysis of all XRF spectra acquired pixel-by-pixel in continuous mode provides the images of the chemical elements distributed on the painted surface. MA-XRF technique allows us to obtain information concerning the nature and origin of raw materials used by the artist (pigments), the execution technique, the artistic process, the conservation state of artworks and in some cases to obtain information on their authenticity. An advantage of the MA-XRF technique is that its results are "images" of easy and immediate interpretation even for users with expertise outside the scientific sectors (e.g., conservatories, archaeologists and art historians, etc.) [1-5]. During the two measurement campaigns aimed to the study of Caravaggio paintings, a high-performance MA-XRF scanner, named LANDIS-X and fully developed in laboratory, has been employed. The LANDIS-X scanner is among the most advanced systems available in terms of lateral resolution of the images (up to 25 microns), dimensions of the analysable area (110×70cm^2) and scanning speed up to 10 cm/s.

Figure 1: (top) MA-XRF analysis of "Seven Works of Mercy" (oil on canvas, 1606-1607, Caravaggio) at the Pio Monte della Misericordia Museum; (bottom) MA-XRF analysis of “The Flagellation of Christ” (oil on canvas,

1607-1608, Caravaggio) at the Capodimonte Museum (Naples, Italy).

The entire surface of the first huge painting "Seven Works of Mercy" ($3.9\times2.6m^2$) was analysed by operating in total 25 scanning at a maximum speed of 10 cm/s and with a lateral resolution of 1 mm. To analyse the entire pictorial surface, a scaffold was installed in front of the painting (Fig. 1- top) and the scanning system was assembled and disassembled during the measurements on the different scaffold floors. The entire MA-XRF analysis lasted a total of 5 working days, also including the scaffold operations. The second painting "The Flagellation of Christ" was analysed under the same experimental conditions and operating 10 scans in total to cover the entire surface ($2.9\times2.1m^2$) in a total time of two working days.
Although the visitors, during measurements, were unable to admire the Caravaggio masterpieces up close, the possibility of carrying out the measurements in situ, inside the museum rooms (Fig.1- bottom), and the analytical results produced in real time during the scanning allowed them to get a preview of the overpaintings hidden under the pictorial layers and unveiled, for the first time, by the MA-XRF technique.

RESULTS

The elemental maps obtained by the application of MA-XRF technique provided a full characterization of the pigments palette used by Caravaggio and mainly composed by calcium, copper, iron, lead and mercury-based pigments. In Fig. 2 the elemental distribution images obtained for the "Seven Works of Mercy" painting are shown. In particular, brown iron-based pigments (ochers) were found in the canvas preparation together with lead white (biacca) and calcium-based pigments (gypsum or chalk) to make it darker. In fact, as it is well known, in the Caravaggio paintings the pictorial compositions emerge on a very dark background, this is also characterized by the presence of bone black pigment containing calcium and phosphorus. Ochres were also used for painting the half-tones and the lead white was used as a filler to define the bright areas up to using the white pigment in a pure way on the surface to illuminate the light areas more and more. Copper-based pigments are found in the green-blue areas and to define the shadows. In addition, Cu-based pigments were used to trace the profiles of the figures. In fact, as it is well known, in the Caravaggio paintings is not present the preparatory drawing, but the artist usually defined it during the pictorial process. Finally, the Hg-based pigment (vermilion) was used for the brightest red regions. The MA-XRF technique, in addition to provide us the identification of the chemical nature of the colours used by the master and how these were used and combined for painting the two masterpieces, thus increasing the knowledge about the original materials and the painting techniques, also allowed the study of the creative process operated by Caravaggio during the execution of the two paintings.

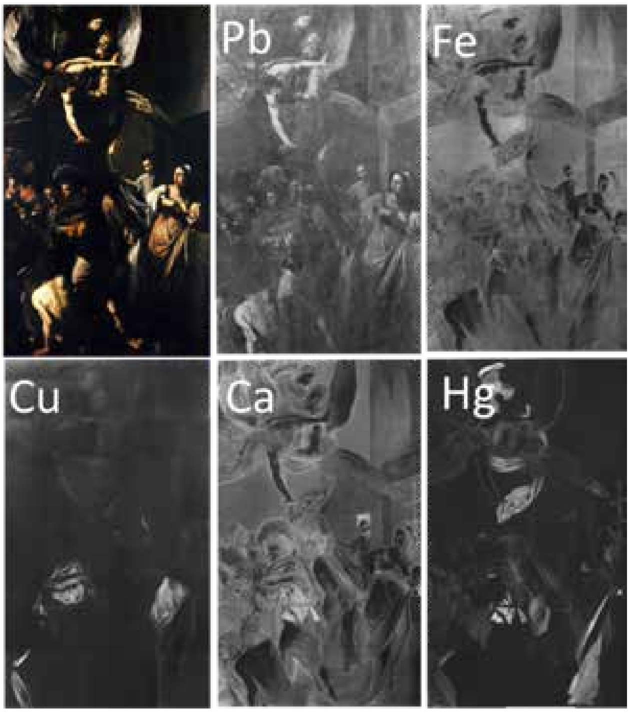

Figure 2: maps of the main chemical elements (Pb, Fe, Cu, Ca, Hg) characterizing the pigments used by Caravaggio for painting "Seven Works of Mercy".

In fact, below the pictorial layers, visible to naked eye, the elemental distribution maps unveiled hidden paintings, in detail the faces of two male characters covered by Caravaggio in the course of painting process. In the light of the analyses conducted, historians and art conservators are carrying out research to know the identity of the two characters and the reason that led Caravaggio to exclude them from the final composition. The two lead distribution maps show clearly the hidden faces found in the two paintings.

Figure 3: lead map that unveils the hidden figure painted and then covered by Caravaggio in "The Flagellation of Christ".

The first figure was painted in correspondence of the shoulder of the torturer on the right in the "Flagellation of Christ" painting (Fig. 3), while the second character is hidden to the left of the deacon holding the torch in the "Seven Works of Mercy" painting (Fig.4).

Figure 4: lead map that shows the hidden male character painted and later covered in the “Seven Works of Mercy” painting

REFERENCES

[1] F. P. Romano et al., *Journal of Analytical Atomic Spectrometry*, (2017), *32*(4), 773-781.

[2] C. Caliri et al., *X-Ray Spectrometry*, (2021), *50*(4), 332-340.

[3] M. Nervo, et al., *X-Ray Spectrometry*, (2021), *50*(4), 253-262.

[4] E. D'Elia et al., Microchemical Journal, (2020), 154, 104541.

[5] A. Križnar et al., X-Ray Spectrometry, (2019), 48(5), 482-489.

THE PRAGUE PROJECT: PROTON RANGE MEASURE USING SILICON CARBIDE DETECTORS

G. Petringa[1,2], M. Guarrera[2], C. Altana[2], A. Amato[2], R. Catalano[2], G. Cuttone[2], D. Margarone[2], G. Messina[2], G. Milluzzo[2], D. Passarello[2], S. Passarello[2], S. Tudisco[2], E. Zappalà[2], G.A.P. Cirrone[2]

1) ELI-Beamlines, Institute of Physics (FZU), Czech Academy of Sciences, Prague, Czechia.
2) Istituto Nazionale di Fisica Nucleare - Laboratori Nazionali del Sud (INFN-LNS), Catania, Italy.

Abstract - In proton therapy, Percentage Depth-Dose (PDD) assessment is part of beam quality control programs. The PRAGUE (Proton RAnGe measure Using silicon carbidE) project implements an innovative method aimed at optimizing the PDD measurement of both clinical proton beam and high intensity proton beam.

RESEARCH FIELD AND STATE OF ART

The measurement of the PDD is fundamental for the characterization of a clinical beam as it allows to estimate the range of the beam, necessary for the correct dosimetric planning of the treatment. Generally, the estimation of the proton range in biological tissue is affected by uncertainties [1] which involve the extension of the treatment volume margins, thus increasing the overall dose absorbed by the patient [2]. PDD is usually measured using the ionometric method which, although well established, exhibits a reduced spatial resolution (of the order of mm) (IAEA TRS 398). Furthermore, this method is not suitable for Flash Radiotherapy due to the ultra-high dose rates involved and the consequent ionic recombination phenomena [3].
Over the years, new dosimetric approaches have been investigated with the aim of increasing the accuracy of PDD measurement and at the same time making it possible to measure it in ultra-high dose rate regimes.
Table 1 lists some of the most widely used detectors today, with the advantages and disadvantages of their use in the clinical setting [4].

THE PRAGUE PROJECT

General objective

PRAGUE's objective is the design, construction and characterization of a detector capable of measuring, in real-time and with high longitudinal spatial resolution, of the PDD of a proton beam with energy between 30 MeV and 150 MeV at high and low intensity.
The detector consists of 60 new generation Silicon Carbide (SiC) devices (sensitive area of 15 × 15 mm^2 and active thickness of 10.3 μm) in stack configuration. The resistance of SiC to radiation damage and the independence of the response from LET (Linear Energy Transfer) and dose rate make them suitable for the characterization of even high intensity hadron beams [5].

Table 1: Detectors mainly used for PDD measurements in ion beam radiotherapy [6].

Detectors	Advantages	Disadvantages
Radiochromic Film (RCF) Stack	Dose-rate independent response, not subject to electromagnetic noise.	Response dependent on the LET and the energy of the radiation; passive detectors.
Stack of scintillators	High spatial resolution	Response dependent on the LET and the energy of the radiation; low resistance to radiation damage
MultiLayer Ionization Chamber (MLIC)	Linear response independent of the LET and the energy of the radiation	Response depending on the radiation dose rate and low spatial resolution (of the order of mm)
Multi-layer Faraday Collector (MLFC) Systems	Linear response independent of the LET, energy and dose rate of the radiation	Low spatial resolution (of the order of mm)

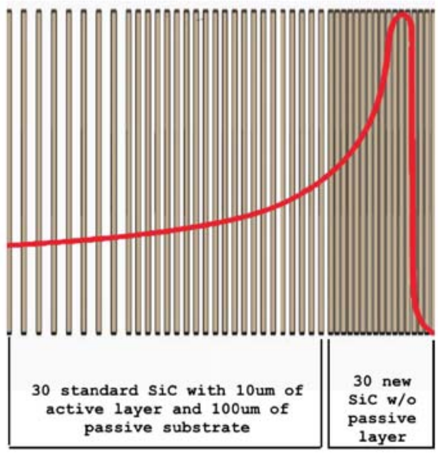

Figure 1: Schematic representation of the different sampling of the Bragg curve through the detectors with passive layer (entrance) and through the detectors without passive layer (distal and proximal part of the peak) [6].

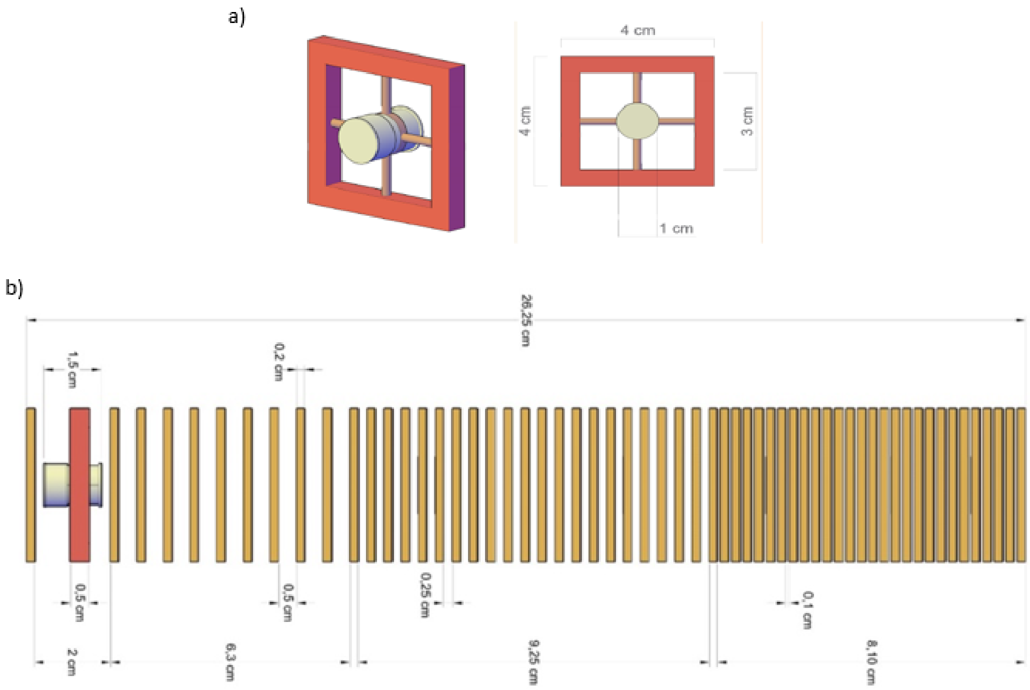

Figure 2: a) Preliminary structure of the biological flask coupled to its support. b) Preliminary configuration for the irradiation of biological samples. Distances are indicative [6].

Description of the device

The first 30 SiC devices, corresponding to the entrance of the Bragg curve, will consist of detectors with an active area of 10.3 µm and a passive substrate of 100 µm. The last 30 detectors, corresponding to the Bragg peak, will consist of SiC devices like those described above, but without the dead layer, to obtain the maximum possible longitudinal spatial resolution (Figure 1). Perspex plates will be interposed between the first 30 SiC to make the system conformable to the different energies of the incident particles.

A charged particle passing through the different layers of the detector will release energy on them according to the depth at which each layer is. The charge produced in each layer will increase with depth, following the trend of the Bragg curve. After an appropriate dose calibration procedure, the PDD, spectrum and range of the beam can be obtained. PRAGUE will allow controlled irradiation of cell samples thanks to the creation of a cell sample holder (Figure 2a); for this purpose, a study will be performed to establish the most suitable configuration (Figure 2b). The electronic chain will be designed to work properly with high and low intensity beams and involves the use of the TERA08 chip [6].

IMPACT

PRAGUE has the potential to change the current landscape of relative beam dosimetry with both clinical dose rate and extremely high dose rate. To date, in fact, there is no detector capable of measuring PDDs in real-time which is scarcely subject to radiation damage, capable of offering a similar longitudinal spatial resolution. The technology described will allow us to obtain information on the dose released in the shot-to-shot biological sample and with a precision compatible with the values indicated on the international dosimetric protocols for patient treatments (IAEA TRS 398). This could represent a significant advance for the community interested in probing the radiobiological effects of Flash Radiotherapy, The proposed technology could also change the landscape of quality control programs in conventional ion therapy, providing a device with a high spatial resolution whose use would involve a reduced consumption of time compared to the procedures currently in force.

REFERENCES

[1] H. Paganetti, Phys Med Biol. 2012 June 7; 57(11): R99–R117. https://doi.org/10.1088/0031-9155/57/11/R99
[2] Neil G Burnet et al., Cancer Imaging (2004) 4, 153–161, https://doi.org/10.1102/1470-7330.2004.0054
[3] Durante M, Bräuer-Krisch E, Hill M. Br J Radiol. 2018;91(1082):20170628. https://doi.org/10.1259/bjr.20170628
[4] P. Bolton et al., Physica Medica (2014), 30: 255-270, https://doi.org/10.1016/j.ejmp.2013.09.002
[5] G. Petringa et al, 2020, JINST 15 CO502 10.1088/1748-0221/15/05/C05023
[6] M. Guarrera, PhD Research Project, UniCt (2020/21)

A new dosimetric chain for flash proton beams

R. Catalano[1], A. Amato[1], G.A.P. Cirrone[1,2], G. Cuttone[1,2], G. Messina[1], G. Milluzzo[1], G. Petringa[1,3], E. Zappalà[1]

1) INFN-LNS, via S. Sofia, 62 - 95125 Catania, Italy

2) University of Catania, Department of Physics and Astronomy, via S. Sofia, 64 - 95125 Catania, Italy

2) Institute of Physics ASCR, v.v.i. (FZU), ELI-Beamlines Project, Na Slovance, 2 - Prague 18221 (Czech Republic)

Abstract – Currently no well-established absolute calibration protocols for the dosimetry of extremely high dose-rate charged particle beams exist, thus requiring each facility to establish its own dosimetric procedure.

We report the innovative dosimetric system for real-time absolute and relative dosimetry under FLASH irradiation conditions successfully developed at the INFN-LNS with pulsed proton beams up to 230 Gy/sec. The overall dose estimation accuracy in terms of relative mean difference between the dose measured with the different adopted detectors was found to be less than 3%.

INTRODUCTION

Many recent studies have shown that ultra-high dose-rate irradiations (> 40 Gy/sec), known as FLASH radiotherapy, based on the delivery of therapeutic doses with dose-rates over four orders of magnitude higher than those currently used in conventional radiotherapy, leads to a remarkable reduction of normal tissues toxicity.

The challenges concerning the possibility to perform an accurate and reliable dosimetry of ultra-intense proton/ion beams, able to meet the specific requirements and tolerances of clinical applications, however, require the development of innovative detectors, methods and procedures. In this paper, we will discuss the innovative dosimetric system for real-time absolute and relative dosimetry under FLASH irradiation conditions successfully developed and tested at the INFN-LNS, in the framework of the ELIMED Project. The proposed approach is based on the use of dose-rate independent detectors (Faraday Cup and Radio-chromic Films) coupled to a specifically designed dual-gaps in transmission ionization chamber, able to correct for any recombination effects, and a secondary electron emission monitor.

MATERIALS AND METHODS

Irradiations were performed with the 62 MeV proton beam accelerated by the INFN-LNS superconducting cyclotron, inside the 'Zero Degree' experimental room. A low energy chopper, located along the injection line [1], was activated to obtain a pulsed beam with time duration in the 10-200 ms range. Each proton pulse was formed with variable nominal beam currents at the cyclotron exit ranging from 5 to 50 nA, corresponding to a wide dose-rate interval between 1.170 and 13.896 kGy/min at the isocenter. The beam size was fixed with a squared brass collimator of 10 × 10 mm^2, positioned downstream the in-air section of the beamline.

The experimental set-up (Fig. 1) was realized in order to allow real-time, in-beam, dosimetry of the pulsed proton beams. Calibrated Radiochromic Films (RCFs), both EBT3 and HD-V2 type, coupled with the Faraday Cup (FC) were adopted for both performing the absolute dosimetry and calibrating the in-beam devices for the online dose measurements. The dual-gap ionization chamber (MGs) and the secondary electron emission monitor (SEM) were used to measure the released dose during each time proton bunch duration.

The FC was designed and realized at the INFN-LNS and consists of two coaxial electrodes biased at +1500V and –800V [2]. The internal electrode is aimed to generate a strong transverse component of the electric field, thus maximizing the deflection of the secondary electrons produced at the entrance window and in the cup material itself, increasing the collection efficiency and reducing the related uncertainties. The FC was specifically tailored, in terms of its electric capacity and front-end electronics, for the acquisition of high-rated pulsed beams.

The MGs ionization chamber (DE.TEC.TOR. S.r.l., Torino, Italy) is a novel in-transmission device designed and realized for on-line dose monitoring. It consists of two consecutive ionization chambers, with different inter-electrode gaps of 5 mm and 10 mm, operated as two independent beam monitor detectors. The presence of the second gap allowed us, exploiting the different collection efficiency among the two chambers, to correct for any ion recombination effect caused by the extremely high dose-rate by means of a reliable calibration curve obtained by applying the Boag-Wilson theory [3].

The SEM detector consists of a 12.5 μm-thick tantalum foil, electrically insulated by means of a PMMA circular frame. This device is able to detect the secondary electrons generated by the interaction of the protons with the detector itself.

The whole adopted dosimetric procedure consists of three consecutive steps: *i)* calibration of the RCFs, used in this study as reference dosimeters because of their response notoriously independent from the radiation beam intensity, in accordance with the IAEA TRS-398 Code of Practice; *ii)* validation of the FC by comparing the absolu-

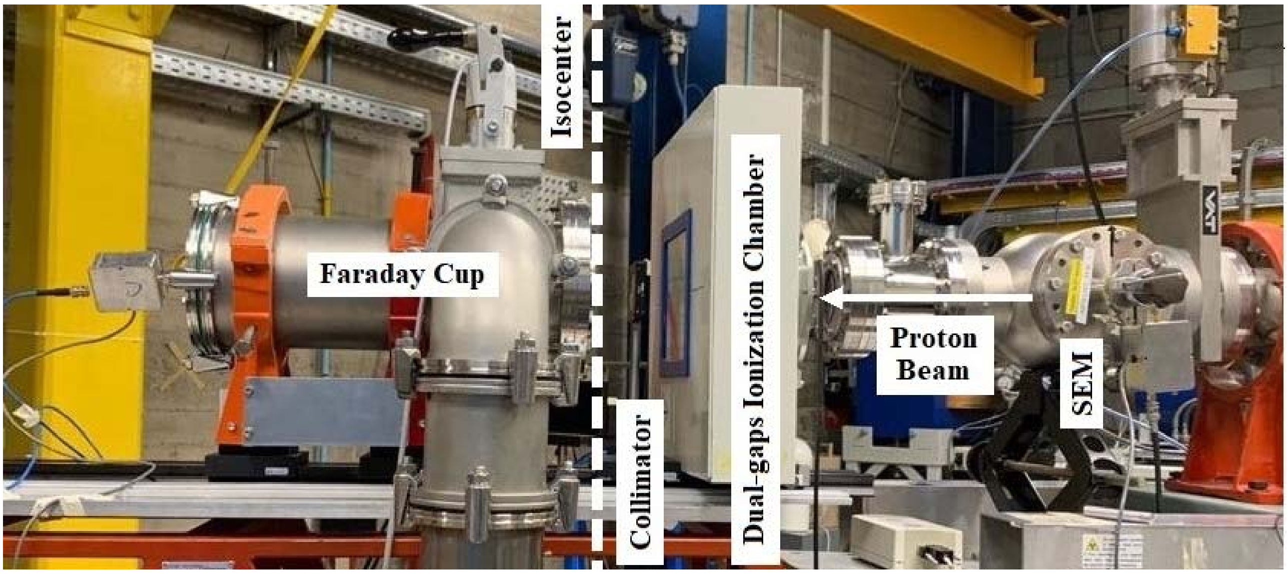

Figure 1: experimental set-up at the INFN-LNS 'Zero Degree' irradiation room

te dose estimated by the FC itself and the RCFs; *iii)* cross-calibration of the SEM and the MGs ionization chamber against the FC for relative dosimetry.

RESULTS

The overall absolute dose estimation accuracy, in terms of relative mean difference between the dose measured with the different detectors, was found to be less than 3% (Fig. 2); no significant differences between the response of the different dosimeters were observed so far when estimating their dependence on the beam intensity, except for the MGs, for which a reliable correction procedure was successfully developed.

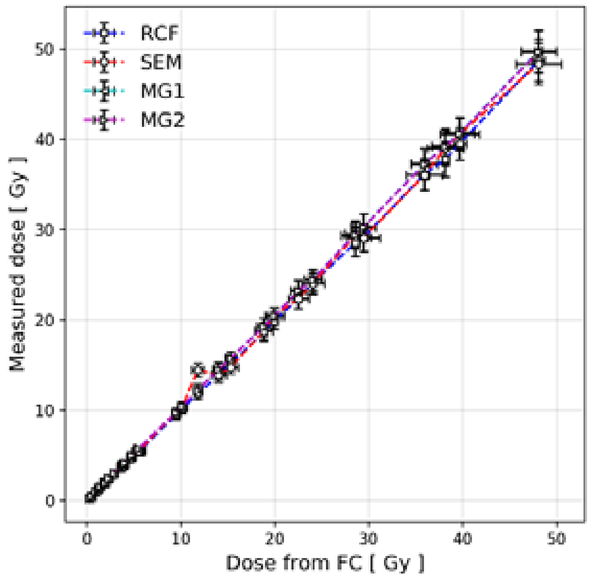

Figure 2: dose measured with the different adopted detectors as a function of the absolute dose estimated with the FC

A remarkable linear behaviour of the FC response was observed with increasing delivered radiation (correlation fitting factor $R^2 > 0.99$) over the released dose range typically adopted in the proton therapy clinic. The short-term reproducibility of the FC, *i.e.* the stability into estimate the absolute dose when repeating measurements over time under the same experimental conditions, was assessed as well and resulted to be smaller than 2.5%, thus indicating a good performance of the whole adopted procedure. Moreover, the charge collected by the FC showed no saturation effects throughout the available beam dose rates.

The agreement between the MGs ionization chambers and the FC clearly increases with increasing delivered dose, reaching a relative difference of less than 2.5% if the measured dose is greater than, typically, 5 Gy per shot. In general, the 5 mm gap ionization chamber showed a slightly better response in terms of dose estimation accuracy.

CONCLUSIONS

The different characteristics of the adopted detectors seem to guarantee the highest flexibility of the entire procedure. The validation of the performance of our dosimetric chain using multiple devices, in particular, allowed us to increase confidence in the accuracy and reliability of the absolute dose estimation, thus reducing the dosimetric uncertainties that could significantly affect the future radiobiological experiments.

REFERENCES

[1] L. Calabretta et al., Proc. of the XVI Int. Conference on Cyclotrons and Applications (2007), AIP.
[2] G.A.P. Cirrone et al., Front. Phys. 8:564907 (2020).
[3] J.W. Boag and T. Wilson, Brit. J. Appl. Phys. (1952), 222.

Monte Carlo methods for LET calculation: a comparison between experimental data with different ion beams

S. Fattori[1], G. Petringa[1,2] , S. Agosteo[3,4] , D. Bortot[3,4] , R. Catalano[1], G. Cuttone[1] , D.Mazzucconi[3,4], L. Pandola[1], G.A.P. Cirrone[1]

1) Istituto Nazionale di Fisica Nucleare - Laboratori Nazionali del Sud (INFN-LNS), Catania, Italy.

2) ELI-Beamlines, Institute of Physics (FZU), Czech Academy of Sciences, Prague, Czechia

3) Politecnico di Milano, Dipartimento di Energia, Sezione di Ingegneria Nucleare, Milano, Italy

4) Istituto Nazionale di Fisica Nucleare, Sezione di Milano,Milano, Italy

Abstract - In the framework of hadron therapy,, we extended the validations of Monte Carlo algorithms for Linear Energy Transfer (LET) calculation, in the case of ion beams, where not only the contribution of secondaries generated in the target fragmentation is essential, but also the projectile fragmentations plays a relevant role.

A series of experimental measurements have been realized at the Italian eye protontherapy facility (INFN-LNS, Catania, I) with two different experimental setups, based on two detector devices. The results of these two campaigns of measurement have been used as a benchmark desk for the validity test of the LET algorithms in the case of ions. .

INTRODUCTION

In the framework of hadron therapy, there is an increasing scientific interest in exploring the use of different brand new hadrons, beyond the classical proton beams.

The understanding of the behaviour of protons in terms of LET has been accurately studied with the development of new algorithms of dose and-track averaged LET, fully taking into account the contribution of secondaries. These algorithms have been validated, against experimental data, via Monte Carlo simulations realized with the Geant4 toolkit for 62 MeV clinical proton beams.[1].

In order to contribute in improving the understanding of the biological effects of ions in hadron therapy, we extended the application of the above mentioned algorithms for LET calculation, in the case of ion beams, where not only the contribution of secondaries generated in the target fragmentation is essential, but also the projectile fragmentations plays a relevant role.

For the validation of the above mentioned algorithms, Monte Carlo simulations in Geant4 [2] were compared with a series of experimental measurements, realized at the Italian eye protontherapy facility (INFN-LNS, Catania, I) with two different experimental setups, based on two detector devices: a Silicon On Insulator (SOI) microdosimeter with 3D Sensitive Volumes developed by the Centre for Medical Radiation Physics of the Wollongong University [3], and a nano-TEPC designed and constructed at the Legnaro National Laboratories of the National Institute for Nuclear Physics (INFN-LNL)[4]

The results of these two campaigns of measurements have been used as a benchmark desk for the validity test of the LET algorithms in the case of ions.

MATERIAL AND METHODS.

Monte Carlo based algorithms for improved LET calculation and their corresponding experimental quantities

Referring to the predecessor study [1] we recall the definitions of the average-LET quantities, which we are implementing here for use with ion beams. This new approach to the LET calculation has its origin in the concept of average-LET, and it has been extended in [1] to fully include the contribution of the secondary ions, generated in the inelastic interactions of the projectile (it was the proton in [1]) with the target nuclei. Specifically we define two types of average-LET: the track-average LET (L_t^{Total}) and the dose-average LET (L_d^{Total}), described with formulas (1) and (2) respectively;

$$\underline{L}_t^{Total} = \frac{\sum_{j=1}^{n}\left[\sum_{i=1}^{N} L_i l_i\right]_j}{\sum_{j=1}^{n}\left[\sum_{i=1}^{N} l_i\right]_j} \qquad (1)$$

$$\underline{L}_d^{Total} = \frac{\sum_{j=1}^{n}\left[\sum_{i=1}^{N} L_i \epsilon_i\right]_j}{\sum_{j=1}^{n}\left[\sum_{i=1}^{N} \epsilon_i\right]_j} \qquad (2)$$

where, for a certain particle, L is the total electronic stopping power, obtained via Monte Carlo approach from the Geant4 look-up tables, l is the track length and ϵ is the energy loss; the index i runs over the total number of steps N carried out by the particle in the considered volume, while the index j runs through all the particles, the primary and the secondary ions, travelling in the considered volume.

The Monte Carlo implementation of the two LET definitions presented above, is based on the extraction, at each step, of the electronic stopping power L, through the ComputeElectronicDEDX() method belonging to the Geant4 G4EmCalculator class. This method retrieves L from the electronic stopping power tables built at the beginning of the simulation, once the particle type, kinetic energy and material are provided. For what concerns the quantities l and ε, they are retrieved, at each particle step, through the Geant4 methods GetStepLength() and GetKineticEnergy() respectively.

As in the predecessor study [1] the averaged LET values (1)–(2), obtained from Monte Carlo simulations, were compared, as suggested in [5], with the experimental values of y_F and y_D, i.e. the frequency-mean lineal energy and the dose-mean lineal energy, described with formulas (3) and (4) respectively:

$$\bar{y}_F = \int y f(y) dy \quad (3)$$

$$\bar{y}_D = \int y\, d(y) dy \quad (4)$$

where y is the lineal energy given by the formula (5):

$$y = \frac{\epsilon}{< l >} \quad (5)$$

with ϵ being the energy deposited in a sensitive volume with an average chord length <l>.

First experimental set-up: the SOI microdosimeter measurements

In the first campaign of measurements the experimental set-up was based on a SOI microdosimeter developed at the CMRP at the University of Wollongong, Australia [3].

The irradiation set-up was realized at the 0° beam line of the LNS laboratories. The ion beam, accelerated by the cyclotron at 62 MeV/n, was passing through a 15 um tantalum foil, then, after exiting the vacuum pipe to air through a kapton window, it was passing through the modulator, consisting of a Ridge filter positioned 40 cm downstream of the vacuum-air extraction point. Then, after crossing the standard monitor chambers of the beam-line, the ion beam was passing through a PolyMethylMethAcrylate (PMMA) slab. At last the ion beam was encountering the SOI microdosimeter. Different thickness of the PMMA slab were used in order to reproduce different positions along the Bragg peak.

Second experimental set-up: the nano-TEPC measurement

In the second campaign of measurements, the experimental set-up was based on a low-pressure avalanche-confinement TEPC capable of simulating tissue-equivalent sites down to the nanometer region. This detector was designed and assembled at INFN-LNL [4].

Also in this case the irradiation set-up was realized at the 0° beam line of INFN-LNS. This time the modulator consisted of a single Ripple filter, positioned 10 cm downstream of the vacuum-air extraction point. The PMMA slab was positioned with its end 160.5 cm downstream of the Ripple filter. At last the TEPC was positioned 9.5 cm downstream of the PMMA slab end. Also in this case different positions along the Bragg peak were reproduced through different thickness of the PMMA slab.

RESULTS

The experimental measurement campaigns were carried out by collecting several microdosimetric spectra in as many depths along the pristine peak and along the SOBP for the following ions: ^{4}He, ^{12}C and ^{16}O. The experimental dose values were measured with a Markus chamber (see Figure 1). The average LET values and their corresponding microdosimetric quantities were determined and compared (see Figure 2).

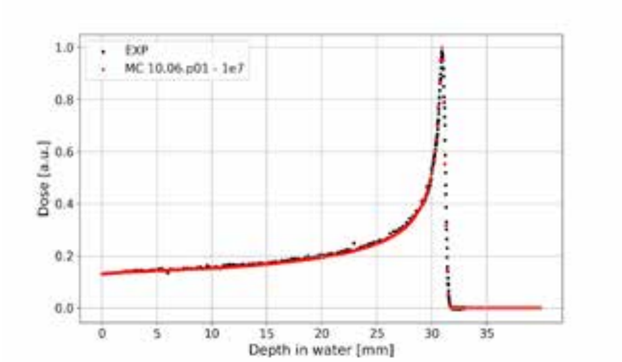

Figure 1: Depth dose profile for pristine ^{4}He peak of the first measurement campaign: in black the experimental values obtained with a Markus chamber and in red the Geant4 Monte Carlo results.

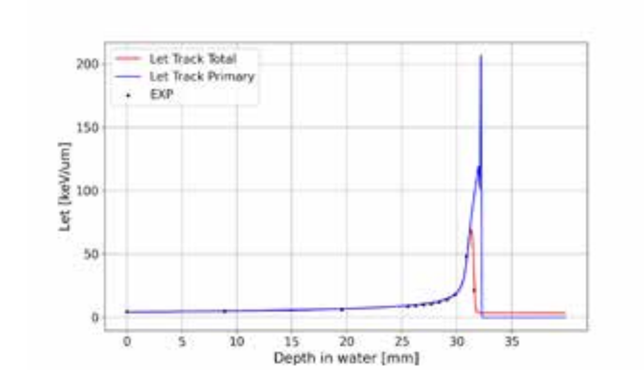

Figure 2: Comparison between the L_t^{Total} and y_F for the pristine peak of the first measurement campaign.

CONCLUSIONS

The results of this study certify the use, even in the case of ions, of a very powerful tool for precise LET calculation, given by a Monte Carlo approach that has the advantage of allowing detailed tracking of nuclear interactions even in complex clinical scenarios.

REFERENCES

[1] G Petringa et al (2020) Phys. Med. Biol. 65 235043 https://iopscience.iop.org/article/10.1088/1361-6560/abaeb9

[2] S. Agostinelli. et al. (2003), Nuclear Instruments and Methods in Physics Research A 506: 250–303..

[3] L Tran et al 2017 Med. Phys. 44 60285–6095 .

[4] D Mazzucconi et al (2019) Radiation Protection Dosimetry 183 5238145 .

[5] M A Cortés-Giraldo and A Carabe (2015) Phys. Med. Biol. 60 2645.

Monte Carlo implementation of new algorithms for the averaged-dose and -track Linear Energy Transfer evaluation in 62 MeV clinical proton beams

G. Petringa[1,2], L. Pandola[2], S. Agosteo[3,4], P. Colautti[5], V. Conte[5], G. Cuttone[2],K. Fan[6], Z. Mei[6], A. Rosenfeld[7], A. Selva[5], G.A.P. Cirrone[2]

1) ELI-Beamlines, Institute of Physics (FZU), Czech Academy of Sciences, Prague, Czechia.
2) Istituto Nazionale di Fisica Nucleare - Laboratori Nazionali del Sud (INFN-LNS), Catania, Italy.
3) Politecnico di Milano, Dipartimento di Energia, Sezione di Ingegneria Nucleare, Milano, Italy
4) Istituto Nazionale di Fisica Nucleare, Sezione di Milano,Milano, Italy
5) Istituto Nazionale di Fisica Nucleare - Laboratori Nazionali di Legnaro (INFN-LNL), Legnaro, Italy
6) Institute of Applied Electromagnetic Engineering,Huazhong University of Science and Technology
7) Centre for Medical Radiation Physics, University of Wollongong, NSW 2522, Australia

Abstract - We exploited the power of the Geant4 Monte Carlo toolkit to study and validate new approaches for the averaged Linear Energy Transfer (LET) calculation in 62 MeV clinical proton beams. The definitions of averaged LET-dose and LET-track were extended, such to fully account for the contribution of secondary generated in the target fragmentation and leading to a more general formulation of LET-total. Moreover, in the new proposed strategies for the LET calculation, we minimised the dependencies with respect to the transport parameters adopted during the Monte Carlo simulations (as the production cut of secondaries particles, voxel size and the maximum steps length). The new proposed approaches were compared against microdosimetric experimental spectra of clinical proton beams, acquired at the Italian eye protontherapy facility (INFN-LNS, Catania, I) with two different detectors: a mini-TEPC developed at the Legnaro National Laboratories of the National Institute for Nuclear Physics (LNL-INFN) and a Silicon On Insulator (SOI) microdosimeter with 3D Sensitive Volumes developed by the Centre for Medical Radiation Physics of the Wollongong University (CMRP- UoW). A significant increase of LET in the entrance region of the SOBP was reported, when the contribution of the generated secondary particles was included in the calculation. This was consistent with the obtained experimental results.

INTRODUCTION

In this paper we exploited the power of the Geant4 Monte Carlo toolkit [1,2,3] to study and validate original approaches for the average LET calculation in 62 MeV clinical proton beams, extending the definition of LET-dose and L-track, such to fully include the contributions of secondaries generated in the target fragmentation and leading to a more general formulation of LET-total-dose and LET-total-track . Moreover, in the new proposed strategies for the averaged-LET calculation, we minimised the dependence of LET with respect to the transport parameters adopted during the Monte Carlo simulations (as the production cut of secondary particles, voxel size and the maximum steps length) and that represented a limitation of our previous formulations [4]. The new proposed approaches were compared against microdosimetric experimental spectra, measured at the Italian eye protontherapy facility (INFN-LNS, Catania, I) [5] with two different detectors: a mini-TEPC [6], developed at the Legnaro National Laboratories of the National Institute for Nuclear Physics (LNL-INFN) and a Silicon On Insulator (SOI) microdosimeter with 3D Sensitive Volumes developed by the Centre for Medical Radiation Physics of the Wollongong University (CMRP-UoW) [7]. The detectors responses were measured under the same experimental conditions and the entire experimental set-up was simulated in detail using the Geant4 Monte Carlo toolkit.

MATERIAL AND METHODS

Monte Carlo approaches for LET calculation

Monte Carlo allows for a precise calculation of the ratio between the total energy deposited in a volume and the corresponding total track lengths of all interacting particles in that volume, the latter representing the main ingredients for a general and rigorous LET evaluation. For the purposes of this work, we extracted from the Geant4 look-up tables the value of the total electronic stopping power, from now on indicated with Li. The four LET definitions were implemented in the Monte Carlo algorithm using the following formulas, each applicable in any given volume of any arbitrary size:

$$\bar{L}_d = \frac{\sum_{i=1}^{N} L_i \varepsilon_i}{\sum_{i=1}^{N} \varepsilon_i} \qquad (1)$$

$$\bar{L}_d^{Total} = \frac{\sum_{j=1}^{n} [\sum_{i=1}^{N} L_i \varepsilon_i]_j}{\sum_{j=1}^{n} [\sum_{i=1}^{N} \varepsilon_i]_j} \qquad (2)$$

$$\bar{L}_T = \frac{\sum_{i=1}^{N} L_i l_i}{\sum_{i=1}^{N} l_i} \qquad (3)$$

$$\bar{L}_T^{Total} = \frac{\sum_{j=1}^{n} [\sum_{i=1}^{N} L_i l_i]_j}{\sum_{j=1}^{n} [\sum_{i=1}^{N} l_i]_j} \qquad (4)$$

The Mini-TEPC detector

The Mini-TEPC detector An upgraded version of the mini-TEPC was recently developed at LNL, can work without continuous gas flow. After proper cleaning procedure (high vacuum pumping plus gas-washing) the detector was filled with propane at a pressure of 45.4 kPa at 21.8 C. The water-equivalent was evaluated by taking into account the mean ratio of the mass-stopping powers of protons in propane and water.

The Micro-Plus probe detector

The MicroPlus probe detector was developed at the CMRP of the University of Wollongong, Australia [8]. It was realised by fabrication of 3D sensitive volumes array of cylindrical shape with each of size similar
to biological cells and fabricated on a silicon-on-insulator (SOI) wafer with a 10 m thick silicon active volume. Additional details on the MicroPlus microdosimeter technology can be found elsewhere [9,10].

RESULTS

Experimental microdosimetric spectra were measured placing the two detectors, at thirteen positions along the Spread-Out Bragg Peak (1.37 mm, 8.40 mm, 15.5 mm, 17.64 mm, 18.33 mm, 19.00 mm, 22.50 mm, 27.20 mm, 28.61 mm, 29.31 mm, 29.66 mm, 30.01 mm and 30.36 mm of water). Equations 5 and 6 were applied to calculate the mean lineal energy values yF and yD for both detectors. The resulting yD was then compared with the simulated LET-dose and the results were reported in Figure 1. In the same plot the corresponding measured and simulated depth dose curve and the simulated proton fluence evolution with depth are shown.
Similarly, the experimental yF was compared with the LET-track (Figure 2). It can be noted that yD curve presented a similar trend with depth as the LET-dose for both detectors.

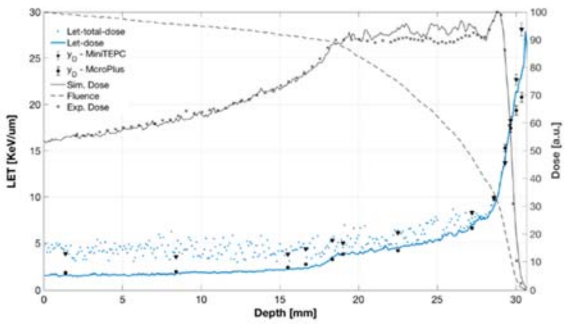

Figure1

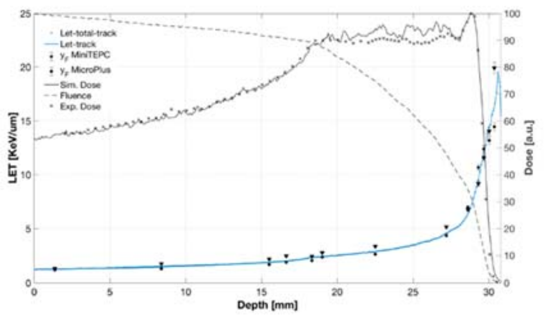

Figure2

CONCLUSION

The main achievement of this work is the implementation, characterization, and experimental verification of new algorithms for the calculation of the averaged LET-dose and LET-track, based on Monte Carlo simulations.
The major novelties lie in the new weighting approach that was adopted in the LET formulation. The calculation is now able to fully take into account the nuclear target fragmentations entailing the production of light ions, whose contribution is not negligible in the entrance region of a proton clinical Bragg peak curve.
This resulted in an increase of LET-total-dose and LET-total-track by a factor of three and 3%, respectively,
in comparison with LET-dose d and LET-track in the entrance region of the SOBP.

REFERENCES

[1] Agostinelli, S. et al. (2003), Nuclear Instruments and Methods in Physics Research A 506: 250–303.
[2] Allison, J., Amako, K., Apostolakis, J. et al. (2006). IEEE Trans. Nucl. Sci. 53: 270–278.
[3] Allison, J., Amako, K., Apostolakis, J. et al. (2016)., Nucl. Instrum. Methods A 835: 186–225.
[4] Romano, F. & other (2014), Phys Med Bio 59(12):
[5] Cirrone, G. et al. (2005), IEEE Transaction Nuclear Science 52: 1756–5
[6] Conte, V. & other (2019)., Phys Med 64: 114–122.

[7] Tran, L. & other (2017), Med Phys 44(11): 60285–6095.
[8] Anderson, S. & other (2017)., Med Phys 44(11): 6029–6037.
[9] Tran, L. & other (2017)., Med Phys 44(11): 60285–6095.
[10] Rosenfeld, A. (2015), NIM A. 809.

A beamline for ocular melanoma treatment: the collaboration between the BEST-cyclotron and INFN-LNS

G. Milluzzo[1], R. Catalano[1], G. Petringa[1], G. Cuttone[1], G.A.P. Cirrone[1], L. Piazza[2]

1) Istituto Nazionale di Fisica Nucleare, Laboratori Nazionali del Sud, via Santa Sofia 62 Catania (Italy)
2) BEST Company, BEST Cyclotron, Vancouver, Canada

Abstract- Recently, a 2-years collaborating contract has been signed between the INFN-LNS and the BEST Cyclotron company to build a new dedicated Proton Therapy passive beamline for the eye-tumor treatment with the 70 MeV protons accelerated from a BEST Cyclotron. The beamline components designed by the LNS-INFN and the complete Monte Carlo Geant4 simulation of the beam transport are shown in the present report.

INTRODUCTION

In Italy, the first protontherapy facility, the Centro di AdroTerapia e Applicazioni Nucleari Avan- zate (CATANA), was built in Catania, at the Istituto Nazionale di Fisica Nucleare-Laboratori Nazionali del Sud (INFN-LNS) [1]. Here the 62-MeV proton beam produced by a Superconducting Cyclotron (SC), is used for the treatment of ocular tumors like uveal melanoma. Thanks to great experiences gained over the years from the researchers at INFN-LNS, recently a collaborative research project was established between the Medical Physics Group of INFN-LNS and the BEST Theratronics LTD company for the joint development and the commercialization of a new Proton Therapy beamline for the treatment of eye tumors with the 70 MeV protons provided by the commercial BEST Cyclotron.
A passive proton beamline is currently being designed at INFN-LNS and will be soon realized in close collaboration with the company. The project which started in 2020, will end in 2022, with the realization of two protontherapy beamlines: one will be installed at the INFN-LNS and one will be commercialized by the BEST company. A complete Monte Carlo Geant4-based application has been also developed in order to provide a support during the design phases for the definition of the beamline components and materials. The simulation has been also useful to predict the beam characteristics at the isocentre and to verify the clinical parameters of the beam.

BEAM LINE COMPONENTS

The beamline structure has been established in order to assure a good quality of the beam, in terms of dose homogeneity and energy spectrum, at the irradiation point. As in the CAANA beamline, the proton beam will exit in air through a flanged 100 um Kapton window placed at the entrance of the beamline.
Just before the window, a secondary emission monitor (SEM) made of 15 um thick Ta foil will be placed in order to provide a real-time relative monitoring of the beam current: the secondary electrons produced when the primary beam traverses the foil, generate a signal which is proportional to the beam current.
The passive components composing the beamline are listed below:

- A double scattering system composed by the first in-vacuum 15 um Ta foil and a second tantalum 25 um thick foil placed in air at about 20 cm from the kapton window. A 9 mm thick 6 mm diameter brass cylinder will be attached at the center of the second tantalum foil to stop the central part of the beam and improve the final dose transversal profiles.
- Remotely controlled range shifter for energy tuning. The primary beam energy will be varied using different thicknesses of PMMA range shifters according to the thickness of the tumor to be treated.
  Usually, the medical physicist needs to manually replace the range shifter for each patient, which leads to a consequent increase in his/her exposure to the possible activation of the touched materials. Possible solution to make the change of the range shifter along the beam line remotely controlled are currently under investigation as the one reported in [2].
- Modulator wheel for depth-dose profiles. The most used technique to obtain a Spread-Out Bragg Peak (SOBP) is based on the use of a modulator wheel, made of PMMA and consisting of a big number of steps of different thicknesses. The SOBP is built superimposing many pristine Bragg peaks of different energy generated by the interaction of the primary beam with the different thickness of the modulator.
- Brass final collimator. A final 9 mm thick brass collimator of different diameters and shape will be used to define the final transversal shape and profile of the beam.

MONTE CARLO GEANT4 SIMULATION OF THE BEAM CHARACTERISTICS

A dedicated Monte Carlo simulation based on the Geant4 toolkit has been developed, reproducing all the passive elements composing the BEST beamline. The geometry of the beamline has been also added in the official Geant4 advanced example "hadrontherapy" as optional transport beam line which can be selected from the user by macro commands.

The proton source, as accelerated from the BEST cyclotron has been used as input of the simulation to predict the final dose distributions at the irradiation point. The source characteristics are reported in the table 1.

Table1. Input beam characteristics.

	Best Cyclotron source parameters
Energy	70 MeV
Energy spread (sigma)	300 KeV
Spot dimension (FWHM)	3 mm
Spatial distribution type	Circular
Angular distribution type	Gaussian
Angular divergency	~ 0.16 ° (sigma)

The proton energy spectrum resulting downstream the beamline, i.e. at 8 cm in air from the last collimator and without any range shifter and modulator, is shown in figure 1. A gaussian energy distribution with a centroid of 66.3 MeV and a standard deviation 0.4 KeV was calculated.

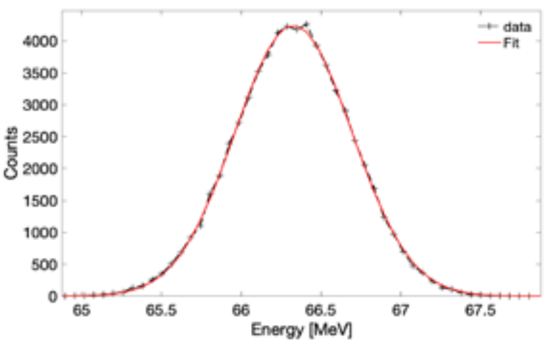

Figure 1. Proton energy spectrum at the isocentre.

The transversal dose profile and beam shape was also evaluated by simulating a water phantom at the isocentre and considering a 25 mm diameter final collimator as shown in figure 2.

The beam parameters, such as the lateral penumbra, the homogeneity and the beam symmetry, have been evaluated as reported in table 2 to verify that the clinical tolerances recommended from the TRS 398 [3] for the treatment of tumors, were achieved.

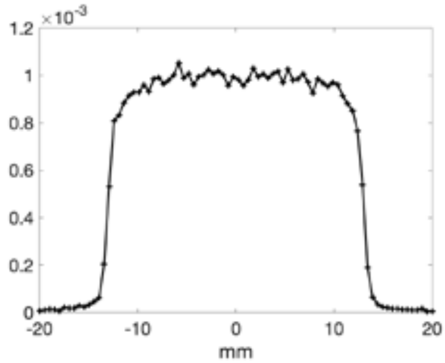

Figure 2. Dose transversal distribution at the isocentre.

Table2. Beam parameters related to the transversal profiles along with the clinical tolerances.

Parameter	**Value**
Lateral penumbra (80%/20%) (<1 mm)	1 mm
H (W90%/50%) (0.9)	0.9
Beam symmetry Sr (<3%)	0.52%

CONCLUSIONS

New solutions are currently under investigation for making the beamline as compact and automatic as possible as for instance for what concern the modulation and the degradation section of the beam line. Moreover, in order to open to the possibility to use the beam line with high-dose rate proton beams (>40 Gy/s in the so-called flash regime) the implementation of an innovative ionization monitor chamber for the relative dosimetry along the beam line which would allow correcting for the ion recombination effect due to the high-dose rate, is currently under discussion.

REFERENCES

[1] G.A.P. Cirrone et al., IEE Nuclear Science Symposium Conference Record, 2003, 3, pp. 1756-1758, J2-5

[2] Agapov, A.V., Mitsyn, G.V. & Shipulin, K.N. An Automated Range Shifter for Proton Radiotherapy. *Biomed Eng* **50,** 266–269 (2016). https://doi.org/10.1007/s10527-016-9635-x

[3] Absorbed Dose Determination in External Beam Radiotherapy: An Interna- tional Code of Practice for Dosimetry based on Standards of Absorbed Dose to Water, IAEA TRS-398

Gamma-Ray Counters for the MICADO Project

F. Longhitano[1], P. Finocchiaro[1,2], L. Cosentino[1], M. Giuffrida[1,2], S. Lo Meo[3], A. Pappalardo[1,†] and G. Passaro[1]

1) INFN Laboratori Nazionali del Sud, 95123 Catania, Italy
2) Centro Siciliano di Fisica Nucleare e Struttura della Materia, 95123 Catania, Italy
3) ENEA Centro Ricerche, 40129 Bologna, Italy
† Current address: Extreme Light Infrastructure Nuclear Physics, 077125 Magurele, Romania

Abstract – A goal of the MICADO Euratom project is to monitor the gamma-rays emitted by radioactive waste drums in storage sites on a medium to long term basis. For this purpose, 36 low-cost gamma-ray counters, based on a scintillating fiber and silicon photomultiplier, named SciFi, were designed and built to act as a demonstrator. These detectors have been tested with a ^{22}Na, ^{137}Cs and AmBe source, and the results are shown.

INTRODUCTION

The MICADO (Measurement and Instrumentation for Cleaning and Decommissioning Operations) Euratom (EU) project is aimed at the full digitization of low-level and intermediate-level radioactive waste management [1].

We have produced and characterized, with ^{22}Na, ^{137}Cs and AmBe sources, 36 detectors devoted to the gamma radiation based on a scintillating fiber readout at each end by a silicon photomultiplier, assembled in a robust arrangement in the form of 80 cm long pipes, named SciFi [2]. These detectors are compact, reasonably inexpensive, robust, easy to use and reliable to meet the objectives of the MICADO project.

THE DETECTOR

To monitoring the gamma radiation coming from the radioactive waste drums (height 76 or 88 cm), we opted for a simple and robust design of the detectors. The scintillating fiber was allocated inside a 2 cm diameter and 1 mm thick aluminium pipe and held in place by two cylindrical holders designed to host a circular PCB with the SiPM and its support circuitry. The holder has a central hole to allow for fiber-to-SiPM alignment and optical coupling by means of a tiny grease drop, and two side grooves to allow for the passage of cables. Two light-tight rubber caps complete the setup, with three cables coming out of one single side of detector for the common voltage bias and the two output signals. A sketch and three pictures of the SciFi detector components are shown in Figure 1.

The operating principle is the following: whenever a gamma-ray interacts with the fiber it deposits a variable amount of kinetic energy, mainly due to the Compton effect, which gives rise to a short flash of scintillation light. A fraction of the scintillation photons is trapped into the fiber and propagates toward both ends. If the number of these photons is large enough to produce a signal above a predefined threshold simultaneously on both fiber ends, such a coincidence event is considered as the detection of a gamma-ray and can be counted.

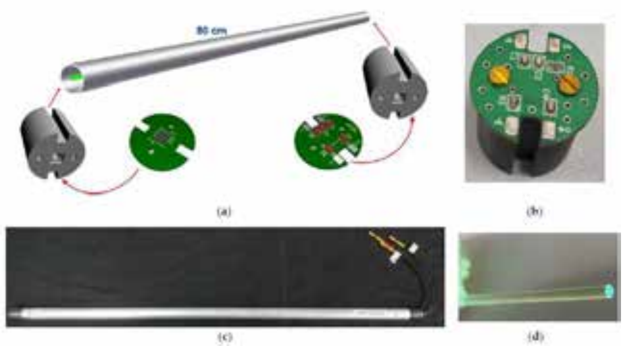

Figure 1: (a) Sketch of the components of the SciFi detector assembly. (b) A fiber holder with the SiPM PCB in place. (c) A detector fully assembled. (d) A 3 mm diameter fiber.

The chosen SiPM for these detectors, after careful evaluation and testing, is the MicroFC-30035-SMT, produced by ON Semiconductor [3]. For all the tests described we made use of a homemade voltage amplifier (200x gain and 4 GHz bandwidth). The SiPM bias was set at a 2.5 V overvoltage, i.e., 27 V bias. We decided to use a threshold at 175 mV that corresponds to ≈3.5 photons and reduces the noise rate by three orders of magnitude down to about 350 counts per second. As the signals have a duration of about 30 ns, a duration of 100 ns for the coincidence window between the two SiPMs makes the probability of spurious coincidences negligible.

The chosen scintillating fiber, after GEANT4 simulation, evaluation and testing, is the 3mm diameter BCF-20 produced by Saint Gobain [4].

MEASUREMENT RESULTS

To characterize the detectors, we made several tests with standard laboratory gamma sources and a high activity gamma and neutron source. The electronic setup was very simple: the outputs of the SiPM amplifiers were connected to two discriminators, with threshold equal to 175 mV. The two logic outputs were used as inputs to a coincidence unit with a 100 ns window, and the final output was sent to a counter.

To validate the detector behaviour was performed by means of a pointlike ^{22}Na source of activity A = 42±2 kBq which emits gamma-rays of 1274 keV. The source was placed at several distances from the fiber, in the range of few centimeters, and the number of detected gamma-rays was recorded. The observed count rate as function of the distance r between the point-like ^{22}Na source and the 3 mm diameter fiber with 1/r fit is shown in Figure 2.

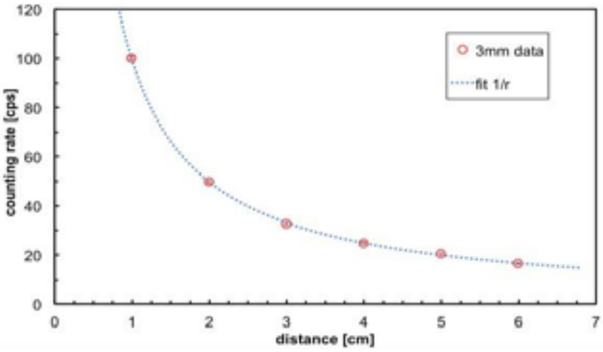

Figure 2: Measured count rate vs distance between the point-like ^{22}Na source and the 3 mm diameter fiber.

To verify the uniformity of the response within the set of 36 SciFi detectors, we have used ^{137}Cs gamma source, with activity A = 1.49±0.07 Mbq, and a detector holder that kept the mid-point of the fiber at a distance d = 52 cm from the source. The counting rate of each detector was measured in 200 s, as well as the background rate and the signal-to-background ratio, and the results are plotted in Figure 3.

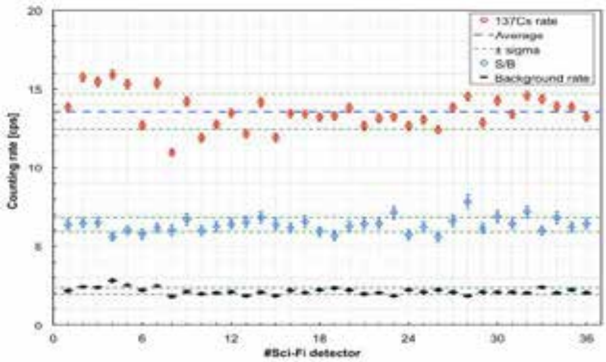

Figure 3: The counting rate measured with the ^{137}Cs, the background rate and the signal-to-background ratio of the 36 SciFi detectors.

A realistic setup resembling the emission from a radwaste drum was employed for a series of tests of the SciFi detectors. We made use of an intense AmBe neutron source, installed in an experimental hall at INFN Laboratori Nazionali del Sud (LNS), which also emits 59 keV gamma-rays. All the SciFi detectors were tested on top of the source box, and the measured counting rate, the background and the signal-to-background ratio are reported in Figure 4.

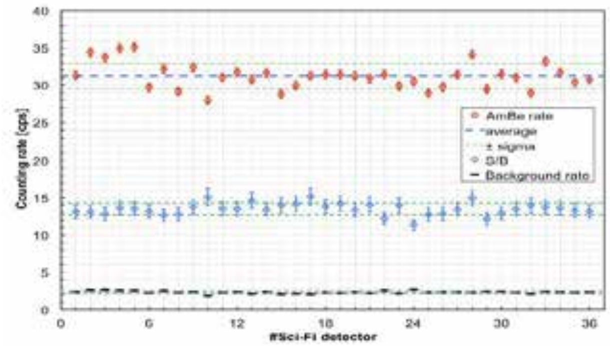

Figure 4: The counting rate measured on top of the AmBe source box, the background rate and the signal-to-background ratio of the 36 SciFi detectors.

For each detector we calculated the ratio between the observed counting rates respectively with the ^{137}Cs and the AmBe sources. The results, plotted in Figure 5, indicate a quite reasonably constant behaviour of this ratio.

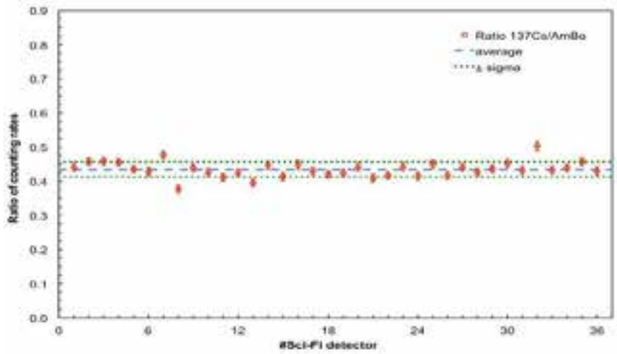

Figure 5: Ratio between the observed counting rates respectively with the ^{137}Cs and the AmBe sources.

CONCLUSION

The simulations, tests, and measurements that we have performed demonstrate that the SciFi detector technology is a good candidate for gamma radiation monitoring of radioactive waste. The 36 detectors that we built have a reasonably uniform behaviour, considering their robustness, low cost, and simple construction based on commercial components. We are now planning to test them soon in a real radwaste storage site in the framework of the MICADO project.

REFERENCES

[1] MICADO Project https://www.micado-project.eu/

[2] Cosentino, L. et al. Gamma-Ray Counters to Monitor Radioactive Waste Packages in the MICADO Project. Instruments 2021, 5, 19. https://doi.org/10.3390/instruments5020019

[3] ON Semiconductor https://www.onsemi.com/products/sensors/silicon-photomultipliers-sipm

[4] Saint Gobain Scintillating Fibers. Available online: https://www.crystals.saint-gobain.com/products/scintillating-fiber

SiLiF Neutron Counters for the MICADO Project

F. Longhitano[1], P. Finocchiaro[1,3], L. Cosentino[1], Q. Ducasse[2], M. Giuffrida[1,3], S. Lo Meo[4], C. Marchetta[1], A. Massara[1], A. Pappalardo[1,†], G. Passaro[1] and S. Russo[1,3]

1) INFN Laboratori Nazionali del Sud, 95123 Catania, Italy
2) CEA, DES, IRESNE, Nuclear Measurement Laboratory, Cadarache, F-13108 Saint-Paul-lez-Durance, France
3) Centro Siciliano di Fisica Nucleare e Struttura della Materia, 95123 Catania, Italy
4) ENEA Centro Ricerche, 40129 Bologna, Italy
† Current address: Extreme Light Infrastructure Nuclear Physics, 077125 Magurele, Romania

Abstract - In the framework of the MICADO project, aimed at the full digitization of low and intermediate level radioactive waste management, a set of 32 solid state thermal neutron detectors named SiLiF has been built and characterized. These detectors were extensively tested with an AmBe neutron source, and the results show a quite uniform and reproducible behaviour.

INTRODUCTION

In the framework of the MICADO (Measurement and Instrumentation for Cleaning And Decommissioning Operations) European Union (EU) project [1], whose goal is to establish new, fully digital assessment and management of low and intermediate level radioactive waste, we have produced and characterized a full set of detectors suitable for monitoring neutrons. In particular, the goal is to set up a granular radwaste monitoring system to be used during the final MICADO demonstration [2]. The proposed system for online real time monitoring consists of an array of many radiation sensors to be deployed all around a number of radioactive waste drums, in order to collect counting rate data in real time and to make them available to a software platform, under development, named DigiWaste. These detectors must be compact, reasonably inexpensive, robust, easy-to-use and reliable [3-4].

THE DETECTOR

Semiconductor detectors, e.g., silicon diodes, can be used in combination with a neutron reactive film, usually made of ^{6}Li or ^{10}B and called neutron converter. Such a film converts thermal neutrons into charged particles which are then detected by the silicon diode. The cross section at thermal neutron energy decreases with the inverse of the neutron velocity. In such a scheme fast neutron can also be detected by surrounding the detector with a suitable moderator box, typically made from polyethylene, which slows neutrons down to thermal energy. The ^{6}Li, following neutron's capture, has a unique decay channel with no gamma rays emitted and with high kinetic energy, and decays into easy-to-detect particles [5]. Since ^{6}Li is chemically very reactive we decided to employ ^{6}LiF, a stable salt enriched at 95% in ^{6}Li, that can be deposited by evaporation onto a suitable substrate. Instead of the direct deposition onto the silicon diode we chose to use independent detector and converter, which allows a better modularity and reconfigurability [6].

The detector configuration, shown in Figure 1, consists of the double sided silicon diode MSX09-300 sandwiched between two ^{6}LiF converter layers deposited onto carbon fiber substrates.

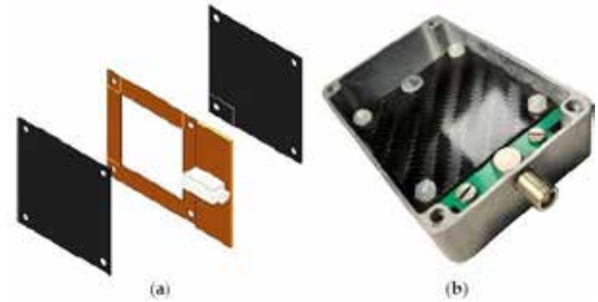

Figure 1: (a) The SiLiF detector arrangement; (b) a real detector assembled inside its aluminium box.

To increase the detection efficiency for faster neutrons one makes use of a moderator. For our purposes we concentrated on the optimization of the moderator for neutrons with energy ranging from thermal to a few MeV. The moderator of 4 cm thickness, shown in Figure 2a, gave the best results and was replicated in 32 units. The detector in its standard configuration, with 10 × 10 × 10 cm^3 size, is shown in Figure 2c.

Figure 2: (a) 3D sketch of the SiLiF detector; (b) a SiLiF hosted in a half moderator; (c) final assembling of a SiLiF.

MEASUREMENT RESULTS

To test and characterize the detectors we made use of an intense AmBe source installed in an experimental hall at the INFN Laboratori Nazionali del Sud (LNS). The source is surrounded by a first polyethylene case followed by 30 cm thick paraffin that slow down the high energy neutrons it emits.

The first set of measurements that was performed was a preliminary check that the detectors were operational and behaved as expected. Each detector in turn, inside its moderator, was placed on a small cart and positioned in front of the source just out of the box with the open door (Figure 3a). A final test was performed using simultaneously 16 detectors aimed at measuring a low intensity flux of fast neutrons. To this purpose the detectors were arranged in a square 4 × 4 array in the top position upon the neutron source box (Figure 3b). The detector was biased at 50 V, in order to operate in full depletion regime and be sensitive on both faces. A charge preamplifier, with a nominal gain of 25 mV/MeV, connected to a spectroscopy amplifier whose output was sent to an Amptek MCA8000A multichannel analyzer was used.

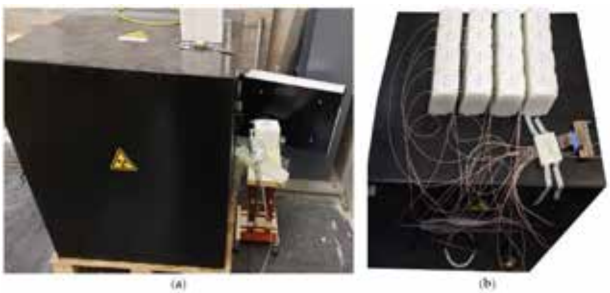

Figure 3: (a) The AmBe neutron source box with a SiLiF detector in the front position. (b) The 4 × 4 array of SiLiF detectors in the top position.

The superposition of the triton and alpha deposited energy, plus the effect of the emission from different depths/angles, produces a characteristic spectrum shape, as can be observed in figure 4, that also proves that all the detectors were working properly. The measurements were compared with Fluka [7] simulations giving an excellent agreement.

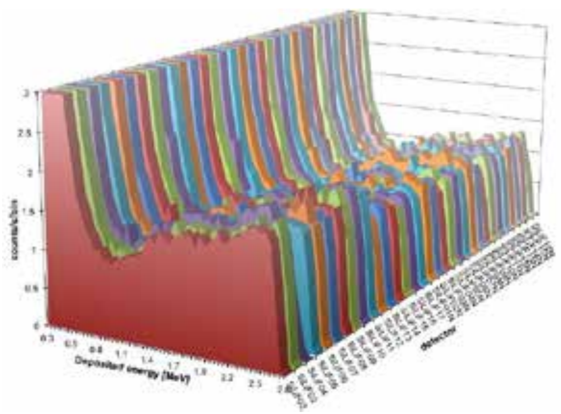

Figure 4: The characteristic spectrum shape, measured for all the SiLiF detectors in the front position

In Figure 5 the result of the final test where we compare the (a) GEANT4 simulated and (b) evaluated fluxes, and then we compare the (c) GEANT4 simulated and (d) measured counting rates. Unfortunately, due to a broken channel in the electronics, a centrally located detector did not provide useful data (white square with 0.00). It is however possible to say that the measurements have a good agreement with the simulations.

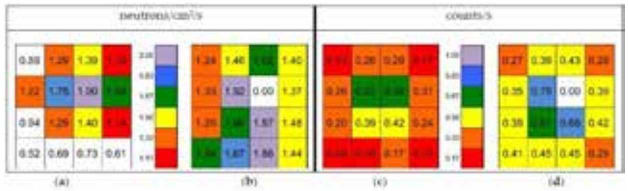

Figure 5: (a) Total neutron flux simulated in the top position in correspondence of the 4 × 4 SiLiF array; (b) The measured total neutron flux with the 4 × 4 array. (c) The simulated neutron counting rates. (d) The measured neutron counting rates.

CONCLUSION

The tests, measurements and simulations have allowed us to prove the suitability of the SiLiF technology for neutron detection. The set of 32 detectors we built proved to have a uniform behavior. We can conclude that SiLiF is quite a promising candidate for future applications for low and intermediate level radioactive waste monitoring and is going to be tested soon in a real environment within the MICADO project.

REFERENCES

[1] MICADO Project https://www.micado-project.eu/

[2] Italy in MICADO WP7. https://www.micado-project.eu/news/particles-of-italian-innovation-project/

[3] Cosentino, L. et al. SiLiF Neutron Counters to Monitor Nuclear Materials in the MICADO Project. Sensors 2021, 21, 2630. https://doi.org/10.3390/s21082630

[4] Cosentino, L. et al. Gamma—Ray Counters to Monitor Radioactive Waste Packages in the MICADO Project. Instruments 2021, 5, 19. https://doi.org/10.3390/instruments5020019

[5] Barbagallo, M. et al. Thermal neutron detection using a silicon pad detector and ^{6}LiF removable converters. Rev. Sci. Instrum. 2013, 84, 033503.

[6] Pappalardo, A. et al. Characterization of the silicon+6LiF thermal neutron detection technique. Nucl. Instrum. Methods Phys. Res. Sect. A 2016, 810, 6.

[7] Fasso, A. et al. P.R. FLUKA: A Multi-Particle Transport Code; CERN Technical Report No. INFN/TC_05/11; CERN-2005-10; 2005.

Neutron detection with different material: Study through simulations with FLUKA

A. Meli[2,3],A. Muoio[1,3], F. La Via[1,3],C.Altana[1] , G.Lanzalone[1,4],S.Tudisco[1,3]

1) INFN Laboratori Nazionali del Sud Catania Italy
2) Dipartimento di Fisica e Astronomia, Università di Catania, Italy
3) *CNR-IMM, Headquarter, Strada VII, Catania, Italy*
4) *Università di Enna "Kore",Via delle Olimpiadi , Enna, Italy*

Abstract - In theoretical and experimental studies of nuclear physics, an important role has always been played by the interaction of neutron beams with matter; in fact, being electrically neutral, they are able to overcome the Coulomb barrier and interact directly with the target's nuclei. They are fundamental for investigating the structure of matter and nuclear reactions. The investigations through simulations were carried out with the Monte Carlo software Fluka [1].

SIMULATION SETUP

A series of simulations were carried out with the following input characteristics of a parallelepipedal detector:

Material = Diamond, SiC, Silicon

Energy Neutron = 14.1 MeV

Thickness=100 – 250 – 500 um

Fluence = 4.45 10^{11} (n/cm^2)

Detector Surface = (5 x 5) mm^2

These last years the semiconductor-based detectors have received considerable attention thanks to their fast responses, low operating voltage high energy resolution and radiation resistance. Most suitable semiconductors for harsh environment applications are Silicon-Carbide (SiC) and diamond thanks to their high atomic displacement energy, that is about 20-35 eV [2] for SiC and 40-50 eV for diamond.

The high displacement threshold energy makes them more radiation resistant than the conventional semiconductors such as Silicone (Si), Germanium (Ge) and Gallium Arsenide (GaAs). Moreover, the wide-bandgap energy and low intrinsic carrier concentration over considerable range of temperature make SiC and diamond interesting for use at high temperature applications.

The results were compared as in the Figure1. From these simulations reported it is possible to observe that the interacting neutrons are much higher in diamonds with respect to SiC and Si because the scattering cross section of carbon is higher than that one of silicon.

In all the materials the interacting neutrons increase by increasing the thickness of detectors, but very thick detectors are difficult to be realized.

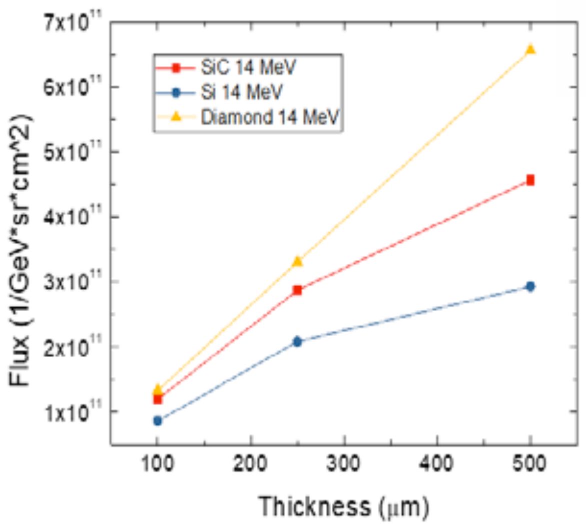

Figure 1: Neutrons Flux versus thickness for different materials (Diamond, Silicon and Silicon Carbide) at different thicknesses (100, 250 and 500 um).

Thanks to the study of the simulations described above and the study of the literature, a series of devices have been created starting from a substrate of 4H-SiC.

A thick epitaxial layer, 250 microns, was grown on this substrate and a deep characterization was performed to evaluate the quality of the epitaxial layer and the carrier lifetime across the entire layer by photoluminescence (PL) and Raman spectroscopy [3].

The results are shown in Figure 2. These values are obtained through Longitudinal Optical phonon-plasmon coupling mode (LOPC) that allows, in specific conditions, to extract carrier density and carrier mobility, after that is possible to obtain carrier lifetime.

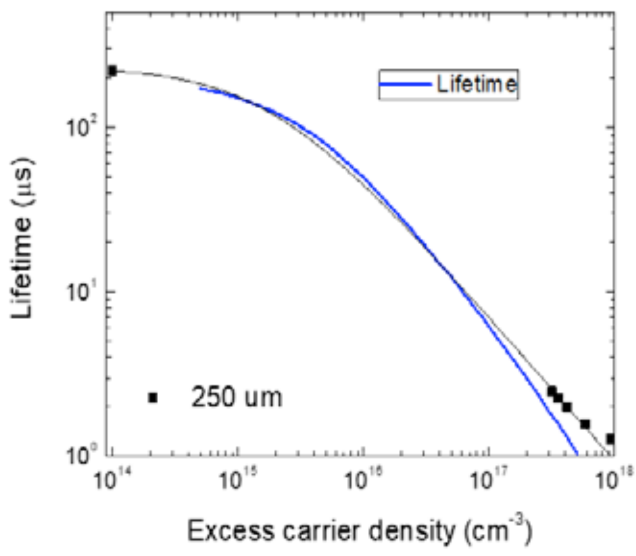

Figure 2. Lifetime as a function of carrier density at high and low injection regime (black points) compared with Kimoto et al. data at 200 us (blue line)

Based on these results, detectors have been developed that should be useful for neutron detection. The Figure 3 shows matrix of detectors fabricated on a quarter wafer of 4H-SiC.

Figure 3. The figure shows the detectors fabricated on SiC epi-layer. On the right there is a magnification carried out with a 5x objective.

Recent attempts to make SiC diodes have revealed a problem with stacking fault (SFs) defects in the epi-layer, leading to unstable devices. This kind of defect can affect strongly the performances of the devices due to the increase of the leakage current and a decrease of the carrier lifetime. In this paper [3], we studied the influence of different kind of SFs defect on carrier lifetime values through micro Raman and PL analysis on and around the defects, as shown in Figure 4.

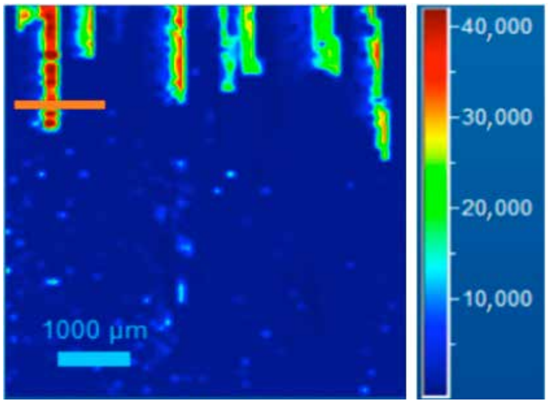

Figure 4. PL map of and isolated defect (SF at 430 nm) and is evidenced the line where the Raman analysis was done.

CONCLUSIONS

SiC is a very attractive material in the nuclear physics field. This work presents the preliminary development, from simulations to devices fabrication, and testing of SiC neutron detector prototypes; the next step will determine the optimal acquisition systems.

REFERENCES

[1] http://www.fluka.org/fluka.php.
[2] O.Obraztsova et al., EPJ Web of Conferences 170, 08006 (2018)
[3] A. Meli; A. Muoio et al. Materials **2021**, 14, 976
[4] Feng, G.; Suda, J.; Kimoto, T. Characterization of stacking faults in 4H-SiC epilayers by room-temperature microphotoluminescence mapping. *Appl. Phys. Lett.* **2008**, *92*, 221906.

SIGEDO and other IT tools for the POTLNS project

G. Vecchio[1], A. Miraglia[1], V. P. Bonanno[1], A. D. Russo[1], G. Torrisi[1], C. Manna[1], M. S. Musumeci[1]

1) Istituto Nazionale di Fisica Nucleare - Laboratori Nazionali del Sud, via S. Sofia 62, 95123 Catania, Italy

Abstract – This document describes the design and development of IT platforms able to optimize and simplify the management of the POTLNS project. They consist in IT tools aim to share information among employees of the LNS and to manage the contract procedures.

INTRODUCTION

The POTLNS project consists of refurbishing and upgrading currently LNS infrastructure devoted to the basic research in Nuclear Physics. The POTLNS project is composed of four Work Packages (WPs): the upgrade of the Superconducting Cyclotron (CS), the construction of a new system for the in-flight production of radioactive beams (FRAISE), the upgrade of MAGNEX beam transport lines required for the NUMEN experiment (MAGNEX) and the upgrade of systems, such as water system, diagnostic system and radiation monitoring system, which are transversal to the above mentioned WPs since useful for all of them (BENI COMUNI).

The Project Management Team of the LNS oversees the management of the POTLNS project making use of different tools like MS Office suite, MS SharePoint, Alfresco and a custom dynamic web site.

Microsoft Office is used to create the large project documentation and to manage activity tasks by using MS Project. The project's documentation is shared on SharePoint platform within the PM office and on Alfresco by using a custom document management system (SIstema di GEstione DOcumentale - SIGEDO) which allows to involve suppliers in the procurement phase.

POTLNS DOCUMENT REPOSITORY

The POTLNS Product Breakdown Structures (PBS) is a hierarchical structure of subprojects and systems designed to get the given assigned objectives.

Fig. 1 shows the project structure: it is possible to consult the related documents on the Alfresco repository by clicking on each PBS button.

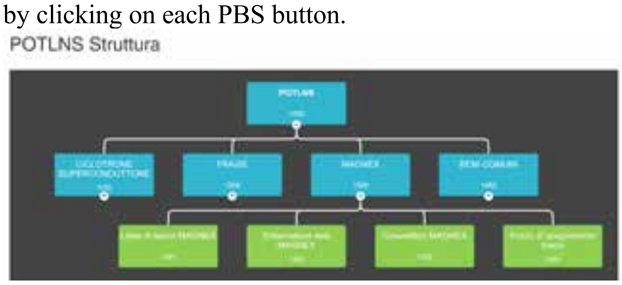

Figure 1 - PBS structure of the whole POTLNS project

Alfresco is an Enterprise Content Management (ECM) that adds a timeline for each content item and, possibly, enforces processes for its creation, approval and distribution.

A site named POTLNS [1] was created in the document repository and a folder tree has been set to follow the production and the asset management of the project.

The PBS was reproduced on Alfresco and specific permissions have been set in each folder in order to give access only to relevant information.

Each document is identified by unique ID and it is processed by a specific workflow that interprets a series of procedural rules to realize an automatic process control.

Each document uploaded on the Alfresco folder is processed by the system. If the document is compliant with the contract specification it will be approved, otherwise it will be rejected.

POTLNS DMS: SIGEDO

For each POTLNS contract, a standard procedure has been implemented for the document management. Each company uploads the required documents on the Alfresco repository where they are processed and analysed at the first by the DMS and finally by the responsible deputed to review them for each procurement procedure.

Fig. 2 shows the system architecture of the whole system. Alfresco is used to store all documents. A Java application, that runs every 6 hours, synchronizes data between Alfresco and the MySQL database. Finally, a powerful HTML5 dashboard shows the status and the overview of the document production.

Figure 2 - Details of the system architecture

Fig. 3 shows the detail of the progress of work and in particular the status of the document for each contract procedure. Every document uploaded on the Alfresco repository is highlighted in grey and then is ready for the approving process. If it is compliant with the rules, that filter the document for its code name, it is approved and it becomes green, otherwise it is rejected and marked in red.

Figure 3 - Status page for each POTLNS contract

The interactive interface permits to have a general overview of the contract and the detail of the whole document at glance.

POTLNS ACTIVITY PLANNING

The project planning is made by using MS Project. An interactive HTML5 Gantt Chart processes the MS Project data and makes an interface to share the schedules information on the project website (see Fig.4).

Figure 4 - Gantt chart of Superconducting Cyclotron activities

A wide panel, installed at the entrance of the LNS, shows activities status. A panel depiction is shown in Fig. 5 and it is available online as well [2].

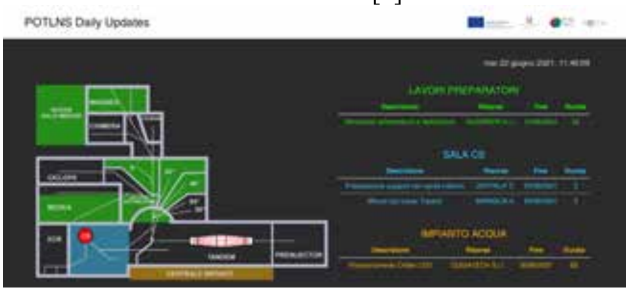

Figure 5 - POTLNS Daily updates panel

POTLNS CATALOGUE

A lot of CS and beam transport lines devices are being disassembled during the POTLNS activities, then it is necessary to catalogue each device/component and to keep track of the storing place and their movements.

Fig. 6 shows the list of devices/components that have been disassembled from the experimental rooms. The powerful search tools allow to manage all items description easily.

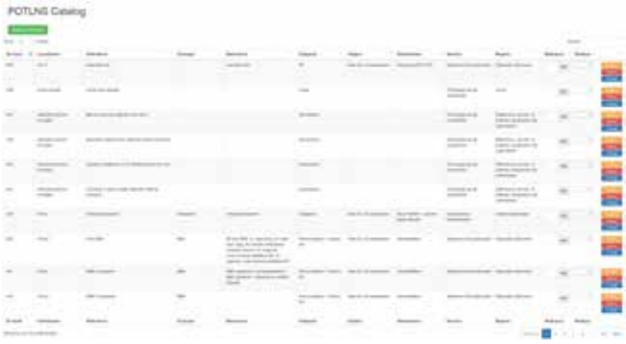

Figure 6 - Catalogue table of objects disassembled from beam lines and Superconducting Cyclotron

As an example, Fig. 7 shows the details of an object that was removed along the beam lines. The datasheet includes general references, category, type, description, brand, model, serial number, date of input and, eventually, a list of movements for that object.

Figure 7 - Detail of disassembled objects

CONCLUSIONS

These platforms, already implemented and used, have been very useful to the internal activities, by sharing the planning and the disassembling procedures and to manage the external activities such as the procurement process with SIGEDO. Moreover, it represents a powerful customizable platform for future projects similar to POTLNS.

ACKNOWLEDGMENT

The authors are warmly grateful to all the people who collaborate to the POTLNS project.

REFERENCES

[1] https://potlns.lns.infn.it/, POTLNS website.
[2] https://potlns.lns.infn.it/it/stato-avanzamento-lavori/daily-updates.html, POTLNS daily updates.

Measurements and estimations of residual activation on the concrete of experimental 20 °and 40 °rooms to be demolished

R. Leanza[1], S.Russo[1]

1) INFN-LNS

Abstract- This report discusses measurements and estimations with a Monte Carlo toolkit, FLUKA, of residual activation on the concrete of experimental 20° and 40° rooms to be demolished, following the upgrading and modification of the LNS (POTLNS).

INTRODUCTION

Following the upgrading and modification of the LNS (POTLNS), the complete disassembly of the shields in the 20° and 40° rooms, which will have a new Layout in the future, is expected. To this end, measurements and estimates of residual radioactivity were carried out on the concrete to be demolished, resulting from its irradiation to the neutron fields produced during the experiments carried out in the same rooms or the adjacent rooms throughout the operating period of the LNS accelerators.

Some measurements were carried out to verify the presence of gamma-emitting radionuclides.

Furthermore, in order to verify the expected radioactivity entity, mainly for the possible presence of pure beta-emitting radionuclides, difficult to detect with GeHP, and to confirm the measurements made for the gamma-emitting radionuclides, simulations were carried out using the code of calculation Monte-Carlo FLUKA.

GeHP MEASUREMENTS

In order to verify the presence of gamma-emitting radionuclides, were carried out measures using a highly efficient hyperpure germanium detector (GeHP). Each measurement lasted from 5 to 7 days in order to identify low activity radionuclides.

In particular, a fixed system with a low-background shield was used on concrete samples taken from the mobile screens present in the room, and measurements were also conducted on site with a portable detector placed on the floor of the rooms concerned.

The radionuclides that could be present in the concrete would derive only from the reactions of capture of environmental neutrons. The accelerated ions activation is excluded because the beams have been transported and used within the high vacuum lines and chambers.

Given the waiting time and the distribution of the experiments over the approximately 36 years of activity, only the radionuclides with the highest half-life, are conceivable. The measurements revealed only the presence of natural radionuclides in the following average concentrations: 600 Bq / kg for 40K, 40 Bq / kg, for 226Ra and 20 Bq / kg for 232Th.

MONTE CARLO SIMULATIONS

Monte Carlo simulations, with the Fluka toolkit, was used to confirm the presence of measurements made for the gamma-emitting radionuclide and determine the presence of pure beta-emitting radionuclides.
A standard "Portland" concrete was used which includes most of the elements that would normally be found in ordinary concrete, adding the presence of europium and cobalt in traces of a few ppm [ref.1].

The irradiation profiles were defined on the workloads of the rooms, from the start of the activity, in 1986, until June 2020. They correspond to the real ones, recorded by the fixed environmental detectors of the which produced an accumulated dose identical to that measured in the same points where the detectors were positioned. The spectra of environmental neutron fields are known [ref 2, 3].

Since it was impossible to carry out a single simulation that included the different beams sent to the rooms for the various experiments, we made several simulations and finally added the obtained activation values. The accumulated dose measured is the total one, it includes both the doses recorded during the experiments carried out in the same rooms where the detectors were installed and those recorded during the experiments carried out in the adjacent rooms. In this second case, the energy spectra of the neutrons incident on the detector had a slower component and a greater presence of thermals because they did not come directly from the target but by the diffusion and moderation of the walls. For greater accuracy, we divided the floor into two portions, corresponding to the 20 ° and 40 ° rooms and we made the calculations on each portion. In this way, the neutrons coming from the same room (mainly direct) from those coming from the other rooms (mainly reflected) are taken into account separately. Furthermore, as a precaution, we considered that during the overall irradiation in each room as many neutrons were produced as were those measured by the detector and accumulated during the whole period, the estimates of each portion of the floor obtained from the sum of the simulations of all the rooms are overestimated.

For 40° room, according to the types of beams received, a simulation was carried out with 12C (4+) with an energy of 8 MeV / A, cautiously selected among the lightest and most energetic ones used for the experiments, incident on a target of Tantalum, for the

Tandem beams and 62 MeV protons, incident on tantalum for the CS bundle.

Figures 1 and 2, in plan and section, show the neutron doses (H *) for the two types of beam, Tandem and CS.

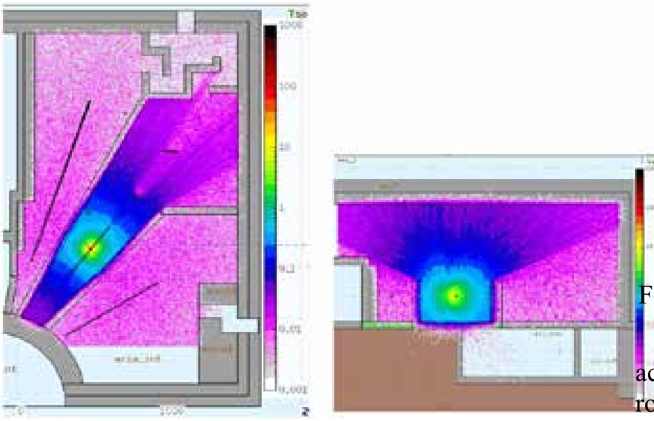

Figure 1: Neutron doses (H*), 8 MeV/A 12C, 40° room

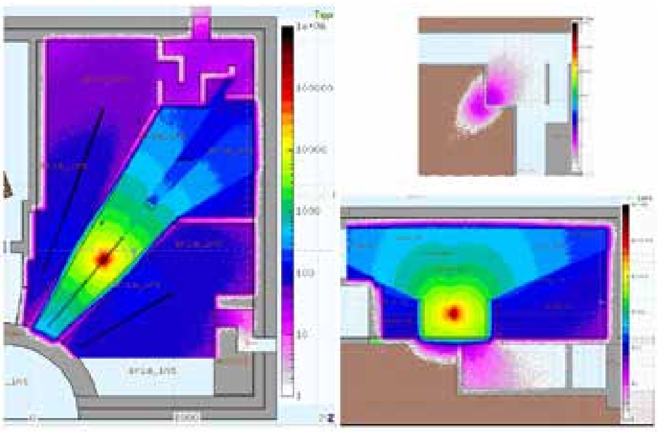

Figure 2: Neutron dose (H*), 62 MeV protons, 40° room

For 20° room until the end of 1996 it received only Tandem beams, from 1997 to 2012 it received only CS beams, and from 2013 onwards it no longer received beams, but only diffuse neutrons from the other rooms. For the Tandem beam 12C (4+) with an energy of 8 MeV / A was used, incident on Tantalum while for the CS beam a simulation was made with 12C of 62 MeV, the only type of beam used in the hall, incident on steel.

The related dose rate plots are shown in fig. 3 and 4.

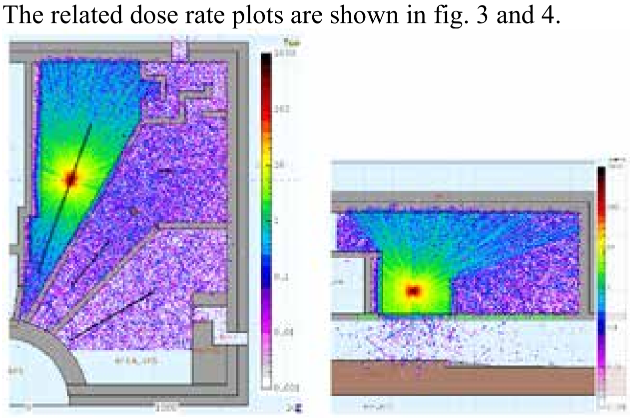

Figure 3: Neutron dose (H*), 8 MeV/A 12C, 20° room

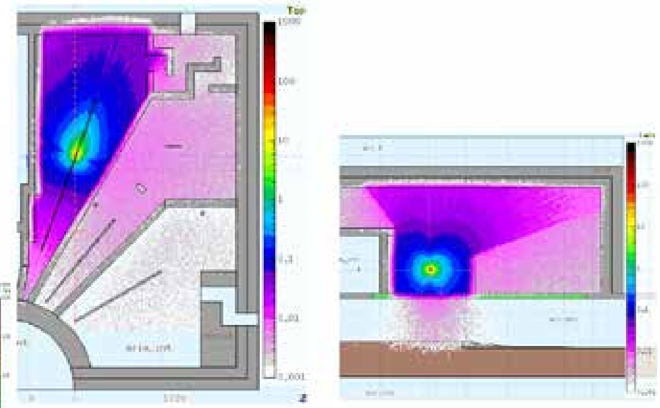

Figure 4: Neutron dose (H*), 62 MeV/A 12C, 20° room

Figure 5 and 6 show the results of the residual activation of all the simulations for the floors of the two rooms.

Figure5: Residual activation, 40° room

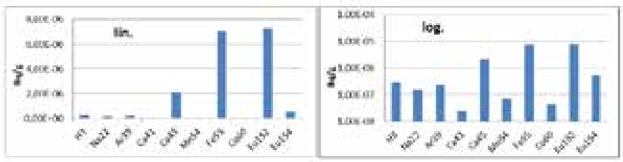

Figure6: Residual activation, 20° room

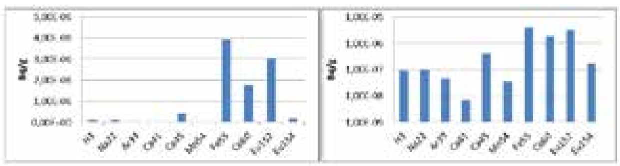

CONCLUSIONS

Both from the measurements and from the simulations, even in the worst condition of the CS beams, the concrete is in the conditions of no radiological relevance. Furthermore, considering that the neutron fields affecting the vertical structures (walls and pillars) are about three orders of magnitude lower than the fields affecting the floor, the residual activations estimated in the vertical structures will be at least three orders of magnitude lower than those of the floors.

REFERENCES

[1] Go Yoshida et al.,Journal of Radioanalytical and Nuclear Chemistry (2020) 325:801–806.

[2] R. Bedogni, et al., Nuclear Inst. and Methods in Physics Research, A, Volume 681, 2012, Pages 110-115.

[3] K. Amgarou, et al., Nuclear Inst. and Methods in Physics Research, A, Volume 654, 2011, Pages 399-405.

Residual radioactivity assessment and measurements of the dipole of the MAGNEX spectrometer

R. Leanza[1], S. Russo[1]

1) INFN-LNS

Abstract- This report discusses measurements and Monte Carlo simulations of residual radioactivity of the dipole of MAGNEX spectrometer [1].

INTRODUCTION

The radioactivity measurements and assessments are related, in particular, to vacuum chamber, upper and lower polar expansions, and some other small parts connected to them.

A complete mapping of objects was carried out in terms of ambient dose equivalent and to detect the presence of all predicted gamma emitter radionuclides.

The external exposure measurements were carried out, using a Berthold ionization chamber, TOL_F model, and a Berthold contamination meter, LB124. The residual radioactivity measurements were carried out using an ORTEC portable hyperpure germanium detector.

Furthermore, simulations were carried out with Monte Carlo code (FLUKA) to assess the possible presence of radionuclides, as pure beta emitters or difficult to measure for the low expected activities, not detectable by the others detectors.

MEASUREMENTS

External exposure

The detectors used to measure the presence of external irradiation were carried out to determine the ambient dose equivalent. A complete mapping of objects was carried out with measurements at a distance of 2-10 cm of each point of the surface. No measurement showed values above the natural background.

Residual radioactivity

An ORTEC portable hyperpure germanium detector, detective model, was used to check for the presence of any low activity gamma emitter radionuclides. Measurements of long acquisitions (10-40 hours) were carried out by placing the detector at a distance of a few cm from the points identified in figure 1.

Only in point 1, corresponding to the beam input (or the entrance to the main neutron field) was detected the presence of all predicted gamma emitter radionuclides (Mn54, Co57, Co60). Due to the complex geometry of the chamber, it is difficult to establish the exact activity of the radionuclides, but the measured values (multiplied by appropriate calibration factors) are certainly consistent with those simulated and listed in figure 2. In the other points 2, 3, 4, 5 and 6, the measurements showed no trace of gamma emitting induced radioactivity above the natural background.

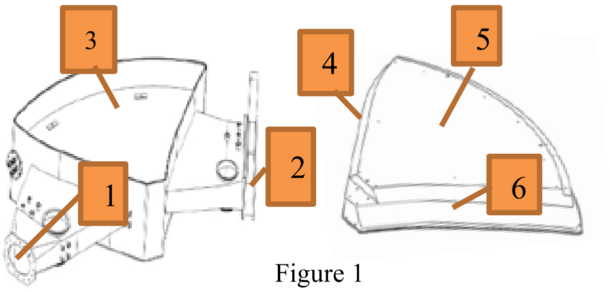

Figure 1

Measurements, with germanium in a shielded box, were also made on the small parts (flanges, valve, pressure devices) connected to the chamber and which will be shipped together with it. The measures confirmed the presence of radionuclides in the expected concentration values.

MONTE CARLO SIMULATIONS

Simulations with a Monte Carlo code (FLUKA) were carried out in order to assess the possible presence of radionuclides not detectable by the germanium resulting from the exposure of the spectrometer to neutrons produced by the interaction of the beam in the scattering chamber or in the beam dump.

For the input data of the simulations, reference was made from the typical beams and energies used in the experiments carried out during the period from 2003 to June 2020. The main starting element for the simulation was also the total neutron flux measured by the environmental monitoring systems present in the room. A single experiment was therefore simulated for the entire period of operation (about 17 years) which produced the same measured neutron field. In the end it was considered a waiting time of 6 months, from June to November 2020.

The results are given in figure 2, where total and specific activities are visible, obtained taking into account the weights and volumes of the objects.

The figure 2 show the maps of the nuclides (Z/A) and the colors show the values of the total activity in Bq.

The most present radionuclides are Fe55 (which emits only beta radiation), Mn54 and Co57. The traces of others radionuclides, present only on the chamber, are very low.

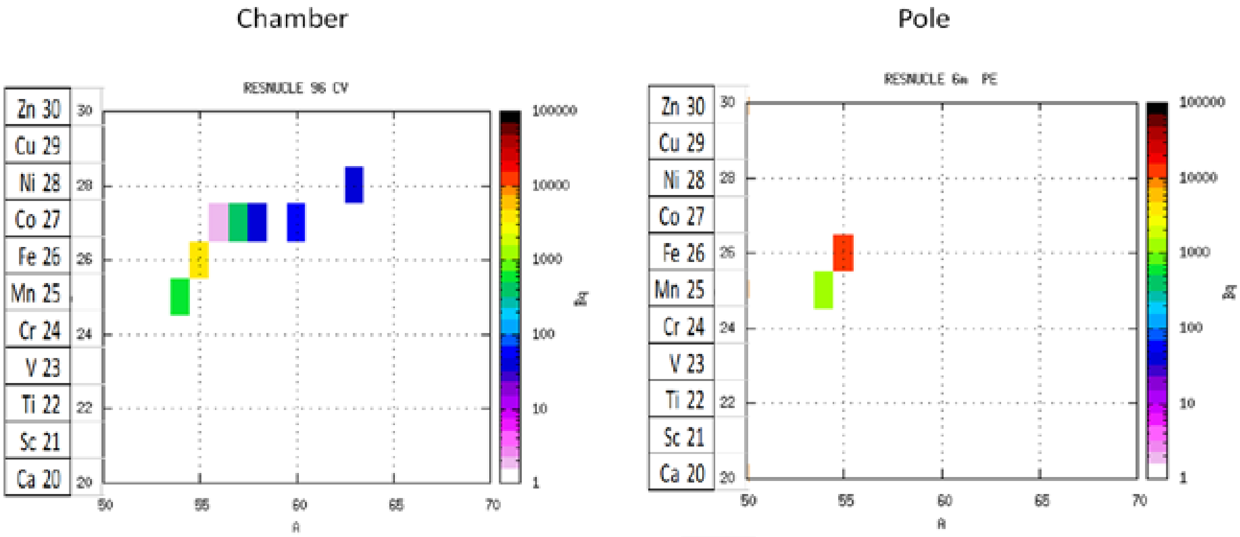

	Bq	Bq/l	Bq/g
Ni63	39,20	0,21	2,58E-05
Fe55	4.530,66	23,85	2,98E-03
Mn54	630,82	3,32	4,15E-04
Co57	316,95	1,67	2,09E-04
Co58	43,20	0,23	2,84E-05
Co60	55,20	0,29	3,63E-05

	Bq	Bq/l	Bq/g
Fe55	10.711,00	15,80	1,97E-03
Mn54	1.066,00	1,57	1,96E-04

Figure 2: Maps of radionuclides (Z/A) and the values of the total activity in Bq

The low concentration values in Bq/l (or Bq/g), taking into account large volumes and the absorption of radiation in the materials, explaining why the Germanium detector does not measure values above the background at almost all points except at the chamber entrance.

The evidence of this most active point is confirmed by the plot in figure 3, of the simulated neutron field, generated in a tipical experiment (Ne 20 beam, 15 MeV/A Energy, 10nA current) carried out on the apparatus.

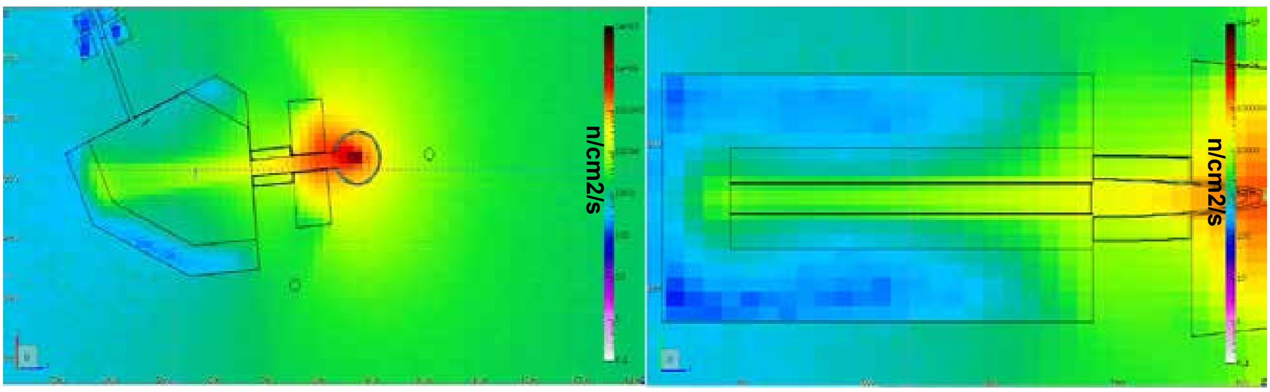

Figure3: Neutron field, Ne 20, 15 MeV/A, 10 nA

CONCLUSIONS

Both, Germanium detector measurements and Monte Carlo simulations, shown the presence of some gamma emitter radionuclides: Mn54, Co57, Co60, and the residual radioactivity, in both, is comparable. Furthermore, with Monte Carlo simulations was shown the presence of Fe55, which emits only beta radiation, not detectable by the germanium. The concentration values, in Bq/l (or Bq/g), are low taking into account the entire period of operation (about 17 years)

REFERENCES

[1] Cavallaro et al., United States: N. p., 2010. Web. doi:10.1063/1.3362574.

LAPSUS – LAboratory Plasma Spectroscopy for Ultraviolet Space

M. Giarrusso[1] on behalf of the LAPSUS team

1) INFN-Laboratori Nazionali del Sud, Catania, Italy

Abstract – We here describe the project LAPSUS (sigla ASI_INAF2018_16) funded to INFN-LNS by the Italian Space Agency in 2020, which aims to build an experimental atomic database in the ultraviolet spectral range useful to interpret astrophysical spectra acquired by space missions.

LAPSUS

LAPSUS (LAboratory Plasma Spectroscopy for Ultraviolet Space) is a project funded to INFN-Laboratori Nazionali del Sud by the Italian Space Agency in 2020 (grant "Analisi Dati, Modellistica, Analisi in laboratorio e/o su campo, Ricerca e Sviluppo" under the agreement ASI-INAF n.2018-16-HH.0 related to "Attività di Studio per la comunità scientifica nazionale Sole, Sistema Solare e Esopianeti"). The project involves reserchers from INFN-LNS, Istituto Nazionale di Astrofisica-Osservatorio Astrofisico di Catania, Università degli Studi di Catania and University of Cambridge.

High resolution spectroscopy allows to investigate astrophysical environments. The analysis of spectral lines relies on atomic data measured in laboratory, that are well known for neutral and weakly-ionised species [1]. On the contrary, experimental atomic parameters are largely missing in the case of highly-ionised species (responsible for transitions in the ultraviolet range), for which databases have to rely on theoretical calculations [2]. As a consequence most of the UV spectral lines emitted by astrophysical plasmas are unidentified, e.g. in the case of solar Corona for which 40% of the ~500 UV lines of SUMER spectra cannot be identified [3].

The lack of experimental UV atomic data is historically due to the difficulty in creating laboratory plasmas with stable high temperature conditions. Nowadays, plasmas created in magnetic traps under controlled conditions reproduce different astrophysical environments (in terms of electron density and temperature) hosting from molecular to highly-ionised species.

The goal of LAPSUS is to measure the missing atomic data by applying high resolution spectroscopy to laboratory plasma emission. For this purpose, the first step of the project is the construction of an échelle spectrograph with spectral resolution 20000 in the wavelength range 70-400 nm, to be coupled to the LNS plasma traps: the Electron Cyclotron Resonance Ion Source AISHa [4], the simple mirror machine with a flexible magnetic field configuration Flexible Plasma Trap [5] and the Microwave Discharge Ion Source Plasma Reactor [6]. By filling them with a single element at a time, the analysis of the acquired spectra will supply the atomic parameters to be included into the CHIANTI database [7].

Fig. 1 shows the spectrograph layout. The opto-mechanical design of the instrument has been completed, the design of its interface with plasma traps is under development. The spectrograph is still under construction because of the delays due to the pandemic.

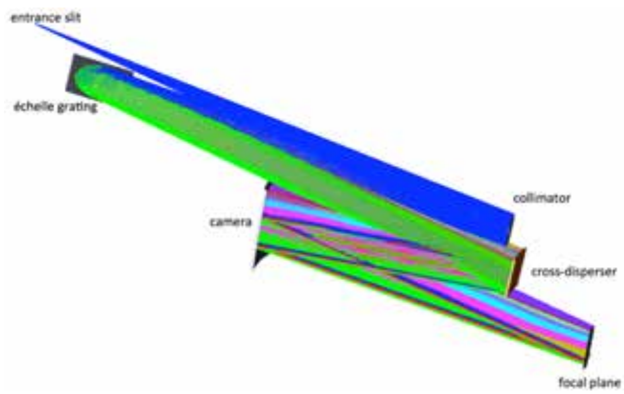

Figure 1: LAPSUS spectrograph layout.

REFERENCES

[1] F. Kupka et al., A&AS 138 (1999) 119
[2] F. C. Bruhweiler, Highlights of Astronomy 9 (1992) 553
[3] W. Curdt et al., A&A 427 (2004) 1045
[4] L. Celona et al., Review of Scientific Instruments 90 (2019) 113316
[5] S. Gammino et al., Jour. Instr. 12 (2017) P07027
[6] G. Castro et al., Plasma Sources Sci. Technol. 26 (2017) 055019
[7] G. Del Zanna et al., A&A 582 (2015) A56

Radiosensitivity of uveal melanoma cells to photons and protons

O. Keta[1], Petković[1], G. Petringa[2,3], G.A.P. Cirrone[2], F. Cammarata[4], L. Minafra[4], G. Cuttone[2], I. Petrović[1], A. Ristić-Fira[1]

1) Vinča Institute of Nuclear Sciences, University of Belgrade, Belgrade, Serbia

2) Istituto Nazionale di Fisica Nucleare, Laboratori Nazionali del Sud, Catania, Italy

3) ELI-Beamlines, Institute of Physics (FZU), Czech Academy of Sciences, Prague, Czechia

4)National Research Council (IBFM-CNR), Cefalù, Italy

Abstract – Even though protons show several benefits for the therapy of ocular tumors, the application of a single RBE value in eye treatment planning is still questionable and requires further investigation. In this work, the effects of protons were experimentally measured on 92.1, a specific uveal melanoma cell line. The chosen irradiation position was the middle of the 62 MeV therapeutic Spread-Out Bragg Peak. The normal, ARPE-19 retinal cells were also used to assess the behaviour of healthy tissue exposed to irradiation. Cells were irradiated with single doses ranging from 1 to 6 Gy, and the clonogenic assay was adopted to evaluate cell survival after irradiation. The radiobiological results suggest that proton irradiation can cause significant lethal damages in both normal and cancerous cells. The obtained experimental data from biological models will serve for comparisons with Monte Carlo simulations and LEM II calculations.

INTRODUCTION

Due to their excellent physical properties, protons offer several advantages for treating localized small sized tumors in comparison to the other radiotherapy techniques [1]. In clinical practice, the relative biological effectiveness (RBE) of proton beams is currently approximated as constant value of 1.1. However, emerging data shows that RBE varies as a function of dose, endpoint, and linear energy transfer (LET) [2]. Nowadays, the use a single RBE value in proton radiation therapy is considered to be an oversimplification which can potentially lead to considerable uncertainties and put healthy tissues at risk [3]. Therefore, a variable RBE would be more appropriate to describe the radiobiological effects of protons on both cancerous and normal cells [4]. Ocular tumors represent a special challenge for radiotherapy because of the close proximity of sensitive tissues which, if altered by irradiation, can lead to serious complications such as visual loss [5].

Since the treatment with protons can affect healthy tissues in the distal parts of the Spread-Out Bragg Peak (SOBP) due to the increase in LET towards the end of the proton beam range, the accurate estimation of the RBE is crucial in proton therapy of the eye [3]. Even though literature data shows favorable clinical outcomes of proton eye therapy [6, 7, 8], more *in-vitro* data about the radiosensitivity of various ocular cancer cells is still required. Incorporation of variable RBE into the future treatment plans holds the potential of reducing the tumor volume while minimizing the concerns about the potential side effects [9].

As a part of an ongoing study, the goal of this work was to provide *in-vitro* data for uveal melanoma cell line which will serve for investigations of the RBE variations along the clinical SOBP. For this purpose, the human 92.1 uveal melanoma cell line representing a highly metastatic form of uveal cancer was chosen. To evaluate damage that arises in typical organ at risk, the normal human retinal epithelial cells was also used. The radiosensitivity of the tested cell lines was estimated by clonogenic assay and will be compared to the results obtained with Monte Carlo calculations and semi-empirical models based on LET experimental measurements.

MATHERIALS AND METHODS

Cell culture conditions

The ARPE-19 human retinal pigment epithelial cell line was purchased from American Type Culture Collections (ATCC, Manassas, VA, USA) while the 92.1 human uveal melanoma was purchased from the Cell Factory-IST (Genoa, Italy). Uveal melanoma cells were cultured in RPMI 1640 cell culture medium (Sigma-Aldrich Chemie GmbH, Steinheim, Germany) while for normal retinal cells DMEM F-12 was used (Sigma-Aldrich Chemie GmbH, Steinheim, Germany). Both cell culture media were supplemented with 10% foetal bovine serum (Sigma-Aldrich Chemie GmbH, Steinheim, Germany) and 1% penicillin/streptomycin (Sigma-Aldrich Chemie GmbH). The cells were maintained in the humidified conditions with 5% CO_2 at 37°C (Heraeus, Hanau, Germany).

Irradiation conditions

Both cell lines were irradiated in the middle of the 62 MeV therapeutic proton SOBP of at INFN-LNS, Catania, Italy. The applied dose rate was ~12 Gy/min. Reference irradiations with photons were performed in Vinča Institute of Nuclear Sciences in Belgrade, Serbia. Irradiations with γ-rays were issued by ^{60}Co source (CIRUS-Cis Bio International, Gif-sur-Yvette, France) at the dose rate of ~1 Gy/min. For both protons and γ-rays, irradiation doses ranged from 1 to 6 Gy.

Colonogenic cell survival

After irradiations, cells were seeded in 6-well plates and incubated for 14 days at 37°C until the formation of visible colonies. For each irradiation dose, cells were seeded at predetermined density. After incubation period, cells were washed in PBS and fixed for 10 minutes with 100% methanol. Afterwards, samples were stained with 1% crystal diluted in dH_2O for 15 min at room temperature. Colonies were defined as groups consisting of more than 50 cells. The samples were counted using ImageJ Analysis PC software. The effect of the different irradiation doses was evaluated based on three individual experiments, each performed in triplicate. The survival curve was fitted by the linear-quadratic (LQ) equation.

RESULTS AND DISCUSSION

Effects of protons on cell survival

The clonogenic capacity of normal and tumor cells after irradiations with γ-rays and protons was tested by clonogenic assay (Figures 1 and 2). The radiobiological response to protons and reference radiation was first tested in normal cells and the fitted curves are shown in Figure 1. According to the results, both γ-rays and protons reduced viability of ARPE-19 cells. The obtained SF2 values indicate that protons have a stronger effect on survival than photons in this cell line with SF2 of 0.47±0.09 and 0.34±0.06, respectively. The capability of a protons to decrease the survival of this cell line can be also described by $RBE_{(2Gy,\ \gamma)}$ and $RBE_{(D10)}$ values. Thus, for ARPE-19 cells, estimated $RBE_{(2Gy,\ \gamma)}$ is 1.37 while $RBE_{(D10)}$ is 1.26. These results indicate the superiority in cell killing of protons over the γ-rays (Figure 1).

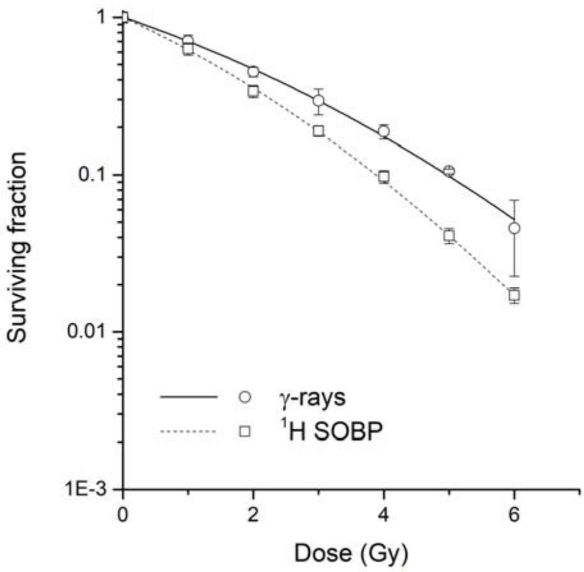

Figure 1. Survival curves of ARPE-19 cells irradiated with γ-rays and protons. Results are presented as mean ± SEM.

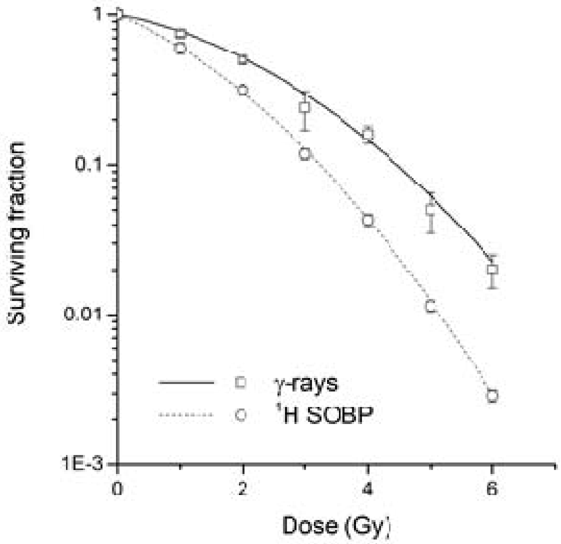

Figure 2. Survival curves of 92.1 cells irradiated with γ-rays and protons. Results are presented as mean ± SEM.

According to the results presented in Figure 2, both irradiation types inactivated uveal melanoma cells. As demonstrated by SF2 values, protons were more effective in reducing the survival of 92.1 cells than γ-rays. The recorded SF2 value after γ-rays is of 0.51±0.2 while this value drops to 0.32±0.06 after the cells have been irradiated with protons. Other radiobiological parameters also point out to the higher radiosensitivity of uveal melanoma cell line to protons than to γ-rays. Thus, the $RBE_{(2Gy,\ \gamma)}$ in this cell line is 1.55 while $RBE_{(D10)}$ is 1.37. When compared to RBE values obtained for ARPE-19 cells, these results show that that protons were somewhat more effective than photons in uveal melanoma than in normal cells.

CONCLUSIONS

The present work provides radiobiological data for uveal melanoma cell line, a model for common tumors of the eye. Obtained data will be compared with data from the experimental measurements of the microdosimetric spectra and from Monte Carlo calculations coupled with the LEM-II model and thus contribute to improvement of the current treatment protocols.

REFERENCES

[1] X. Tian et al., Mol Clin Oncol., 8 (2018) 15.
[2] H. Paganetti et al., Int J Radiat Oncol Biol Phys. 53 (2002) 407.
[3] H. Paganetti. Phys Med Biol. 43 (1998). 2147.
[4] H. Willers et al., Radiother Oncol. 128 (2018) 68.
[5] B. Damato et al., Saudi J Ophthalmol. 27 (2013) 151.
[6] C. Spatola et al., Applied Sciences. 10 (2020) 9071.
[7] G. Cirrone et. al., Front Oncol. 7 (2017) 247.
[8] H. Liu et al., Chin J Cancer. 30 (2011) 315.
[9] R. Mohan et al., Acta Oncol. 56 (2017) 1367.

Analysis of radiation-induced DNA double strand breaks after exposure to alpha particles: γ-H2AX staining method

V. Petković[1], O. Keta[1], G.A.P. Cirrone[2], G. Petringa[2,3],
G. Cuttone[2], A. Ristić-Fira[1], I. Petrović[1]

1) Vinča Institute of Nuclear Sciences, University of Belgrade, Belgrade, Serbia
2) Istituto Nazionale di Fisica Nucleare, Laboratori Nazionali del Sud, Catania, Italy
3) ELI-Beamlines, Institute of Physics (FZU), Czech Academy of Sciences, Prague, Czechia

Abstract – The aim of this study was to analyse the γ-H2AX foci in HTB177 non-small lung cancer cells after irradiation with helium ions. Cells were irradiated in three different positions along the widened Bragg peak to follow formation of DNA DSB with respect to LET values. To compare diverse approaches in γ-H2AX foci analysis, we applied the method of foci quantification and total fluorescence intensity measurements. It was shown that helium ions significantly increased the number of γ-H2AX in all irradiated cells. Somewhat higher number of foci was found in samples irradiated within the LET of 24 keV/μm than in those exposed to 4.8 and 37 keV/μm. The same trend was observed after γ-H2AX total fluorescence analysis, showing a good correlation with the results of γ-H2AX foci counting. Further analysis of foci size, as well as colocalization with other DSB repair factors would complement these analyses and give more information about the nature of DNA lesions induced by helium ions.

INTRODUCTION

Irradiation provokes different types of DNA lesions, where double strand breaks (DSB) are considered as the most lethal. In response to DSB, repair factors are recruited to the lesion site and the process of the DNA repair is initiated [1]. One of the important proteins involved in DSB repair is the histone molecule H2AX. In presence of DSB, H2AX localises close to the lesion site where it becomes phosphorylated (γ-H2AX) and attracts other proteins involved in the repair. Known as an early DSB signalling molecule, γ-H2AX is frequently used as its marker B [1,2].

Fluorescent immunocytochemical labelling of proteins is a reliable tool for DNA damage analysis. It can be used to estimate the distribution of repair factors in injured cells [3]. This approach is commonly applied in γ-H2AX analysis, where foci counting is considered as the most precise. Another way for foci analysis is to measure intensity of the total fluorescence signal. This method is considered less precise comparing to foci counting, because of the background influence on the fluorescent signal [4].

Charged particle cancer therapy currently involves the application of protons and carbon ions [5]. These particles have favorable characteristics over conventionally used photon radiation: high linear energy transfer (LET) and a localized dose distribution. Moreover, they allow a precise dose-delivery to the tumour by reaching the dose maximum at the end of their path, in the Bragg peak region [5]. Among charged particles, helium ions are seen as a new approach for cancer treatment. They show good physical characteristics and could enable better sparing of surrounding tissue comparing to carbon ions. With respect to protons, helium ions show lower lateral scattering [6].

In this study we analysed formation of γ-H2AX foci in HTB177 cells after irradiation with helium ions of different LET. To compare diverse approaches in foci analysis, γ-H2AX quantification and total fluorescence measurements were made.

MATHERIALS AND METHODS

Cell culture

Non-small cell lung carcinoma cell line HTB177 was obtained from the American Type Culture Collection (ATCC, Manassas, Va, USA). Cells were grown in RPMI 1640 medium, supplemented with 10% foetal bovine serum (Sigma-Aldrich Chemie GmbH, Steinheim, Germany) and 1% penicillin/streptomycin (Sigma-Aldrich Chemie GmbH), in humidified environment under optimal conditions with 5% CO_2 and 37°C (Heraeus, Hanau, Germany).

Irradiation procedure

Cells were seeded in slide flasks (Thermo Fisher Scientific, Waltham, Massachusetts, USA) at appropriate cellular densities and maintained in standard conditions. On the next day, cells were irradiated with 62 MeV/u helium ions in three different positions along the somewhat widened Bragg peak. The irradiation positions were attained by interposing Perspex plates of different thickness before the cell monolayer, as previously described [7]. The values of LET for these irradiation positions were 4.8, 24 and 37 keV/μm. Samples were irradiated in pre-cooled growth medium on +4ºC [8]. The irradiation dose was 1 Gy with dose rate ~12 Gy/min. The procedure was carried out at 0° beam line at INFN-LNS in Catania, Italy.

Immunocytochemical γ-H2AX foci analysis

Cells were incubated for 0.5 h post-irradiation, in order to analyse the highest number of foci that could arise after irradiation [2]. After incubation, the growth medium was discarded, cells were rinsed with PBS and fixed in 4% PFA for 15 minutes at room temperature. The permeabilization solution 0.2% Triton-X in PBS was applied for 10 min at 4°C. Blocking and incubation with anti γ-H2AX antibody (Alexa Fluor 488, BioLegend Inc. San Diego, California, United States) was performed as described elsewhere [8]. Micrographs were obtained using laser confocal microscope Leica TCS SP5 II (Leica Microsystem CMS GmbH; Wetzlar, Germany) and processed with LAS AF Lite software (Leica Microsystem CMS GmbH). ImageJ Analysis PC software was used for foci quantification and measurements of total fluorescence intensity. Results are shown with respect to the control that was normalised to 1.

Statistical analysis

Statistical significance was determined with Student's t-test. Results are shown as means ± SEM, while the level of significance was $p < 0.05$.

RESULTS AND DISCUSSION

Quantitative γ-H2AX foci analysis

The HTB177 cells were irradiated with the dose of 1 Gy, as higher doses can cause signal overlap [9]. Irradiation with helium ions increased the number of γ-H2AX foci in all examined samples, around six times when compared to the control ($p<0.001$). Slightly higher number of foci was observed after irradiation with 24 keV/μm when compared to those at 4.8 and 37 keV/μm values of LET. However, no significant differences were found between these experimental groups (Figure 1).

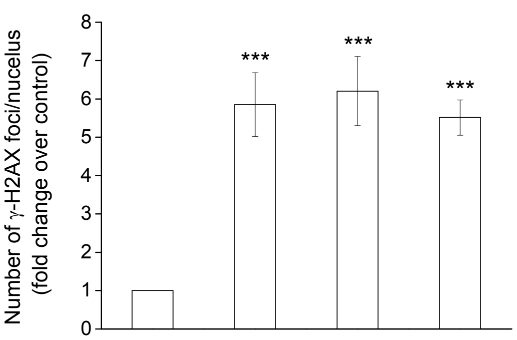

Figure 1. Quantitative analysis of γ-H2AX foci in HTB177 cells, performed 0.5 h after irradiation with helium ions of different LET (4.8, 24 and 37 keV/μm). Cells were irradiated with 1 Gy and results are presented as mean±SEM. *** 0.001 < p.

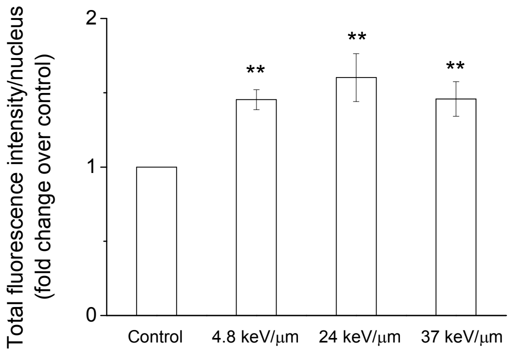

Figure 2. Analysis of γ-H2AX total fluorescence intensity measured per nucleus in HTB177 cells. Samples were irradiated with helium ions of different LET (4.8, 24 and 37 keV/μm). Analysis was performed 0.5 h after irradiation with 1 Gy and the results are presented as mean±SEM, ** $0.001 < p < 0.01$.

Total fluorescence analysis

Total fluorescence analysis showed a significant increase in fluorescent signal 0.5 h post-irradiation in all analysed samples ($p<0.01$). The intensity of fluorescence was the highest in samples irradiated within the 24 keV/μm value of LET, but no significant change was found between different irradiation positions (Figure 2). These findings are confirmed by γ-H2AX foci counting, meaning that there is a good correlation between these two approaches of data analysis.

CONCLUSIONS

Irradiation with helium ions significantly increased the number of γ-H2AX foci in HTB177 cells. Somewhat stronger response of HTB177 cells was noted after irradiation with LET of 24 keV/μm, comparing to 4.8 and 37 keV/μm values of LET. We found good correlation between quantitative γ-H2AX foci analysis and measurements of the total fluorescent signal. The further foci analyses regarding their size and colocalization with other repair proteins are needed for obtaining more information on their complexity.

REFERENCES

[1]. E Rogakou et al., J Biol Chem, 273 (1998) 5858.
[2]. J Banáth et al., CANCER Res, 64 (2004) 7144.
[3]. E Rogakou et al., J Cell Biol, 146 (1999) 905.
[4]. I Suzumel, Chrom Alter, (2007) 145Y.
[5]. H Suit et al., Radiother Oncol, 95 (2010) 3.
[6]. K Held et al., Front Oncol, 6 (2016) 1.
[7]. I. Petrovic et al., Int J Radiat Biol, 96(2020):1400.
[8]. A. Ristic-Fira et al., J Radiat Res App Sci, 13 (2020) 672.
[9]. W. Böcker W et al., Radiat Res. 165 (2006) 113.